ARENBERG DOCTORAL SCHOOL
Faculty of Science

Improving urban land-cover parametrization in regional climate models

The role of urban aerodynamic, thermal and radiative properties, anthropogenic heat and water retention

Hendrik Wouters

Dissertation presented in partial fulfilment of the requirements for the degree of Doctor in Science

May 2014

Improving urban land-cover parametrization in regional climate models

The role of urban aerodynamic, thermal and radiative properties, anthropogenic heat and water retention

Hendrik WOUTERS

Examination Committee:
Prof. Dr. A. Van Rompaey, chair
Prof. Dr. N. P. M. van Lipzig, supervisor
Dr. K. De Ridder, co-supervisor
(Flemish Institute for Technological Research)
Dr. M. Demuzere, co-supervisor
Prof. Dr. S. Carl
Prof. Dr. B. Somers
Dr. R. Hamdi (Royal Meteorological Institute of Belgium)
Prof. Dr. S. Grossman-Clarke (Arizona State University)

Dissertation presented in partial fulfilment of the requirements for the degree of Doctor in Science

May 2014

D/2014/10.705/24
ISBN 978-90-8649-715-7

Preface

Er wordt veel geschreven en verteld over de milieu -en klimaatsproblematiek. Ondertussen draait de wereld maar door, en lijkt alles zijn normale gang te blijven gaan. “Zijn er dan geen mensen die aan de wereldproblemen ook effectief iets doen?” Dat moest ik gedacht hebben alvorens mijn leven even een wending nam, en ik met de post-graduaatopleiding weer -en klimaatmodellering aan de UGent begon. Wat ik op dat moment nog niet wist, is dat één van de docenten Clemens Mensink een onderzoeksgroep leidt waarin ik binnenkort heel veel zal mee te maken krijgen. Hij was immers de cruciale link die me naar een vacature voor een doctoraatsbeurs over modellering van stedelijke luchtkwaliteit op de VITO-website heeft geleid. Ik stuurde een bericht via de website, en kreeg ik van Koen snel een uitnodiging voor een gesprek. Hoe langer hoe en meer werd duidelijk dat deze doctoraatsbeurs op mijn lijf geschreven stond, en ging volop aan de slag tot het maken van een doctoraatsplan. Mijn vreugde was dan ook enorm groot toen ik vernam dat mijn mandaat mocht starten.

En dan begon het doctoraat. Hierbij rolde ik met het Belgisch spoormaterieel gestaag van de ene kant naar de andere kant van het land, tussen Wetteren, VITO en KU Leuven. De verschillende onderzoeksmilieu’s gaven me de mogelijkheid om verscheidene wetenschappelijke inzichten methodologieën te combineren. Tussen de werkplekken, thuisfront en congressen heen was dit doctoraat een erg boeiend avontuur, waarin ik telkens mijn grenzen kon verleggen op wetenschappelijk en maatschappelijk vlak.

Tijdens mijn doctoraat werd ik begeleid door een opmerkelijk triumviraat van promoteren. Elk op hun totaal verschillende maar steeds enthousiaste manier droegen zij complementair bij aan dit meerjarenwerk. Zij leverden ontzettend veel interessante ideeën en input aan bij het tot stand brengen van dit doctoraat. Tegelijk lieten ze mij ook de vrije loop, en speelden ze daar elegant op in. Ze moedigden oa. ook aan op bepaalde zaken wat langer stil te staan, ook al nam het oorspronkelijk plan hierdoor een wending. Ook mede dank zij hen heb ik ontzettend veel skills opgedaan, en met de vele congressen een internationaal netwerk uitgebouwd.

Maar nu is het af, ’t is gedaan, ’t is gelukt! Ik blik dan ook met enorme fierheid terug op de afgelegde weg. Nu kan ik verder gaan met een groot vertrouwen in de wereld en mezelf, nieuwe horizonten tegemoet.

Ik wil vooreerst mijn co-promotor Koen bedanken voor de kans om dit doctoraat te kunnen starten. Zonder jouw aanzet tot dit doctoraatsproject, had dit boekje nooit bestaan. Je was niet zuinig met het aangeven briljante ideeën en vernieuwende, vernuftigde onderzoeksmethodologieën. Ook deed jij de grootste inspanning om mijn - toegegeven,

soms wel warrige - hersensspinsels te begrijpen, en dit mij naar meer begrijpelijke taal te doen omzetten. Omgekeerd, jij hebt de bewonderenswaardige gave om heel erg moeilijke concepten op zo'n natuurlijke, heldere en aangename manier te kunnen uitleggen, waar ik ontzettend veel heb van geleerd.

Vervolgens wil ik mijn co-promotor Matthias mijn grote dank betuigen. Toen je terugkwam van Australië bleek al snel dat onze interesses en kijk op de wereld erg overlappen, en dat we goede vrienden zouden worden. Jouw onuitputtelijke drang voor het opnemen van verantwoordelijkheden en het in gang zetten van nieuwe initiatieven heb ik altijd erg gewaardeerd. Met jouw ongelooflijk management talent, zie je al van in het begin waar de zaken fout lopen en zoek je naar oplossingen. Wat ik ook vooral geleerd heb van jou is dat doctoreren eigenlijk zo goed als gelijk staat aan amuzeren. Deze wetenswaardigheid is van hoogst belang, vooral wanneer tijdens doctoraatsonderzoek de limieten van ons wetenschappelijk brein worden afgetast. Voorts zal ik de vele nerdy momenten tijdens het sleutelen aan ons warmdraaiend reken/opslag-station niet gauw vergeten. Ook bewonderenswaardig is jouw magische glazen bol, die wetenschap en wijsheid aanreikt tot voorbij de horizon aan de andere kant van de wereld. Mijn doctoraat is hier dan ook van doordrongen. Jouw drang naar avontuur en nieuwe uitdagingen trok me dan ook mee naar verre oorden waar 's nachts de stadsturbulentie maar bleef hangen ... tot in de vroege uurtjes. YAMAS!!!

Bij deze wil ik ook mijn promotor Nicole bedanken. Via de group meetings moedigde je de interactie en verbanden binnen de diverse onderzoeksdomeinen in onze RCS-groep aan. Je was ook niet schuw voor het geven van stevige portie kritiek, echter zonder iemand te hoeven schofferen. Tegelijk stond je op moeilijke momenten klaar met een luisterend oor. Met jouw opmerkzame en nauwgezet analytische vermogen zie je de belangrijke wetenschappelijk verbanden tussen onze RCS-groep en andere takken van de vakgroep geografie, de onderzoeksgroepen van de KU Leuven en daarbuiten, én je reikt hen de hand. Dit alles leidt tot een aangename sfeer en hoogstaand-academisch niveau binnen onze onderzoeksgroep waar ik tijdens mijn doctoraat zeer graag deel van uit heb gemaakt. Je lijkt wel onvermoeibaar, ondanks jouw drastische gezinsuitbreiding, en de gepaardgaande kinderopvangbacteriëen die je te verwerken kreeg. Daar kijk ik naar op.

Speciale dank gaat ook uit naar de collega's van het MAP-team in VITO voor hun ondersteuning, waaronder Dirk, Bino, Lisa, Peter, Peter, Nele, Nele, Wouter, Filip, Guy, Felix, Hans, Jean, Wim, Stijn, Stijn, Mieke en nog vele andere. De gezellige momenten onder de middag aan Sas-6 (toen ze maandag nog open waren) met een fris bier tussen de wielertoeristen zal ik niet vlug vergeten. Ook wil ik jullie bedanken voor jullie heel leerzame input bij voorbereidingen voor en tijdens dit doctoraat. In het bijzonder wil ik ook Dirk bedanken die me heeft ingeleid in het hele VITO -en doctoraatsgebeuren, en die me tijdens de voortgang van mijn doctoraat enorm heeft geholpen en gemotiveerd. Speciaal wil ik ook de directieleden en unit-managers van VITO bedanken voor mijn onderzoeksvoorstel te laten opstarten, zo ook voor hun feedback bij de voortgangsrapportering.

I would like to thank the rest of the members of the supervisory committee and exam jury of my PhD, namely Rafiq Hamdi, Shaun Carl, Susanne Grossman-Clarke, Ben Somers, and Anton Van Rompaey. They have given a huge amount of interesting input to this work, in particular for reviewing the manuscript.

I would also like to thank all the members of the CLM-community, in particular: Barbara Früh and Andreas Will, for the coordination, Edouard Davin, the coordinator of the SOILVEG working group who motivated me for coordinating the URB working group, Kristina and Sebastian for our cooperation within our urban intercomparison project, Gerhard Smiatek, Ulrich Blahak and Gerd Vogel who all offered great support to my work. I will always remember our great assembly times in Cava De' Tirenni, Rome, Frankfurt, Zürich, and Leuven.

Enorme dank gaat uiteraard uit naar de collega's van het rode verdiep van het GEO instituut voor de vele gezellig babbels onder koffie -en theegeslurp, in het bijzonder: mijn nieuwe lokaalgenoten, Matthias, Karolien, Jianlin, Lotte, Marjolein, Jan, en Huang, mijn vorige Lokaalgenoten, Wim (Clymans), Klaartje, An, Du, Florin, Tim en vele andere, the members of the RCS-group, Sam, Wim, Fabien, Tom, Kristof, Sajjad, Stef, Jan , Erwan, Annemarie and Irina (in particular for all their valuable input), het secretariaat en technisch personeel voor alle ondersteuning.

Hierbij wil ik ook de Vlaamse Instelling voor Technologisch Onderzoek (VITO) speciaal bedanken die dit doctoraatsmandaat heeft gefinancierd. Ook wil ik het Federaal Wetenschapsbeleid (BELSPO) bedanken voor de bijkomende fondsen. Voorts wil ik het Vlaams Sumercumputer Centrum (VSC) bedanken voor de nodige computertijd op de VIC cluster en de TIER1 cluster, in het bijzonder Jan Ooghe en Martijn Oldenhof voor technische ondersteuning. Ook wil ik de mensen bedanken die zich hebben toegewijd tot het uitvoeren van metingen, waarvan ik in dit doctoraat dankbaar gebruik heb gemaakt, in het bijzonder Daniel Tielemans (VMM), Johan Camps (SCK-CEN), en mijn collega's Bino, Dirk en Koen (VITO).

Speciale dank gaat ook uit naar mijn (schoon)ouders, (schoon)familie (Arnold, Johan, Tom, Kris, Jonathan, Tim, Pascal, Goedele, Heidi, Lieselot, Sarah, Rebekka, Goedele, Anna, Louisa) voor de vele gezellige familiebijeenkomsten. Ook zij hebben me enorm gesteund, in het bijzonder bij het maken van soms moeilijke beslissingen die aan de basis lagen van dit meerjarig gebeuren. Ook wens ik mijn thuisvrienden (Jonas, Bernd, Koen, Domien) en huisgezellen (Jonathan, Sonny en Rebekka) bedanken, die altijd erg nieuwsgierig waren naar wat ik in dit doctoraat allemaal heb zitten bekokstoven.

Als laatste wil ik mijn enorme liefde en dank betuigen aan mijn fantastische vrouw Helena. Gij waart de verademing, de oase, tijdens de ups en downs van dit doctoraat. Je gaf me tijdens mijn doctoraat een gezonde, stevige portie relativeringsvermorgen, en wees je me op de échte belangrijke dingen van het leven. Hiermee hield je mij niet te ver van het aardoppervlak dicht bij jou, de dansvloer op. Naarmate het einde van mijn doctoraat naderde, kreeg je echter meer en meer verantwoordelijkheden op jouw schouders. Deze vielen dan ook enorm zwaar toen het voor ons tegenslagen begon te regenen. Ondanks de lange dagen heb ik dank zij jouw ontzaggelijke inzet kunnen genieten van de eerste levensjaren van onze prachtige dochter, ons Bérilune!

Tot slot wens ik deze thesis op te dragen aan mijn grootmoeder, Jenny Montaelt, die eergisteren is overleden.

Hendrik

Wetteren, 4 mei 2014.

Abstract

Outdoor thermal comfort is essential to our health and that of the environment. For the last 200 years, the global population has increased sevenfold resulting in a strong urban expansion. Consequential changes in the landscape have lead to drastic climate modifications, which ranks among the most significant human impacts on the environment. Most remarkable is that cities are exposed to higher air temperatures than those in the natural surroundings. This phenomenon - known as the urban heat island - causes serious health risks for many people in the city. Especially in large cities, mortality rates are higher during heat waves, such as that of the European summer of 2003. At the same time, it is expected from global climate change that cities are more often exposed to extreme weather, including the increased number of strong heat waves. More severe droughts, floods and the deterioration of air quality will place increasing pressure on the livability of cities as well. As the proportion of people living in cities increases globally, mayors are faced with the big challenge of mitigating climate change and adapting their cities exposed to it.

The general goal of this thesis is to provide an efficient and reliable assessment tool for urban climate change at the regional scales available for a wide research network. Herein, we aim for enabling a full assessment for every mid-latitude synoptic season and weather type, including summer heat waves, storms and cold winters. Therefore, we contribute several important improvements to urban-climate modelling research. Finally, we provide a model-based description of the urban climatic drivers of the surface energy balance and the urban heat island effect, including their diurnal cycle, daily variability and seasonal dependency.

The diurnal cycle and spatial extent of the urban heat island of Paris are acquired for a heat-wave of 2006 with a model-based approach first. Besides the changes in the surface-energy balance such as the nocturnal excess in surface sensible heat flux, it is demonstrated with an idealized advection model that a reduced vertical adiabatic cooling over Paris compared to cropland brings an additional urban heat island build-up of 25%. The urban heat island and its vertical extent are strongly affected by the boundary-layer temperature lapse rate, nocturnal low-level jet and radiative cooling as well. Therefore, model developments to better represent these nocturnal boundary-layer features in atmospheric models are needed for more reliable assessment of the urban heat island during heat waves.

A new efficient urban land-surface parametrization TERRA-URB is developed for the regional climate model CCLM. It is dealt with important deficiencies in state-of-the-art

urban-climate modeling. Firstly, an efficient algorithm is developed for calculating the surface-layer turbulent momentum and energy transfer between urban environments and the atmosphere above. Simulations with TERRA-URB configured for an urban site at Toulouse centre demonstrate that our algorithm considerably improves to model performance in terms of the surface-energy balance compared to CCLM's standard procedure. Furthermore, TERRA-URB coupled to CCLM configured for Belgium is able to simulate the urban heat island of Antwerp, whereas the standard CCLM model fails to. Secondly, we provide a simple formulation for the infra-red opacity of water vapor for urban land-surface modelling evaluation with observations from sensors installed a few tens of metres above roof level. The formulation eliminates an overestimation - reaching values of over $35\,\mathrm{W\,m^{-2}}$ for sunny days - for the upward infra-red radiation. Thirdly, a new water-storage parametrization for urban land-use is developed for which a distribution of water reservoirs on the impervious surface is considered. Parameters for urban water storage are obtained for Toulouse centre with model sensitivity experiments. Herewith, TERRA-URB reproduces the timing, magnitude and persistence of evaporation increase after rainfall better than employing more arbitrary water-storage parametrizations. Finally, modelling the annual urban surface energy balance and the urban heat island with TERRA-URB is improved by applying a dataset of anthropogenic heat release (i.e., waste heat from human activity) with an annual and diurnal cycle.

Model runs with TERRA-URB for Toulouse centre show augmented evaporation rates of $60\,\mathrm{W\,m^{-2}}$ on average after rainfall which lasts for 12 daytime hours on average. The annual-mean evaporation from the urban impervious surfaces ($5.7\,\mathrm{W\,m^{-2}}$) is an order of magnitude lower than that from the natural surroundings ($45\,\mathrm{W\,m^{-2}}$). These results indicate that the water storage, evaporation and run-off induced by urban expansion can affect atmospheric moisture, precipitation, and the occurrence of pluvial flooding.

Sensitivity experiments with CCLM coupled to TERRA-URB over Belgium have led to an overall better understanding of the drivers leading to the urban heat island and their seasonal dependency at the regional scales. It turns out that both urban structure, anthropogenic heat release and their interaction determine the seasonal variability of the urban heat island intensity. Remarkably, the averaged contribution of urban structure to the nocturnal urban heat island for the cities in and around Belgium ($+0.41\,\mathrm{K}$ for Brussels) during winter is smaller than that from the anthropogenic heat ($+1.24\,\mathrm{K}$). Conversely, the contribution of urban structure ($+1.97\,\mathrm{K}$) dominates that of the anthropogenic heat ($+0.68\,\mathrm{K}$) during summer. The respective contributions mostly counteract each other during summer ($-0.21\,\mathrm{K}$), whereas they enhance each other during winter ($+0.25\,\mathrm{K}$).

Within the general assessment of climate change projections, land-use change scenarios and urban-climate mitigation, we recommend to account for the impact of both urban structure, anthropogenic heat, their interactions and their seasonal dependency on the regional climate. Hereby, their respective influences on the urban thermal comfort both in a positive or negative way needs to be considered as well. Finally when employing policies needed for mitigation and adaptation of climate change on the global scale through urban modifications, one needs to account for the possible consequences on the regional scale in urban areas as well.

Korte samenvatting

Thermisch comfort buitenshuis is essentieel voor ons welzijn, dat van onze omgeving en van ons milieu. In de laatste 200 jaar is de globale populatie verzevenvoudigd wat resulteerde in sterke groei van steden. De daaruit voortvloeiende veranderingen in het landschap heeft geleid tot drastische klimaatswijzigingen behorend tot de meest significante menselijke invloeden op de omgeving. Het meest opvallende is dat hogere temperaturen worden waargenomen in steden dan in de nabije natuurlijke gebieden. Dit fenomeen - bekend als het stedelijk warmte-eiland - brengt ernstige gezondheidsrisico's met zich mee voor de vele mensen in de stad. Vooral in grote steden worden hogere sterftecijfers waargenomen tijdens hittegolven, zoals die van de Europese zomer van 2003. Terzelfdertijd verwacht men van de klimaatsverandering dat steden meer en meer blootgesteld worden aan extreme weersomstandigheden, inclusief de stijging van het aantal sterke hitte golven. Ook de toename van droogtes, overstromingen, en luchtvervuiling zullen de leefbaarheid van steden meer en meer in het gedrang brengen. Met de toename van het aandeel van stadsbewoners worden burgemeesters geconfronteerd met de grote uitdaging tot mitigatie van klimaatsverandering en tot adaptie van hun steden hieraan blootgesteld.

Het algemene doel van deze thesis is het verschaffen van een efficiënt, betrouwbaar hulpmiddel voor de beoordeling van stedelijk klimaat op regionale schaal beschikbaar voor een groot onderzoeksnetwerk. Hierin beogen we een integrale beoordeling van elke synoptische weersconditie op gematigde breedtegraden, inclusief hitte golven, stormen en koude winters. Voorts worden een aantal belangrijke bijdragen aangeleverd tot verbetering van stedelijke klimaatsmodellering en onderzoek. Tot slot bieden we een modelmatige beschrijving van de stedelijke invloeden op de oppervlakte-energiebalans en het stedelijk warmte-eiland, dit met inbegrip van hun dagelijkse cyclus, dagelijkse variabiliteit en seizoensgebonden afhankelijkheid.

Eerst brengen we met een modelmatige aanpak de dagelijkse cyclus en ruimtelijke omvang van het stedelijk warmte-eiland van Parijs in kaart tijdens een hittegolf in 2006. Naast de verandering in de oppervlakte-energiebalans, zoals het nachtelijk exces in de voelbare warmte, wordt aangetoond met een geïdealiseerd advectiemodel dat de reductie van verticale adiabatische afkoeling over Parijs t.o.v. de omgevende gewassenvelden verantwoordelijk is voor een verhoging van de intensititeit van het stedelijk warmte-eiland met 25%. Voorts wordt het stedelijk warmte-eiland en zijn verticale uitstrekking sterk beïnvloed door de nachtelijke grenslaagstabiliteit, de low-level jet en afkoeling door infraroodstraling. In dit opzicht zijn ontwikkelingen die de voorstelling van deze nachtelijke grenslaageigenschappen verbeteren in atmosfeermodellen cruciaal voor een

betrouwbaardere beschrijving van het stedelijk warmte-eiland tijdens hittegolven.

Een nieuwe, efficiënte parametrisatie voor stedelijke oppvlakken TERRA-URB wordt ontwikkeld voor het regionale klimaatsmodel CCLM. Hierbij worden belangrijke tekortkomingen in state-of-the-art stedelijke klimaatsmodellering behandeld. Ten eerste wordt een efficiënt algorithme ontwikkeld voor de berekening van de turbulente momentum -en energieuitwisseling tussen stedelijke omgevingen en hun bovenliggende atmosfeer. Onze modelsimulaties met TERRA-URB voor een stedelijke site in het centrum van Toulouse tonen aan dat dit algorithme de modelperformantie in termen van de oppervlakte-energiebalans sterk verbetert t.o.v. de standaardprocedure in CCLM. Simulaties met TERRA-URB gekoppeld aan CCLM over België zijn in staat om de intensiteit van het stedelijke warmte-eiland voor Antwerpen the reproduceren, iets waarin het standaard CCLM model in faalt. Ten tweede verschaffen we een eenvoudige formulering om de ondoorzichtheid van waterdamp in het infrarood-spectrum in rekening te brengen in stedelijke modelevaluatie met observaties van sensoren geïnstalleerd op enkele tientallen meter boven dakhoogte. Deze correctie eliminieert de overschatting - die waarden bereikt van meer dan $35\,\mathrm{W\,m^{-2}}$ voor zonnige dagen - van opwaartse infraroodstraling. Ten derde, een nieuwe wateropslagparameterisatie voor stedelijke landoppervlaken wordt ontwikkeld waarin een distributie van waterreservoirs op ondoordringbare oppervlakken wordt beschouwd. Parameters voor stedelijke wateropslag worden verkregen via een gevoeligheidsexperiment met TERRA-URB. Hiermee kan TERRA-URB de timing, magnitude en persistentie van de verhoogde verdampingssnelheid na regenval beter voorspellen dan het toepassen van meer arbitraire wateropslagparametrisaties. Tenslotte wordt de modellering van de jaarlijkse oppervlakte-energie balans en het stedelijk warmte-eiland verbeterd door het gebruikmaken van een dataset voor anthropogene warmte (i.e. warmte die verloren gaat bij menselijke activiteit) met een jaarlijkse en dagelijkse cyclus.

Simulaties met TERRA-URB voor het centrum van Toulouse tonen verhoogde verdampssnelheden aan startende van $60\,\mathrm{W\,m^{-2}}$ na regenval, en deze duren gemiddeld 12 daguren. De jaarlijks gemiddelde verdamping van stedelijke ondoordringbare oppervlakken ($5.7\,\mathrm{W\,m^{-2}}$) is een grootteorde kleiner dan dat van deze van de natuurlijke omgeving ($45\,\mathrm{W\,m^{-2}}$). Dit suggereert dat wateropslag, evaporatie en run-off geïnduceerd door stedelijke uitbreiding de atmosferische waterdamp, neerslag en het optreden van overstromingen.

Simulaties met CCLM gekoppeld aan TERRA-URB voor België hebben geleid tot een beter inzicht in de oorzaken van het stedelijk warmte-eiland en hun seizoensafhankelijkheid op regionale schaal. Zowel stedelijke opbouw, anthropogene warmte, als hun interactie blijken de seizoensverandering van het stedelijk warmte-eiland te bepalen. Opvallend is dat de gemiddelde bijdrage van stedelijke opbouw tot het nachtelijk warmte-eiland voor steden in en rond België ($+0.41\,\mathrm{K}$ voor Brussel) kleiner is dan deze van antropogene warmte ($+1.24\,\mathrm{K}$) tijdens de winter. Daarentegen domineert de bijdrage van stedelijke opbouw ($+1.97\,\mathrm{K}$) deze van de anthropogene warmte ($+0.68\,\mathrm{K}$) tijdens de zomer. De respectievelijke bijdragen werken mekaar meestal tegen tijdens de zomer ($-0.21\,\mathrm{K}$), terwijl deze mekaar versterken tijdens de winter ($+0.25\,\mathrm{K}$).

Binnen de algemene beoordeling van projecties voor klimaatsverandering, landgebruikscenario's en mitigatie van stedelijk klimaat bevelen we aan om de impact van zowel stedelijke opbouw, anthropogene warmte, hun interacties en hun seizoensafhankelijkheid op het regionale klimaat in rekening te brengen. Hierbij moeten ook de respectievelijke invloeden

op het stedelijk thermisch comfort - zowel in de positieve als negatieve zin - beschouwd worden. Tot slot verwachten we dat het in voege brengen van beleidsmaatregelen op vlak van stedelijke aanpassing, die nodig zijn voor mitigatie en adaptatie van klimaatverandering op globale schaal, ook het stedelijk klimaat zullen beïnvloeden op regionale schaal.

Contents

List of Figures

List of Tables

Chapter 1

Introduction

Changes in the landscape by urbanization have lead to drastic climate modifications, which ranks among the most significant human impacts on the environment. Most remarkable is that cities experience air temperatures in excess of rural values, a phenomenon known as the urban heat island (UHI), see Fig. 1.1. The night-time temperature differences are, on average, a few degrees, but can increase to more than 8-9 K under favorable conditions during calm weather conditions. Moreover, the occurrence of heat waves

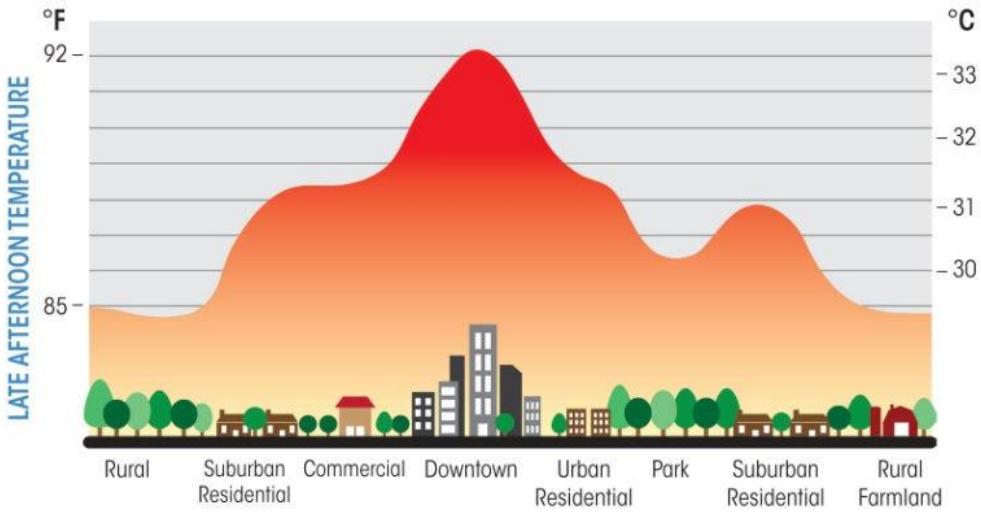

Figure 1.1: The schematic representation of the temperature profile of the urban heat island and its variation with the type of the elements in the urban area. This figure is reprinted from `http://www.cleanairpartnership.org/files/urbanheatisland.jpg`

have been growing for the past few decades as stated in Chapter 14 of the Contribution of Working Group I to the Fifth Assessment Report of the Intergovernmental Panel

on Climate Change (IPCC AR5 WGI Chapter 14) (Christensen et al., 2013). Climate projections indicate that the frequency, intensity, and duration of heat waves are very likely to increase as well. Therefore, cities are expected to be more often exposed to extreme heat stress. More severe droughts and floods will place increasing pressure on the livability of cities as well (Rosenzweig et al., 2011). Making matters worse, it is expected that the proportion of people living in cities will rise on average from 50 % to 69 % in 2050 (United Nations, 2009). In more developed regions, the proportion of people living in cities is expected to reach even 86 % by mid-century whereas in less developed regions, the urban population is projected to increase to 67 % (Breu et al., 2009). All this together makes urban climate one of the most challenging threats of climate change confronting humanity today and in the future.

1.1 Background

1.1.1 Processes affecting urban climate

Cities comprise of a large number of buildings in a rough geometrical configuration, and consist of impervious building materials with large heat capacities. This stands in stark contrast to the natural surrounding areas that comprise of water-permeable soil mostly with vegetation. Therefore, urbanization leads to several modifications in the surface energy balance (Oke, 1982, 1987; Landsberg, 1981). On the one hand, many excess sensible heat sources are found in urban areas in comparison to rural areas:

- First of all, urban areas experience a **large reduction** in **evapotranspiration (ET)** compared to the surrounding rural areas, so that more solar energy is converted to sensible heat and less into latent heat.
- The excess energy is further enhanced by the complex geometry of street canyons which **decreases the effective**[1] **albedo** of cities due to **multiple reflections of shortwave radiation** between the walls of building (see Fig. 1.2).
- **Anthropogenic heat** is released into the atmosphere by combustion of fuels, traffic, households, economic activity and metabolism.
- The complex structure of urban terrain leads to **trapping-effects** (reabsorption of emitted radiation) reducing the **infra-red radiation** emitted by the surface towards the atmosphere

On the other hand, the large **heat capacity** and **conductivity** of the urban building materials including concrete, asphalt, stone, and bricks, together with the reduced surface ventilation within street canyons below roof level, leads to an enhanced surface-heat uptake or **heat-storage** during daytime. This is followed by a prolonged release of stored heat to the atmosphere during the night. A **building-area index** (the outward area of buildings and streets per unit ground surface area) **larger than unity** further increases the effective conductivity and effective heat capacity of urban terrain.

[1] i.e. as observed if one would disregard the urban morphology

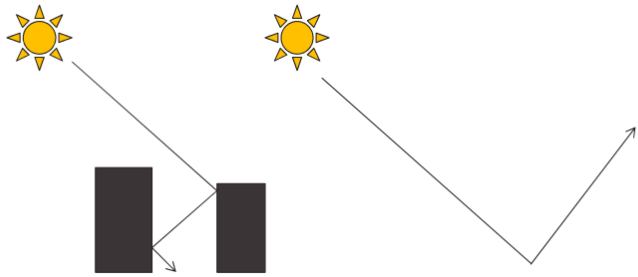

Figure 1.2: Schematic overview of the decreased effective albedo in the presence of buildings

In general, the above-mentioned changes in the surface energy balance directly influence the temperature of the urban-stucture surfaces and the air above, the wind fields and vertical turbulent mixing. The most remarkable impact from the additional heat sources are the higher ground-level temperatures (see Fig. 1.3) and smaller diurnal temperature ranges (DTR), especially for clear-sky conditions during summer. Moreover, the slowdown of the wind speed and differential heating compared to the natural surroundings can lead to changes in the wind circulation in the proximity of the city.

1.1.2 The effect of urbanization on the planetary boundary layer (PBL)

The planetary boundary layer (PBL), also known as the atmospheric boundary layer (ABL), is the lowest part of the atmosphere that is directly influenced by the contact with the planetary surface (Stull, 1988). It acts as an interfacing layer towards the atmosphere above. Consequently, surface roughness and changes in the surface energy balance established by urbanization inevitably influences the turbulent state and vertical extent of the PBL in comparison to the natural surroundings.

The PBL is mainly established by the wind drag initiated the surface roughness, and the buoyancy forces by the surface-atmosphere heat exchange. This induces large variations in wind speed and direction. As a result, large fluctuations occur within the PBL for the physical quantities such as temperature, moisture and pollutant concentrations. This eventually leads to vertical turbulent transport of heat, moisture and pollutants, and drag on the mean horizontal wind flow throughout the PBL. Two principle types of boundary layers exist. This first one is the convective boundary layer (CBL) in which the turbulent flow is mainly established by the drag on the wind and the thermal instability. In the latter, the heating of the surface by solar irradiation sometimes assisted with water-vapor condensation - establishes strong convective updrafts (upward moving air) compensated by downdrafts (downward moving air). This also leads to an mixing (entrainment) of air of the CBL with a air above within the entrainment zone (in Fig. 1.4, this is indicated as 'Entr. Zone'). This results in a growing mixed-layer that can extend over several kilometres above the ground. The entrainment zone mostly occurs as a capping inversion (small strongly-stable atmospheric layer) blocking the convective updrafts from rising

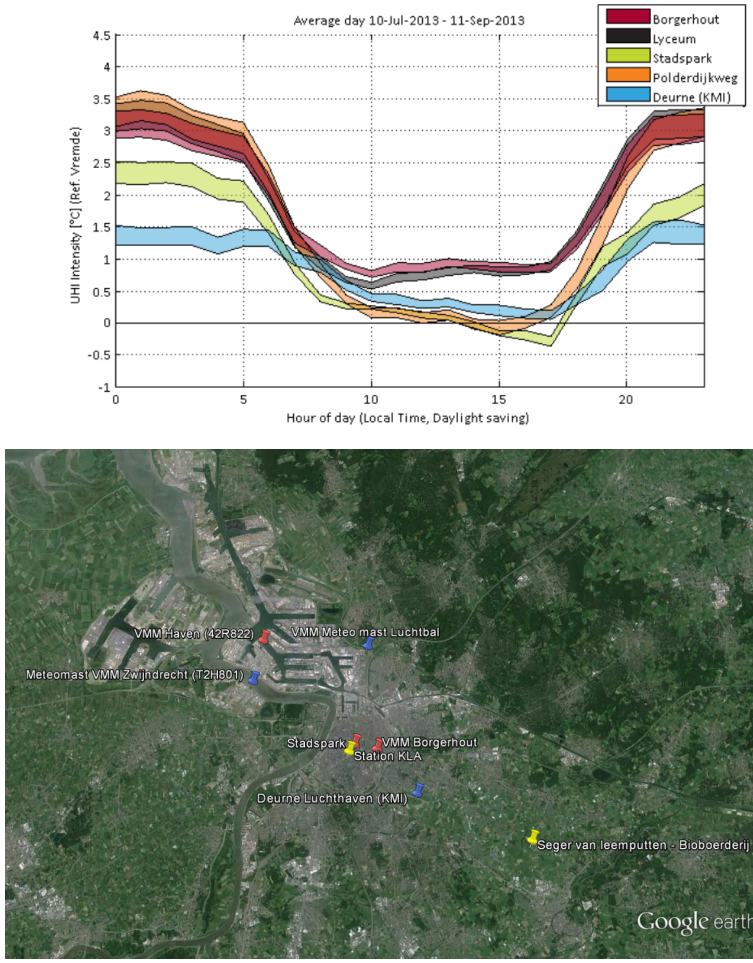

Figure 1.3: The upper panel shows the mean diurnal cycle of the differences in air-temperature (UHI) between various sites within the city of Antwerp, including Borgerhout, Koninklijk Lyceum of Antwerp ("KLA"), city park of Antwerp ("Stadspark"), Polderwijweg, and Deurne) and a reference rural reference site at Vremde (Seger van Leemputten - Bioboerderij). The temperature measurements are established with actively-cooled thermometres. The colored areas represent the uncertainties on the averages. The UHI intensity varies with the location, e.g. lower values in the city park (green line). A map of the observation sites in and around Antwerp are found in the lower panel.

further. Such an inversion layer generally prevents thunderstorms from being developed and this layer can the persist overnight to the next day. The second one is the stable boundary layer (SBL), in which the turbulent flow is solely established by the drag on the wind and dampened by thermal stability. The SBL occurs mostly during the nighttime. In that case, it is referred to as the nocturnal boundary layer (NBL).

In general, the PBL follows a diurnal cycle, see Fig. 1.4: In the morning, a well-mixed CBL is formed when the surface is heated by the sun, and its depth increases throughout

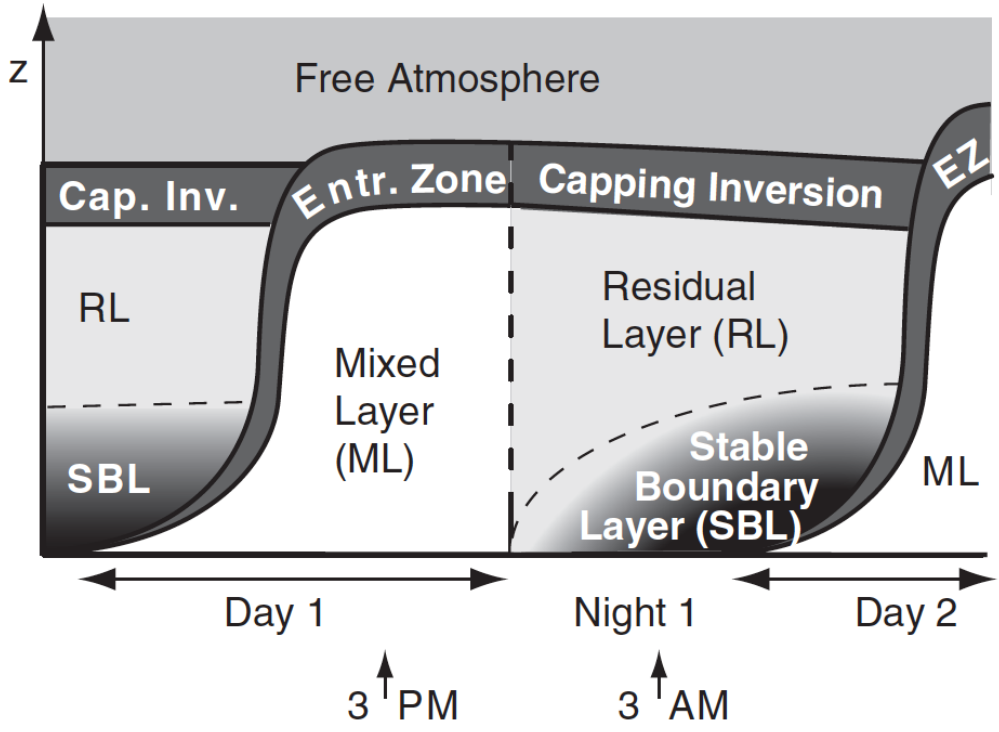

Figure 1.4: The diurnal cycle of the planetary boundary layer (PBL). Figure reprinted from Stull (2005)

the day. At dusk when the heating of the surface stops, the surface temperature decreases by the radiative emission in the infra-red spectrum (wave-lengths of more than 5 µm). As a result, the cooling of the atmosphere by the surface establishes a small SBL. At the same time, an overlying 'residual layer', as the left-over of the daytime CBL, persists in which the vertical turbulent transport is considerably decreased.

Urbanization enhances the vertical motion and turbulent exchange of heat and mass throughout the boundary above by thermal destabilization. A remarkable feature of the UHI is that it becomes much more pronounced in late evening hours (Fig. 1.3): The excess nocturnal surface heating terms by the urban terrain (see Section 1.1.1) inhibits nocturnal cooling at ground level. Instead of the formation of a SBL, a small, well-mixed CBL persists above and downwind of the city.

1.1.3 The impact of urban climate on human health

Even though cities comprise only a very small fraction of the Earth's land-cover, and effects are mostly experienced in the vicinity of urban areas itself, it still holds important health risks for the majority of global population living and working there. A strong relationship between mortality and temperature was found for 11 major cities in the United States by Curriero et al. (2002). In particular, mortality rate generally decreased

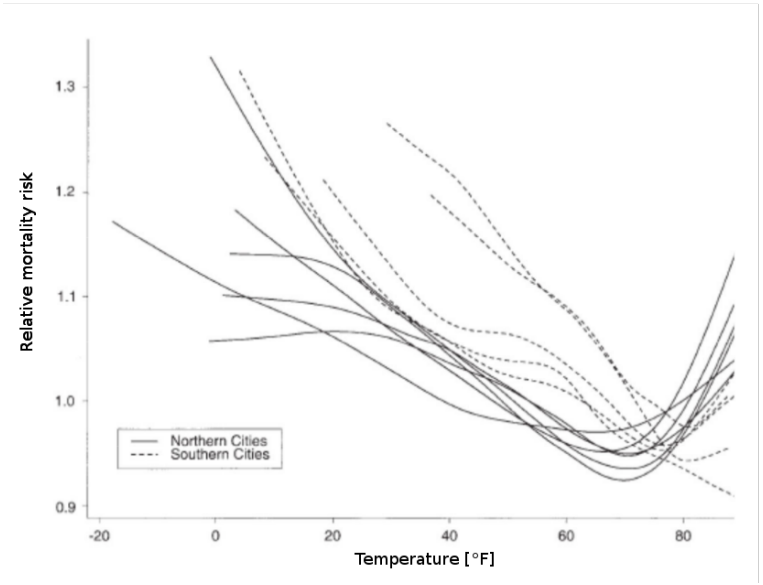

Figure 1.5: Relation between temperature and relative mortality risk for 11 cities in the US. Northern cities: Boston, Massachusetts, Chicago, Illinois, New York, New York, Philadelphia, Pennsylvania, Baltimore, Maryland, Washington DC; Southern cities: Charlotte, North Carolina, Atlanta, Georgia, Jacksonville, Florida, Tampa, Florida, Miami, Florida. $°C = 5/9 \times (°F - 32)$. Figure reprinted from Curriero et al. (2002).

as temperature increased from the coldest days to a certain threshold temperature. Those authors also found the mortality risk to rise above a certain temperature threshold. These results suggests that urban climate affects the overall mortality rate for citizens compared to countrymen both in winter and summer (Fig. 1.5). The relation is also found to be dependent on the particular climatic conditions. This confirms the finding of (McMichael et al., 2006) that people in hotter countries are more affected by colder temperatures, and people in cooler climates are more affected by warmer temperatures.

Elevated temperatures lead to increased mortality as reviewed by Basu (2002). Hereby, a long exposure to high temperatures inhibits the human body to cool down by sweating (Desforges en Simon, 1993). In July 1995, Chicago sustained a heat wave that resulted in more than 600 excess deaths and 3300 excess emergency department visits (Dematte et al., 1998). More than 52000 Europeans died from heat in Summer 2003 (in Italy, France, Germany, Spain, England and Wales, Portugal, Netherlands, Belgium and Switzerland), see `http://www.earth-policy.org/plan_b_updates/2006/update56`. Figure 1.6 shows the increase in mortality in Paris for 2003 compared to the years 1999-2002.

Noting the negative impact of extreme heat stress on human health, the mortality risk of heat waves - when also the UHI reaches a maximum - becomes larger within cities. As reviewed by Patz et al. (2005), There is a growing evidence that climate-health relationships pose increasing health risks under future projections of climate change. They also indicate that the warming trend over recent decades has already contributed to

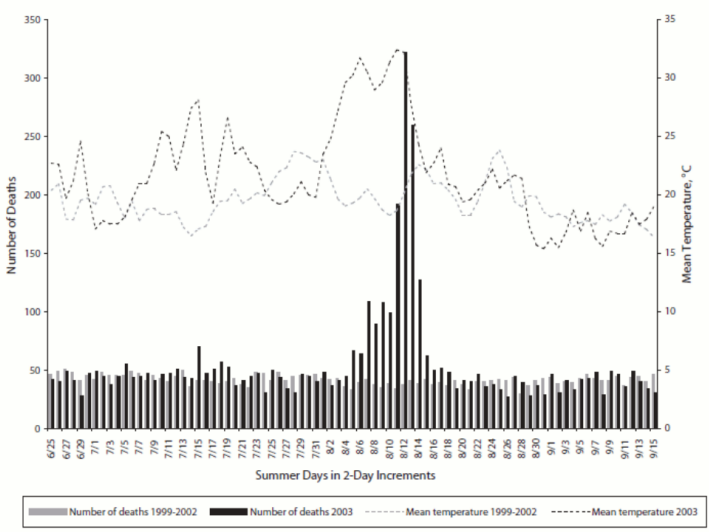

Figure 1.6: Comparison of daily mortality and mean temperature for Paris for 2003 and averaged over 1999-2002, taken from `http://ajph.aphapublications.org/cgi/reprint/94/9/1518.pdf`

increased mortality, which is intensified by the UHI. A recent study on Berlin by Gabriel and Endlicher (2011) found that the mortality rates are higher in the city, especially in its most densely built-up districts, during heat waves. Laaidi et al. (2011) found that in Paris during the heat wave of the summer of 2003, areas exhibiting the highest remotely sensed night-time infrared surface temperature suffered the highest heat-related excess mortality. An important influence of the UHI is its threat on people's night rest when the nocturnal cooling is decreased during heat waves (Ohnaka and Takeshita, 2005; Di Nisi et al. 1989; Libert et al. 1991; Libert et al. 1998)

The UHI also has a positive effect on human thermal comfort in winter, which - apart for the heat stress in summer - should be taken into account by citizen planners as well. In Barrow (Alaska), urban dwellers are exposed to less extreme winters with an averaged increase of 2.2 K in the village compared to the hinterlands (Hinkel et al., 2003). The UHI magnitude generally increased with decreasing air temperatures. They argued that this stems from extra input of anthropogenic heat for maintaining interior building temperatures. Noting the left-hand side of the curve in Fig. 1.5, this suggests less casualties in winter.

1.1.4 Other effects: air quality, energy consumption, sustainability, pluvial flooding and social issues

Apart from the direct health effects, urban climate also has implications on other aspects of the urban society and livability in cities. This includes air quality, energy consumption,

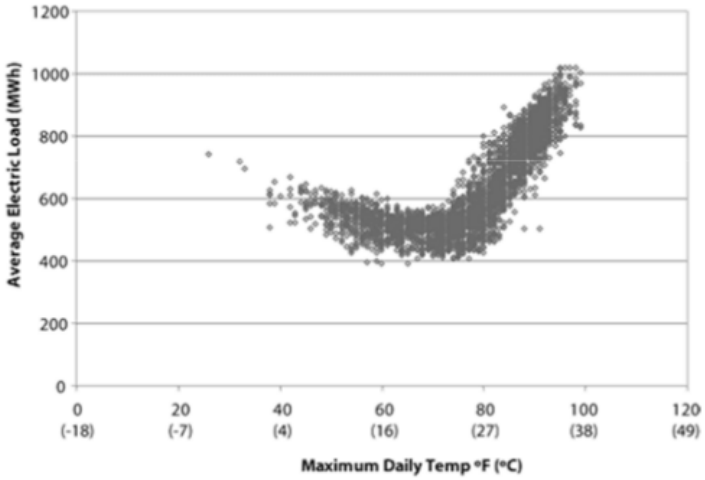

Figure 1.7: Electric energy consumption as a function of ambient air temperature, New Orleans (USA), see Santamouris et al. (2001).

but also implications durability of infrastructure, on the social interactions and hydrology. These are given in more detail below.

Meteorology has a very strong impact on air quality (Seaman, 2003). Emission of pollutants and thus the deterioration of air quality affecting human health occur mostly in urban areas. The important question arises: What are the interactions between the urban climate and **air quality**? Hereby, it is noteworthy that urban climate features such as the UHI occur for similar synoptic weather conditions as episodes of smog with high particulate concentrations during winter, or photochemical smog with high ozone concentrations during summer. Recent urban air-quality studies clearly demonstrate that the UHI phenomenon has considerable implications for air quality (Ryu et al., 2013; Davies et al., 2007; Sarrat et al., 2006).

The increased heat-stress during heat waves acts as a cooling demand (Short et al., 2009). Therefore, **energy consumption** from e.g. air-conditioning is increased (Sailor and Munoz, 1997), and consumes lots of electricity (Akbari et al.,2001). Fig. 1.7 shows an example of the electric energy consumption as a function of ambient air temperature in New Orleans. A very steep increase in energy consumption is seen for temperatures higher than 25 °C, which is related increased cooling demand for increased temperatures (e.g. by air conditioning). The UHI effect directly lead to more energy consumption as demonstrated for several cities, such as Sacramento (Simpson 1998), Rotterdam (Bade et al.,2011) and Toronto. For example, Banting et al., 2005 estimated that a mean decrease in summer temperature of 2 °C in Toronto would lead to an annual cost-saving of 12.4 miljon dollar, or about 5 dollar per citizen per year.

Urban climate has an impact on the endurance of **urban infrastructure**. Kumar en Imam (2013) reviewed the possible effects of climate change on infrastructure. Hereby, high temperatures lead to faster deterioration of certain building materials (e.g. concrete, asphalt, stone, and bricks) of railway and road infrastructure. The heat wave of 2003

resulted in deformed railways which has lead to delays and a total cost of more than 3.5 million pounds. Kumar and Imam (2013) expect a increase in deformations of railway by more extreme summer temperatures. A review of Royne et al. (2005) indicate that photovoltaic panels may experience both short-term (efficiency loss) and long-term (irreversible damage) degradation due to excess temperatures. In the one hand, increased temperatures in winter also suggests positive effects such as a less freezing of roads in winter. This may lead to fewer road accidents in cities and less need for sea-salt spreading which damages the roads and increases corrosion to motor vehicles. Less cold-stress to rail-way infrastructure cities may also imply fewer delays in public transportation. The increases in winter temperature may also have negative effects. For example in Barrow (Alaska), there is concern that earlier snow-melt after winter threatens the structural stability of roads, buildings, and pipelines (Hinkel et al., 2003). Urban climate has also a positive impact on vegetation in cities: Cook-Anderson (2004) discovered from satellite imagery that the growing season in 70 cities of the north-east of America has extended by 15 days in comparison with the surrounding countryside. On the other hand, vegetation become less healthy during droughts because more water in cities is lost to run-off by the large share of impermeable surfaces. The latter makes the city vulnerable to **pluvial flooding** and river floods.

Urban climate also affects outdoor **social activity**, (sporting) events, tourism and hospitality industry. On the one hand, the UHI increases the risk of heat problems for the human body during sporting activities even for healthy middle-age people (Kovats and Ebi 2006), so that it leads to cancellation of sporting events. Other social implications to extreme heat stress are 'social isolation' (Klinenberg, 2003; McGeehin en Mirabelli, 2001), but also psychological problems that leads to aggressive behavior (Nitschke et al. 2007). On the other hand, higher temperatures in the evening suggests more favorable weather for outdoor social activity and (sporting) events in spring and autumn for mid-latitude cities.

1.2 State-of-the-art urban-climate research

1.2.1 Urban Climate modelling

Urban climate modelling is increasingly considered a relevant tool for the assessment and efficiency of urban adaptation measures aiming at the improved climate resilience of cities. Over the past decades, numerical schemes of varying complexity have been developed to represent urban surface physics in atmospheric models (I). They are used to perform urban climate modelling impact studies (II), and to evaluate adaptation strategies (III). A more detailed overview the state-of-the art urban-climate research areas is given below (I to III).

I. Model developments

Besides the main climatic features specified in Section 1.1.1, the heterogeneity of urban design with respect to physical properties (Stewart and Oke, 2012) of the used urban materials and the urban morphology could lead to complex exchange processes with

respect to aerodynamics and energy transfer. In fact, the complex processes lead to a high variability of the wind flow (speed and direction) and of the components energy balance (radiation transfer, heat storage, turbulent heat transfer). This further leads urban subgrid-scale micro-climates, for which local differences in air temperatures are found (mostly below roof level) . For instance, such urban micro-climates are established by the presence of terraces, gardens, street canyons and street corners, facades of large buildings, versus open market places and/or parks with vegetation. A more detailed overview of the physical processes established by the heterogeneity of the urban environment is given below.

Firstly, the complex urban structural design, which encompass building heights and space in between, street-canyon orientation relative to the wind direction, presence of back-yards, and specific building forms, leads to large variabilities in the wind flow patterns and surface ventilation. Secondly, radiation effects that occur in urban environment imposed by the same urban structural design include radiative trapping, and the variability of the radiative trapping depending on the sun position. Sunlit and shaded facets and the heterogeneity of the urban materials in the urban landscape enhances the temperature heterogeneity of the urban surface, so that the turbulent heat exchange with the air above, radiative emission and heat storage among them can impose large variabilities. Interactions can arise (such as advection) between different land-uses within urban environment including green areas with vegetation besides the urban structure. Lastly, additional heat sources from anthropogenic heat release from buildings (either through traffic exhausts, vent holes in buildings, chimneys, ventilation systems and/or heat transfer through walls, windows and the consequential enhanced heat release through radiative emission and surface-to-air turbulent transfer) further complicate the urban exchange processes.

Inherent to any modelling task, one needs to make certain assumptions to represent the above-mentioned urban physical processes. Hereby, a simplified representation of the relevant processes occurring in urban environments needs to be made. The large complexity of the urban climatic features have triggered the development of a wide range of model (approaches) which strongly vary in complexity. An important issue discussed within the urban-climate research community until recently is the relation between model performance and model complexity as discussed in Grimmond et al. (2010, 2011).

Substantial efforts have been made for the representation of the urban urban climatic processes with urban land-surface models in terms of radiation processes in street canyons (e.g. Oleson et al., 2008; Martilli et al., 2002; Masson, 2000; Hénon et al., 2012; Schubert et al., 2012), turbulent transport of momentum, heat and mass (Kanda et al., 2007), heat capacity of urban terrain (Demuzere et al., 2008; De Ridder et al., 2012), evapotranspiration (Grimmond and Oke, 1991; Sailor, 2011), anthropogenic heat release (Pigeon et al., 2007; Makar et al., 2006; Flanner, 2009; Sailor, 2011; Allen et al., 2011)). Most of these models employ a tile approach in which natural vegetated fraction in cities are treated seperately from the pure urban impervious structures (e.g. Masson, 2000; Hamdi and Schayes, 2007; Grimmond et al., 2010). Recent additional model developments have been undertaken to capture the complex exchange processes imposed by heterogeneities of the urban terrain.

Furthermore, relevant urban climatic features could be identified and implemented. For example, sensitivity tests of Schubert et al. (2012) show that the employment of the

double-canyon radiation scheme (DCEP), the separate treatment of diffuse and direct solar irradiation, and physical consistency in the the urban energy balance are important in the case of urban regions with large variety in building heights. Explicit representation of vegetation in between buildings (Lemonsu et al., 2012b; De Ridder et al., 2014) could improve the urban-climate modelling performance. Some numerical schemes include the representation of wind drag and heat exchange by high buildings penetrating the higher atmospheric levels (Martilli et al., 2002; Schubert et al., 2012).

II. Impact studies

Urban climate modelling impact studies has been performed for the past 15 years by coupling urban parametrizations to regional climate models. Most of them focus on the assessment of the urban heat-island (Harman and Belcher, 2006; Van Weverberg et al., 2008; Lemonsu et al., 2009; Sarkar and De Ridder, 2010; Grossman-Clarke et al., 2010; Bohnenstengel et al., 2011; Hamdi and Van de Vyver, 2011), the consequential (re-)circulation (Lemonsu and Masson, 2002) and changes in precipitation (Hamdi et al., 2012; Lemonsu et al., 2012a) by urbanization at the regional scale with regional-climate models (RCMs). Others have been focussing on the urban impact on the global scale (Zhang et al., 2013; Oleson et al., 2011). As urban expansion drastically alters the surface energy and water balance, it alters the precipitation over and downwind of the city and pluvial flooding. For instance, increased turbulence over cities could trigger convective updrafts, and this leads to more localized precipitation (Hamdi et al., 2014).

III. Heat-stress mitigation and adaptation

Urban-climate models are used to investigate various heat-stress mitigation and adaptation strategies including green urban infrastructure, high-reflective surfaces and thermal properties of building materials and vegetation (Schubert and Grossman-Clarke, 2013; Oleson et al., 2010; Taha, 1997; Taha et al., 1988). These strategies directly lower the day-time heat storage in urban structures through shading, evapotranspiration, and reflection of radiation. Urban infrastructure for enhanced water storage in tanks, water infiltration and evapotranspiration (Coutts et al., 2012; Demuzere et al., 2014) allows for designing water-sensitive cities (see `http://watersensitivecities.org.au/water-for-sustainable-cities/`)) as well by keeping the precipitated water inside cities. Apart from the beneficial impact on reducing the urban heat stress, this would reduce the risk of pluvial flooding and water scarcity as well.

1.2.2 Urban climate (modelling) of the future

As stated by IPCC AR5 WGI Chapter 14 (Christensen et al., 2013), heat waves can be amplified by drier soil resulting from warming in Europe (Vautard et al., 2007; Seneviratne et al., 2010; Hirschi et al., 2011) In particular, global climate change would imply an occurrence of severe heat waves (e.g. the summer 2003) at least every 2 years at the end of this century (Diffenbaugh and Giorgi, 2012; Schär et al., 2004). Preliminary results of the ESA UHI project 8 (`http://www.urbanheatisland.info`) shows a strong correlation between the mean UHI at 22:00 UTC and mean air-temperature (Fig. 1.8)

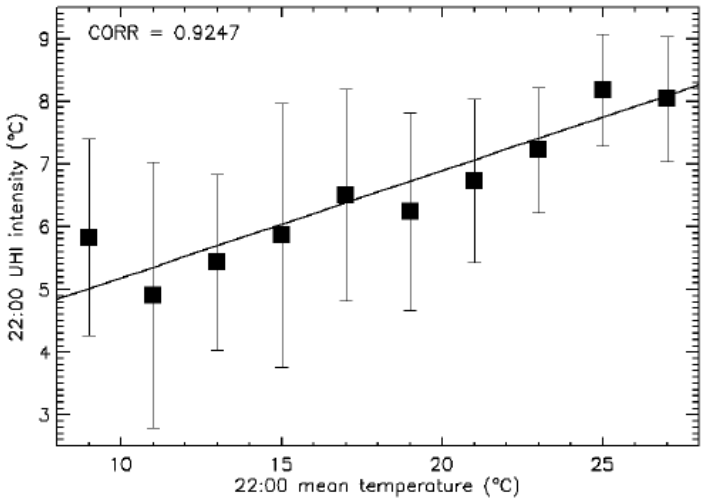

Figure 1.8: The markers represent the mean UHI intensity and their standard deviation UHI of Paris at 22:00 UTC during may-september 2003. These UHI values values are binned with intervals of 2 °C for the mean air-temperatures.

during the summer months. A possible explanation is that cities consisting of urban impervious dry land-cover without vegetation are less capable to counteract heat waves than their natural surroundings (Li and Bou-Zeid, 2013), see Fig. 1.9. Therefore, the impact of urbanization on the local urban/regional climate on top of global climate change itself is expected to become even more severe.

Recently, urbanization has been implemented in regional climate models to study climate change in cities. For example, WRF simulations by (Hara et al., 2010) show a nocturnal UHI increase of 20% under the SRES A2 scenario for Tokyo. Results of future urban heat island studies at the RMI (Hamdi et al., 2014) suggest a decrease of precipitation in the future during summer, which may decrease the counteracting-capability of natural areas as well. It will lead to soil dryness, and this would decrease the overall UHI (Lemonsu et al., 2012a), as the difference between urban and surrounding areas would become smaller. In either case, most cities can expect more frequent, longer, and hotter heat waves than they have experienced in the past(Rosenzweig et al., 2011).

Urban expansion and climate change poses a risk on the increased pluvial flooding. On the one hand as stated by IPCC AR5 WGI Chapter 14 (Christensen et al., 2013), several studies indicate general increases in the intensity and frequency of extreme precipitation in the mid-latitudes during the last four decades. It is expected that the intensity of rainfall will increase further in the future (Rosenzweig et al., 2011). On the other hand, urbanization leads to an increased water run-off, thus increased water-loss to sewage systems and rivers. For instance, Poelmans et al. (2011) calculated that the flood frequency and flood extent by the increased number of extreme precipitation (as presented by 'wet future climate scenarios' minus 'dry future climate scenarios') and the increased urban expansion will amplify each other for the Molenbeek River catchment in Belgium. This is in agreement with (Hamdi et al., 2011) who found that the effect

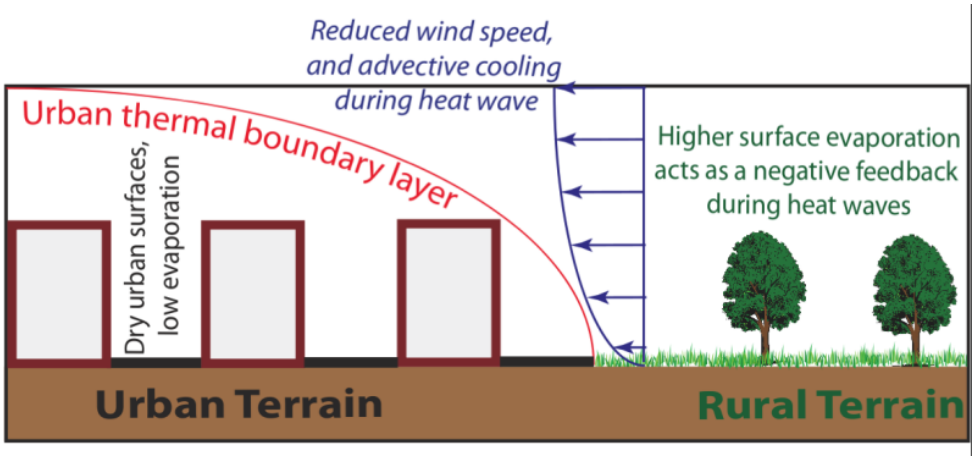

Figure 1.9: Illustration from Li and Bou-Zeid (2013) explaining the increased UHI effect for increased heat-wave intensity: more evapotranspiration at that time acts as a negative feedback to (i.e. counteract) the heat waves in rural areas. This negative feedback is absent for dry urban land cover.

of historical urbanization of Brussels and the effect of a future increased-precipitation scenario exacerbate each other(Rosenzweig et al., 2011).

1.2.3 The need for coordinated climate change projections for cities

Given the risks that urban amplification of climate change poses to the future human society, there is a need for downscaling future climate change projections to the regional scale taking into account urbanization. This includes the seasonal variability of the UHI, urban-induced regional (re-)circulation, changes in precipitation and pluvial flooding. Such urban climate scenarios would be a milestone towards next-level urban-climate mitigation and adaptation, thus an essential task when shaping the sustainable cities of the future. Fortunately, the resolution of regional climate models increase, so that urban climate features such as the UHI and city-induced recirculation can be resolved. However, it becomes more and more problematic that many regional-climate models still **lack a standard urban-land surface parametrization**. Furthermore, **several deficiencies** listed in the next Section still exist **in urban-land surface parametrizations**. Moreover, **efficient and reliable urban regional-climate models applicable for any weather condition, encompassing summer heat waves, severe weather storms and extremely cold winters, are absolutely necessary.** Availability of efficient urban schemes in regional climate models would open the avenue of considering different ensemble members from the future climate-change scenarios. This would allow for a broader risk-management approach (Kunreuther et al., 2013) and more robust policy-making by examining a range of possible outcomes as well as the surrounding uncertainty.

1.2.4 Deficiencies in urban-climate parametrizations for atmospheric numeric models

Several clear deficiencies still exist in urban-land surface parametrizations and urban regional-climate models which hamper the downscaling of future urban-regional climate scenarios and their reliability. Some of the most important deficiencies of current urban-land surface parametrizations are listed below (D1 to D4), and will be addressed in this thesis by identifying their respective relevant physical processes.

D1 Non-iterative calculations in the standard surface-layer transfer schemes are not available for urban areas.
An important issue is that non-interative procedures used in surface-layer transfer coefficients for momentum and heat of atmospheric models are not able to deal with urban land-covers. Hereby, non-iterative procedures are preferred over iterative ones, because they can save a considerable amount of computational cost. This results from the fact that atmospheric models in the early days had a coarse resolution only resolving the synoptic scales, so that the relative small fraction of the earth's surface consisting of urban land-use (only 2% of the total land-cover) could not be resolved. Therefore, the impact of urbanization on these scales is small, and these were ignored. Model developments have only focused on capturing the surface-atmosphere interaction for natural land-cover. With the increase of the resolution of regional climate models, cities become explicitly resolved in the model, so that local impacts such as the urban heat island can be resolved. Therefore, an efficient non-iterative procedure that can deal with urban land-cover, and that is widely applicable in the standard surface-layer transfer schemes of the atmospheric models already using a former non-iterative procedure, becomes important.

D2 The apparent overestimation of day-time infra-red radiation.
A remarkable fact is that most urban parametrizations overestimate the upward infra-red radiation (wave-lengths of more than 5 μm) observed by the tower masts (Grimmond et al., 2011, see their Fig. 5). Moreover, the overestimation becomes more pronounced at the time when the urban-climate modelling becomes very relevant, in particular during hazardous heat waves when also the UHI reaches a maximum. Urban-climate research has been focussing on the improvement of modelling the radiation balance over cities, for instance by explicitly accounting for urban structural design such as accounting for multiple reflections and (re-)absorptions in the street canyon. However, none of these model developments lead to an improved modelling of upward infra-red radiation. At the same time, atmospheric constituents such as water vapor (H_2O), CO_2 and ozone (O_3) can contribute significantly to the absorption of radiation (Gaussorgues, 1993). In the case urban surfaces reach much higher temperatures than the air (and thus also its constituents) above during summer heat waves, the absorption of radiation emitted at a high temperature and re-emission at a low temperature becomes important.

D3 Uncertainty of urban water retention in urban areas.
Another important deficiency in current urban climate models is the uncertainty of water retention in cities. This encompasses urban evapotranspiration (ET), water-storage and run-off. In fact, the quantification of urban ET (Grimmond and Oke, 1999; Masson et al., 2008; Rotach et al., 2005; Sailor, 2011) and its modelling

is limited (Grimmond and Oke, 1991). In particular, many urban models ignore evaporation of stored water on urban water-impermeable swaths (roofs and streets) or use arbitrary model parametrizations. In general, the impact of taking arbitrary assumptions on the accuracy of urban climate modelling, especially the magnitude and duration after rainfall, is unknown. Furthermore, irrigation in the city is ignored by most urban land-surface models. These deficiencies makes evapotranspiration the least modeled flux of the surface-energy balance in urban models (Grimmond et al., 2011). Yet, it is important for urban-climate modelling research, because it determines the routing of precipitation to either water storage, evaporation and run-off. In turn, it alters the moisture, hence rain patterns down-wind of the city. For instance, wetted streets, roofs and walls drying out quickly can lead to a short excess of urban evaporation just after rainfall. It also leads to deficiencies of the other components in the surface energy balance (Grimmond et al., 2011). Finally, the deficiencies can lead to errors in modelling the water that is lost to run-off through the river system. The latter can lead to inaccurate assessment of pluvial flooding in urban areas. A better representation of this partitioning would allow for a better assessment and adaptation towards more water-sensitive cities.

D4 The role of anthropogenic heat to urban climate.
Until recently, research on the role of anthropogenic heat on the regional (urban) climate is limited, and even sometimes believed to be neglegible. While it is true that anthropogenic heating is small compared with summertime mid-day solar insolation, it could play a major role in the surface energy balance at times when the urban heat island effect is at its maximum, i.e. during night time and winter (Sailor, 2004). Yet, recent research indicates that anthropogenic heat could still play a small but important role on the meso-scales (Sailor, 2004) and the global scales (Flanner, 2009; Zhang et al., 2013).

Several quantative and qualitative methodologies and inventories have been made within recent research activities (Allen et al., 2011; Sailor, 2011; Flanner, 2009; Pigeon et al., 2007; Makar et al., 2006). Technological developments in building-insulation and energy efficiency reduces the energy demand in economic and domestic activities and thus anthropogenic heat release, whereas the increased human activity by economic growth, households, growing need for (human) facilities, traffic, and urban expansion leads to an overall increase in anthropogenic heat release. Up to now, the increase in anthropogenic heat by increased human activity has always been larger than the decrease in anthropogenic heat by energy efficiency due to technological developments. A particular interesting example is that the train of Brussels to Paris hundred years ago consumed less energy than the high-speed trains of today. Changes in anthropogenic heat release including its seasonal and climatic dependence in the future remains uncertain. It largely depends on policies, such as increased energy efficiency by greenhouse-gas legislation. For instance, changes in the building materials affects the anthropogenic heat, especially during winter, but also has an impact on the heat storage during heat waves. Therefore, changes in society in this respect may alter the future urban climate as well.

Anthropogenic heat may also lead to 'feedback' effects to urban climate during heat waves. Indeed, (Hassid et al., 2000) found a significant increase of both the cooling energy and peak demand in Athens as a result of the UHI effect. The waste heat that is rejected by air conditioning equipment in the urban atmosphere feeds back

on the temperature itself. Indeed, Wen and Lian (2009) demonstrated that the waste heat of air conditioners can result in a temperature increase up to 2.5 K in the city centre of Wuhan (China), On the one hand, the demand for air-conditioning increases. On the other hand, the temperature feedback induces a yet higher electricity demand of each air conditioner. Sailor and Munoz, (1997) found that for a representative building, the cooling load almost doubled in the central Athens area compared to the natural surroundings, while peak electricity load may be tripled. Hsieh et al. (2007) calculated that the additional electricity consumption for air conditioners is 11 % due to the waste heat of urban air conditioners in the city centre of Taipei using both building-energy and computational fluid dynamics software. A model-based study (de Munck et al., 2013) found an increase of 1 K in the streets of Paris due to the current heat releases of air-conditioning equipment.

Finally, urbanization largely affects the structure and processes within the planetary boundary layer, and they in turn affect urban climate (see Section 1.1.2). Therefore, accurate modelling of the boundary-layer processes may be of crucial importance in urban-climate modelling studies. Until recently, atmospheric models still have difficulties in capturing the boundary-layer processes. For instance, the parametrization of radiative divergence within the nocturnal boundary layer is still problematic in state-of-the-art atmospheric models (e.g., Steeneveld et al., 2010). This occurs at the time the urban heat island intensity reaches a maximum. To the best of our knowledge, the impact of the representation of the physical processes within the boundary layer in regional climate models on modelling urban climate has not been investigated.

1.3 The aim of this thesis

The general goal is to provide an efficient and reliable tool for the assessment of urban climate change on the regional scales available for a large research network. This enables the scientific community to setup an efficient risk-management for the mitigation and the adaptation of urban climate with respect to global climate and land-use change. Herein, we aim for enabling a broad assessment urban-climatic impacts encompassing every mid-latitude synoptic season and weather type, including summer heat waves, storms and cold winters. To reach this general goal, several specific aims are defined below, in which we refer to the deficiencies of current urban land-surface parametrizations (D1 to D4 described in section 1.2.4).

1. What is the role of the boundary-layer processes on the urban-climate? How does the modelling performance in terms of boundary-layer structure affects modelling the urban heat-island intensity and its spatial extent (Chapter 2)?

2. Can we develop an efficient - thus non-iterative - procedure for calculating surface-layer transfer coefficients applicable for urban environments accounting for the roughness-sublayer effects, and that is widely applicable in many atmospheric models (D1; Chapter 3)?

3. How can we improve the evaluation of urban surface parametrizations with mast observations at several tens of metres above the ground (D2; Chapter 4)?

4. Can we improve urban climate modelling by developing and implementing a water-storage parametrization (D3)? What is the magnitude of urban water storage, evapotranspiration, run-off, in response to the rainfall throughout the year (Chapter 5)?

5. Can we improve urban climate modelling by taking into account anthropogenic heat release (i.e. waste heat from human activity) (D4)? What is the relative impact of anthropogenic heat release versus urban structure (i.e. the presence of roads and buildings) on the seasonal variability of the urban heat-island in Belgium (Chapter 6)?

6. What are the priorities for further regional-climate model developments towards improved urban-climate modelling? What can be recommended for downscaling urban climate projections and for performing urban land-use change scenarios (Chapter 7)?

1.4 Structure of the remainder of this thesis

A structure-overview of the remainder of this thesis is given below, whereas its workflow is illustrated in in Fig. 1.10).

- At the start of this work, regional-climate model simulations were available at VITO ("Flemish Institute for Technological Research") that were performed with ARPS, the Advanced Regional Prediction System (Xue et al., 2000, 2001). In chapter 2, this is used to explore to what extent an urban parametrization in ARPS containing the simplified urban physics can reproduce the UHI for Paris during a heat wave in summer 2006. We also investigate the driving processes leading to the development of the nocturnal urban heat island effect and its spatial extent in the horizontal and vertical direction. Therefore, an idealized boundary-layer advection model was developed and applied. The processes include the role of the surface energy balance, but also the role of nocturnal boundary-layer processes and structure. In recent years, ARPS has not been used in a (European) Climate Research context. Therefore, the rest of this thesis will focus on the development and application of a new urban parametrization TERRA-URB for the regional climate model CCLM (the COSMO model in CLimate mode) for which the basis is similar to that developed for ARPS (De Ridder, 2006; Demuzere et al., 2008; Van Weverberg et al., 2008; Sarkar and De Ridder, 2010; De Ridder et al., 2012). In contrast to ARPS, the regional-climate model CCLM (Rockel et al., 2008) is currently actively used and further developed by the large (extra-)European research network (`http://www.clm-community.eu`). This research network is also affiliated to the "COnsortium for Small-scale MOdeling" (COSMO) using the eponymous numerical-weather prediction system COSMO (Steppeler et al., 2003). The latter is used by the forecast for MeteoSwiss and the Deutsche Wetterdienst.

- In chapter 3, we develop an efficient non-iterative procedure for calculating surface-layer transfer coefficients applicable for urban environments and accounting for the roughness-sublayer effects. Such a procedure is easily adoptable by many atmospheric models that already use a non-iterative approach, such as CCLM.

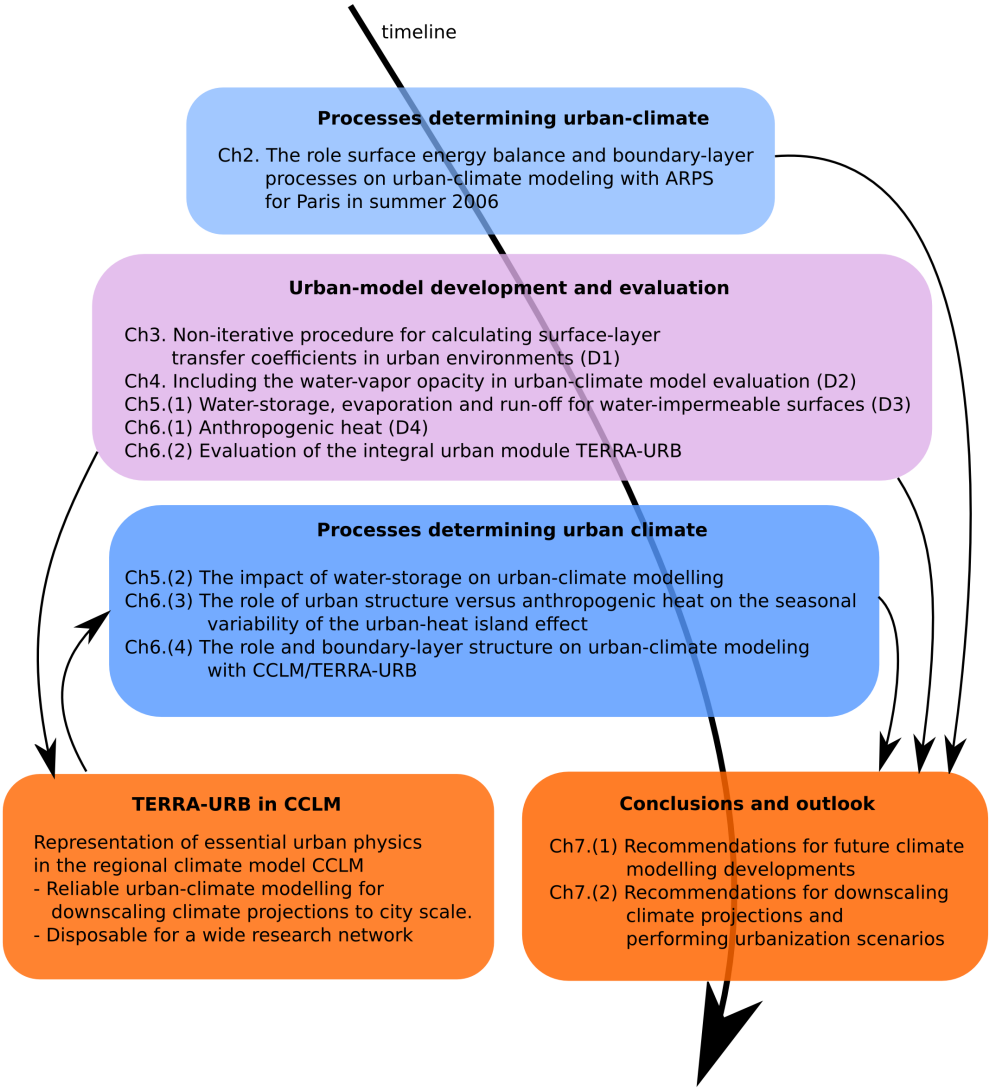

Figure 1.10: Schematic overview of the remainder of the thesis.

- In chapter 4, we present the technical description of the new efficient urban-land surface parametrization TERRA-URB first. It extends the SVAT model TERRA-ML for its applicability in urban environments preserving consistency among the urban the rural land-use types. Hereby, TERRA-ML is the standard SVAT model of the regional-climate model CCLM (the COSMO model in CLimate mode). For reasons of computational efficiency and the fact that simple models have equal performance as the more complex ones, it is chosen for a 'bulk' approach. In order to capture the main urban physics described in Section 1.1.1, such a 'bulk' scheme assigns certain bulk parameters to the urban terrain which is represented

as a rough, impermeable slab. Afterwards, we discuss to what extent the altitude of observation towers above the urban terrain affects the evaluation of urban-land surface parametrizations in terms of infra-red radiation for which clear overestimations are found at daytime during heat waves. Hereby, we develop a formalism to account for the impact of the absorption and re-emission on urban-model evaluation with tower masts of several tens of metres high.

- In chapter 5, we develop a new water-storage parametrization for water-impermeable facets of the urban terrain. Hereby, a distribution of water reservoirs is assumed, which allows for a more precise modelling and a better interpretation of the surface-water storage, evaporation and run-off. Thanks to the computational efficiency of TERRA-URB, we will employ a parameter-sensitivity study with TERRA-URB to find estimates of the water-storage parameters for the impervious urban facets found in the city-centre of Toulouse. We further investigate the impact of water-storage parametrization on urban-climate modelling (performance) - more particularly on evaporation, run-off and the surface-energy balance - in response to the rainfall throughout the year.

- In chapter 6, a multi-seasonal evaluation is performed with TERRA-URB (TU) in 'offline' (i.e. stand-alone) mode for Toulouse centre first. Hereby, the atmospheric conditions above the ground for wind, temperature, humidity and incoming radiation as input for TERRA-URB are specified from mast-tower measurements instead of that from atmospheric model CCLM. Such a decoupling of the SVAT model from its atmospheric counterpart allows to focus on its particular performance in terms of the surface-energy and surface-water balance, thus excluding the errors and uncertainty arising from modelling the atmospheric processes above. This is done by comparing the modeled components of the surface-energy balance including upward infra-red radiation, reflected short-wave radiation, sensible heat and latent heat against observations from the same mast tower. We investigate how urban climate modelling (performance) is affected by the urban-land surface parametrization, including the appliance of the new surface-layer transfer coefficients, the water-storage parametrization for water-impermeable surfaces, the inclusion anthropogenic heat and the vegetation within the city. This is achieved by applying a step-wise changes to the SVAT model TERRA-ML towards the full urban extension TERRA-URB. Afterwards, we perform an 'online' multi-seasonal evaluation of the coupling of TERRA-URB with the regional-climate model CCLM. Hereby, the urban climate of Belgium is simulated for the year 2012, and the performance in terms of capturing UHI evaluated with urban-climate observations. Particular focus is also given on the performance of the representation of the boundary-layer structure during heat waves and how it affects modelling the UHI at that time. This is done by comparing the model results with contrasting vertical profiles of temperature from 150-metre high mast-towers for both urban and rural environments. This chapter will discuss the role of anthropogenic heat versus urban structure on the seasonal variability of the urban heat-island, including the respective interactions among the resulting physical processes. The limitations and advantages of using a bulk approach instead of more complex urban land-surface parametrizations are addressed in the discussion of this chapter as well.

Chapter 2

The diurnal evolution of the urban heat island of Paris: A model-based case study during summer 2006

This chapter is based on the publication: *Wouters, H., De Ridder, K., Demuzere, M., Lauwaet, D., van Lipzig, N. P. M., 2013. The diurnal evolution of the urban heat island of Paris: a model-based case study during Summer 2006. Atmospheric Chemistry and Physics 13 (17), 8525-8541.*

2.1 Introduction

Temperature tends to be higher in cities than in their natural surroundings, especially during the night (Landsberg, 1981; Oke, 1987; Arnfield, 2003). This is known as the urban heat island (UHI) effect. Urban surfaces distinguish themselves from their natural surroundings by particular urban surface characteristics such as increased thermal inertia (Cai et al., 2008), a lowered vegetation cover and impervious land cover which reduces the evapotranspiration (Grimmond and Oke, 1999), a different albedo, emissivity and aerodynamic characteristics due to presence of streets and buildings. Together with the release of anthropogenic heat, this leads to the UHI effect reaching its maximum during the night. It is especially favoured by high solar irradiation (clear-sky) during the preceding daytime period, no precipitation, low wind speeds and stable stratification. Under these conditions, a large amount of solar radiation reaches the surface, which is better transformed to heat, and subsequently retained as storage heat (Grimmond et al., 1999) for a longer time in urban areas compared to rural areas.

Accounting for the UHI is important when studying the effect of land-use change (e.g. forest to croplands, or vegetation cover to urban land) on climate on the mesoscale and

global scale or to test mitigation strategies (e.g., Bowler et al., 2010; Dimoudi, 2003; Alexandri and Jones, 2007). In addition, the inclusion of urban effects can also serve to improve weather forecasts as shown in Hamdi et al. (2012). In this respect, it is indispensable to fully understand all the boundary-layer processes that contribute to the UHI.

The aim of this paper is to investigate the dominant heating terms that contribute to the maximum UHI intensity, and their interactions with boundary-layer processes and circulations. Therefore, two model runs are performed with the state-of-the-art atmospheric model ARPS (Xue et al., 2000, 2001) updated with a simple urban surface parametrization. The first run accounts for the today's land-use including the urbanization of Paris. For the second run, the urban land cover is replaced by cropland. By looking at the differential output between the two runs, the impact of urbanization on the surface energy balance, the consequential UHI and its vertical extent are analyzed. Even though the surface energy balance of the urban surface and the consequential boundary-layer UHI has already been addressed in earlier studies such as Lemonsu and Masson (2002), their direct interaction with the nocturnal boundary-layer have not been investigated in detail. It is known that the mixed-layer height is at least eight to ten times smaller during the night than during the day so that urban heat release is mixed over a significantly smaller depth (Bohnenstengel et al., 2011). Yet, the direct link between the urban surface heating and nocturnal increase in boundary-layer UHI intensity has not been investigated. The interaction of urban surface heating with nocturnal boundary-layer stability, near-surface radiative cooling, low-level circulations such as the low-level jet and the vertical motion induced by orography haven't been addressed as well. Moreover, the representation of these boundary-layer features during the night remains a challenge in state-of-the-art atmospheric models. It is not known to what extent these uncertainties affect the representation of the UHI at that time. In order to address these questions, an idealized advection model is developed in which a moving air column is advected over the city during the night. The model is used to study the underlying mechanisms that favour a maximum boundary-layer UHI buildup at night even though the urban surface heating is relatively low at that time. In addition, it is investigated how the UHI extends in the vertical under nocturnal boundary conditions. The idealized advection model also allows to determine the interaction of urban surface heating with boundary-layer features including orographical effects, the low-level jet, radiation cooling and stability. Therefore, it provides insight to which extent uncertainties of the nocturnal boundary layer affects the representation of the UHI.

The structure of the paper is as follows. The methodology Section consists of the description of the atmospheric model and its configuration (Section 2.2.1) and the theoretical background of the idealized boundary-layer advection model (Section 2.2.2). The results for a five-day period for which the UHI reaches its maximum are presented in Section 2.3. Hereby, we start with the evaluation of a reference run with the ARPS model results and UHI intensity (Section 2.3.1). Afterwards, the different contributions of urbanization to urban surface heating and their relative importance for the development of the UHI intensity are investigated by analyzing the surface energy balance (SEB) in Section 2.3.2. The spatial extent of the maximum UHI intensity in the horizontal and vertical for Paris are analyzed in Section 2.3.3. We apply the idealized advection model (Section 2.3.4) for an in-depth analysis of the evolution of the boundary layer over the city during the night. Hereby, the sensitivity of the nocturnal UHI buildup to the

different boundary-layer processes and stability are investigated. Our conclusions are formulated in Section 2.4.

2.2 Method

2.2.1 Mesoscale model description and setup

Meteorological fields are simulated using the Advanced Regional Prediction System (ARPS), a non-hydrostatic mesoscale atmospheric model developed at the University of Oklahoma (Xue et al., 2000, 2001). The turbulent fluxes of momentum and sensible heat are calculated by accounting for stability effects and the roughness sublayer (Garratt, 1992). Therein, flux-profile relationships for wind speed and temperature from Cheng and Brutsaert (2005), Businger (1966) or Dyer (1967), and De Ridder (2010) are used. These flux-profile functions are solved for $\zeta = z/L$ iteratively (z is the lowest model layer height above the displacement height and L the Obukhov Length) by establishing a relation involving the bulk Richardson number Ri_{B} (Arya, 2001), and using Ridders (1979) root finding scheme as described in Press et al. (1992). The land-surface scheme used in these simulations is that of De Ridder and Schayes (1997), which contains advanced parametrizations of plant transpiration. Temperature and water content of the vegetation canopy and of five soil layers are calculated using prognostic conservation equations, and water flow in the soil is calculated using Richard's equation (Garratt, 1992). Soil moisture and temperature were initialised using data from the Global Land Data Assimilation System (GLDAS see Rodell et al., 2004). For reasons of consistency, the soil texture was taken the same as that used in GLDAS. From the soil texture information that comes with the GLDAS data, we estimated domain-mean fractions of clay, sand, and silt, with contributions of 25, 35, and 40%, respectively. The corresponding soil textural parameters of the Clapp and Hornberger (1978) relations used in our model are based on Cosby et al. (1984). It should be noted that, even though the soil moisture simulation is not directly relevant to anthropogenic urban materials such as concrete and asphalt, it does influence the urban-rural temperature difference, which is the focus of this study, hence the care taken here to properly simulate this quantity.

The land-surface scheme was extended to represent urban surfaces as described in Demuzere et al. (2008). The main feature of that extension is the use of Zilitinkevich (1970) thermal roughness length parametrization in urban areas, the thermal inertia which is assigned a value of $1800\,\mathrm{J\,m^{-2}\,s^{-1/2}\,K^{-1}}$, and the inclusion of anthropogenic heating. The latter was specified as in Demuzere et al. (2008) for Marseille, though scaled up for Paris. In Demuzere et al. (2008), the estimated anthropogenic heat flux for Marseille was found to vary between approximately $15\,\mathrm{W\,m^{-2}}$ (night) and $30\,\mathrm{W\,m^{-2}}$ (day), with a linear transition between these two values during the morning and evening hours. The detailed time profile is shown in Fig. 10 of Demuzere et al. (2008). The scaling up for Paris was achieved using observed satellite-based anthropogenic light irradiance (visible nocturnal lights from space). As explained in Makar et al. (2006), such information can be related to the annual mean anthropogenic heat flux. While for Marseille the estimated annual mean anthropogenic heat amounts to $28.8\,\mathrm{W\,m^{-2}}$, for Paris this value reaches $59.6\,\mathrm{W\,m^{-2}}$ (see `http://www.iiasa.ac.at/Research/TNT/WEB/heat/`). The

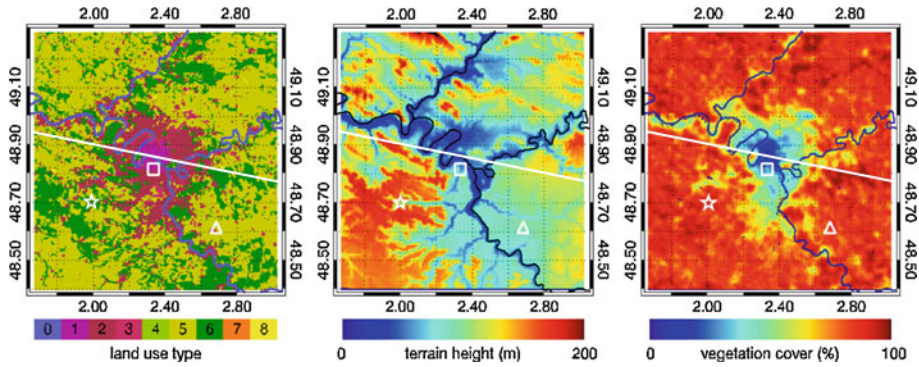

Figure 2.1: Land-use types (left), terrain height (middle) and vegetation cover (right) of the Paris 1-km simulation domain. The different land-use types are defined as water (0), urban (1), sub-urban (2), industrial (3), grass(4), crops (5), forest (6), snow/ice (7), shrubs (8). The rectangular and the triangular box represent the locations of the urban (Paris-Montsouris, square) and rural (Melun, triangle) stations respectively. The star indicates the location of the radio soundings at Trappes. The line indicates the vertical transect along the prevailing east wind in the base run used for the vertical profile analysis.

diurnal anthropogenic heat flux over Paris were obtained applying this ratio of 2.07 (= 59.6/28.8) to that of Marseille.

Aerodynamic roughness length, albedo, emissivity, and the unconstrained stomatal resistance were specified as a function of land-use type, which was interpolated from the CORINE land-cover map (European Commission 1994), see Fig. 2.1. Terrain height was interpolated from the Global 30 Arc Second Elevation dataset (GTOPO30) distributed by the U.S. Geological Survey. Sea-surface temperature was derived from MODIS thermal imagery. The vegetation abundance was specified as a linear function of normalised difference vegetation index (NDVI) values interpolated from satellite imagery of the VEGETATION instrument onboard the SPOT satellite platform, following relations established by Wittich and Hansing (1995) and Gutman and Ignatov (1998).

The land-surface scheme employs the mosaic approach, allowing different land-use types to co-exist within a surface grid cell. The surface energy balance is computed individually for each land-use class, and the energy flux for each grid cell is calculated as the weighted average.

We employ a three-level one-way grid nesting at horizontal resolution of 16, 4, 1 km. Each of the nesting domains was run in a configuration of 100 by 100 grid cells in the horizontal direction, and 35 levels in the vertical direction, with vertical resolution starting at 25 m near the surface to approximately 1 km near the model top located at an altitude of 15 km. The 1-km model domain chosen for the simulation is the larger area of Paris, as shown in Fig. 2.1. The 16-km simulation was forced at its lateral boundaries by 6-hourly analysis fields from the operational model of the European Centre for Medium Range Weather Forecasting (ECMWF), available at a spatial resolution of 0.25° in latitude and longitude.

The model setup and configuration is applied for the period of the 1st to 13th June 2006 and is the same as from the model configuration used in Sarkar and De Ridder (2010). This run is hereafter referred to as the 'base run'. The period is characterised by calm weather, low wind speeds, limited cloud and precipitation and strong temperature inversion during the night, which all favour the development of the urban heat island.

Besides the base run, an additional scenario run is performed during the same period for which the model setup is exactly the same, except that the urban and sub-urban fractions have been replaced by crops. For the concerned areas, obviously no NDVI satellite data is available, so the specification of vegetation abundance is problematic. To tackle this problem, an image-processing technique is used. The basic idea is to determine vegetation abundance from a probability distribution for crops that corresponds to the one from the current-day situation. Furthermore, a Lee (1986) smoothing filter and a sharpening filter (Jain, 1989) are applied subsequently to get a realistic map for the vegetation abundance. More details of this data generation procedure can be found in Van Weverberg et al. (2008).

The urban heat island is estimated from the difference in output between the two runs. We are interested in a time span of maximum urban surface heating, i.e., for meteorological conditions that favour a strong UHI-effect. As the heat island intensity evolves from modest to high values over the course of the period during 1 to 13 June both in the observations as in the model results, a period is selected for which the overall temperature difference between the base run and the scenario run is the highest. These conditions occur during the second half of the model run, namely during a five-day period between 8 June and 13 June.

2.2.2 Idealized boundary-layer advection model

In order to get better insight in the development of the nocturnal boundary-layer UHI, an idealized Lagrangian single-column advection model is developed. Hereby, an air column that moves along the prevailing east wind is considered. This model takes into account the nocturnal surface sensible heat flux $(\overline{w'\theta'})_0$, the initial boundary-layer profile upwind of the city and vertical wind w_h.

The application of our new idealized advection model facilitates the identification of the responsible driving mechanisms of the urban-heat island intensity.

By excluding any other atmospheric process that may be resolved by ARPS, our idealized advection model allows to easily investigate to what extent the maximum urban heat island intensity that is reached during the night can be related to the boundary-layer features, including the nocturnal surface sensible heat, horizontal advection, vertical uplift and nocturnal stability. Moreover, the idealized advection model allows for performing sensitivity experiments in an efficient way to assess each specific role of the boundary-layer structure and features, as will be done in Section 2.3.4. In contrast, the structure and features cannot be controlled by the 3D-model ARPS in an easy way.

A distinction needs to be made between upward (to atmosphere) and downward (to surface) surface sensible heat flux. Therefore, sets of equations for the convective boundary

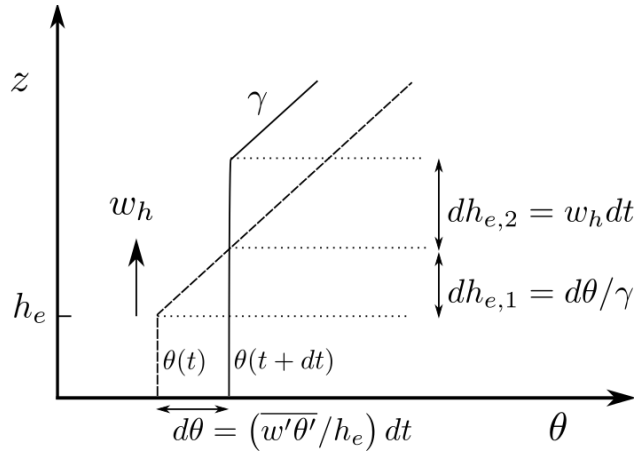

Figure 2.2: The evolution of the vertical potential temperature profiles for the CBL as a function of height z. The vertical velocity is indicated with w_h. $d\theta$ represents the mixed-layer temperature change due to the surface heat flux $\left(\overline{w'\theta'}\right)$. γ is the temperature slope above the mixed-layer height h_e. $dh_{e,1}$ and $dh_{e,2}$ are the changes in mixed-layer height due to the surface sensible heat flux and vertical velocity. The thick dashed line depicts the temperarature profile time t, and the full lines that of a time step dt later. $\theta(t)$ and $\theta(t+dt)$ are the corresponding mixed-layer temperatures.

layer (CBL) with surface heating and for the nocturnal (stable) boundary layer (NBL) with surface cooling are considered in Sections 2.2.2 and 2.2.2, respectively.

Slab model for the convective boundary layer

For the CBL, the slab model from Garratt (1992) is used. It is extended to account for a constant vertical velocity at the top of the CBL (Fig. 2.2) as demonstrated in Section 2.3.4.

The temperature θ of the mixed layer changes due to the upward surface sensible heat flux which is distributed over the mixer-layer height h_e:

$$\frac{d\theta}{dt} = \frac{(\overline{w'\theta'})_0}{h_e}, \tag{2.1}$$

The mixer-layer height increases due to vertical advection of potential temperature and temperature increase:

$$\frac{dh_e}{dt} = w_h + \frac{1}{\gamma}\frac{d\theta}{dt}, \tag{2.2}$$

where γ is the temperature slope of the stable temperature profile above the mixer layer, and w_h is the vertical wind speed at the mixed-layer height. This set of equations lead to a transcendental differential equation in h_e:

$$\frac{dh_e}{dt} = \frac{(\overline{w'\theta'})_0}{\gamma h_e} + w_h, \tag{2.3}$$

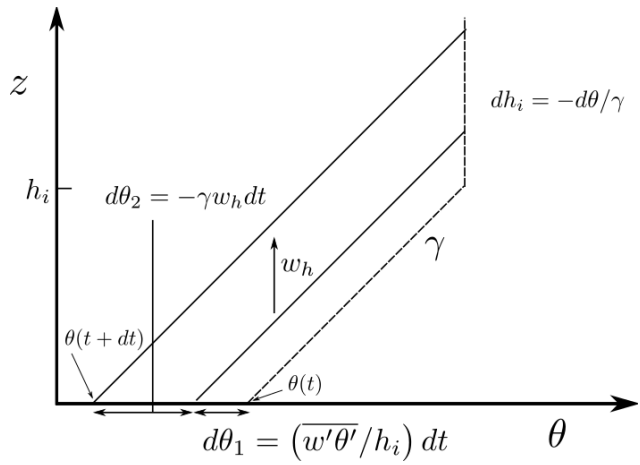

Figure 2.3: Idem to Fig. 2.2, but for the the NBL. h_i is the inversion height. dh_i is the change in inversion height due to surface sensible cooling and upward motion. The temperature changes at the surface due to negative surface sensible flux and upward motion are indicated with $d\theta_1$ and $d\theta_2$, respectively.

which can be solved with the Newton-Raphson numerical method (see appendix 2.5.2). Afterwards, the evolution of the temperature can be integrated from Eq. 2.2:

$$\theta(t) = \theta(0) + \gamma(h_e(t) - h_e(0)) - \gamma w_h t \tag{2.4}$$

Slab model for the nocturnal boundary layer

In case surface cooling occurs, an NBL model can be applied based on Garratt (1992), Eq. (6.74) in section 6.2.6. Such an inversion-layer model is illustrated in Fig. 2.3.

The potential temperature at the surface (θ) changes due to the surface cooling which decreases the temperature homogeneously up to the inversion height h_i, and due to vertical advection of potential temperature which vertically shifts the temperature profile:

$$\frac{d\theta}{dt} = \frac{(\overline{w'\theta'})_0}{h_i} - \gamma w_h \tag{2.5}$$

$$\frac{dh_i}{dt} = -\frac{1}{\gamma}\frac{d\theta}{dt} \tag{2.6}$$

where w_h is the vertical wind speed at the inversion height. Eq. 2.5 covers the following physical processes: the surface cooling cools the stable layer homogeneously up to the inversion height h_i (first term), and vertical advection of potential temperature vertically shifts the temperature profile. The fact that the temperature slope remains the same, is expressed by equation 2.6, so that a change in h_i is related to a change in temperature θ at the surface. This set of equations can be converted to a differential equation for the inversion height:

$$\frac{dh_i}{dt} = \frac{-(\overline{w'\theta'})_0}{\gamma h_i} + w_h \tag{2.7}$$

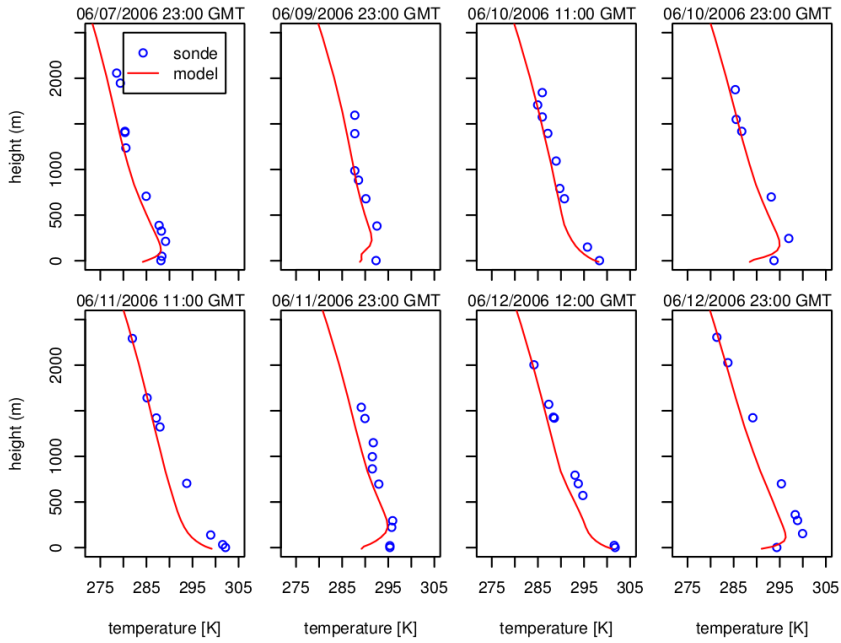

Figure 2.4: Comparison between radio soundings and model output (base run) at Trappes from 7th of june 23:00UTC until the 12th of june 06/12/2006UTC, which encompasses our selected five-day period of clear-sky conditions (8th of june until 13th of june)

It can be solved in a similar way as the CBL model equations. Again, the temperature evolution follows from integration of Eq. 2.6:

$$\theta(t) = \theta(0) - \gamma(h_i(t) - h_i(0)) \tag{2.8}$$

2.3 Results

2.3.1 Model evaluation

In this section, the ARPS model results are evaluated for the selected week of maximum urban surface heating between 8 June 2006 (00:00 UTC) and 13 June 2006 (00:00 UTC). Radio soundings of temperature profiles, and two-metre temperature ground measurements including the urban/rural temperature difference are investigated. A comparison between the temperature profiles from the model and those from radio soundings at Trappes (location, see Fig. 2.1) is shown in Fig. 2.4. The model profiles at this rural site have an overall negative bias of $-1.75\,\mathrm{K}$ and a mean absolute error of $1.5\,\mathrm{K}$. Yet, the model is able to reproduce the overall increase in temperature over the selected period, and correctly captures day-night differences in the observed profiles. Furthermore, the two-metre temperatures of two fixed ground stations and their difference, resp. at

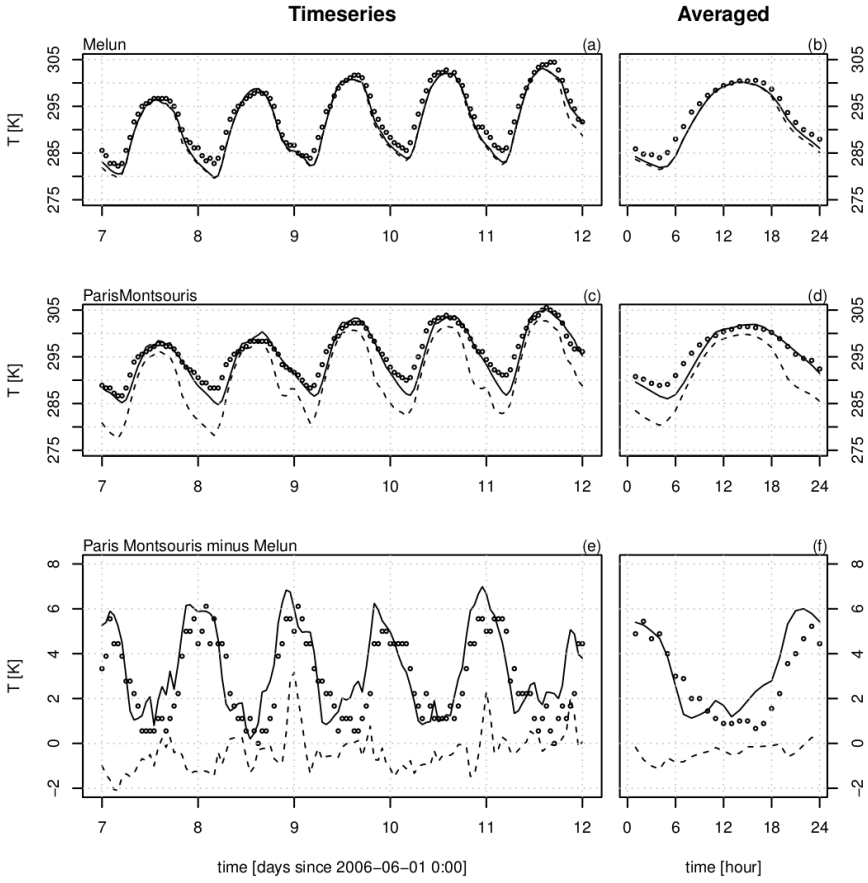

Figure 2.5: The temperature time series for Melun (a), Paris-Montsouris (c), and the difference between the sites (e), for the observations (circles), base run (full line) and scenario run (dashed line), and their hourly averaged diurnal cycle (b,d,f).

Melun in a rural area and Paris-Montsouris near the city centre (locations, see Fig. 2.1), are compared between the model output and observations for the selected five-day period (see Fig. 2.5). The values for the two-metre temperature of the model are extrapolated from the lowest vertical model layer (approximately 12.5 meter) using Monin-Obukhov surface-layer profiles accounting for stability effects. We find a correlation of 0.97 and 0.99, absolute errors of 1.4 K and 1.6 K, and a cold bias of -0.92 K and -1.45 K for the urban and rural station, respectively. The overall too stable vertical temperature profiles at the rural site Trappes and negative bias in the two-metre temperatures mainly occur during the night. This is accompanied by wind profiles with a too strong nocturnal low-level jet. Hereby, an overestimation of the peak in wind speed could reach a factor

two in some of the nocturnal profiles at Trappes. A possible reason is the uncertainty in the turbulent mixing parametrization for stable boundary-layer conditions, see e.g., Cuxart et al. (2006). Furthermore, the vertical turbulent mixing generated by low-level circulations due to topography or the urban UHI itself could be underestimated by the ARPS model. This could result in nocturnal temperature profiles that are too stable, which further reduces the turbulent mixing. This 'feedback' of reduced vertical mixing may explain the overestimation of the nocturnal low-level jet. In this respect, the effect of nocturnal stability and the low-level jet on the UHI buildup are addressed in Section 2.3.4.

The temperature *difference* between the two stations, which reflects the thermal contrast between the urban and rural areas, is now evaluated. The modeled and observed differences and their diurnal cycle are shown in Fig. 2.5. The differences have a daily mean of 2.81 K and 3.35 K respectively, and we find a correlation of 0.80. The model overestimates the temperature difference by 0.54 K, which starts to increase too early in the evening. The (nocturnal) maximum UHI intensity averaged for the five days is well captured by the model, but with a slight overestimation. We find temperature differences of 6.0 K and 5.5 K for model output and observations respectively, so it is overestimated by 0.5 K (or 9.1%). Although the model has an overall negative bias during the night, the urban-scale temperature fluctuations, which includes the UHI, are well represented in the model. Furthermore, the fact that the temperature difference between the urban and rural station becomes zero in the scenario run (for which the urban surface is replaced by crops) confirms that it is caused by the urban surface heating.

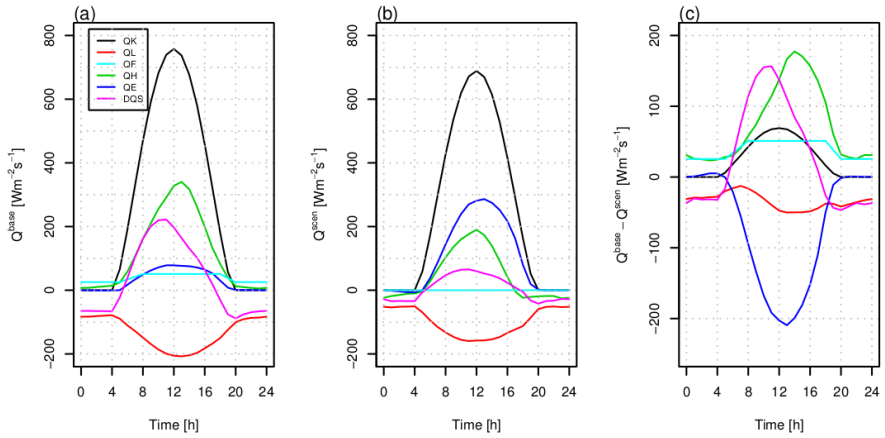

Figure 2.6: The five-day averaged diurnal cycle of the surface energy fluxes at Paris-Montsouris (city centre) for the base run (a), the scenario run (b) and their difference (c).

2.3.2 Impact of urbanization on the surface energy balance

As a start to investigate the effect of urban surface heating on the evolution of the UHI, the surface energy balance (SEB) in the city centre is analyzed. The averaged diurnal cycle over the selected period is considered so that short-term fluctuations are averaged out (see Fig. 2.6).

The surface energy balance, which is a statement of the energy conservation at the surface, can be written as:

$$Q^* + Q_\mathrm{F} = Q_\mathrm{H} + Q_\mathrm{E} + \Delta Q_\mathrm{S}, \tag{2.9}$$

where Q^* is the net all wave radiation flux density, Q_F the anthropogenic heat flux, Q_H the surface sensible heat flux, and Q_E surface latent heat flux release. The storage heat flux ΔQ_S represents the total heat transfer to/from the urban surface/ground that includes buildings (roofs and walls) and roads, and is equivalent to the ground heat flux. Furthermore, Q^* is composed of net shortwave (Q_K) and long-wave radiation (Q_L):

$$Q^* = Q_\mathrm{K} + Q_\mathrm{L} = (K_\downarrow - K_\uparrow) + (L_\downarrow - L_\uparrow), \tag{2.10}$$

where $K_\downarrow$ and $L_\downarrow$ are the incoming short-wave and long-wave radiation, and $K_\uparrow$ and $L_\uparrow$ the outgoing short-wave and long-wave radiation.

The surface fluxes at Paris-Montsouris are compared between the base run and scenario run. In the former, the grid-cell has 85% of urban land surface. In the latter, the urban surface is replaced by vegetation in which similar surface fluxes are obtained as for the base run at the rural location at Melun.

Several source terms in the energy budget appear during the day owing to the urban surface, which is also found in earlier model studies of Van Weverberg et al. (2008); Lemonsu and Masson (2002); Lemonsu et al. (2009); Bohnenstengel et al. (2011). Hereby, the large reduction in latent heat release ($Q_\mathrm{E}^\mathrm{base} - Q_\mathrm{E}^\mathrm{scen}$) dominates the increase in absorbed solar radiation ($Q_\mathrm{K}^\mathrm{base} - Q_\mathrm{K}^\mathrm{scen}$) and the additional anthropogenic heat flux Q_F. These urban source terms are balanced by an increased net outgoing long-wave radiation ($-(Q_\mathrm{L}^\mathrm{base} - Q_\mathrm{L}^\mathrm{scen})$), a storage heat flux $\Delta Q_\mathrm{S}^\mathrm{base} - \Delta Q_\mathrm{S}^\mathrm{scen}$ and sensible heat flux $Q_\mathrm{H}^\mathrm{base} - Q_\mathrm{H}^\mathrm{scen}$ in the city centre. The increased sensible heat release leads to a minor increase in the two-metre temperature of 2 K during the day (see Fig. 2.5).

The urban source terms at nighttime are very different to those at daytime. A nocturnal excess in storage heat ($\Delta Q_\mathrm{S}^\mathrm{base} - \Delta Q_\mathrm{S}^\mathrm{scen}$) release which was stored during the day is the same magnitude as the anthropogenic heat flux Q_F at that time. They are balanced by an increased net outgoing long-wave radiation ($-(Q_\mathrm{L}^\mathrm{base} - Q_\mathrm{L}^\mathrm{scen})$) and sensible heat ($Q_\mathrm{H}^\mathrm{base} - Q_\mathrm{H}^\mathrm{scen}$). In particular, $Q_\mathrm{H}^\mathrm{base}$ is positive as opposed to $Q_\mathrm{H}^\mathrm{scen}$ which is negative. It is remarkable that the impact on the two-metre temperature is increased further during the night, even though $Q_\mathrm{H}^\mathrm{base} - Q_\mathrm{H}^\mathrm{scen}$ is much smaller than during the day. It can be explained by the stable stratification during the night which retains the urban source terms much closer to the ground than the unstable stratification during the day, as mentioned in Bohnenstengel et al. (2011). The further intensification of the UHI during the night with relative small difference in surface sensible heat flux is demonstrated more precisely in Section 2.3.4 with the single-column Lagrangian advection model.

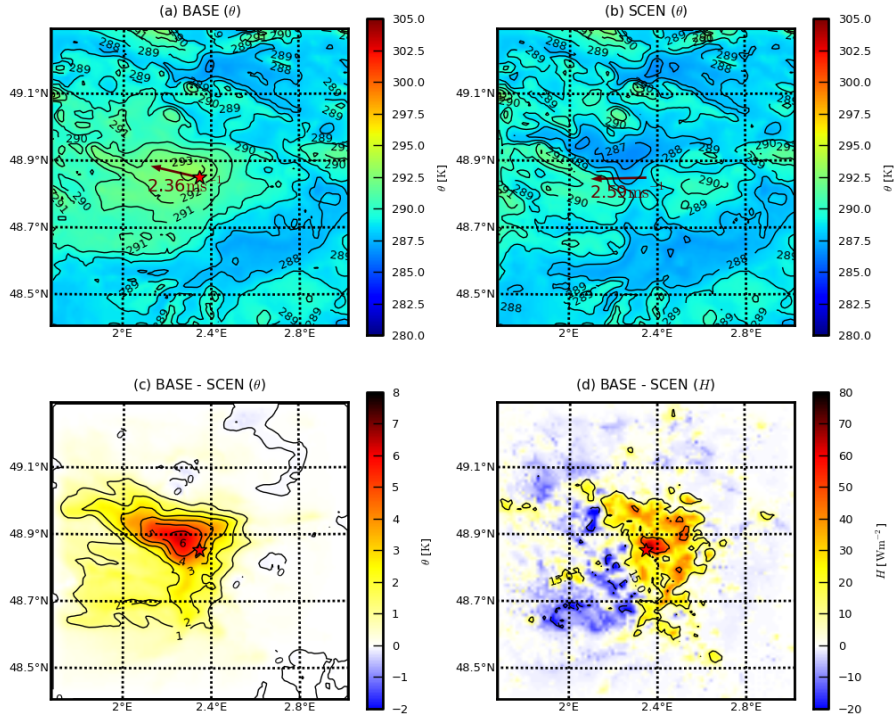

Figure 2.7: The potential temperature in K over Paris at 23:00 UTC at 12.5 m for the base run (a), scenario run (b) and the difference (c). The difference in surface sensible heat between the base run and scenario run is given by Panel (d). The city centre is indicated with the red star and the horizontal wind with the red arrow.

Note that over the urban surface, in which we are dealing with bluff-rough elements, much lower thermal roughness lengths occur in the city (Sugawara and Narita, 2008) compared to vegetative areas which reduce the turbulent transfer of heat from the surface during the day. This is in contrast to what one may expect from high roughness lengths for momentum in cities which actually tend to increase the turbulent transfer. This turbulence inhibition which blocks the surface sensible heat release during the day, together with the higher heat capacity of the urban surface with a large amount of buildings (Lemonsu and Masson, 2002; Harman and Belcher, 2006; Oleson et al., 2010), is important because it favours an increase of storage heat. The latter is released subsequently as sensible heat during the night and this directly influences the nocturnal temperature (profile) demonstrated in Section 2.3.4.

In the early morning, a decrease in temperature difference between urban and rural station is partly explained by the increased storage heat opposed to the excess sensible heat. This stems from the already mentioned large heat capacity of urban surfaces and from the heat blocking effect due to very low thermal roughness lengths for bluff-rough elements typical for urban areas. This could even lead to an urban 'cool' island

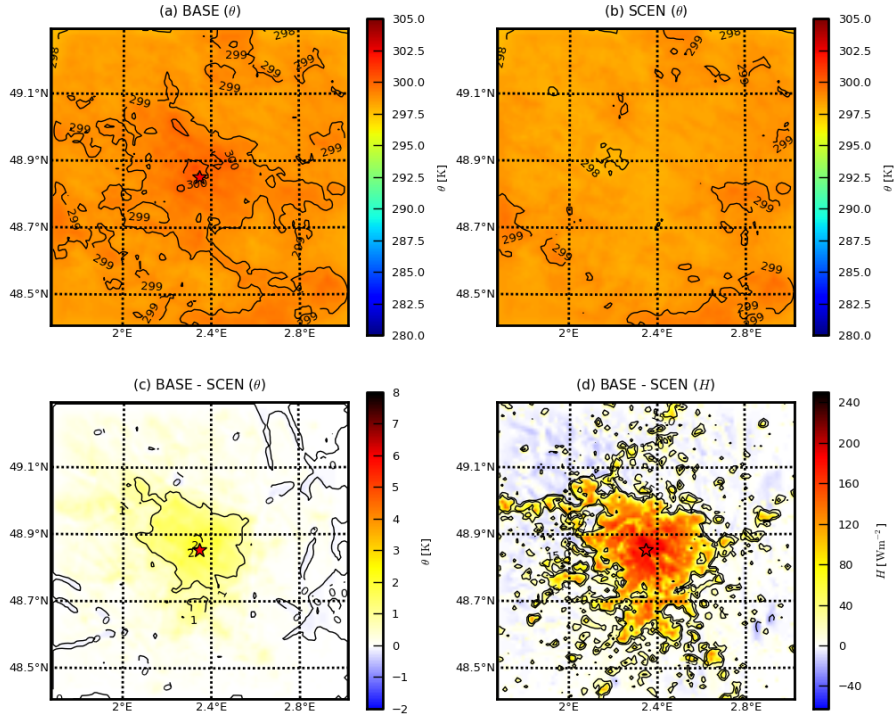

Figure 2.8: Idem to figure 2.7, but for 15:00 UTC.

which can last for the whole day, as found over Oklahoma city (Lemonsu et al., 2009). Nevertheless in this case study for Paris, the excess in sensible heat release remains positive in the morning which would still suggest an increase instead of decrease in temperature difference. Yet, the UHI intensity is reduced since the excess in sensible heat and temperature is distributed by turbulent diffusion due to the development of a convective boundary layer.

To conclude, the large reduction of the latent heat release, and to a lesser extent the reduced reflected solar radiation and anthropogenic heat for urban surfaces basically explain the large increase in storage heat uptake at noon and sensible heat release in the afternoon. The latter results in a modest impact on the near-surface temperature as it is mixed over a larger depth because of unstable stratification. The heat which was stored during the day and, to a lesser extent, the added anthropogenic heat results in a small impact on the sensible heat during the night. However, this leads to a much stronger impact on the near-surface temperature compared to the day. At that time, the UHI is at its maximum as this extra heat is retained close to the ground because of stable stratification.

2.3.3 The horizontal and vertical extent of the urban heat island

The maximum UHI intensity at 23:00 UTC of 6.1 K is found at about 6 km downwind of the city centre along the wind vector (Fig. 2.7). This downwind shift is also found in Bohnenstengel et al. (2011). In fact, the boundary-layer UHI increases when moving over the city along the wind vector up to the location where the excess in sensible heat release induced by the urban surface vanishes. The extent of the UHI has approximately the same horizontal size as the total area of the suburban and urban terrain of Paris. The UHI intensity is much lower during the day (Fig. 2.8), even though the magnitude and extent of the differential sensible heat flux is much larger than during the night. The downwind shift of the UHI intensity is negligible in the results for the day.

During the day between 09:00 UTC and 18:00 UTC, the large excess in sensible heat is found (see Section 2.3.2). This is distributed over large depth of the convective boundary layer during the day (Fig. 2.9). This vertical distibution limits the UHI intensity to at most 2.5 K near the surface, but a small impact on the vertical temperature of 0.5 K is still found up to the mixing height of 800m. During the night, a positive instead of negative $Q_{\mathrm{H}}^{\mathrm{base}}$ is found. As a consequence, a neutral mixed layer with a small depth is formed over the city, while the temperature profile becomes stable over cropland. The UHI intensity increases up to 6.1 K at 23:00 UTC 6 km downwind of the city centre with a decreasing lapse rate of $0.05\,\mathrm{K\,m^{-1}}$ (Fig. 2.10). The UHI intensity is confined to 150 m depth under nocturnal boundary-layer conditions, hence the large impact of a relative small excess in sensible heat. This is discussed hereafter with the idealized advection approach. The differential surface sensible heat remains positive for the entire night under nocturnal stability. Therefore, the UHI persists with only a slight decrease until the morning (6:00 UTC) when a convective boundary layer with a large depth is formed. Note that a small cooling of about -0.5 K occurs at 200-400m above the city. This can be ascribed to the cross-over effect (Cermak et al., 1995; Oke, 1982): entrainment occurs at the elevated inversion base above the city due to roughness and buoyancy effects. This cross-over effect might then correspond to the layer from which heat has been removed by entrainment.

2.3.4 Contributions and impacts on the nocturnal UHI buildup with the advection model

Advection model setup

The advection model is applied for both scenarios between 22:00 UTC and 23:00 UTC starting 6 km upwind of the city centre traveling a distance of 12.6 km over Paris, see Fig. 2.11. The meteorological conditions as input for the advection model are adopted from the ARPS model output averaged for the five-day period between 22:00 and 23:00 UTC for the respective scenarios. Hereby, the advection model accounts for the synoptic east wind of $3.5\,\mathrm{ms^{-1}}$. For the base case which includes the urban surface, a constant sensible heat sink of $-10\,\mathrm{Wm^{-2}}$ is considered for the first 12 minutes (NBL) and a heat source of $15\,\mathrm{Wm^{-2}}$ during the 48 subsequent minutes (CBL). For the scenario case (hereafter scen case) for which urban surface is replaced by cropland, a surface sensible heat sink of $-20\,\mathrm{Wm^{-2}}$ is prescribed for the entire hour (NBL). Idealized piecewise linear profiles

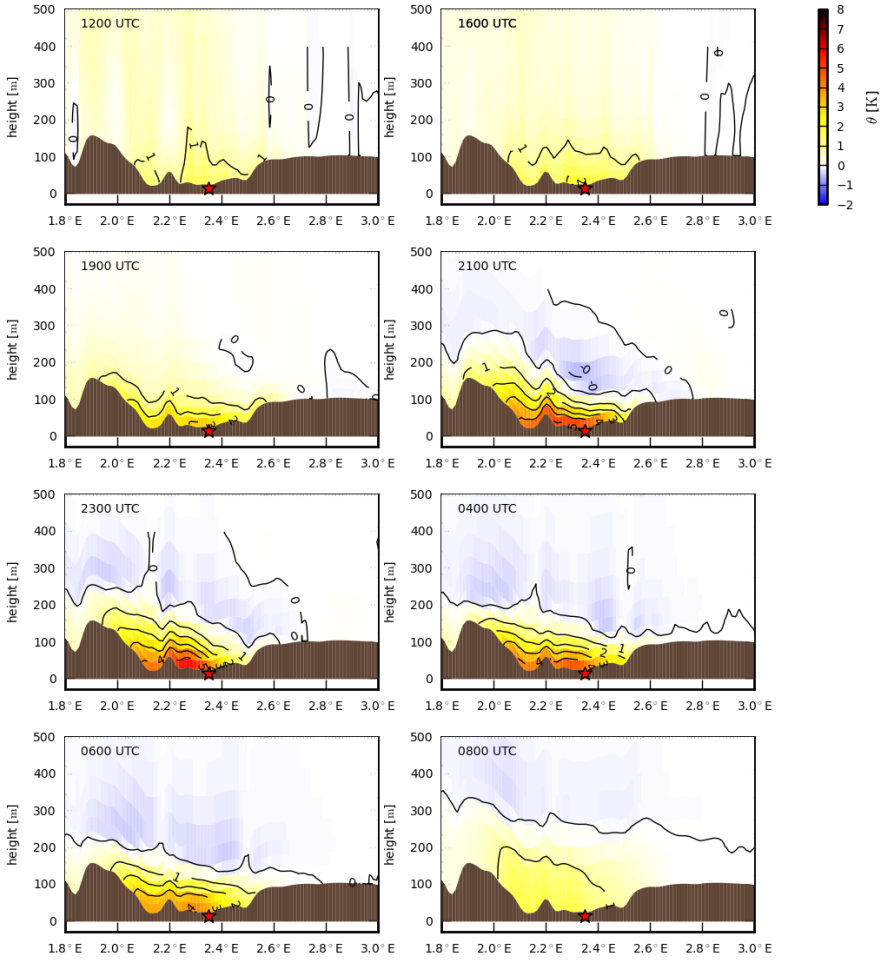

Figure 2.9: five-day averaged diurnal cycle of the potential temperature profile differences between the base run and scenario run through Paris along the wind direction. The city centre is indicated with a red star.

need to be considered for the initial state of the advection model. The profile of the lowest 150 m is fitted with linear regression from the ARPS model results at 22:00 UTC 6 km upwind (east) of the city centre for both scenarios (Fig. 2.12 (a)). Hereby, profile slopes of 0.26 K km^{-1} and 0.58 K km^{-1} were found for the base and scen case, respectively. The temperature at the inversion height was calculated from the average between 150 and 400m above ground level. Note that the profile of the base case is already somewhat destabilized because of the less negative surface sensible heat compared to the scenario case before 22:00 UTC.

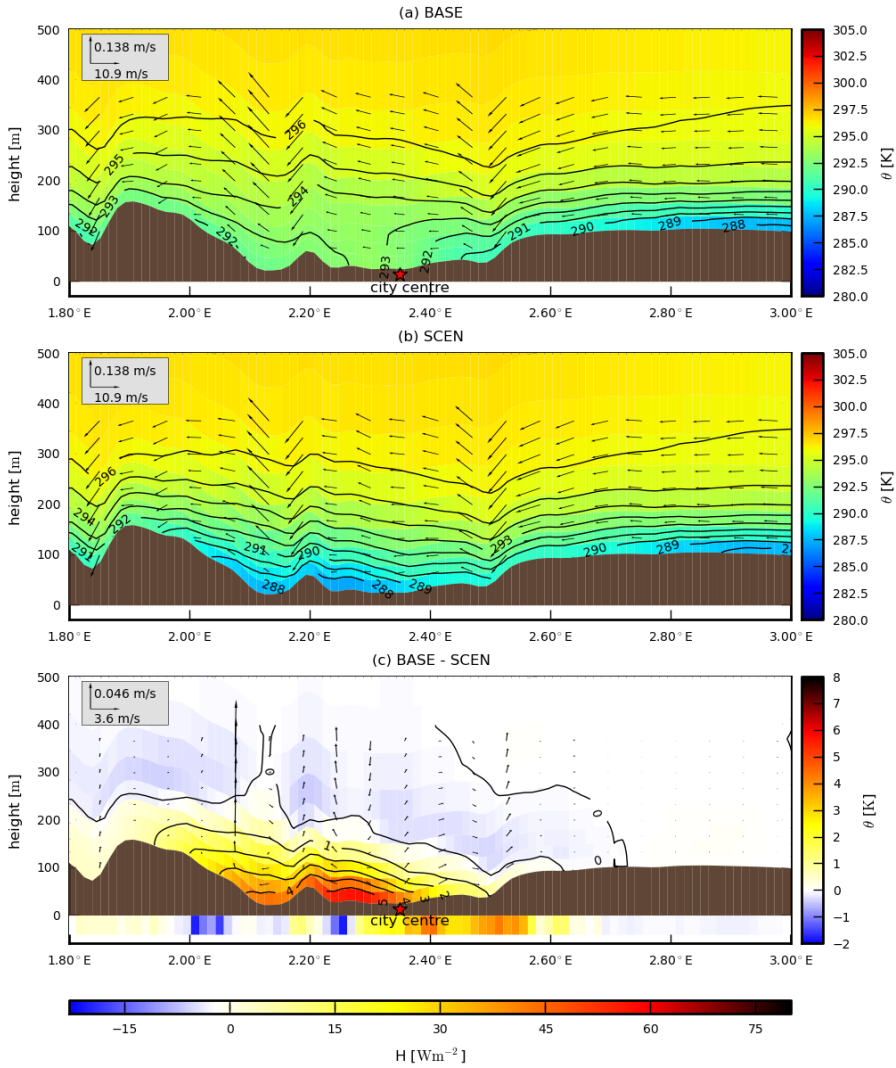

Figure 2.10: five-day averaged vertical profiles of potential temperature over Paris at 23:00 UTC for the base run (a), scenario run (b) and their difference (c). The differential surface heat flux is added to the bottom of panel (c).

We consider a upward wind relative to the surface topography of $0.012\,\mathrm{ms}^{-1}$, which appears over a considerable part of the city in the ARPS output. As demonstrated in appendix 2.5.1, this is established by the flow over the ramp east of the city centre due to the synoptic east wind. Hereby, the order of magnitude of this vertical uplift relative to the surface can be reproduced theoretically by considering a stratified flow over an idealized ramp in which the acceleration occurs at the downward slope east of the city centre. Note that the radiative cooling is neglected in the CBL and NBL models. This is discussed in Section 2.3.4.

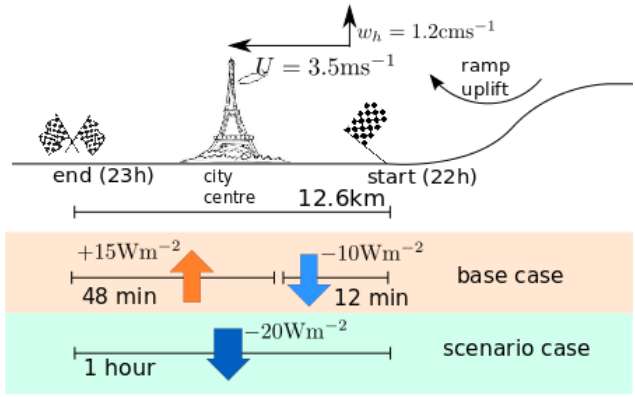

Figure 2.11: Overview of the idealized advection model setup over Paris for the base case and the scenario case. Surface sensible heat fluxes, horizontal and vertical wind speed and duration of simulation are shown.

Advection model results

The idealized CBL and NBL advection models are compared with the ARPS model output for the base case and scen case. They could reproduce the evolution of the temperature profile for the lowest 150m very well for an air column moving with the wind in the respective scenarios (Fig. 2.12 (b)). They clearly demonstrate that the nocturnal surface sensible heat flux and vertical ramp uplift (indicated with LIFT) are the processes dominating the changes in the respective temperature profiles. These processes also explain the increase in UHI intensity between 22:00 UTC and 23:00 UTC and the UHI maximum of 6.1 K, even though the nocturnal difference in surface sensible heat between the two scenarios is much smaller than during daytime. This UHI buildup was about the same as from the ARPS model results.

In the base case with the city of Paris, a mixed layer is formed up to a height h_e of 80 m due to surface heating, and a stable layer remains aloft. In the scen case where the city of Paris is replaced by cropland, a stable profile persists which is cooled efficiently in the vertical up to the inversion height h_i due to a constant surface cooling, but also due to the vertical advection of potential temperature. The latter process is explained in more detail in the next subsection. Meanwhile, the inversion height is displaced in the upward direction.

Impact of adiabatic cooling due to vertical motion

As mentioned in Section 2.3.4, the synoptic east wind results in an uplift relative to the surface caused by the ramp upwind of the city centre. As the wind speed and direction changes depending on the synoptic situation, this topographic effect doesn't always take place. For example, weak synoptic pressure gradients would lead to a downslope wind

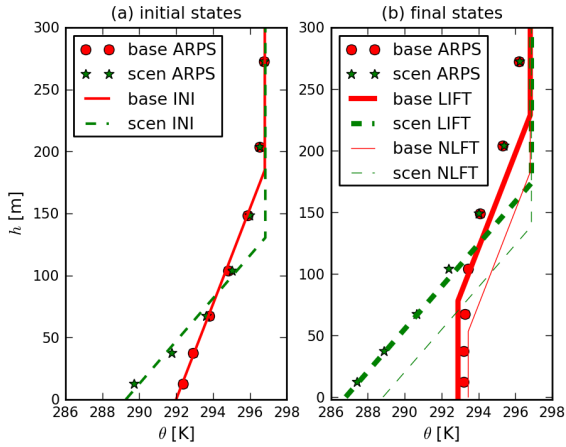

Figure 2.12: Vertical potential temperature profiles from ARPS and from idealized boundary-layer advection models. h indicates the height above ground level. The initial (22:00 UTC, 6.3km upwind) and final states (23:00 UTC, 6.3km downwind) are plotted on panel (a) and (b), respectively. In both panels, the profiles from the ARPS output are indicated with red circles and green stars for the base run and scenario run, respectively. The full red line in panel (a) represents the fitted initial state for the idealized advection models for the base case (base INI), and the dashed green line that for the scenario case (scen INI). In panel (b), *thick* lines are referring to the final states of the idealized models *with* orographic uplift (LIFT), and *thin* lines *without* orographic uplift (NLFT) for the respective scenarios.

from the west just parallel to the surface. In this respect, the impact of this vertical motion induced by orography on the vertical temperature profile over both the city and cropland is now studied. Therefore, two additional runs with the idealized advection model (indicated with NLFT) are performed which now exclude the upward motion ($w_h = 0$).

In the base case, the effect of neglecting the uplift on the near-surface temperature is small (0.57 K), but the layer between 50 m and 200 m is now significantly warmer because of the absence of vertical adiabatic cooling. The mixed-layer height is also reduced from 80 m to 55 m. In contrast, the effect of the uplift on the near-surface temperature is much greater in the scen case (2.03 K) where the city of Paris is replaced by cropland. It even turns out that in the scenario run, the cooling and increase in inversion height because of vertical heat advection is much greater than from the surface cooling alone. The reduced sensitivity of the near-surface temperature to the uplift in the base case compared to the scen case results from the formation of a small mixed layer in response to positive sensible heat flux over the city. In this mixed layer where the potential temperature is constant, the vertical temperature advection becomes zero even though there is vertical motion. Only a slight reduction in the mixed-layer temperature appears because the sensible heat is mixed over a slightly increased mixed-layer height due to the uplift. For the base case, the largest sensitivity to vertical temperature advection is not close to the

surface, but only in the layer between 50 to 200 m where the potential temperature is not constant and adiabatic cooling is important. For the scen case, the impact of the adiabatic cooling is large for the entire NBL up to the inversion height.

Excluding the upward motion, the differential surface heating between the base case and scen case between 22:00 UTC and 23:00 UTC results in an UHI buildup from 2.7 K to 4.6 K at the surface (compare 'base NLFT' with 'scen NLFT' in Fig. 2.12 (b)). This UHI buildup is smaller than for the simulations including the vertical motion (6.1 K). It can be explained by the difference adiabatic cooling at the surface between the base case and the scen case explained above. Hence, an additional UHI buildup at the surface of 1.5 K is explained by the decrease in adiabatic cooling over the city compared that over cropland. This amounts to 25% of the total UHI intensity. Because of the distinct impact of vertical motion on the vertical temperature profile over the city (base case) and over cropland (scen case) explained in the previous paragraph, the whole vertical extent of the UHI is affected by the ramp uplift as well.

Note that the adiabatic cooling due to orographic forcing only exists for the nocturnal situation, and does not affect the near-surface temperature or UHI intensity during the day. Indeed, the near-surface potential temperature for the scenario run (Fig. 2.7 (b)) resembles the orography around Paris (Fig. 2.1), which is not the case in the scenario run for the day (Fig. 2.8). It stems from the fact that during the day, it is dealt with a CBL in both scenarios for which the (change in) vertical heat advection is negligible as mentioned above, especially when the mixed-layer height is very high.

Sensitivity to the nocturnal stability

As mentioned in the evaluation, the ARPS-model tends to produce too stable surface-temperature profiles. Therefore, the impact of nocturnal stability on the UHI buildup is discussed. This is done by dividing the slopes of initial temperature profiles at 22:00 UTC by a factor 2, see Fig. 2.13. The cases excluding the uplift are considered first. On the one hand, the change in the near-surface temperature for the base case along the trajectory is decreased by 0.4K, because the positive heat flux gets distributed over a deeper mixed-layer. On the other hand, the near-surface temperature change remains about the same for the scen case (at least if one considers the same inversion height). Therefore, a decrease in nocturnal stability results in a decrease in UHI buildup when the uplift is excluded. Furthermore, if one includes the uplift, the adiabatic cooling is decreased by 1.0K for the scen case while the lower adiabatic cooling in the base case is only decreased by 0.2K (compare difference in thick and thin dashed lines between Figs. 2.12 and 2.13 for the final states). As a result, the overall reduced adiabatic cooling due to destabilization results in an additional decrease of the overall UHI intensity of 0.8K as well. Hence, the decrease in stability by a factor two leads to a total decrease of the UHI buildup of 0.8K + 0.4K = 1.2K (20% of the overall UHI intensity). Therefore, the too stable boundary temperature profiles found at natural land-covers in the ARPS model may explain its overestimation of the UHI buildup.

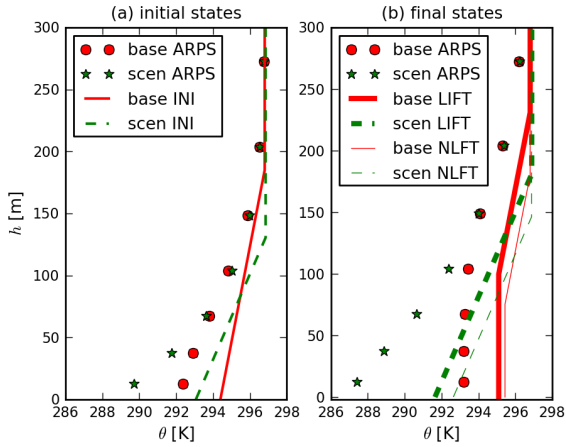

Figure 2.13: Idem to Fig. 2.12, except that the stability of the initial profiles for the base and scen case are now reduced by a factor two.

Sensitivity to the nocturnal low-level jet

The ARPS model tends to reproduce a too strong nocturnal low-level jet. In this respect, the effect of a reduction of the nocturnal low-level jet is now explained with the idealized advection model. Hereby, it is assumed that the near-surface horizontal wind speed below is reduced by the same factor as the nocturnal low-level jet aloft, see Fig. 2.14. On the one hand without considering the vertical uplift, such a decrease results in an increase of the UHI buildup: when halving the wind speed ($1.75\,\mathrm{m\,s^{-1}}$ instead of $3.5\,\mathrm{m\,s^{-1}}$), the air-column would need twice as much time for the trajectory under consideration, so two hours instead of one hour. For the CBL in the base case without upward motion and starting from a zero mixed-layer depth ($h_e = 0$), it can be derived from Eqs. 2.3 and 2.4 that the increase in surface temperature (now 2.05K instead of 1.45) along the trajectory reduces by the square root of this time factor two. Analogously for the NBL in the scen case starting from a inversion height of 150 m, one can show with a Taylor expansion that the decrease in temperature (now -0.90 instead of -0.45K) is enhanced by the time factor itself. This means that without upward motion the UHI-buildup over the trajectory increases from 1.90K to 2.95K due to a decrease in horizontal wind speed. As a result, the UHI-intensity would reach a value of 5.65K instead of 4.60K (considering the same intial value at the starting point of 2.72K). On the other hand, the vertical uplift tends to decrease by a factor two as well (cfr. Eq. 2.16). This means that the rate of strong adiabatic cooling at the surface due to vertical advection, which mostly occures over cropland in the scen case, is reduced. Consequently, the overall UHI buildup is now reduced. This is partially counteracted by the fact that the air column now takes twice as much time over the same trajectory. Accounting for these opposing effects, the overall adiabatic cooling in the base case becomes slightly larger (-0.76K instead of -0.57K), whereas for the scen case, it becomes smaller (-1.58 instead of -2.03K). As a result, the impact of a reduced horizontal wind speed on the reduction of the adiabatic cooling (base minus scen) is -0.64K, so contributes negatively to the overall UHI buildup. In

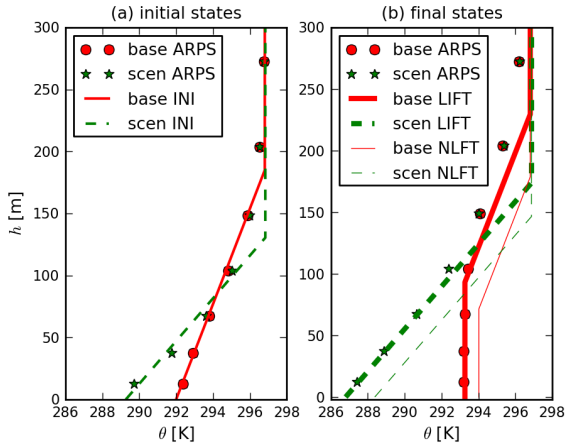

Figure 2.14: Idem to Fig. 2.12.The horizontal and vertical wind speed for both scenarios are reduced is by a factor two in the advection model. The final states of the advection model represents the temperature profile for 00:00 UTC at 6.3km downwind of the city centre, because the time over the trajectory of 12.6 km is increased by a factor two. These are compared with the ARPS profiles for 23:00 UTC at the same position.

summary, an overestimation of the nocturnal jet could lead to an underestimation of UHI buildup. In the absence of the ramp uplift, the underestimation becomes larger.

Impact of radiative cooling

The impact of this radiative cooling on the UHI buildup is discussed. This was excluded in the idealized advection model. Therefore, the radiative cooling to ground and space in the boundary-layer is estimated from the boundary-layer temperature profiles and surface temperatures from ARPS during the trajectory. For the scen case, the difference between the surface temperature (T_s = 281K) and screen-level temperature ($T_{2\mathrm{m}}$ = 284K) amounts to 3K over the trajectory between 22:00 and 23:00 UTC in the ARPS results. Applying Eq. 8.41 from Pielke (2002) and using a mixing ratio of q = $7.5\,\mathrm{g\,kg^{-1}}$ from the ARPS model output, this leads to a radiative cooling to space for the first 150m above the surface lower than $-0.03\,\mathrm{K\,h^{-1}}$ for both scenarios, so this was neglected. In contrast, the radiative cooling rate to the ground for a thin layer of four meter above the surface at the screen-level temperature ($T_{2\mathrm{m}}$ = 284K) amounts to $-1.76\,\mathrm{K\,h^{-1}}$. However, the large radiative cooling is limited to a thin layer above the surface that could lead to a negative curvature of the temperature profile found in ARPS. Even more extreme cooling rates were found in Steeneveld et al. (2010) between 1.3m and 10m above the surface of up to $-3.5\,\mathrm{K\,h^{-1}}$ for very stable conditions. Hereby, one should note that the idealized advection model only accounts for a piecewise linear vertical temperature profile in which cooling rates are constant over the CBL or NBL. Therefore, one can not capture the extra radiative cooling near the surface. This cooling near the surface could be partially counteracted by a possible redistribution of the vertical temperature profile

by turbulent mixing. Furthermore, the radiative cooling of the next 150 metre (above this thin layer) is much smaller ($-0.29\,\mathrm{K\,h^{-1}}$) than for this thin layer. Hereby, a constant temperature of T = 293K representative for the top of the NBL is considered, so this cooling rate can be considered as a (negative) upper limit. Both Savijärvi (2006) and Ha and Mahrt (2003) find radiative cooling rates no lower than $-0.5\,\mathrm{K\,h^{-1}}$ with similar nocturnal situations, except for a thin layer close to the ground. Yet, this cooling rate of the NBL is of the same order as the cooling due to the negative surface sensible heat flux of $-0.45\,\mathrm{K\,h^{-1}}$ (scen case NLFT minus INI), but lower than the adiabatic cooling for the scen case of $2\,\mathrm{K\,h^{-1}}$ (scen case LIFT minus NLFT).

For the base case, one finds surface temperatures of $T_s = 290$K, screen-level temperatures of $T_{2\mathrm{m}} = 291$K and mixed-layer temperatures of 295K. On the one hand, the cooling rate of a four-metre thin layer above the surface amounts to $0.63\,\mathrm{K\,h^{-1}}$, which is lower than the radiative cooling rate of $-1.76\,\mathrm{K\,h^{-1}}$ in the scen case. This differential cooling rate may lead to an extra heat-island buildup of $1.1\,\mathrm{K\,h^{-1}}$ but only for a 4m thin layer close to the surface ignoring a possible vertical redistribution of the vertical temperature profile. On the other hand, the cooling rate of the neutral layer of 80m above this thin layer is $-0.12\,\mathrm{K\,h^{-1}}$. As a result, the differential radiative cooling between the scenarios could only slightly enhance the UHI build-up by $0.17\,\mathrm{K\,h^{-1}}$. This is much smaller than the UHI buildup due to the differential surface sensible heat of $1.9\,\mathrm{K\,h^{-1}}$ or the differential reduction in adiabatic cooling of $1.5\,\mathrm{K\,h^{-1}}$.

2.4 Conclusions

Using the the Advanced Regional Prediction System (ARPS) at a horizontal resolution of 1 km and covering an area of 100 km × 100 km, the urban heat island over Paris during summer 2006 is studied. A base run is performed in which the present-day (urban) surface characteristics are represented, and an additional scenario run in which the urban surface is replaced by cropland. A five-day period is analyzed for which the (boundary-layer) UHI intensity is high. Even though the urban parametrization is not sophisticated, the UHI intensity is simulated very well. In particular, the maximum difference in 2m temperature between urban and rural areas stemming from the urban heating is reproduced with a relative error of less than 10%.

The dominant heating terms and their relative importance for the development of the maximum UHI intensity occurring during the night are analyzed. The interactions between the urban surface heating, boundary-layer stability, and orography were investigated. It was found that the increased storage-heat uptake during the day, which is subsequently released during the night, is the most important reason for the difference in surface sensible heat during the night. The increased storage heat uptake stems from the reduced evapotranspiration in the city, the large heat capacity and the very small thermal roughness lengths of the urban surface. The nocturnal anthropogenic heat release is also important for the differential surface sensible heat.

The maximum UHI intensity averaged over the selected five-day period is described. Its maximum occurs at 23:00 UTC. Because the differential surface sensible heat between urban and vegetative areas remains constant under nocturnal stability, the urban heat island persists with only a slight decrease until 06:00 UTC in the morning when a

large convective boundary layer is formed. The ground-level UHI intensity reaches its maximum at 23:00 UTC and located 6 km downwind of the city centre where a value of 6.1 K is found. The spatial extent of the maximum ground-level UHI intensity has an ellipsoidal shape stretched along the prevailing wind direction.

Even though the nocturnal differential urban sensible heat is much lower than during the day, the UHI intensity reaches its maximum during the night. In order to investigate this behaviour in a rigorous way, idealized advection models for the NBL and CBL are developed which account for the prevailing wind, turbulent surface heating/cooling and vertical uplift. Hereby, the nocturnal evolution of the temperature profile was well reproduced for both scenarios. It is shown that the vertical and horizontal advection and the exchange of surface sensible heat between the surface and the overlying atmosphere are the dominant processes explaining the boundary-layer structure both in the city and over cropland. It is demonstrated that the main part of the UHI buildup is directly related to the small differential surface sensible heat flux during the night. Despite this low differential sensible heat compared to the day, the UHI intensity reaches a maximum because of its confinement to the lowest 150 metres under nocturnal stability. Hereby, the slightly positive sensible heat over the city at night results in a mixed layer of 50 m, instead of a downward sensible heat flux of 20 Wm^{-2} over the croplands for which the boundary layer remains stable. This implies that any further increase in urban surface heating (such as anthropogenic heat from e.g. air conditioning) during the night would likely have a larger impact on the near-surface temperature, and thus impact on human health, than a similar heat increase during the day.

An air uplift is explained by the synoptic east wind and a ramp upwind of the city centre. This induces a strong vertical adiabatic cooling over cropland for the nocturnal boundary layer. The adiabatic cooling is decreased in the case of the mixed layer over the city. This reduction could explain an important part (25%) of the maximum UHI intensity. The differential adiabatic cooling has an impact on the vertical extent of the UHI as well. Furthermore, the UHI is affected by the nocturnal stability and the nocturnal low-level jet. Therefore, excessive nocturnal stability found in ARPS may lead to an overestimation of the UHI buildup, whereas a too strong low-level jet may result in an underestimation. The reduction of the radiative cooling to the surface due to the mixed-layer above the city compared to the NBL over cropland may enhance the UHI buildup as well, but only for a few metres above the surface. From this idealized study it can be concluded that, not only the nocturnal urban surface heating itself, but also its interactions with orographic forcing, shear mixing, boundary-layer stability, the low-level jet and boundary-layer radiation determine the evolution of the whole vertical profile of the UHI. Therefore, improvement of representing these boundary-layer features in atmospheric models are important for UHI studies.

2.5 Appendix

2.5.1 Orographic flow over a ramp

As apparent from Section 2.3.4, the vertical uplift plays an important role in explaining the evolution of the nocturnal temperature profiles, both for the base case as the scenario

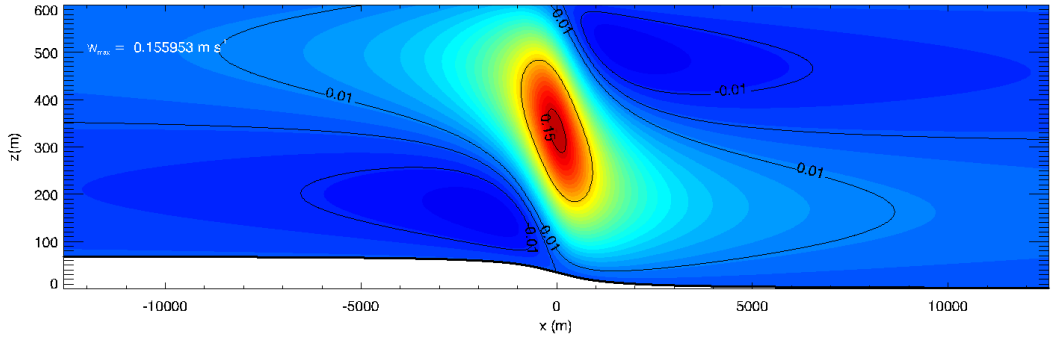

Figure 2.15: Vertical velocity relative to the slope-following wind induced by a ramp in a stably stratified flow for a vertical atmospheric slice. In this figure, the wind comes from the left

simulation. ARPS simulation results clearly show uplift over the city at the western (downwind) side of a ramp located at approx. 2.55°E. Here, we try to verify whether this orographic feature (i.e, the ramp) is capable of explaining the simulated (in ARPS) vertical wind field relative to the slope wind, which is characterized by wind speed values of the order of a few $\mathrm{cm\,s^{-1}}$.

We calculate the flow field induced by a ramp (Fig. 2.15) for a stably stratified atmosphere characterized by a lapse rate and a (constant) wind speed U, following Lin (2007). We assume that the stable stratification extends to infinity in the vertical direction, which is obviously a gross simplification compared to the actual situation (cfr. ARPS result), in which a stably stratified inversion layer is located underneath a residual neutral layer. We describe the orography of the ramp with height h_m and horizontal scale a as

$$h_m(x) = \frac{1}{2}\,\overline{h}_m \left[1 - \frac{2}{\pi}\arctan\frac{x}{a}\right] \tag{2.11}$$

This functional form has the advantage of having a derivative that can be easily Fourier-transformed (see below).

As in Lin (2007), we obtain the perturbation vertical velocity $w'(x,z)$ by solving the Scorer equation for its Fourier-transform $\hat{w}(k,z)$,

$$\frac{\partial^2 \hat{w}}{\partial z^2} + k^2 - l^2 \hat{w} = 0 \tag{2.12}$$

with k the horizontal wavenumber, and $l = N/U$ the vertical wave number, with $N = \sqrt{g\gamma/\theta_0}$ the Brunt-Väisäla frequency, g the gravitational acceleration and $\theta \simeq 300\,\mathrm{K}$ a reference temperature.

The lower boundary condition on the vertical velocity is given by

$$w'(x,0) = U\frac{dh_m}{dx} = -\frac{U\,\overline{h}_m}{\pi}\frac{a}{a^2+x^2} \tag{2.13}$$

and its Fourier transform is

$$\hat{w}(k,0) = \frac{1}{2\pi}\int_{-\infty}^{+\infty} w'(x,0)e^{-ikx}dx = -\frac{U\,\overline{h}_m}{2\pi}e^{-ka} \tag{2.14}$$

with the requirement that $k > 0$.

The vertical velocity is then obtained by applying the inverse one-sided Fourier transform,

$$\begin{array}{rcl} w'(x,z) & = & 2\Re\left\{\int_0^\infty \hat{w}(k,0)e^{ikx}dk\right\} \\ & = & -\frac{U\,\overline{h}_m}{\pi}\frac{a\cos(lz)-x\sin(lz)}{a^2+x^2}. \end{array} \tag{2.15}$$

However, as we are interested in an ABL slab that follows the terrain, the terrain-following vertical velocity $w'(x,0)$ has to be substracted, so that finally

$$w'(x,z) = -\frac{U\,\overline{h}_m}{\pi}\frac{a\cos(lz)-1-x\sin(lz)}{a^2+x^2}, \tag{2.16}$$

which is shown in Fig. 2.15 for $U = 3.5\,\mathrm{ms}^{-1}$, $a = 1000\,\mathrm{m}$, $\gamma = 0.04\,\mathrm{Km}^{-1}$, $h_m = 70\,\mathrm{m}$, and $\theta_0 = 300\,\mathrm{K}$.

From this, it appears that, despite the simplifications, our simple orographic model is capable of reproducing the order of magnitude of the vertical wind speed.

2.5.2 Solution of Eq. 2.3

In this appendix we seek a solution for:

$$\frac{dh_e}{dt} = \frac{\overline{w'\theta'}}{\gamma h_e} + w_h \tag{2.17}$$

Subject to the initial condition $h_e(0) = h_0$.

Performing a change of variable $h_e \equiv p^{-1}$, this equation converts into a somewhat more manageable form, which can be integrated to yield, at time t,

$$\frac{\overline{w'\theta'}}{\gamma w_h^2}\ln\left[\frac{\overline{w'\theta'}\gamma^{-1}+w_h h_0}{\overline{w'\theta'}\gamma^{-1}+w_h h_e t}\right] + \frac{h_e t - h_0}{w_h} - t = 0. \tag{2.18}$$

This is a transcendental equation in $h_e(t)$, which can be solved to any desired accuracy by mean of, e.g., the Newton-Raphson iterative zero-finding algorithm. In the case of $w_h = 0$, Eq. (2.18) cannot be applied, but the solution of (2.17) is then trivial, and given by:

$$h_e(t) = \sqrt{h_0^2 + \overline{w'\theta'}\gamma^{-1}t}. \tag{2.19}$$

Chapter 3

Comprehensive Parametrization of Surface-Layer Transfer Coefficients for Use in Atmospheric Numerical Models

This chapter is based on the publication: *Wouters, H., De Ridder, K., van Lipzig, N. P. M., Jun. 2012. Comprehensive Parametrization of Surface-Layer Transfer Coefficients for Use in Atmospheric Numerical Models. Boundary-Layer Meteorology 145 (3), 539-550.*

3.1 Introduction

Turbulent fluxes of momentum, sensible heat and latent heat from the surface to the atmosphere largely determine the interaction between the surface and the air above. Consequently, they have a substantial affect on wind, temperature, moisture and concentrations of other air constituents near the surface. A common approach to calculating the surface transfer coefficients and the consequential fluxes is by means of the Monin-Obukhov similarity theory (MOST). Within this framework, transfer coefficients generally need to be calculated iteratively. As iterative solutions for the transfer coefficients are computationally expensive, analytical approximations have been investigated for the past 30 years.

To simplify this problem, early analytical approximations such as Louis (1979), Byun (1990), Lee (1997) and Viterbo et al. (1999) assume $z_{0\mathrm{H}} = z_0$ (z_0 and $z_{0\mathrm{H}}$ are the aerodynamic and thermal roughness lengths, respectively). Others assume a constant $z_{0\mathrm{H}}/\, z_0$ ratio, or a fixed $kB^{-1} = \ln(\, z_0/\, z_{0\mathrm{H}})$, as in Pleim (2006). More sophisticated methods such as Garratt (1992, see p. 243), Uno et al. (1995), Launiainen (1995), Holtslag and Ek (1996), Mascart et al. (1995), Song (1998), De Bruin et al. (2000), Blümel (2000) and Li et al. (2010) allow a varying kB^{-1}. A few of the above-mentioned analytical

approaches have been compared in van den Hurk and Holtslag (1997). As stated by their respective authors, the analytical approaches above can reproduce the iterative procedure very well yet for limited ranges of z/z_0 (z is the reference height, or typically the height of the first vertical model level), kB^{-1} and/or Ri_{B} (bulk Richardson number). However, they fail to reproduce the full range $-0.5 \leq kB^{-1} \leq 30$, $10 \leq z/z_0 \leq 10^5$ and $-5.0 \leq Ri_{\mathrm{B}} \leq 2.5$. In particular, the case of urban surfaces, for which very high kB^{-1} values of more than 10 (see Voogt and Grimmond, 2000; Sugawara and Narita, 2008) and very low z/z_0 values down to 10 are found, is problematic. As the horizontal resolution of atmospheric models increases, urban areas may well extend over several grid boxes. Therefore, a new analytical parametrization for turbulent fluxes applicable for this situation is necessary.

We present herein new bulk transfer coefficients for both unstable and stable surface-layer conditions as an approximation to the iterative procedure within the MOST framework. As opposed to existing parametrizations, they are applicable for $10 \leq z/z_0 \leq 10^5$ and $-0.5 \leq kB^{-1} \leq 30$ that capture all surface types and model configurations. They also account for the roughness-sublayer (RSL) effect, which is important when z/z_0 becomes small (see Garratt, 1992, section 3.3.4). The advantage of an analytical form is its easy implemention in models that already use an analytical approach. In addition, analytical formulations avoid slow or non-convergence that can occur with iterative procedures. More particular, a recent paper (Li et al., 2014) indicates that number of needed iterations needed for convergence could exceed over 80. According to the interactive discussion of Li et al. (2014), the overall computational cost of our non-iterative procedure reduces the computational cost with a factor factor 20 compared to an iterative procedure.

The structure of the chapter is as follows: a summary of the MOST is given in Section 3.2 including a brief description of the iterative procedure. Section 3.3 describes the new analytical approximation, and in Section 3.4, the results of the new analytical procedure are shown. In Section 3.5, a comparison is made between existing analytical procedures, the new analytical procedure and the iterative approach. Finally, conclusions are given in Section 3.6.

3.2 Iterative solution for the transfer coefficients

The turbulent fluxes of momentum and sensible heat between the surface and the atmosphere are given by

$$(\overline{u'w'})_0 = -u_*^2 = -C_{\mathrm{M}} u_a^2, \tag{3.1}$$

$$(\overline{w'\theta'})_0 = -u_*\theta_* = -C_{\mathrm{H}} u_a(\theta - \theta_s), \tag{3.2}$$

where u_a and θ are the absolute wind speed and potential temperature at the reference height (or height of the first model level) z above the displacement height, θ_s is the surface potential temperature, C_{M} and C_{H} are the drag coefficients for momentum and sensible heat respectively, u_* is the friction velocity, and θ_* is the turbulent temperature scale. Based on MOST (Monin and Obukhov, 1954) and including RSL effects (e.g. Physick and Garratt, 1995; De Ridder, 2010), one assumes surface profiles for wind and

temperature. Hereby, the lower boundary conditions, i.e. the zero wind and $\theta = \theta_s$, are considered at $z = z_0$ and $z = z_{0\mathrm{H}}$, respectively. The transfer coefficients within this framework can be calculated by:

$$C_\mathrm{M} = k^2 \left[\ln \frac{z}{z_0} - \Psi_\mathrm{M}(\zeta) + \Psi_\mathrm{M}\left(\frac{z_0}{z}\zeta\right) + \Psi^*_\mathrm{M}\left(\zeta, \frac{z}{z_*}\right)\right]^{-2}, \tag{3.3}$$

$$C_\mathrm{H} = k\sqrt{C_\mathrm{M}} \left[\ln \frac{z}{z_{0\mathrm{H}}} - \Psi_\mathrm{H}(\zeta) + \Psi_\mathrm{H}(\frac{z_{0\mathrm{H}}}{z}\zeta) + \Psi^*_\mathrm{H}\left(\zeta, \frac{z}{z_*}\right)\right]^{-1}, \tag{3.4}$$

where $\zeta = zkg\theta_*/(u_*^2\theta_0)$ is the stability parameter, Ψ_M and Ψ_H are the (integrated) stability functions for momentum and heat, Ψ^*_M and Ψ^*_H are the profile corrections to account for the RSL, θ_0 is a reference potential temperature, $g = 9.81\,\mathrm{m\,s^{-2}}$ is the gravitational acceleration, and z_* is the roughness sublayer height. These surface-layer transfer coefficients can be calculated once ζ is known. One can find a relation between Ri_B and ζ (see e.g. Arya, 2001, Section 13.4), that can be solved for ζ iteratively using e.g. the root finding scheme of Ridders (1979) as described in Press et al. (1992). The ultimate challenge is to find an analytical expression for ζ that makes the iterative method dispensable.

To conclude this section, the flux-profile relationships used in the iterative solution and for calculating the transfer coefficients are given below. For unstable surface-layer conditions ($\zeta < 0$), the integrated profile functions of Paulson (1970) derived from the profile functions of Dyer (1967) or Businger (1966) are adopted:

$$\Psi_\mathrm{M} = 2\ln\frac{1+x}{2} + \ln\frac{1+x^2}{2} - 2\tan^{-1}x + \pi/2, \tag{3.5}$$

$$\Psi_\mathrm{H} = 2\ln\frac{1+y}{2}, \tag{3.6}$$

where $x = (1-\gamma_m\zeta)^{1/4}$ and $y = (1-\gamma_h\zeta)^{1/2}$ and $\gamma_m = \gamma_h = 16$. When including RSL effects (see below), one needs the original non-integrated profile functions as well:

$$\phi_\mathrm{M} = (1-\gamma_m\zeta)^{-1/4}, \tag{3.7}$$

$$\phi_\mathrm{H} = (1-\gamma_h\zeta)^{-1/2}. \tag{3.8}$$

For stable conditions ($\zeta > 0$), integrated profile functions are taken from Cheng and Brutsaert (2005) as recommended by Guo and Zhang (2007):

$$\Psi_\mathrm{M}(\zeta) = -a\ln\left[\zeta + \left(1+\zeta^b\right)^{\frac{1}{b}}\right], \tag{3.9}$$

$$\Psi_\mathrm{H}(\zeta) = -c\ln\left[\zeta + \left(1+\zeta^d\right)^{\frac{1}{d}}\right], \tag{3.10}$$

with $a = 6.1$, $b = 2.5$, $c = 5.3$, $d = 1.1$. The corresponding non-integrated profile functions are:

$$\phi_{\rm M} = 1 + a\frac{\zeta + \zeta^b \left(1+\zeta^b\right)^{\frac{1-b}{b}}}{\zeta + \left(1+\zeta^b\right)^{\frac{1}{b}}}, \tag{3.11}$$

$$\phi_{\rm H} = 1 + c\frac{\zeta + \zeta^d \left(1+\zeta^d\right)^{\frac{1-d}{d}}}{\zeta + \left(1+\zeta^d\right)^{\frac{1}{d}}}. \tag{3.12}$$

To account for RSL effects, the following approximation for $\Psi^*_{\rm M}$ and $\Psi^*_{\rm H}$ proposed by De Ridder (2010) is adopted:

$$\Psi^*_i\left(\zeta, \frac{z}{z_*}\right) \simeq \phi_i \left[\left(1 + \frac{\nu}{\mu z/z*}\right)\zeta\right] \frac{1}{\lambda} \ln\left(1 + \frac{\lambda}{\mu \frac{z}{z_*}}\right) e^{-\mu \frac{z}{z_*}} \tag{3.13}$$

where $\lambda \simeq 1.5$, $\mu = \mu_M \simeq 2.59$, $\mu = \mu_H \simeq 0.95$ and $\nu \simeq 0.5$. For both the iterative procedure and the analytical approximation presented below, a ratio of $z_*/\, z_0 = 16.7$ is adopted from Sarkar and De Ridder (2010).

3.3 The analytical expression for the transfer coefficients

The analytical approximation to the transfer coefficients is presented below. In essence, an approximate analytical expression for ζ is derived as a function of $Ri_{\rm B}$, $z/\, z_0$ and the ratio $z_0/\, z_{0\rm H}$ for unstable and stable conditions, seperately.

3.3.1 Unstable surface layer

The following analytical expression for the unstable surface layer ($Ri_{\rm B} < 0$) that accounts for the RSL is proposed:

$$\zeta = (1 + pQ)\, \frac{(\, L^*_{0\rm M})^2}{L^*_{0\rm H}}\, Ri_{\rm B}, \tag{3.14}$$

where $p = \ln(1 - \, Ri_{\rm B})$,

$$\begin{aligned} Q = &-0.486 + 0.219p - 0.0331p^2 - 4.93e^{-\,L_{0\rm H}} - 3.65\, L^{-1}_{0\rm H} \\ &+ 0.38p\, L^{-1}_{0\rm H} + 14.8\, L^{-2}_{0\rm H} - 0.946p\, L^{-2}_{0\rm H} - 10.0\, L^{-3}_{0\rm H} \\ &+ 0.392\, L_{0\rm M}\, L^{-1}_{0\rm H} - 0.0840p\, L_{0\rm M}\, L^{-1}_{0\rm H} + 0.368\, L_{0\rm M}\, L^{-2}_{0\rm H}, \end{aligned} \tag{3.15}$$

and

$$L_{0i} = \ln(z/z_{0i}), \tag{3.16}$$

$$L^*_{0i} = L_{0i} + \frac{1}{\lambda} \ln\left(1 + \frac{\lambda}{\mu_i \frac{z}{z_*}}\right) e^{-\mu_i \frac{z}{z_*}}. \tag{3.17}$$

The coefficients appearing in the expression for Q are found by multiple linear regression similar to Yang et al. (2001). Eq. 3.14 incorporates the correct limit behaviour for $\zeta \to 0$, for which the (integrated) flux-profile relationships can be linearized in which the slope at the origin $(Ri_{\rm B}, \zeta) = (0, 0)$ is given by $(L^*_{0\rm M})^2 / L^*_{0\rm H}$.

3.3.2 Stable surface layer

For the stable surface-layer ($Ri_{\rm B} > 0$), the normalized transfer coefficients $C_{\rm M}/C_{\rm Mn}$ and $C_{\rm H}/C_{\rm Hn}$ have a remarkable behaviour (see Section 3.4). The values change drastically for a change from 'small' to 'large' values of kB^{-1}. Therefore, we distinguish between weakly and strongly stable conditions. The weakly stable solution for ζ is given in Section 3.3.2. Afterwards, it is connected to a strongly stable solution in Section 3.3.2.

The weakly stable solution

For weakly stable conditions (small positive ζ), we first linearize ϕ_i and Ψ_i. Afterwards, the relation between $Ri_{\rm B}$ and ζ is inverted analytically from which we find an expression for ζ.

As in Yang et al. (2001), a linear approximation for (3.9)-(3.10) can be made for weakly stable conditions by putting $\Psi_i(\zeta) \simeq -\beta_i \zeta$. The relation between $Ri_{\rm B}$ and ζ now reduces to:

$$Ri_{\rm B} = \zeta \frac{L^*_{0\rm H} + S^*_{0\rm H}\,\beta_{\rm H}\zeta}{(L^*_{0\rm M} + S^*_{0\rm M}\,\beta_{\rm M}\zeta)^2}, \tag{3.18}$$

where

$$S^*_{0i} = 1 - z_{0i}/z + \left(1 + \frac{\nu}{\mu_i \frac{z}{z_*}}\right) \frac{1}{\lambda} \ln\left(1 + \frac{\lambda}{\mu_i \frac{z}{z_*}}\right) e^{-\mu_i \frac{z}{z_*}}. \tag{3.19}$$

It is now possible to obtain ζ from Eq. 3.18 analytically as in Byun (1990) for $z_0 = z_{0\rm H}$ or Yang et al. (2001) for $z_0 \neq z_{0\rm H}$:

$$\zeta = \frac{-L^*_{0\rm M}}{S^*_{0\rm M}\,\beta_{\rm M}} - \frac{BC}{4(S^*_{0\rm M}\,\beta_{\rm M})^3 (B^2 + |C\,r|)} + \frac{B - \sqrt{B^2 + C\,r} + \dfrac{BC\,r}{2(B^2 + |C\,r|)}}{2(S^*_{0\rm M}\,\beta_{\rm M})^3\,r}, \tag{3.20}$$

where

$$r = Ri_{\rm B} - S^*_{0\rm H}\,\beta_{\rm H}/(S^*_{0\rm M}\,\beta_{\rm M})^2, \tag{3.21}$$

$$B = S^*_{0\rm M}\,\beta_{\rm M}\,L^*_{0\rm H} - 2\,S^*_{0\rm H}\,\beta_{\rm H}\,L^*_{0\rm M}, \tag{3.22}$$

$$C = 4(S^*_{0\rm M}\,\beta_{\rm M})^2\,L^*_{0\rm M}\,(S^*_{0\rm H}\,\beta_{\rm H}\,L^*_{0\rm M} - S^*_{0\rm M}\,\beta_{\rm M}\,L^*_{0\rm H}). \tag{3.23}$$

The best agreement between the iterative solution and the analytical approximation is obtained with $\beta_{\rm M} = 4.76 + 7.03\,z_0/z + 0.24\,z_{0\rm H}/z_0$ and $\beta_{\rm H} = 5$. Although this rarely happens, the last term of (3.20) has to be omitted when $r = 0$ to avoid division by zero. In that case (i.e. $Ri_{\rm B} = S^*_{0\rm H}\,\beta_{\rm H}/(S^*_{0\rm M}\,\beta_{\rm M})^2 \simeq 0.2$), the correct analytical limit for $r = 0$ is given by the first two terms.

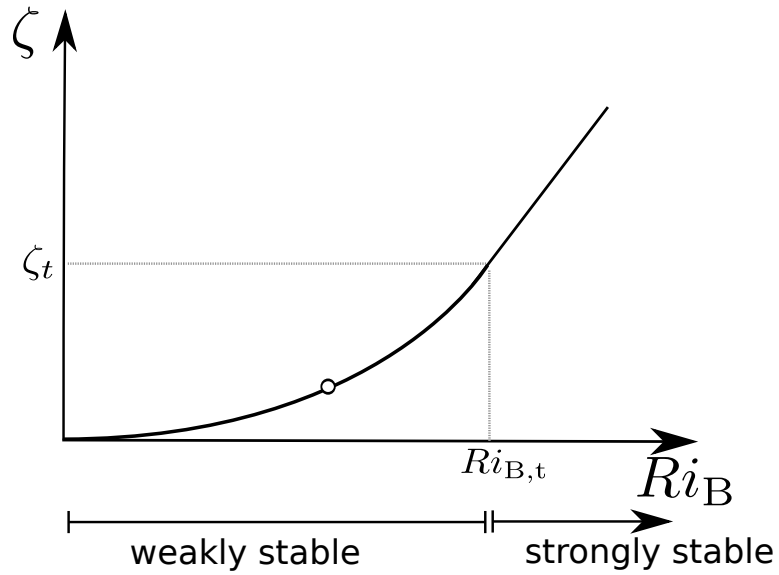

Figure 3.1: The analytical approximation of ζ for the stable surface layer. The intercept of the strongly stable solution ($Ri_{B,t}$, $\zeta_{\rm t}$) that connects the weakly and the strongly stable regimes is shown. The location where $r = 0$ in (3.20) and for which we have to exclude the third term is indicated with an open circle. See text for further information.

The connection of the weakly stable solution with a strongly stable solution

As suggested by Li et al. (2010), a linear relation between $Ri_{\rm B}$ and ζ for strongly stable conditions (large positive ζ) can be assumed to approximate the iterative solution. Its constant slope $d\zeta/d\,Ri_{\rm B}$ and its intercept ($Ri_{B,t}$, $\zeta_{\rm t}$), at which the weakly stable solution ceases and the strongly stable solution commences, is now determined. Therefore, it is assumed that the slope of the strongly stable solution $d\zeta/d\,Ri_{\rm B}$ is equal to the slope of the weakly stable solution at the intercept $Ri_{B,t}$. The latter is expressed by:

$$D(\zeta_t) = \frac{(\,L^*_{0\rm M} + \,S^*_{0\rm M}\,\beta_{\rm M}\,\zeta_{\rm t})^3}{L^*_{0\rm M}\,L^*_{0\rm H} + \,\zeta_{\rm t}(2\,S^*_{0\rm H}\,\beta_{\rm H}\,L^*_{0\rm M} - \,S^*_{0\rm M}\,\beta_{\rm M}\,L^*_{0\rm H})}, \tag{3.24}$$

which can be obtained by taking the reciprocal of the derivative of (3.18). The following two criteria now have to be fulfilled simultaneously for the intercept ($Ri_{B,t}$, $\zeta_{\rm t}$) at which the weakly stable solution ceases and the strongly stable solution commences. Firstly, $\zeta_{\rm t}$ should be lower than the maximum ζ for which the weakly stable solution ($\zeta < \zeta_{\rm t}$) is a good approximation. Secondly, $D(\,\zeta_{\rm t})$ given by (3.24) should be a representative value for the slope of the strongly stable solution ($\zeta \geq \zeta_{\rm t}$). The following expression for $\zeta_{\rm t}$ meets these two criteria:

$$\begin{aligned}\zeta_t \;\; = \;\; & -0.316 - 0.515e^{-\,L_{0\rm H}} + 25.8e^{-2\,L_{0\rm H}} + 4.36\,L_{0\rm H}^{-1} \\ & -6.39\,L_{0\rm H}^{-2} + 0.834\,(\ln\,L_{0\rm M}) - 0.0267\,(\ln\,L_{0\rm M})^2\,.\end{aligned} \tag{3.25}$$

Then, $Ri_{B,t}$ can be obtained by calculating (3.18) at $\zeta_{\rm t}$:

$$Ri_{B,t} = \,\zeta_{\rm t}\frac{L^*_{0\rm H} + \,S^*_{0\rm H}\,\beta_{\rm H}\,\zeta_{\rm t}}{(\,L^*_{0\rm M} + \,S^*_{0\rm M}\,\beta_{\rm M}\,\zeta_{\rm t})^2}. \tag{3.26}$$

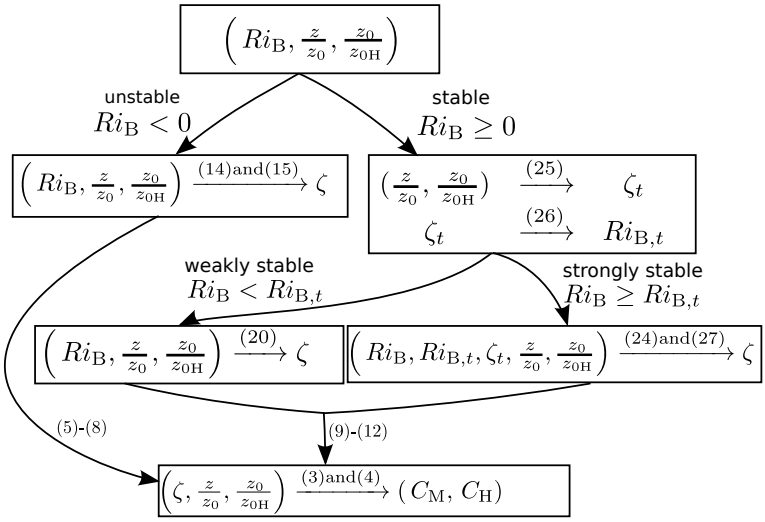

Figure 3.2: A decision tree for calculating ζ and the consequential transfer coefficients

The expression for the strongly stable solution ($Ri_{\mathrm{B}} > Ri_{B,t}$) is now given by:

$$\zeta = \zeta_{\mathrm{t}} + D(\zeta_{\mathrm{t}})(Ri_{\mathrm{B}} - Ri_{B,t}). \tag{3.27}$$

For the weakly stable solution ($Ri_{\mathrm{B}} \leq Ri_{B,t}$), the solution is given by (3.20). An analytical solution for the whole stable range has now been constructed.

Figure 3.2 gives an overview of the presented analytical solution for both unstable and stable conditions for easy implementation.

3.4 Results

The normalized transfer coefficients $C_{\mathrm{M}}/C_{\mathrm{M,n}}$ and $C_{\mathrm{H}}/C_{\mathrm{H,n}}$, for which 'n' refers to neutral stability ($Ri_{\mathrm{B}} = 0$), are compared for the approximate analytical and iterative solution for $kB^{-1} = \{-0.5, 0, 2, 10, 20, 30\}$, $z/z_0 = \{10, 10^3, 10^5\}$ and Ri_{B} between -5 and 2.5 by steps of 0.02. The reference height (i.e. height of the first model level) is typically 10 to a few tens of metres, and consequently z_0 values up to 1.5 m - typical for urban surfaces - are captured. The resulting transfer relations are shown in Figs 3.3 and 3.4, and are discussed below.

For the stable region, the resulting analytical transfer relations follow the iterative solution very well, despite the fact that the functions change shape drastically when going from low to high kB^{-1} values. In particular, they decrease drastically from a certain Ri_{B} value and this value itself depends strongly on the ratio z/z_0 and kB^{-1}. This is captured very well, because the analytical approximation has a variable transition point $Ri_{B,t}$ between the weakly stable and the strongly stable regime that depends on z_0 and kB^{-1}. Because of the linear approximation for the strongly stable solution, there can be a substantial deviation between the analytical and iterative solutions for ζ as a function of Ri_{B} for strongly stable conditions. However, this has a minor effect on the final values

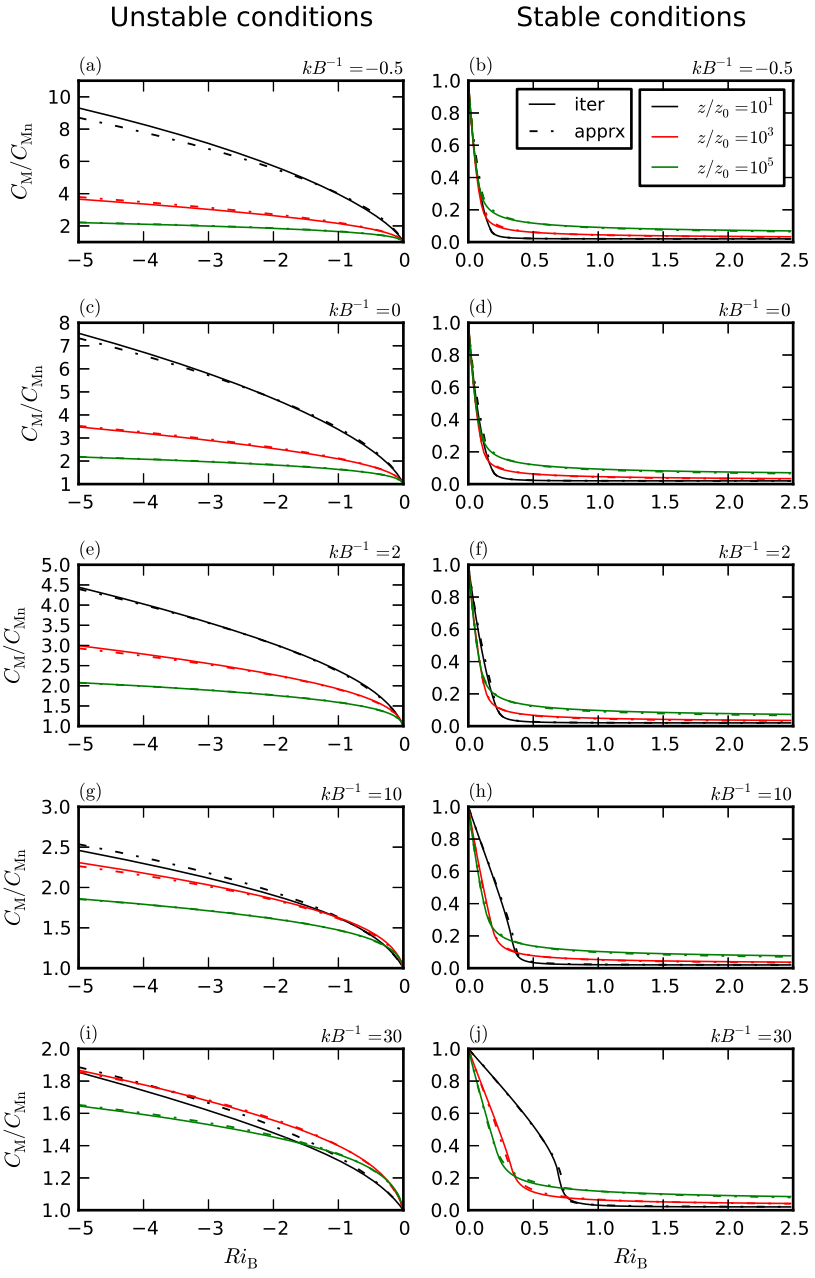

Figure 3.3: The approximate (apprx) and iterative (iter) transfer relations for momentum are demonstrated. Unstable and stable conditions are shown respectively on the left in panels (a)-(c)-(e)-(g)-(i)-(k) and on the right in panels (b)-(d)-(f)-(h)-(j)-(l). kB^{-1} is set to -0.5, 0, 2, 10, 20 and 30 in panels (a)-(b), (c)-(d), (e)-(f), (g)-(h), (i)-(j) and (k)-(l), respectively. In each panel, values for $z/\,z_0$ are shown in different colours.

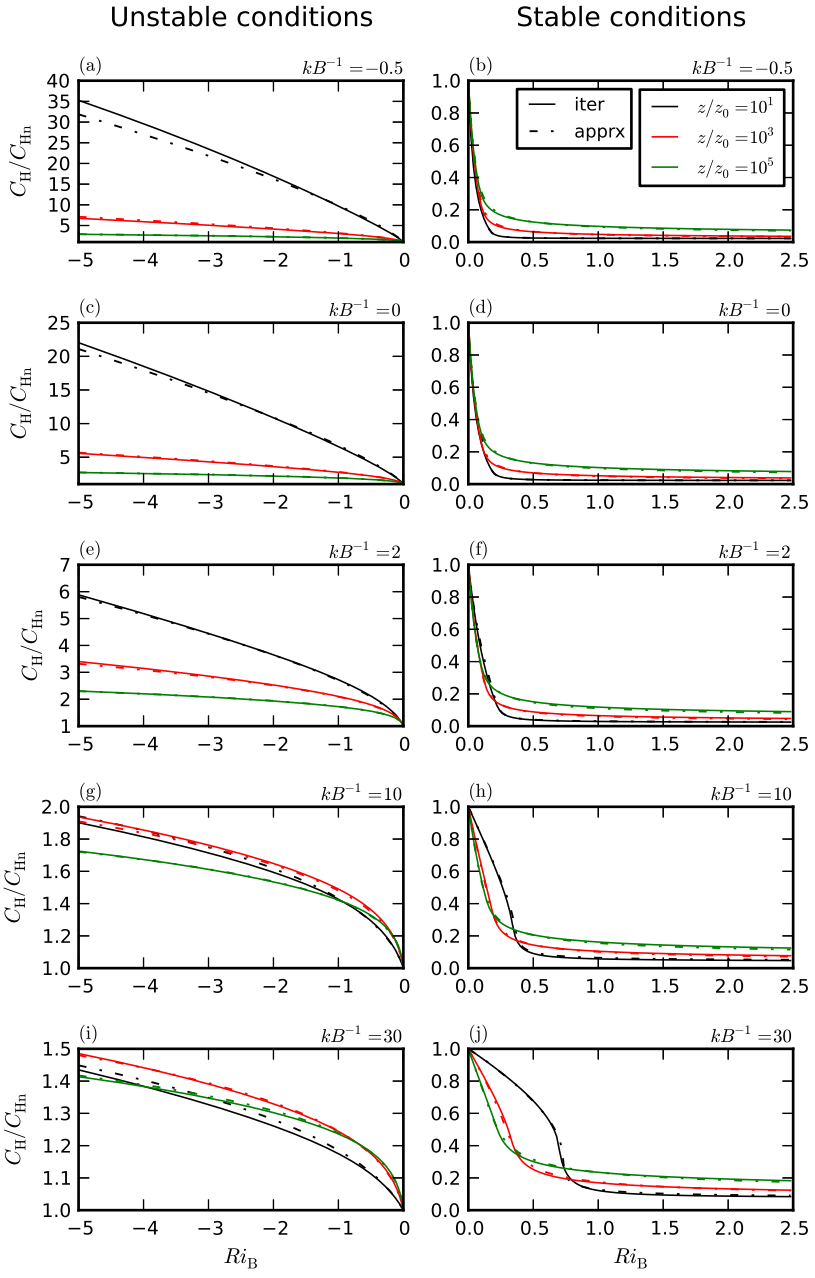

Figure 3.4: As in Fig. 3.3, but for the transfer relations for heat instead of momentum.

of the transfer coefficients, because they are nearly constant for strongly stable conditions. The relative error is less than 10%, except at an Ri_B-range around $Ri_{B,t}$, at which the

transfer coefficients fall abruptly with increasing Ri_{B}. For this narrow range, the relative error can be up to 40% for $kB^{-1} > 15$. Because of the dramatic drop around $Ri_{B,t}$ and the sensitivity of the position for this drop on z/z_0 and kB^{-1}, the error of the analytical approximation around $Ri_{B,t}$ is actually small compared to other uncertainties of either Ri_{B}, z/z_0 or kB^{-1}. Moreover, uncertainties in the flux-profile relationships are much larger than the error of the analytical solution for very stable conditions. This can be seen when comparing the iterative solution obtained with the flux-profile relationships of Beljaars and Holtslag (1991) with that obtained with the flux-profile relationships of Cheng and Brutsaert (2005), see Section 3.5. For unstable conditions, we obtain good agreement for $C_{\mathrm{M}}/C_{\mathrm{Mn}}$ and $C_{\mathrm{H}}/C_{\mathrm{Hn}}$: the relative error of the transfer coefficients is always $< 10\%$ for $-5 \leq Ri_{\mathrm{B}} < 0$.

3.5 Discussion: comparison with other non-iterative methods

A comparison is made between existing non-iterative parametrizations from Yang et al. (2001) and Li et al. (2010), the non-iterative parametrization presented herein and the iterative solution. This is done under conditions for which our parametrization was developed, i.e. urban surfaces. A typical value for the roughness length (z_0) for urban areas is 1 m and this leads to a ratio $z/z_0 = 15$ when assuming a height of the first model layer of $z = 15\,\mathrm{m}$. With this configuration, we discuss the normalized transfer coefficients $C_{\mathrm{H}}/C_{\mathrm{Hn}}$ as a function of kB^{-1} for four stability conditions in Fig. 3.5 (similar results are found for $C_{\mathrm{M}}/C_{\mathrm{Mn}}$).

For the weakly unstable case ($Ri_{\mathrm{B}} = -0.08$), Li et al. (2010) has a large deviation from the iterative solution for high kB^{-1} values. In contrast, Yang et al. (2001) and the current parametrization compare very well with the iterative solution. For the weakly stable case ($Ri_{\mathrm{B}} = 0.08$), Yang et al. (2001) gives the best comparison with the iterative solution with flux-profile relationships from Beljaars and Holtslag (1991) and the new proposed analytical solution with the flux-profile relationships from Cheng and Brutsaert (2005). A large deviation is found for Li et al. (2010) compared to the iterative solution for $kB^{-1} > 4$: the ratio $C_{\mathrm{H}}/C_{\mathrm{Hn}}$ becomes > 1, i.e. the drag coefficient for the stable case becomes higher than that for the neutral case which is unrealistic. For the strongly unstable case ($Ri_{\mathrm{B}} = -3$), similar results are obtained as in the weakly unstable case. In addition, Yang et al. (2001) has a substantial deviation for very large kB^{-1} values between 20 and 25, while it is invalid for $kB^{-1} > 25$. For the strongly stable case ($Ri_{\mathrm{B}} = 1$), Yang et al. (2001) does not have a solution, but now Li et al. (2010) performs relatively well. Again here, the new parametrization performs well for all kB^{-1} values. As mentioned before, the new analytical approximation for stable stratification is constructed using flux-profile relationships from Cheng and Brutsaert (2005) for stable stratification. In contrast, the analytical approximation of Li et al. (2010) is constructed using those from Beljaars and Holtslag (1991). For the strongly stable case, a substantial difference occurs between the iterative solutions using the different flux-profile relationships, and consequently also in their respective analytical approximations. This results from a large discrepancy between the different flux-profile relationships for strongly stable stratification (Guo and Zhang, 2007). Given this uncertainty for

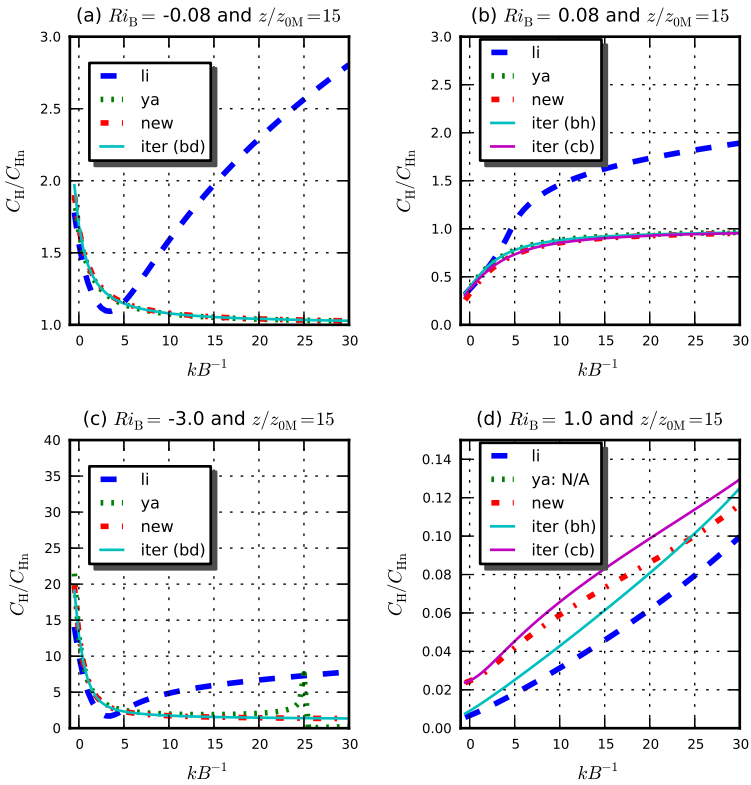

Figure 3.5: Normalized transfer coefficients for heat as a function of kB^{-1} between -0.5 and 30 for a fixed value of $z/z_0 = 15$. Weakly unstable ($Ri_B = -0.08$), weakly stable ($Ri_B = 0.08$), strongly unstable ($Ri_B = -3$) and strongly stable ($Ri_B = 1$) surface-layer conditions are demonstrated in panel (a), (b), (c) and (d) respectively. Results for the analytical approximations of Yang et al. (2001) (ya), Li et al. (2010) (li), the new parametrization (new) and the iterative solution (iter) are shown. For unstable stratification, the iterative solution (bd) uses (integrated) flux-profile relationships from Paulson (1970) for the unstable case. For the stable situations, the iterative solutions are shown using flux-profile relationships from Beljaars and Holtslag (1991) (bh) and from Cheng and Brutsaert (2005) (cb) respectively.

strong stability, the errors made with the new analytical approximation over the iterative solution are negligible.

To conclude, both the analytical approximations of Li et al. (2010) and Yang et al. (2001) perform well for the particular ranges of their interest for kB^{-1} and Ri_B values. However, they fail to approximate the iterative solution(s) for the full range $-0.5 \leq kB^{-1} \leq 30$ and $-5 \leq Ri_B \leq 2.5$, as they not have aimed for it. In particular, large kB^{-1} values typical for urban surfaces are problematic. In contrast, the new non-iterative solution proposed herein captures the full range very well.

3.6 Conclusions

In order to determine turbulent fluxes momentum and sensible heat between the surface and the atmosphere in a mesoscale atmospheric model, a new analytical method is presented to approximate the iterative transfer coefficients within the MOST framework, including RSL effects. Essentially, an analytical expression for ζ as a function of Ri_{B} is found from which the transfer coefficients for momentum and sensible heat are obtained. The transfer coefficients for other scalar variables such as moisture (q) can be taken equal to the transfer coefficient of sensible heat as shown in e.g. Andreas and Murphy (1986). For the unstable case ($Ri_{\mathrm{B}} < 0$), an ζ is obtained by multiple linear regression, in which the correct limit behaviour for $Ri_{\mathrm{B}} \to 0$ is incorporated. For weakly stable conditions, the exact solution for ζ using linear stability functions is used, and for strongly stable conditions a linear relation between Ri_{B} and ζ is assumed. The weakly and strongly stable solutions are smoothly connected by a transition point ($Ri_{B,t}$, ζ_{t}) that depends on kB^{-1} and the ratio z/z_0.

The transfer coefficients resulting from this analytical approximation reproduce the iterative solution very well for $10 \leq z/z_0 \leq 10^5$ and $-0.5 \leq kB^{-1} \leq 30$ that represents most, if not all, existing surface types. This should lead to an overall better performance with regard to the momentum exchange and energy balance at the surface. As most existing global and regional atmospheric models use an analytical approach already, our new method will require only a small change to the model code[1]. Especially, the presented bulk parametrization that avoids any iterative procedure can be used to simulate the contrasting behaviour among different land-surface types, for example to study the urban heat island effect as in Van Weverberg et al. (2008), Demuzere et al. (2008) and Sarkar and De Ridder (2010).

[1]The Fortran code for the presented non-iterative approximation can be obtained from the authors on request.

Chapter 4

The influence of water-vapor opacity on the evaluation of offline urban-climate modelling

Parts of this chapter have been submitted for publication in: *Wouters, H., Demuzere, M., De Ridder, K., van Lipzig, N. P. M.: The impact of impervious water-storage parametrization on urban-climate modelling. Submitted to urban climate on 23/12/2013*

4.1 Introduction

In urban climate model evaluation, upward infra-red radiation (wave-lengths of more than 5 μm) is the component of the urban surface energy balance with consistent discrepancy between tower observations and most, if not all, urban land-surface models (Grimmond et al., 2011, see their Fig. 5). Especially, a large and systematic overestimation is found during clear-sky conditions in summer for which the urban-canopy surface becomes very hot. The performance of urban surface parametrizations is very crucial at that time, because the urban heat island effect can become the large at that time. Therefore, this chapter focusses on urban-climate modelling evaluation in terms of upward infra-red radiation.

With the development and first tests of the new urban parametrization TERRA-URB presented in this chapter, similar overestimation of upward infra-red radiation was experienced as well. Our initial hypothesis for this overestimation of infra-red upward radiation was the simplified bulk representation of the radiation effects in TERRA-URB. In fact, the combination of urban structure and building materials leads to complex infra-red radiation effects within the urban canopy, thus deteriorating the modelling performance. Yet, the overestimation persists in urban models with very complex radiation schemes (e.g., Hénon et al., 2012). Hence, this suggests that the reason for this overestimation needs to be found elsewhere. At the same time, a phenomenon

not considered yet in the evaluation is the impact of infra-red water-vapor opacity (i.e. absorption and emission) on the upward infra-red radiation $R^{\uparrow}(z_{\mathrm{ref}})$ at an elevated sensor on a tower at height z_{ref}.

We first present TERRA-URB, a new simple and efficient urban land-surface parametrization for the regional climate model CCLM in section 4.2.2. In order to capture the main physical processes found for urban terrain (see section 1.1.1, a bulk approach is employed. Such a land-surface scheme assigns certain bulk parameters to the urban surface which is represented as a rough, impermeable slab. Afterwards, we develop the theoretical framework for the opacity (ie. absorption and emission) by water vapor in the infra-red spectrum in section 4.2.3. In section 4.3, an overview of the model setup and forcing is given. Finally, the impact of water-vapor opacity on urban-climate modelling evaluation for upward infra-red radiation of TERRA-URB is discussed in section 4.4. The evaluation concerning the other components of the surface-energy balance is given in chapter 6

4.2 Methodology

4.2.1 The Soil-Vegetation-Atmosphere Transfer model TERRA-ML

TERRA-ML (Grasselt, 2008) is the SVAT (Soil-Vegetation Atmosphere Transfer) component of the regional atmospheric model COSMO (Consortium for Small-scale Modeling), mainly used as operational forecast model by the German Weather Service (COSMO-EU and COSMO-DE, see Baldauf et al. (2011)) and more recently applied on climate scales (COSMO-CLM, see Rockel et al. (2008)). It is also part of the operational global atmospherical model GME from the German Weather Service (Majewski et al., 2002).

We give a brief description of TERRA-ML; for a more detailed description, see Doms et al. (2011); Grasselt (2008). TERRA-ML basically simulates the heat-transfer and hydrological transfer within the ground with a stacked Multi-Layer (hence ML) approach, as well as the plant transpiration and variable snow cover. It uses an implicit solution of the heat conduction equation for the ground layers, solving a three-diagonal linear system. The water budget of the soil model layers for the natural land cover depends on the conditions at the upper and the lower boundaries, on the water extraction by evapotranspiration, on gravitational and capillary transports, and on runoff formation. Net evapotranspiration is the sum of bare soil evaporation, plant transpiration, sublimation from the snow and evaporation from the interception store weighted by their respective areal coverages. Bare soil evaporation and plant transpiration is parametrized according to the BATS scheme (Biosphere Atmosphere Transfer Scheme) developed by Dickinson (1984). The hydraulic conductivity and hydraulic diffusivity both depend on soil moisture, pore volume, and the air dryness point. The coefficients for pore volume, and soil moisture at the air dryness point depend on soil texture. Hereby, hydraulic and thermal parameters of different soil types are specified according to a lookup table (Doms et al., 2011, see their tables 11.1 and 11.2). The vegetation in TERRA-ML is characterized by a number of parameters, being LAI, plant cover, root depth and roughness length. The surface albedo is acquired from that of the (wetted) soil, vegetation

and snow-cover weighted according to the areal proportion of plant cover and snow within the grid cell. Albedo and soil texture are depending on six spatially-varying soil types. TERRA-ML employs a prognostic snow albedo and temperature. The coupling between the atmosphere and the underlying surface is modeled by a stability and roughness-length dependent surface flux formulation. Hereby, the atmospheric conditions above the ground for wind, temperature, humidity and incoming radiation need to be specified. In the coupled version with the atmospheric part of COSMO or CCLM, these are specified from the first model layer above the ground. In the stand-alone (ie. 'offline') version, these are specified from mast-tower measurements. The model's response in terms of momentum and heat transfer between the surface and the air above are calculated with surface-layer transfer coefficients for momentum and heat between the surface:

$$(\overline{u'w'})_0 = -u_*^2 = -C_{\mathrm{M}} u_a^2, \tag{4.1}$$

$$Q_{\mathrm{H}} = \rho c_p (\overline{w'\theta'})_0 = -\rho c_p u_* \theta_* = -\rho c_p C_{\mathrm{H}} u_a (\theta - \theta_s), \tag{4.2}$$

where u_a and θ are the absolute wind speed and potential temperature at the reference height (or height of the first model level) above the displacement height, θ_s is the surface potential temperature, C_{M} and C_{H} are the transfer coefficients for momentum and heat respectively, u_* is the friction velocity, and θ_* is the turbulent temperature scale. In the standard version, the transfer coefficients are obtained with Louis-type non-iterative transfer relations (Louis, 1979).

4.2.2 Urban-land surface parametrization TERRA-URB

TERRA-URB implements a built-in representation (see Fig. 4.1) of the urban physical processes in TERRA-ML. This processes include the closure of the urban surface energy balance (Oke, 1988):

$$Q_* + Q_F = Q_{\mathrm{H}} + Q_{\mathrm{E}} + \Delta Q_S + \Delta Q_A \tag{4.3}$$

where Q_* is the net radiation at the top of the urban canopy, Q_F is the anthropogenic heat, Q_{H} is the surface sensible heat flux, Q_{E} is the latent heat flux, and ΔQ_A is the heat (or equivalent latent heat) advection through the sides of the control volume (neglected). The storage heat flux ΔQ_S represents the total heat transfer to/from the urban surface/ground that includes buildings (roofs and walls) and roads, and is equivalent to the ground heat flux. Therefore, an urban surface class is added to the surface module. In order to capture the main physical processes found in urban environments (see Section 1.1.1), a bulk approach is implemented. Hereby, the urban land-cover is represented as a rough water-impermeable slab (no soil-hydrology). Urban bulk parameter values for the surface roughness length, albedo, emissivity Sarkar and De Ridder (2010), thermal conductivity and volumetric heat capacity (Demuzere et al., 2008; De Ridder et al., 2012) are assigned to the urban land-use. The turbulent and radiative fluxes are calculated for both urban and natural land-use combined with a tile approach, thus weighted according the respective fractional areas. For each tile, stability-dependent surface-layer transfer coefficients for momentum and heat are now replaced with an efficient non-iterative calculation following chapter 3. They account for roughness sublayer effects (De Ridder, 2006), and are generally applicable for urban environments. As stated in chapter 3, the

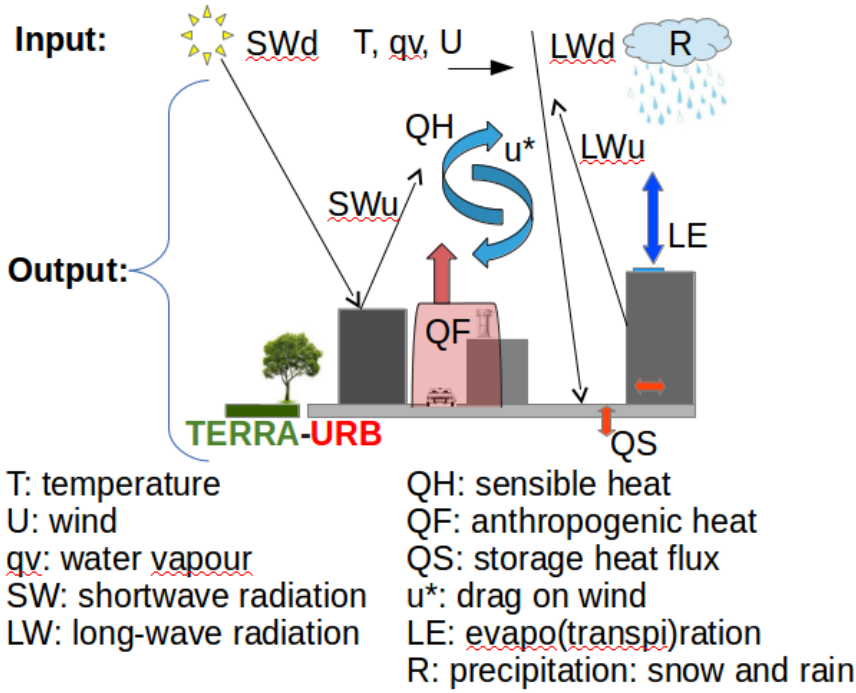

Figure 4.1: An overview of the urban-canopy processes implemented by TERRA-URB.

non-iterative methodology matches very well an iterative procedure for a wide range of aerodynamic and thermal roughness lengths, so that it comprehends both natural and urban land-cover types in an efficient way. This is done for both the urban and natural land-cover fraction. The thermal roughness length for the urban land-cover is obtained with a parametrization of the inverse Stanton number (De Ridder, 2006; Demuzere et al., 2008, as in):

$$kB^{-1} = \ln\left(\frac{z_0}{z_{0h}}\right) \tag{4.4}$$

with k the von Kàrmàn constant. The values taken for the urban land-cover is:

$$kB^{-1} = 1.29 Re_*^{0.25} - 2.0 \tag{4.5}$$

where $Re_* = u_* z_0/\nu$ is the roughness Reynolds number, and $\nu = 1.461 \cdot 10^{-5}\,\mathrm{m^2 s^{-1}}$ the kinematic vicosity of air. For the natural land-cover fraction, the inverse Stanton number equal to $kB^{-1} = 2.0$ is adopted from Garratt (1992). Anthropogenic heat is accounted for by adding externally-prescribed additional heat to the surface sensible heat flux.

The anthropogenic heat release in urban environment is established in different ways. On the one hand, it can be released as a direct additional heat source to the air, e.g. from traffic exhausts, chimneys, vent holes, and ventilations systems of buildings. On

the other hand, it can also be released indirectly by heat transfer through walls and windows from buildings leading to higher surface temperatures. In turn, this indirectly leads to additional heating terms to the atmosphere above through enhanced radiative emission of the surface and enhanced surface sensible heat release. Noting these different ways of the anthropogenic heat release, the above-mentioned method of accounting for anthropogenic heat releases in TERRA-URB is rather arbitrary. For instance, another way of accounting for anthropogenic heat release is by adding the additional heat terms to the soil. Yet, our arbitrary choice is still justified, because Sailor (2004) found that the resulting impact on modelling near-surface air-temperatures appears to be more sensitive to boundary-layer parametrization scheme than to the method of anthropogenic heat addition.

In this chapter, evaporation from the urban impervious surface is ignored. However, the evaporation will be considered later in more detail with a new impervious water-storage parametrization in chapter 5. As TERRA-URB is basically an extension of TERRA-ML and thus closely related, it automatically incorporates the standard features and further developments of TERRA-ML, such as the recent developments of representing snow-cover (Kazakova and Rozinkina, 2011).

4.2.3 Theoretical framework for water-vapor opacity for urban-climate model evaluation

In this section, we develop the theoretical framework for accounting for the infra-red absorption and emission by water vapor, see also Fig. 4.2. We start from the standard expression for the change in $R^{\uparrow}(z_{\mathrm{ref}})$ along the vertical (see Eq. 8-41 Pielke, 2002):

$$\frac{\partial R^{\uparrow}(z)}{\partial z} \simeq \frac{d\epsilon(q_v, u)}{dz} \left[\sigma T_a^4(z) - L^{\uparrow}\right], \tag{4.6}$$

where q_v is the water-vapor mixing ratio, $u = \int_0^z \rho dz$ is the normal path length, z is the height above the averaged urban canopy height, σ is the Stefann-Boltzmann constant, T_a is the air temperature, and $L^{\uparrow}$ the upward infra-red radiation emitted and reflected by the urban-canopy surface (and generally considered in urban models). Hereby, we have replaced the outgoing radiation from the ground σT_G^4 assuming a black-body surface at temperature T_G introduced in Pielke (2002, pp. 215) with the actual upward radiation $L^{\uparrow}$ from the surface (not necessarely assuming a black body). We obtain the following expression for water-opacity Assuming ρ and q_v constant and approximating T_a by the averaged air temperature $\overline{T_a}$ between the urban surface and the sensor leading to:

$$R^{\uparrow}(\, z_{\mathrm{ref}}) \simeq \epsilon(q_v, \delta u)\sigma\, \overline{T_a}^4 + [1 - \epsilon(q_v, \delta u)]\, L^{\uparrow} \tag{4.7}$$

where δu is the normal path length between the effective canopy height from where surface radiation originates ($z = z_s$) and the tower sensor ($z = z_{\mathrm{ref}}$). An intuitive representation of water-vapor opacity given by this equation is given in Fig. 4.3. According to Atwater (1974) (see also Pielke, 2002), the following expression is used for infra-red broadband emissivity for water vapor between the urban canopy and sensor:

$$\epsilon(q_v, \delta u) = \epsilon'(\delta P) = 0.136 \log_{10}(\delta P) + 0.54, \text{ for } \log_{10}(\delta P) > 0. \tag{4.8}$$

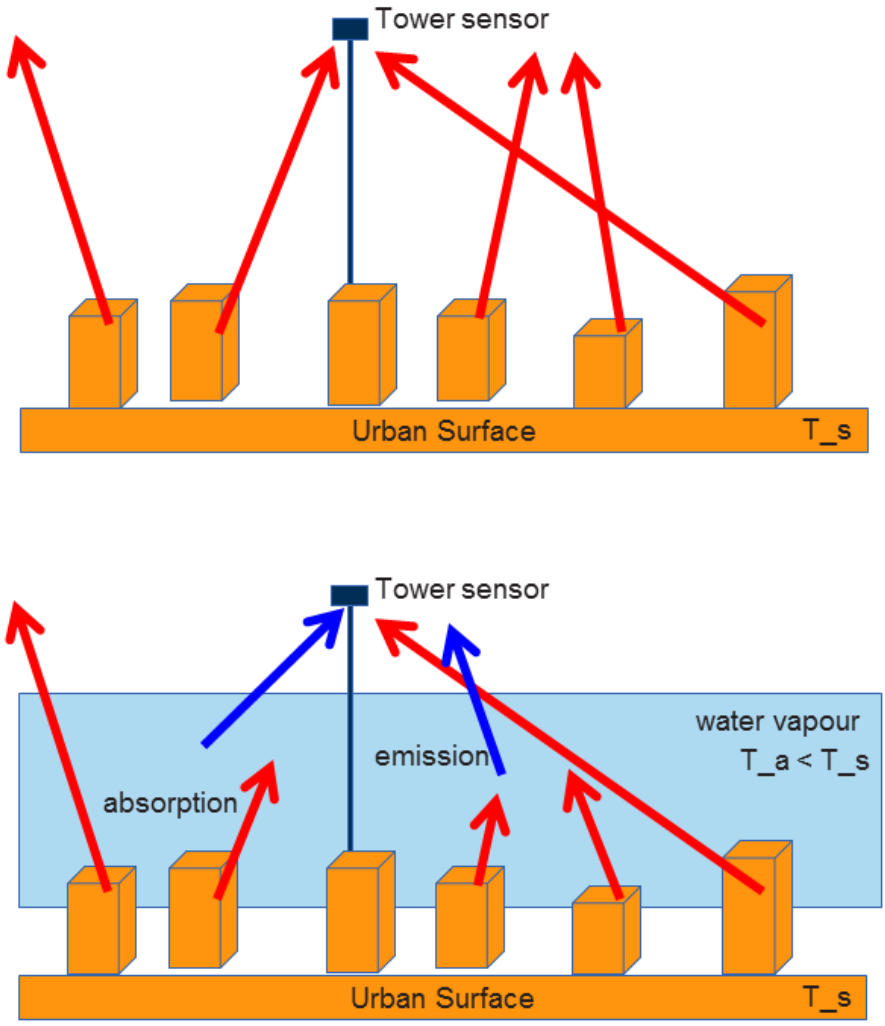

Figure 4.2: Overview and set-up of a tower sensor measuring the infra-red upward radiation in an urban area. The upper panel represents the situation without water vapor (or any other absorbing gas constitutent), and the lower panel that with water vapor (lightblue area). The red arrows represent the infra-red radiation emitted at temperature T_s by the hot urban surface (e.g. during a summer heat-wave at day-time), and the blue arrows that of the gas emitted at a lower temperature ($\overline{T_a} < T_s$). Both absorption and emission occurs by the water vapor.

where $\delta P = \int_{z_s}^{z_{\rm ref}} \rho q_v dz$ is the optical path length in g cm^{-2}. The averaged air temperature between the urban canopy and the tower sensor is approximated by:

$$\overline{T_a} = [(T^4(z) + T_{\rm 2m}^4)/2]^{1/4} \tag{4.9}$$

where $T_{\rm 2m}$ is the temperature at 2 metre above the displacement height d (see Section 5.2.3) extrapolated from the tower temperature at a height $z_{\rm ref} - d$ above the displacement

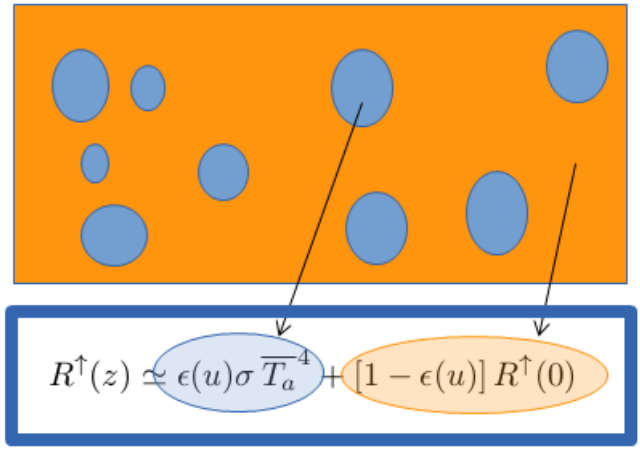

Figure 4.3: A top plan view of the tower sensor measuring the upward infra-red radiation as an intuitive representation of equation 4.7. The orange area represents the infra-red radiation originating from the urban-canopy surface at high temperature T_s (e.g. during a heat wave), whereas the blue area that from the water vapor above at lower averaged temperature $\overline{T_a}$ smaller than T_s.

height using:

$$T_{2\mathrm{m}} = T(z_{\mathrm{ref}}) + \frac{\theta^*}{\kappa}\left[\ln(2\,\mathrm{m}/(z_{\mathrm{ref}}-d)) - \psi(2\,\mathrm{m}/L) + \psi(z_{\mathrm{ref}}-d)/L)\right] \tag{4.10}$$

4.3 Model setup and forcing for Basel

Offline runs with TERRA-URB are configured for an urban tower-mast site at Basel (Sperrstrasse) during the Basel UrBan Boundary Layer Experiment (BUBBLE) in Rotach et al. (2005). The mean building height of $h = 14.6\,\mathrm{m}$ is obtained from `http://www.mcr.unibas.ch/Projects/BUBBLE/textpages/ob_frameset.en.htm` and the urban impervious fraction of 77% from the soil sealing database of the EEA (`http://www.eea.europa.eu/articles/urban-soil-sealing-in-europe`) upscaled to 1 km resolution. The roughness length is calculated from the mean building height ($z_0 \simeq 0.075h \simeq 1.1\,\mathrm{m}$). The remainder 23% consists of the natural surface fraction consists of loam with a plant cover of 95%. The surface module accounts for seasonal variation of the Leaf-area index between 1 and 3.9 (Smiatek et al., 2008). The anthropogenic heat is prescribed following the methodology of Flanner (2009).

Observations to force and evaluate TERRA-URB were obtained from sensors mounted on a mast tower during the BASEL campaign. The mast has a height of 32 m above the road. The corresponding effective reference height of the observation tower was obtained by subtracting the displacement height of $d \simeq 10z_0 = 11\,\mathrm{m}$, resulting in 21 m.

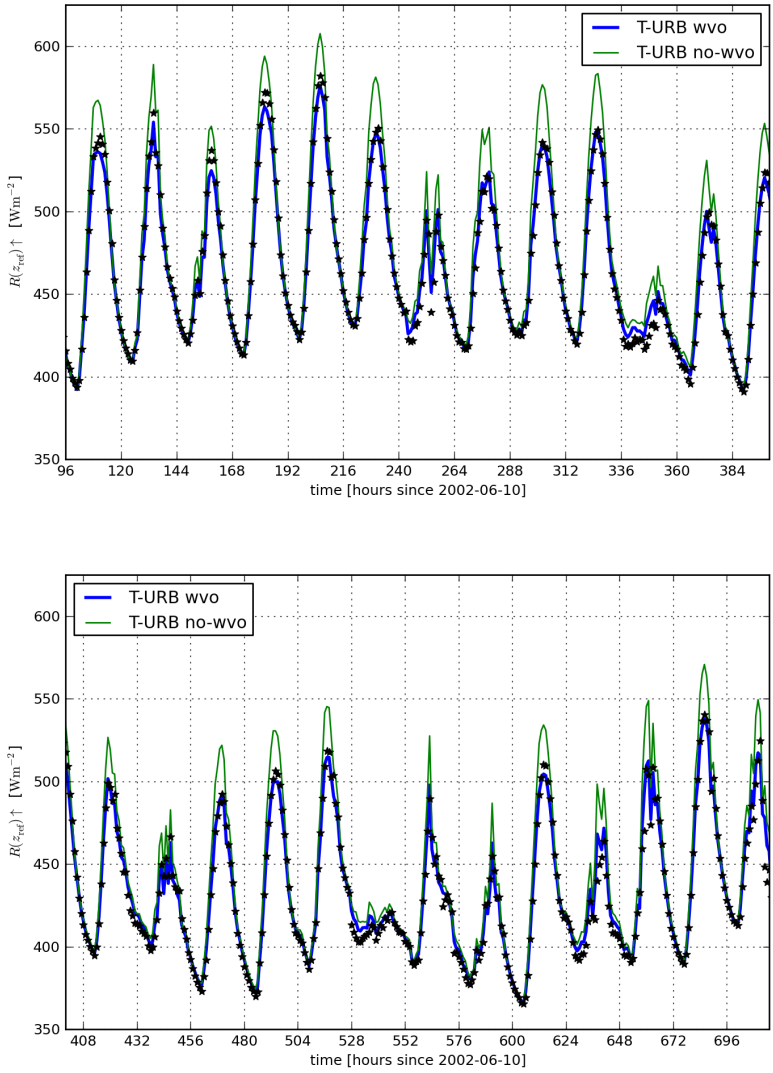

Figure 4.4: Comparison of tower observations for upward infra-red radiation and model results with TERRA-URB during the BUBBLE campaign. The blue line represents the results including the water-vapor opacity developed in Section 4.2.3, and the thin green line those excluding the water-vapor opacity.

4.4 Results and discussion

The results with TERRA-URB for the modelled upward infra-red radiation at sensor height are shown in Fig. 4.4 and scores are given in Tab. 4.1. The results of the offline runs with TERRA-URB show a large improvement on the modeled values of infra-red outgoing radiation. In particular, the large positive bias at noon exceeding $35\,\mathrm{W\,m^{-2}}$

	$R\uparrow(z_{\mathrm{ref}})$	
	T-URB wvo	T-URB no-wvo
RMSE	**4.99**	10.76
BIAS	**0.52**	10.55
R2	**0.995**	0.986

Table 4.1: The root-mean-square error (RMSE), bias (BIAS), and correlation (R2) for the output for the upward infra-red radiation at mast hight $R^{\uparrow}(z_{\mathrm{ref}})$ of TERRA-URB offline simulations during the BUBBLE campaign, taking account for infra-red water-vapor opacity (T-URB wvo) and neglecting it (T-URB no-wvo), respectively. The best scores are marked in bold.

is eliminated. A particular reason of the large impact of water-vapor opacity for urban canopies during heat-waves stems from the large temperature difference between the urban-canopy surface and the air temperature (including the water vapor), reaching several tens of °Cat day-time during clear-sky conditions. The impact of the water-vapor absorption on infra-red downward radiation is much smaller (not shown), because the difference between air-temperature below and above the elevated sensor is much lower as well.

4.5 Conclusions and recommendations

In this chapter, the new urban parametrization TERRA-URB for the regional climate model CCLM (the COSMO model in CLimate mode) is presented first. TERRA-URB extends the Soil-Vegetation Atmosphere Transfer (SVAT) model TERRA-ML for its applicability in urban environments. Hereby, TERRA-ML is the standard SVAT model of the regional-climate model CCLM. The computational efficiency of the TERRA-URB is preserved by adopting a stability-dependent non-iterative procedure for calculating surface-layer transfer coefficients both applicable for urban environments and accounting for the roughness-sublayer effects. The turbulent and radiative fluxes are calculated for both urban and natural land-use combined with a tile approach, thus weighted according the respective fractional areas. In order to capture the surface-energy balance found in urban areas, an urban surface class is added to the surface module which represents the urban land-cover as a rough water-impermeable slab. It adopts appropriate values for the surface roughness length, albedo, emissivity, thermal conductivity and volumetric heat capacity of the urban terrain.

A theoretical framework for taking into account the influence of broad-band water-vapor opacity (i.e., absorption and emission) on the upward infra-red radiation at an elevated sensor above the urban surface is presented afterwards.

The influence of water-vapor opacity on the upward infra-red radiation at sensor height modeled by TERRA-URB was investigated for an urban mast site at Basel (Sperrstrasse). Hereby, TERRA-URB was forced with meteorological parameters from the Basel UrBan Boundary Layer Experiment (BUBBLE) during the summer Intensive Observation Period in 2002.

A large impact (reduction of more than $35\,\mathrm{W\,m^{-2}}$) on the modeled upward infra-red radiation at sensor height was found during summer for Basel when taking into account the infra-red opacity of water vapor below the sensor. At the same time, much better agreement with observations from the sensor is found when taking into account the water-vapor opacity. Together with the disagreement between observations and urban-model results in other studies excluding water-vapor opacity, it is concluded that taking account of water-vapor opacity is essential for future urban-climate model evaluation and comparison with mast measurements.

Chapter 5

The impact of water-storage parametrization on urban climate modelling

Parts of this chapter have been submitted for publication in: *Wouters, H., Demuzere, M., De Ridder, K., van Lipzig, N. P. M.: The impact of impervious water-storage parametrization on urban-climate modelling. Submitted to urban climate on 23/12/2013*

5.1 Introduction

Urban climate simulations have become of great interest for several reasons. Urban climates impact the majority of the world's population, so it is a strategic topic of research. The question rises how urban expansion impacts on future temperature and precipitation patterns in making climate-change projections. To date, only little attention is given to evapotranspiration (ET) and run-off in urban areas (Grimmond and Oke, 1991; Masson, 2000; Kanda et al., 2005; Nakayoshi et al., 2009; Demuzere et al., 2013). Urban ET stands in stark contrast to natural environments where raindrops are retained by the natural pervious soil and vegetation. This is because a much greater part of the rain falling on urban impervious surfaces is lost to run-off. Therefore, one finds much smaller annual-mean ET rates from urban impervious surfaces, which is also less persistent throughout the year, compared to the natural surroundings. A much higher Bowen Ratio in urban areas (Velasco et al., 2010) is one of the major factors in increasing temperatures (Taha, 1997). Yet, it has been demonstrated from measurements that ET can become quite large for urban environments after rainfall (Grimmond and Oke, 1999). This is because, streets, building roofs and walls all become wet, and lead to an instant increase in evaporation. Evaporation from impervious surfaces may be enhanced by the fact that urban structures generally have a much higher temperatures at daytime (De Ridder et al., 2012) than natural areas. Therefore, evaporation from the urban impervious soil could exceed $100\,\mathrm{Wm}^{-2}$ shortly after the rainfall. As a result, urban

ET can still be an important source of water vapor in the atmosphere at that time. Furthermore, it can also be an important sink in the surface energy balance (SEB) as well, and consequently can influence the near-surface temperature and boundary-layer structure. Aside from the other contrasting features of urban areas compared to their natural surroundings, the discrepancies in ET could have an additional influence on the moisture, cloud formation, precipitation and temperature. Besides the climatic impacts, the water run-off can lead to pluvial flooding in urban areas during extreme rainfall.

In order to improve the impact assessment of future urban expansion on temperature, precipitation, it is essential to understand and properly represent all the contributions to ET from cities in atmospheric numeric models. Besides the contribution of evaporation from urban impervious surfaces to ET described above, other important contributions emerge from natural land-cover and vegetation in the city. Anthropogenic sources could play an important role as well (see review Sailor, 2011). These sources consist of combustion from households, heating of buildings, traffic, and industrial processes. Other anthropogenic contributions include evaporative cooling and air conditioning of buildings, and irrigation in the city (Kalanda et al., 1980). However, large uncertainties still exist in all the contributions to urban ET. For instance, the (relative) magnitude of these contributions may vary from place to place, throughout the day and throughout the year. Furthermore, one could also expect that evaporation from the impervious soil occurs in a spatially heterogeneous way. First of all, the heterogeneous building properties and materials could lead to an inhomogeneous water storage capacity and varying surface temperatures. As a consequence, water is distributed on the impervious surface in an inhomogeneous way. Secondly, the heterogeneous evaporation could be enhanced by radiation effects as well. For instance, south-oriented sloping roofs, may dry out much faster than roads or footways in the shadow. Lastly, the urban morphology could result in a varying ventilation and thus transport of moisture.

Various urban models do not consider evaporation from the impervious surfaces as a first approximation to the reduction of ET in cities (Hénon et al., 2012; Martilli et al., 2002; Schubert et al., 2012). Other models (Masson, 2000; Kanda et al., 2005; Oleson et al., 2008; Demuzere et al., 2013) use an arbitrary water-interception parametrization for the water-storage on the impervious surfaces. In particular, impervious water-storage parameters, including the maximum amount of water that can remain on the urban impervious surface and the maximum effective wet surface fraction, have not been estimated before. The scarce investigation and evaluation of modelling ET for cities (e.g. Grimmond and Oke, 1991; Demuzere et al., 2013) is hampered by the fact that available observations for latent heat over urban areas (e.g. from Rotach et al., 2005; Masson et al., 2008; Velasco et al., 2010) or over urban-scale models (Pearlmutter et al., 2009; Nakayoshi et al., 2009, e.g.) are limited, especially during rainfall periods. As a result, the role of evaporation and run-off through urban expansion and climate change to urban climate and the load of water drainage remains unknown.

A simple and physically-based framework for the evaporation from impervious surfaces is developed by representing water storage with a Surface water Interception Distribution (hereafter SID). As a forward step to unravel the uncertainties of ET in cities, evaporation from the urban impervious surfaces is simulated by implementing this SID-formulation in the urban surface module TERRA-URB. The latter has been presented in chapter 4.2.2. The SID parameters for the urban impervious surfaces at Toulouse are estimated

by employing a match between the modelled and observed quantities for latent heat after rainfall. Hereby, measurements from an intensive urban measurement campaign CAPITOUL (Masson et al., 2008) are used. An evaluation is performed for the different components of the energy balance for this campaign, but also cross-validated with an independent dataset from the BUBBLE campaign (Rotach et al., 2005). Furthermore, we assess the annual-mean and variability of ET from the urban areas in contrast to the natural environment. Finally, we investigate its impact on the different components of surface energy balance.

5.2 Methodology

5.2.1 Surface Interception Distribution (SID) for impervious surfaces

The SID conceptual model considers a set of water puddles (reservoirs) spread over the (urban) impervious surface, and assumes a certain distribution for their holding capacity (depth) D. Throughout the simulation, the water level $h(D)$ of a particular water reservoir with depth D changes due to precipitation, evaporation and run-off. For the situation that all water reservoirs are saturated, the impervious water storage reaches its maximum storage capacity $w = w_m$. Hereby, the level of each reservoir reaches their respective depth, see also Fig. 5.1 (a):

$$h_s(D) = D \tag{5.1}$$

At the time just after rainfall (when saturation is reached for all reservoirs) the surface becomes unsaturated due to evaporation and all water reservoirs (independent of their current level) loose an equal height of water (Fig. 5.1a). As a result, the level of all water reservoirs decreases with the same value, say h_t (for all $D > h_t$), except for those that are already dried out (for all $D \leq h_t$). This can be summarized with the following expressions for the level of wet reservoirs as a function of their reservoir depth:

$$h(D) \quad = D - h_t, \quad \forall D > h_t \tag{5.2}$$

$$h(D) \qquad = 0, \qquad \forall D \leq h_t \tag{5.3}$$

Hereby, the shallow water reservoirs for which $D < h_t$ are dried out. Note that for the saturated case, $h_t = 0$, and we get back Eq. 5.1.

Define $\phi(D)dD$ as the fraction of the impervious surface covered by water reservoirs with a depth ranging between D and $D + dD$. As urban surfaces are generally not perfectly flat, it consistents of both deep and shallow reservoirs. Therefore, we take the hypothesis that the probability density function $\phi(D) = \frac{d\delta}{dD}$ constantly decreases with depth and turns zero at the maximum reservoir depth D_m (Fig. 5.1b). As a result, the surface fraction of water reservoirs with capacity depth between D and $D + dD$ can be expressed by:

$$\phi(D)dD \quad = c(D_m - D)dD, \quad \forall D > h_t \tag{5.4}$$

$$\phi(D)dD \qquad = 0, \qquad \forall D \leq h_t, \tag{5.5}$$

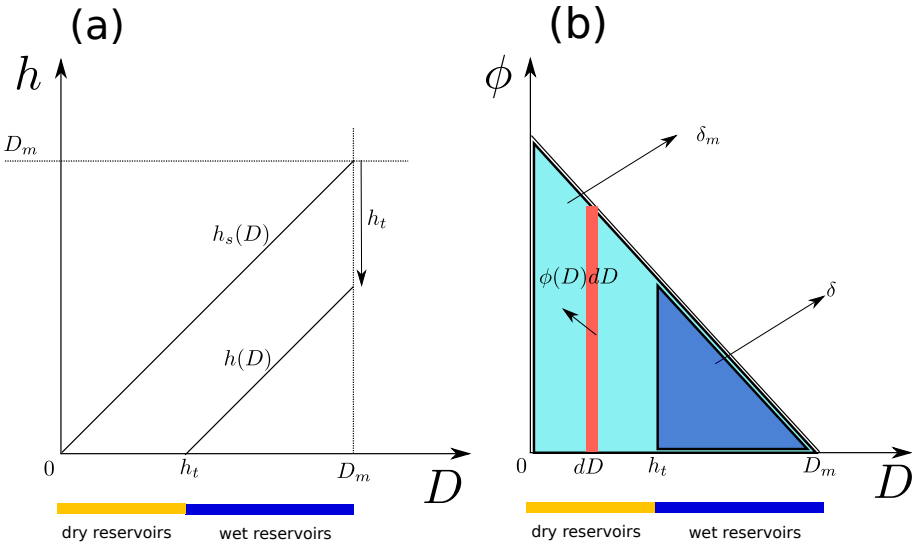

Figure 5.1: The reservoir level (h) as a function of the fixed reservoir holding capacity (depth) D for the saturated case ($h_s(D)$) and the unsaturated case ($h(D)$) (a). The arrow directed downwards indicates the evolution of the level of the water reservoirs during evaporation. Hereby, all water reservoirs loose an equal height of water given by h_t. Panel (b) shows the probability density function ϕ of the water storage reservoirs as a function of their depth (D). The surface area of the red rectangle is equal to the fraction of the impervious surface with reservoirs having a depth between D and $D + dD$.

and their water content by:

$$\rho_w h(D)\phi(D)dD = \rho_w(D - h_t)c(D_m - D)dD, \quad \forall D > h_t \tag{5.6}$$

$$\rho_w h(D)\phi(D)dD = 0, \quad \forall D \leq h_t \tag{5.7}$$

where c is a constant to be determined and $\rho_w = 1000\,\mathrm{kg\,m^{-3}}$ is the water density. These reservoirs from which evaporation occurs are spread over the fractional wet area δ relative to the impervious (urban) landcover. The effective wet surface fraction (i.e. the evaporative fraction of the impervious surface) δ and total amount of water per m^2 impervious surface w are given by the respective integrals over all wet water reservoirs:

$$\delta = \int_{h_t}^{D_m} c(D_m - D)dD \tag{5.8}$$

$$w = \int_{h_t}^{D_m} \rho_w(D - h_t)c(D_m - D)dD \tag{5.9}$$

Hereby, the integral boundaries account for the fact that $D > h_t$ (or $h > 0$) for the wet reservoirs and that we have a maximum reservoir depth ($D < D_m$), see also Fig. 5.1.

Coming back to the case of a saturated water storage ($h_t = 0$), we obtain the integrals for the maximum wet surface area and the maximum water storage on the impervious

surface, respectively:

$$\delta_m = \int_0^{D_m} c(D_m - D)dD \tag{5.10}$$

$$w_m = \int_0^{D_m} \rho_w D c(D_m - D)dD. \tag{5.11}$$

Considering that these two integral quantities are known water-storage parameters of the impervious surface, one obtains an expression for the constant c and D_m:

$$c = 2\delta_m / D_m^2 \tag{5.12}$$

$$D_m = 3\frac{w_m}{\delta_m \rho_w} \tag{5.13}$$

Therefore, the assumptions of a maximum total water storage w_m, a maximum wet surface fraction δ_m, a linear decreasing interception distribution (Eqns. 5.4-5.5) and a homogeneous desaturation of the interception stores (Eqns. 5.2-5.3), lead to the following expression for the surface interception distribution:

$$\phi(D) = 2\delta_m(D_m - D)/D_m^2 \tag{5.14}$$

These assumptions also imply that the deepest reservoirs have a capacity three times that of the average storage capacity w_m/δ_m of the maximum evaporative surface fraction δ_m (that is, if both are expressed in mm water equivalent). Substituting Eqns. 5.12-5.13 into the integrals for w and δ for the unsaturated case (Eqns. 5.8 and 5.9), we obtain:

$$\delta = \delta_m \frac{(D_m - h_t)^2}{D_m^2} \tag{5.15}$$

$$w = \delta_m \frac{\rho_w}{3} \frac{(D_m - h_t)^3}{D_m^2} \tag{5.16}$$

These two equations yield the relation between the evaporative surface fraction δ and the impervious water content w:

$$\delta = \delta_m \left(\frac{w}{w_m} \right)^{2/3} \tag{5.17}$$

The following expression is used for the water loss from the impervious surface due to evaporation:

$$\frac{dw}{dt} = -E_p\delta = \rho_w(\overline{w'q'})_0\delta = \rho_w C_{\mathrm{H}} u_a (q - q_{sat})\delta, \tag{5.18}$$

where E_p is the potential evaporation rate, $\overline{w'q'}_0$ is the turbulent surface-layer moisture transfer, C_{H} is the surface-layer scalar transfer coefficient, q the specific humidity at reference height, q_{sat} is the saturated specific humidity at the temperature of the surface,

and u_a is the wind speed. The following analytical solution can be found when integrating Eq. 5.18 and using Eq. 5.17 one timestep Δt:

$$w(t+\Delta t) = \left(w(t)^{1/3} - \frac{\delta_m E_p \Delta t}{3 w_m^{2/3}} \right)^3 \tag{5.19}$$

The 2/3 power relation in Eq. 5.17 is replaced by a 1/2 power relation when assuming a uniform (constant) surface interception distribution $\phi(D) = C^{\mathrm{st}}$ instead of a linear one. If one would assume that all reservoirs have the same depth (i.e. no distribution), then δ in Eq. 5.18 is a constant.

We assume that rain lost to run-off increases with the amount of water already present on the impervious surface. This is expressed by the following expression for the change in water storage w ($\mathrm{kg\,m^{-2}}$) due to rain R_0 ($\mathrm{kg\,m^{-2}s^{-1}}$) and run-off:

$$\frac{dw}{dt} = R_0 \left[1 - e^{(w/\, w_m - 1)} \right] \tag{5.20}$$

Hereby, all rain is lost to run-off as soon as w approaches the maximum water storage w_m. This expression can be integrated assuming a constant rainfall during the timestep Δt:

$$w(t+\Delta t) = w_m \left[1 - \ln \left(1 - \left[1 - e^{\left(1 - \frac{w(t)}{w_m}\right)} \right] e^{-\frac{R_0 \Delta t}{w_m}} \right) \right] \tag{5.21}$$

5.2.2 Direct heat-transfer of Q_r by rain-drops

We consider the heat transfer Q_r between the surface and raindrops hitting the ground as an extra term at the left part of Eq. 4.3. The following approximation is used:

$$Q_r = \rho_w c_w R \overline{\Delta T} \tag{5.22}$$

where R is the rainfall rate in metres per second, ρ_w the density of water, c_w the specific heat of the water, and $\overline{\Delta T}$ the averaged temperature change of the raindrops on the surface. It is assumed that raindrops are initially at the reference temperature (either from a mast measurement or from the first model layer above the ground), and that they reach thermodynamic equilibrium with the surface before they are lost to run-off or evaporate. Their temperature change can be approximated by:

$$\overline{\Delta T} = T_{\mathrm{rain}} - T_s \tag{5.23}$$

where T_{rain} is the rain temperature, and T_s is the surface temperature. The former is approximated by the reference temperature. For large rainfall, Q_r could have a considerable impact on the surface energy balance, and consequently on the surface temperature. On the one hand, if $10\,\mathrm{kg\,m^{-2}}$ water falls on the impervious surface during a two-hour rainfall event and 90% of this water is lost to run-off, 10% of the rain water may evaporate during the succeeding 6 hours. Ignoring a possible time-dependent factor for evaporation and heating, the associated latent heat flux amounts to $10\,\mathrm{kg\,m^{-2}} \times 10\% \times 2260\,\mathrm{kJkg^{-1}}/6\,\mathrm{h} = 105\,\mathrm{Wm^{-2}}$. On the other hand, when raindrops are on average 5 K cooler than the surface, 100% of this water amount is heated by the surface in two hours and this acts as a heat sink to the SEB of $5\,\mathrm{K} \times 10\,\mathrm{kg\,m^{-2}} \times 4.18\,\mathrm{kJ\,kg^{-1}\,K^{-1}}/2\,\mathrm{h} = 29.0\,\mathrm{Wm^{-2}}$. This example demonstrates that direct transfer of heat from rainwater to the surface or vice versa could have a small, yet non-negligible, impact on the time evolution of the SEB just after the rainfall.

5.2.3 Model setup and forcing

Toulouse

TERRA-URB is configured for a one-year offline run at an urban site at Rue de la Pomme in Toulouse for which measurements are available from the Canopy and Aerosol Particle Interactions in TOulouse Urban Layer (CAPITOUL), see Masson et al. (2008). The mean building height $h = 14.9\,\mathrm{m}$ and the urban fraction of 92% are adopted from the detailed information of Masson et al. (2008), representative for the circular footprint area with radius 500 m around the measurement tower used in earlier studies (Pigeon et al., 2007). The remainder natural surface consists of loam with a plant cover of 95% and a Leaf-area index with seasonal variation between 1 and 3.9. These surface characteristics are obtained from the dataset described in Smiatek et al. (2008). The rooting depth was set to 2.0 m which is representative of vegetation inside the city that mainly consists of large trees. Following Sarkar and De Ridder (2010), we calculated the roughness length of $z_0 = 0.075h \simeq 1.12\,\mathrm{m}$ with h the mean building height equal to 14.9 m. A detailed inventory of anthropogenic heat from has been made specifically for Toulouse, see (Pigeon et al., 2008). In view of more general applications with TERRA-URB and the climate model COSMO-CLM, the globally applicable determination of anthropogenic heat (Flanner, 2009) is implemented instead (see also `http://www.cgd.ucar.edu/tss/ahf/`). It also allows for a consistent approach between the Toulouse site and Basel site (described hereafter). The methodology accounts for country-specific data of energy consumption from non-renewable sources. This was apportioned according to population density (conserving the national total) and converted to annual-mean gridded energy flux at a fine resolution (2.5×2.5 minute). Latitudinally-dependent diurnal and seasonal distribution functions are superimposed on this annual-mean (see Fig. 6.3).

Observations to force and evaluate TERRA-URB were obtained from sensors mounted on a pneumatic tower during the CAPITOUL campaign (Masson et al., 2008). They include temperature, wind speed, precipitation and the radiative and convective terms of the surface energy balance. The radiative fluxes were measured using four-component radiometry and those of sensible heat, latent heat (evaporation) by eddy covariance techniques. The base of the mast was on a roof at a height of 20 m, with the top of the mast being 47.5 m above the road. During operations the mast height was adjusted. The total tower height varied between 47.5, 38.5 and 26 m depending on the weather conditions. The corresponding effective reference height of the observation tower was obtained by substracting the displacement height of $d \simeq 10z_0 = 11.2\,\mathrm{m}$, hence it varied between 36.3, 27.3 and 14.8 m.

Basel

The evaluation follows the same setup for TERRA-URB as described in section 4.3

5.2.4 Determination of the water-storage parameters w_m and δ_m

We present a methodology for estimating the values of the water storage parameters introduced in Section 5.2.1. As in De Ridder et al. (2012) for estimating the thermal

inertia of Paris urban area, a probability density function for the water-storage parameters is constructed by employing the match between the simulated and observed Q_{E} timeseries of multiple offline runs each with different water storage parameters. Given the timeseries $Q_{\mathrm{E}o}(t)$ with a standard deviation σ, the likelihood of a particular parameter combination $P(m) = (\, w_m(m),\, \delta_m(m))$ with modelled output $Q_{\mathrm{E}m}(t)$ is given by:

$$\wp(P(m)) = \frac{\exp\left[\sum_i -0.5(\, Q_{\mathrm{E}o}(t_i) - \, Q_{\mathrm{E}m}(t_i))^2/\sigma^2\right]}{\sum_{m'} \exp\left[\sum_i -0.5(\, Q_{\mathrm{E}o}(t_i) - \, Q_{\mathrm{E}m'}(t_i))^2/\sigma^2\right] \Delta\, w_m(m') \Delta\, \delta_m(m')} \tag{5.24}$$

which is normalized over the parameter range under consideration. Estimates of either the model parameters (i.e. the water-storage parameters), or either the corresponding model output (statistics) such as modelled (annual-mean) evaporation, are obtained by multiplying their value with the probability density function and summing over the model parameter combinations $P(m)$:

$$\langle R \rangle = \sum_m R(m) \wp(P(m)) \Delta\, w_m(m) \Delta\, \delta_m(m) \tag{5.25}$$

and their standard deviation is calculated by:

$$\sigma_R^2 = \sum_m (R(m) - \langle R \rangle)^2 \wp(P(m)) \Delta\, w_m(m) \Delta\, \delta_m(m) \tag{5.26}$$

Mauder et al. (2006) did extensive evaluation of several experimental set-ups for observations of latent heat, including the LICOR7500 used during the CAPITOUL campaign. They found a root mean square difference between the LICOR7500 and their reference equipment (CSAT3/KH20) of $35.7\,\mathrm{Wm^{-2}}$ (see their table 10). Assuming that the observation errors for the two set-ups are not correlated, this can be considered as an upper limit to σ for the LICOR7500. Hence, this value was used for the parameter estimation.

The parameter estimation needs continuous daytime measurements for Q_{E} after rain fall. However, many data gaps were present during the CAPITOUL- experiment especially at that time. Therefore, rainfall periods were carefully selected by applying the following objective criteria. Firstly, we select large rainfall events (i.e. $\geq 1\,\mathrm{mm}$ that have a continuous observation records for 24 daytime hours just after). Hereby, the "daytime" observation records exclude the hours for which the three-hourly averaged incoming solar radiation is less than $150\,\mathrm{Wm^{-2}}$ leading to only very low ET rates. In order to have sufficient rainfall events, the observation only needs to start from 6 daytime hours after the rainfall because Q_{E}-measurements were not always available just after the rainfall. Secondly, the whole period under consideration needs to have a rainfall rate of no more than 0.2 mm each hour (either night-time or daytime). This allows us to focus on the evaluation of the undisturbed depletion of the impervious water storage, hence without the impervious storage partially being refilled. As a result, four events are selected with at least 18 continuous daytime sample hours after the rainfall. All the available daytime observations of up to four days after each selected rainfall event were taken into account.

As will be discussed in Section 5.3.2, an overall negative bias in Q_{E} appears in the model output of TERRA-URB compared to observations during the CAPITOUL campaign. In

particular, the negative bias was also found during the dry periods, so thus originates from sources other than the the modelling the urban impervious evaporation (The latter is zero at that time). A similar negative bias may occur just after the rain events when evaporation from the urban impervious surface is different from zero. Therefore, we employ a correction for this model bias during the periods before performing the parameter estimation. The bias is obtained from the dry periods of four days before the rainfall event.

As TERRA-URB was computationally very efficient, it allows for multiple one-year offline simulations for the water-storage parameter estimations needed for the parameter estimation.

5.3 Results

5.3.1 Estimation of the impervious water-storage parameters for Toulouse centre

Following the methodology and data selection procedure presented in Section 5.2.4, the probability density functions $\wp(p_n)$ are constructed for a range of parameter sets $P(n) = (\, w_m,\, \delta_m)$ that have been introduced in 5.2.1, see Figure 5.2. Hereby, the root mean square error (RMSE) and correlation (R^2) of the Q_{E} results are shown as well.

The following values for the water-storage parameters are found using Eq. 5.25: $w_m = 1.31 \pm 0.20\,\mathrm{kg\,m^{-2}}$ and $\delta_m = 12 \pm 4\%$. These model parameters imply that the potential evaporation rate from the entire impervious surface is never reached, even when the impervious water storage is saturated just after rainfall. As mentioned in Section 5.2.1, the used 2/3rd power function for δ considers a linear function for the SID. Such a linear reservoir distribution with $\delta_m = 12\%$ obtained from the parameter estimation yields that most of the water is stored in (and evaporates from) deep water reservoirs that only cover a small surface fraction of the impervious surface. This leads to an evaporation at a slow rate after rainfall, hence a persistence in evaporation. At the same time, our parameter estimation yields a large fraction of the impervious surface consisting of water reservoirs with a negligibly small storage capacity that dry out immediately or just remain dry, or evaporates water at a reduced rate. This fraction may represent sloping roofs with a negligible water-storage capacity, dry vertical walls, or roads and footpaths lying in the shadow. On the contrary, a δ_m equal to 100% would lead to a much quicker evaporation just after rainfall. This would correspond to a SID in which more water is collected in small water reservoirs leading to evaporation from a much larger surface fraction. This seems not to be the case according to our parameter estimation.

5.3.2 Offline evaluation during rainfall at Toulouse

An offline evaluation of TERRA-URB and a sensitivity study for the water-storage parametrization is performed during the Toulouse CAPITOUL campaign. We start from the reference run (LD12) with TERRA-URB employing the Linear decreasing surface interception Distribution (i.e. a 2/3th power law for δ) with the impervious water-

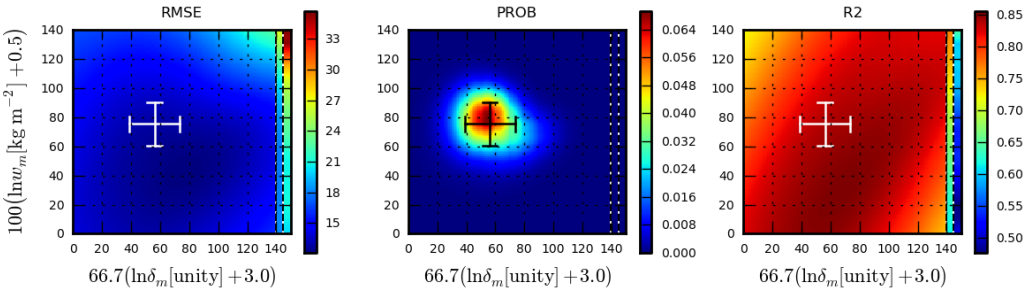

Figure 5.2: Scores and probability for the offline runs over Toulouse with different values of w_m and δ_m. The crosses indicate the standard deviation of the parameter estimates. The two streaks on the right of each figure show the probability and scores using $\delta_m = 1$ (LD100) and $\delta = 1$ (ND100) as discussed in Section 5.3.2. PROB refers to the probability, namely $\wp$.

	LD12	LD100	ND12	ND100	DRY
$w_m[\mathrm{kg\,m^{-2}}]$	1.31	1.31	1.31	1.31	0
$\delta_m[\%]$	12	100	12	100	0
h	Eqns. 5.2-5.3	Eqns. 5.2-5.3	$\frac{\min(w,w_m)}{\rho_w \delta_m}$	$\frac{\min(w,w_m)}{\rho_w \delta_m}$	0
$\phi(D)$	Eq. 5.14	Eq. 5.14	N/A	N/A	N/A
δ	$\delta_m \left(\frac{w}{w_m}\right)^{2/3}$	$\delta_m \left(\frac{w}{w_m}\right)^{2/3}$	δ_m	δ_m	0

Table 5.1: Overview of the different water-storage parametrizations for modelling evaporation from the urban impervious fraction. The parameter values for w_m and δ_m are given by the first two rows. The expression for the water-level h of the interception reservoirs is given by the third row. The fourth row contains the assumed surface interception distribution (SID) for the water-storage depth. The last row shows the resulting δ-expression corresponding to the assumed expressions for h and the SID ($\phi(D)$).

storage parameters adopted from Section 5.3.1 ($w_m = 1.30\,\mathrm{kg\,m^{-2}}$; $\delta_m = 12\%$). 5.2. A second run (LD100) uses a similar impervious water-storage, but with δ_m equal to 100%. Two additional runs (ND12 and ND100) are performed that assume No interception Distribution, and all reservoirs have the same depth, hence the levels (h) among the reservoirs are the same as well. Hereby, the effective wet surface fraction δ is constant with a value of 12% and 100% for the respective runs. Finally, the DRY run assumes no evaporation from the impervious surface, which means that ET only originates from the natural fraction. An overview of the different water-storage parametrizations can be found in Table 5.1. The runs are evaluated against measurements for Q_E, Q_H, and $R^\uparrow(z_\mathrm{ref})$ during the rain events selected according to Section 5.2.4, see Figures 5.3, 5.4 and 5.5, and Table 5.2. We use the water-vapor opacity correction developed in chapter 4) for comparing the model results of upward infra-red radiation (wave-lengths of more than 5 µm) with tower measurements.

The reference simulation (LD12 run) improves the performance for Q_E after rainfall for each of the separate rainfall events compared to the other runs (LD100, ND100, ND12, DRY), see Figures 5.3 and 5.4. First of all, the increase in Q_E after rainfall

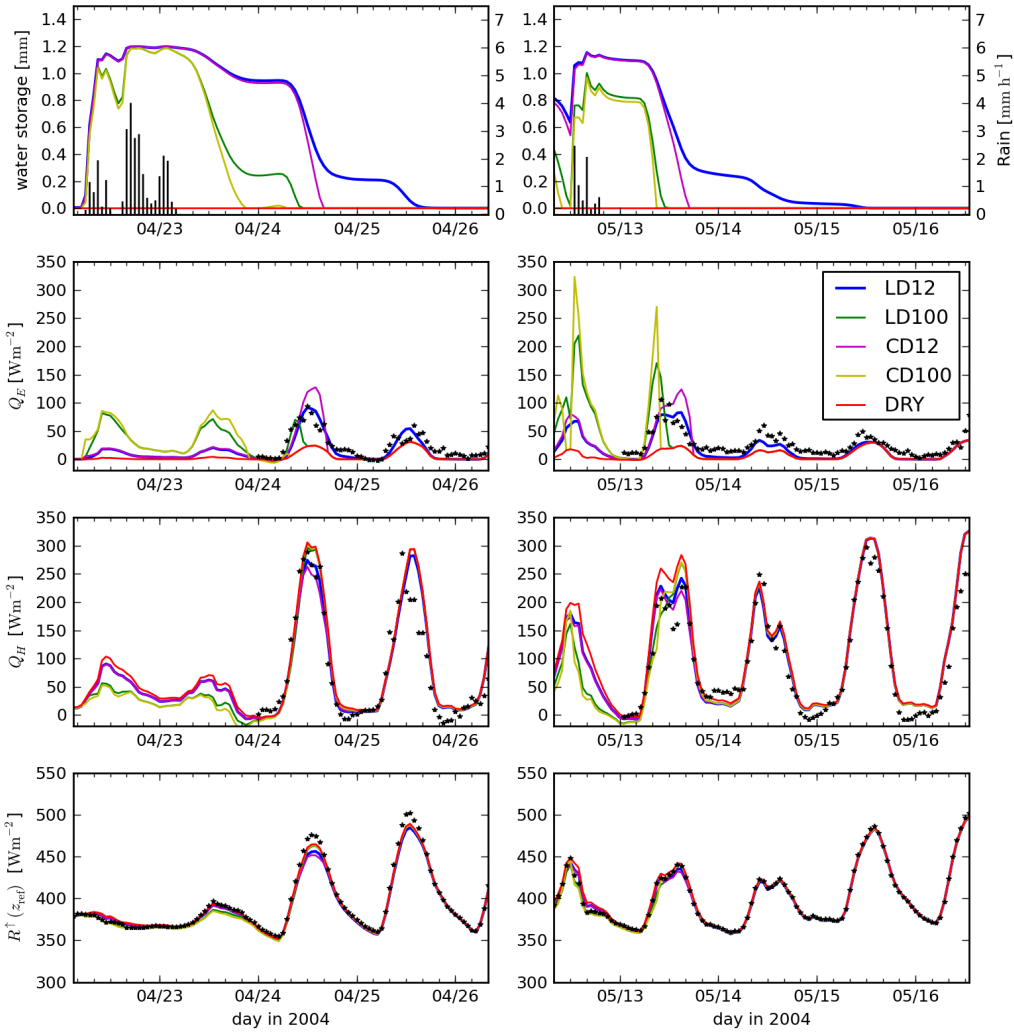

Figure 5.3: Model evaluation at Toulouse for the rain events during spring selected according to the procedure described in Section 5.2.4. The model runs (full lines) are described at the beginning of Section 5.3.2. The first row of figures display the hourly observed precipitation amount (vertical lines) and the modelled amount of water storage on the impervious surface. The next rows of figures show model results (lines) and observations (stars) for Q_{E}, Q_{H} and $R^{\uparrow}(z_{\mathrm{ref}})$, respectively. LD12, LD100, CD12, CD100 and DRY refer to the runs LD12, LD100, ND12, ND100 and DRY.

is largely underestimated in the DRY run. Furthermore, the persistence in ET after rainfall appearing in the measurements is better-captured by LD12 than the other runs. Focussing on the rain event for which Q_{E} measurements are available the morning just after the rainfall (Figure 5.3 column 2), the LD100 and ND100 runs largely overestimate Q_{E} at that time, whereas they underestimate Q_{E} afterwards. This results in better scores of the reference simulation LD12 during the rainfall events compared to the other

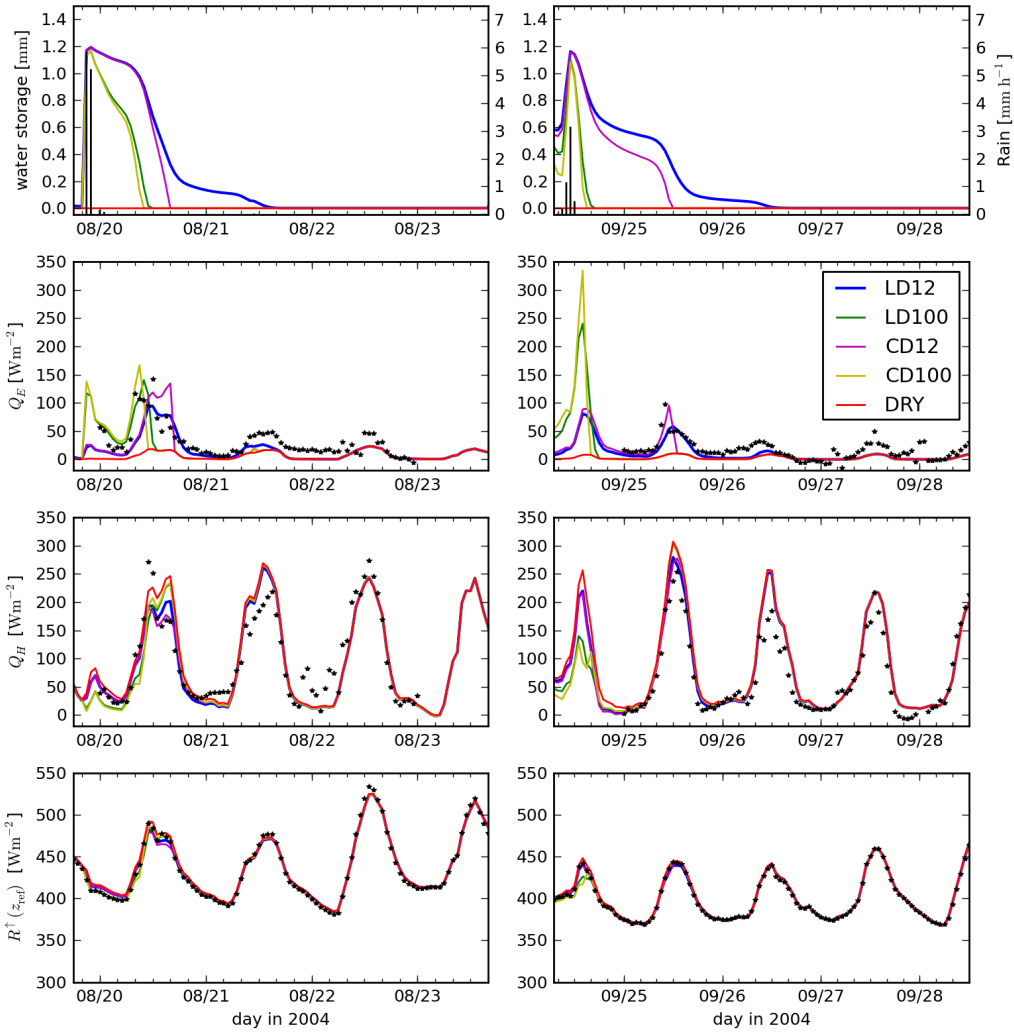

Figure 5.4: Idem as for Figure 5.3, but for periods during summer and fall.

water-storage parametrizations (LD100, ND100, ND12) and the DRY run excluding evaporation from the impervious surface, see 5.2. Furthermore from Figure 5.2, one also finds a much lower probability and worse scores for LD100 and ND100 runs also when employing any other w_m value different from $1.31\,\mathrm{kg\,m^{-2}}$ compared to the reference simulation LD12. These results show that the water-storage parametrization largely affects the model performance in terms of Q_E.

When focusing on the daytime hours (i.e. the hours for which the incoming solar radiation exceeds $150\,\mathrm{Wm^{-2}}$) for which evapotranspiration is important, the improved persistence in evaporation in the reference simulation LD12 compared to the other runs is very clear in Figure 5.5. In particular, the deep water-reservoirs represented in the LD12 run, which is responsible for the delayed evaporation after rainfall (discussed before in Section 5.3.1)

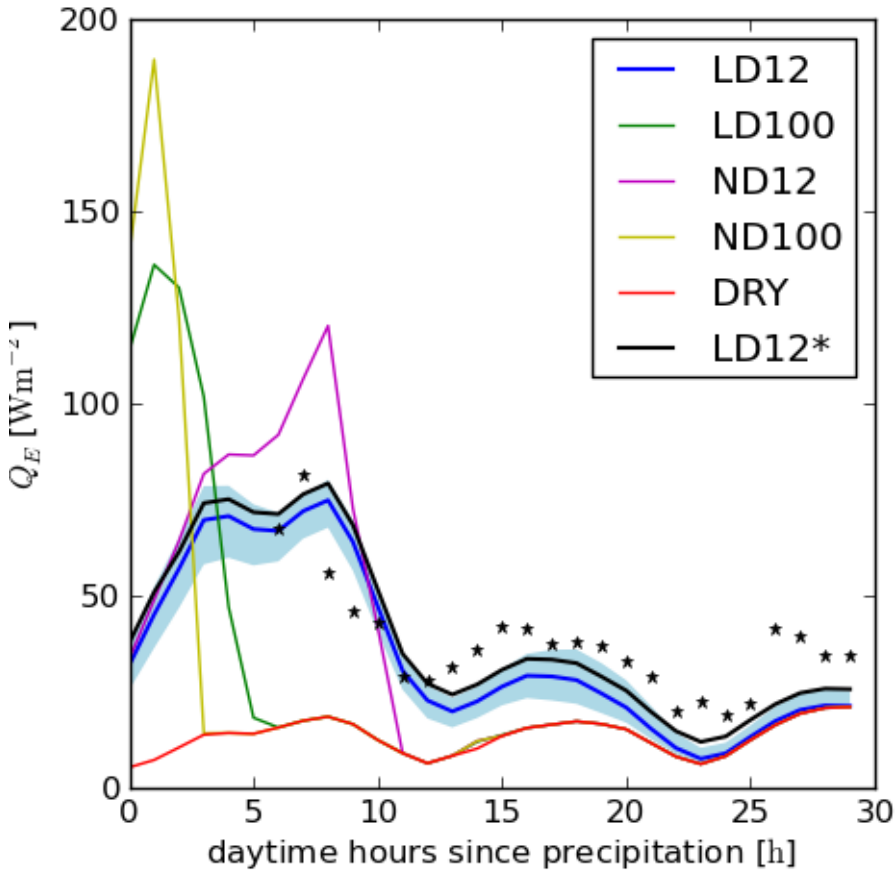

Figure 5.5: The averaged Q_{E} during the daytime hours (i.e. the hours for which the incoming solar radiation exceeds 150 Wm^{-2}) of the four cases after rainfall which have been selected according to the procedure described in Section 5.2.4, except the fact that the latent heat don't have to be available. The model runs (full lines) are described at the beginning of Section 5.3.2. The observations are indicated with stars. The light-blue area represents the uncertainty in the model output due to uncertainty in the water-storage parameters. The black line LD12* corresponds to the reference run (LD12) applying a bias correction with the bias found during 4 days before the rainfall events.

appear to be very important for modelling ET in urban areas. As the runs LD100 and ND100 do not represent these deep water reservoirs, they both underestimate Q_{E} from 9 daytime hours after the rain events on average. More particularly, these runs could not capture the delayed evaporation from the deep water reservoirs. The ND12 run assuming no SID also underestimates ET from 14 hours after the rainfall. These results clearly demonstrate the benefits of both the inclusion of evaporation from the impervious surface, the impervious SID and the SID parameter estimates.

	Q_E				
	LD12	LD100	ND12	ND100	DRY
RMSE	**13.27**	17.32	18.79	22.15	17.91
BIAS	**-8.84**	-13.31	-9.16	-13.86	-17.67
R2	**0.82**	0.69	0.75	0.54	0.65
	Q_H				
	LD12	LD100	ND12	ND100	DRY
RMSE	**27.72**	30.45	28.89	30.47	29.41
BIAS	7.58	9.36	**7.57**	9.51	14.24
R2	**0.96**	0.95	0.95	0.95	0.95
	$R^{\uparrow}(z_{\mathrm{ref}})$				
	LD12	LD100	ND12	ND100	DRY
RMSE	4.71	**4.11**	4.88	4.35	4.51
BIAS	**-0.34**	-1.53	-0.50	-1.83	1.57
R2	0.99	**0.99**	0.99	0.99	0.99

Table 5.2: The root-mean-square error (RMSE), bias (BIAS), and correlation (R2) of the offline model results for Q_{E}, Q_{H} and $R^{\uparrow}(z_{\mathrm{ref}})$ for Toulouse during the rainfall events shown in Figures 5.3 and 5.4 (including both available daytime and nighttime observations). The latter are selected according to the procedure described in Section 5.2.4. An overview of the model runs using different water-storage parametrizations can be found in Table 5.1. The best scores among the different runs are marked in bold.

Throughout the year, the reference simulation shows an overall negative bias in Q_{E} compared to the measurements (results not shown). Especially during the night, the model shows zero evaporation for both urban and natural fractions, while a slight positive ET appears in the measurements. A similar negative bias also occurs for dry periods when there is no evaporation from the impervious surface (thus only ET from the natural fraction), especially during summer and winter (not shown). On the one hand, the overall apparent negative bias compared to the measurements could be caused by inaccuracies in the observations using eddy-correlation techniques. For instance, Mauder et al. (2006) experiences a positive bias for latent heat estimated from the LICOR7500 compared to their reference equipment (CSAT3), see their table 10. On the other hand as already mentioned in the introduction, it could also result from anthropogenic sources due to combustion from house heating and motor vehicles, evaporative cooling and air conditioning of buildings (see review Sailor, 2011), and irrigation in the city (Kalanda et al., 1980) in summertime. The overall underestimation for the output averaged for the different events is partially reduced when applying the bias correction with the bias found during 4 days before the rainfall events, see Figure 5.5. Therefore, this overall negative model bias partly explains the underestimation of Q_{E} during rainfall as well.

As the evaporation from the impervious surface acts as a heat sink to the SEB, the performances in sensible heat Q_{H} and the upward infra-red radiation at tower height ($R^{\uparrow}(z_{ref})$) are also affected by water-storage parametrization. As we are dealing with indirect effects, the impact of evaporation on these fluxes are much smaller as discussed in more detail in Section 5.4.3. Therefore, these performance changes are much smaller

than those from Q_{E} itself. In particular, the impact of water-vapor opacity on the upward infra-red radiation at tower height ($R^{\uparrow}(z_{ref})$) was much larger than the impact of evaporation from the impervious surface. Hereby, the large overestimation of $R^{\uparrow}(z_{ref})$ around noon also found for other urban models employed for the same site, Hénon et al. (2012); Demuzere et al. (2013) was eliminated when accounting for the water-vapor opacity correction as described in chapter 4. Still, it can be found that the positive bias in Q_{H} in LD12 is reduced during rainfall compared to the DRY run. Moreover, an overall improvement in Q_{H} is found compared to both the LD100, ND100 runs as well. The latter is also the case for $R^{\uparrow}(z_{ref})$.

5.3.3 Evaluation for Basel

In this section, an evaluation of TERRA-URB employing the different water-storage parametrizations is performed on an independent urban site at Basel during the two-month intensive observation period BUBBLE, (see Table 5.3, Figures 5.6 and 5.7). We employ offline runs with TERRA-URB using the same water-storage configurations and water-storage parameters as those for Toulouse described in the beginning of Section 5.3.2, see also Table 5.1.

It should be noted that the evaluation of the different water-storage parametrizations for the evaporation from the impervious surface is much more limited than for the Toulouse site. For instance, the natural fraction of the Basel site (28%) is larger than the Toulouse site (only 8%). Therefore, the uncertainties due to ET from the natural fraction may lead to a larger extent interfere with the evaluation and comparison of the different water-storage parametrizations for Basel. In addition, the ET observations are also subject to larger scatter in which sequential daytime hourly changes of ET over $50\,\mathrm{Wm}^{-2}$ are found.

The reference simulation LD12 better captures the increase in ET after rainfall compared to the DRY run without evaporation from the urban impervious surface. Furthermore, the persistence in ET after rainfall for LD12 is better captured compared to the other water-storage parametrizations (LD100, ND12 and ND100) as for the Toulouse site. The impact of the water-storage parametrization of the other other components of the SEB ($R^{\uparrow}(z_{\mathrm{ref}})$, and Q_{H}) is very small (see Figure 5.6) and 5.7). Therefore, the impact on the respective performances are very small as well (not shown). A negative model bias for ET is found for the Basel site similar to that of the Toulouse site, and this also appears during dry periods and during the night when there is no modelled evaporation from the impervious surface. As for the Toulouse site, this may result from anthropogenic sources, model deficiencies and inaccuracies of the eddy-correlation measurements.

5.4 Discussion

5.4.1 Implications of the SID and the related $2/3$rd power law

As demonstrated in Section 5.2.1, the assumptions of a maximum total water storage, a maximum effective wet surface fraction, a linear SID, and a homogeneous desaturation

	Q_E				
	LD12	LD100	ND12	ND100	DRY
RMSE	**26.10**	26.53	26.99	29.43	28.05
BIAS	-7.82	-9.42	**-7.60**	-10.06	-13.33
R2	**0.79**	0.78	0.78	0.73	0.74

Table 5.3: The root-mean-square error (RMSE), bias (BIAS), and correlation (R2) of the offline model results for Q_{E} for urban site at Basel Sperrstrasse during the BUBBLE campaign 2002. An overview of the model runs using different water-storage parametrizations can be found in Table 5.1. The best scores among the different runs are marked in bold.

of the interception stores, leads to the 2/3-power relation in Eq. 5.17. This relation is similar to the one used in the urban model TEB (Masson, 2000), and CLM-U (Oleson et al., 2008). Herein, no physical explanation was provided. Instead, it was adopted from Deardorff (1978) describing a plant interception storage. At its turn, this was chosen over an exponential decay to avoid an amount of water on the foliage always different from zero. The SID formulation now provides a robust physical basis that supports the use of a 2/3-power relation. The SID formulation highlights the assumptions being made when employing such a relation. Furthermore, it provides a physical interpretation of the estimated parameter values in Section 5.3.1, and that of the evaluation of the water-storage parametrization (Sections 5.3.2, and 5.3.3), and its impacts (Section 5.4.3). It allows one to address its possible restrictions as well, see Section 5.4.2. Finally, it should be noted that our SID formulation may also be applicable for the representation of water-storage (ponding) on other impervious surface types besides the urban land-cover, such as rocks, other (semi-)impervious natural surfaces (i.e. farmland) and on vegetation.

The smaller decrease in water-storage after the rainfall in the LD12 (LD100) run compared to the ND12 (ND100) run found Section 5.3.2 can be explained as follows. On the one hand when assuming a SID that decreases lineary with the water-storage depth (cfr. LD12 and LD100 runs), and considering E_p constant in Eq. 5.18, it can be demonstrated that δ and thus the evaporation decreases quadratically with time. Meanwhile, the water-storage decreases as a cubic function, cfr. Eq. 5.19. On the other hand when assuming No interception Distribution (cfr. ND12 and ND100 runs) and also a constant effective wet surface fraction δ, a linear decrease in w with time is found. Indeed, the decrease in w of the LD12 and ND12 runs are similar at the beginning just after rainfall, but the former becomes smaller and gets delayed after some time.

When employing the linear SID, the initial larger decrease of the effective wet surface fraction just after rainfall than that some time after may seem to be counter-intuitive. Indeed, The 2/3 power relation implies that, when w is close to w_m, one needs more water loss through evaporation before δ has decreased to a certain amount, than for the case when w is smaller. From this, one would rather expect an initial slow decrease of the effective wet surface fraction after rainfall. Yet, one indeed has more water loss for w close to w_m (cfr. cubic function) because the fractional wet surface δ is also larger than when w is smaller.

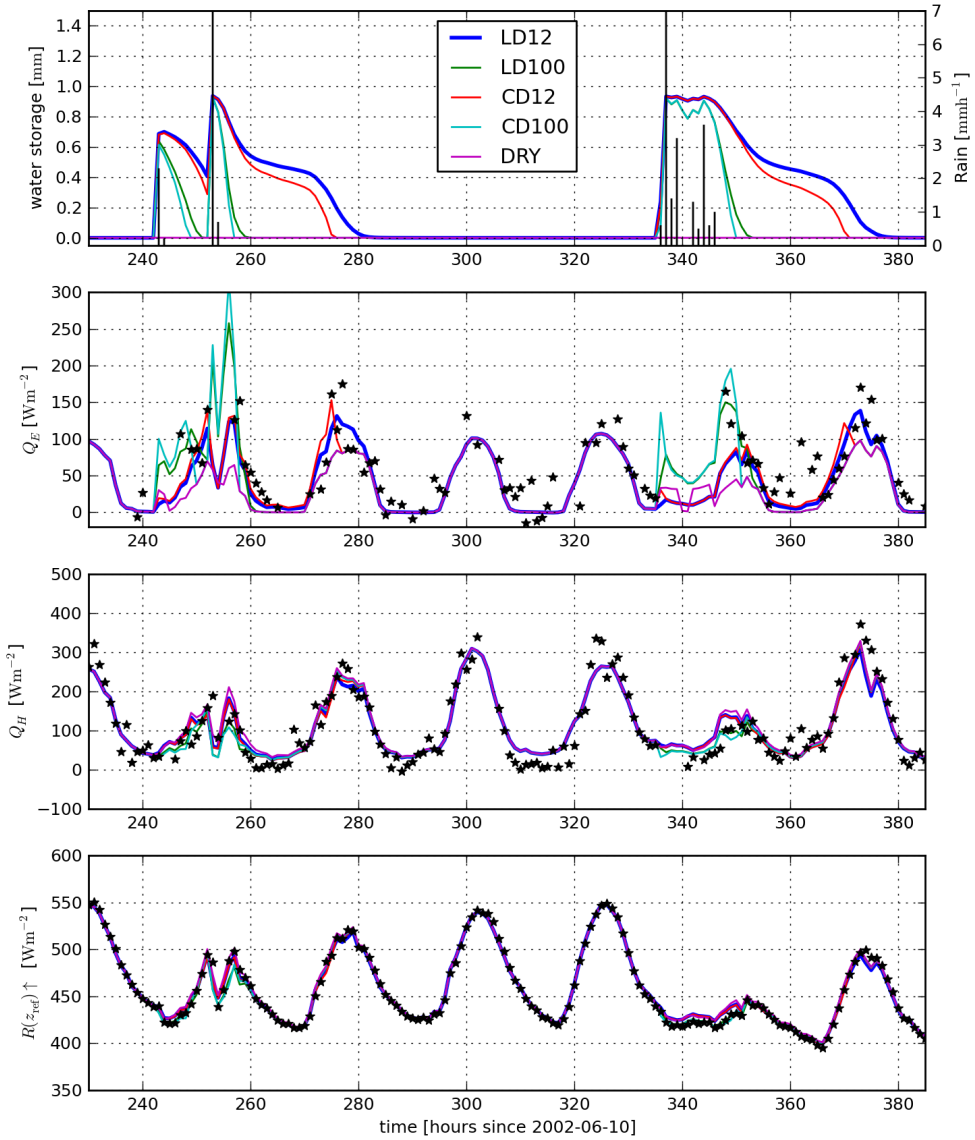

Figure 5.6: First part of the TERRA-URB runs for the Basel site using different impervious water storage parameters as indicated in Table 5.1.

5.4.2 Limitations of the $2/3$-th power law for evaporative surfaces

Even though the delayed evaporation from the impervious surface originating from the deep water reservoirs is well-captured using the linear SID, and the parameter estimates (see Sections 5.3.2 and 5.3.3), the evaluation for Toulouse and Basel of the reference run LD12 still indicate a slight underestimation of Q_{E} just after the rainfall (see Figures 5.3 and 5.6). Therefore, it seems that the number of small water reservoirs (that would lead a

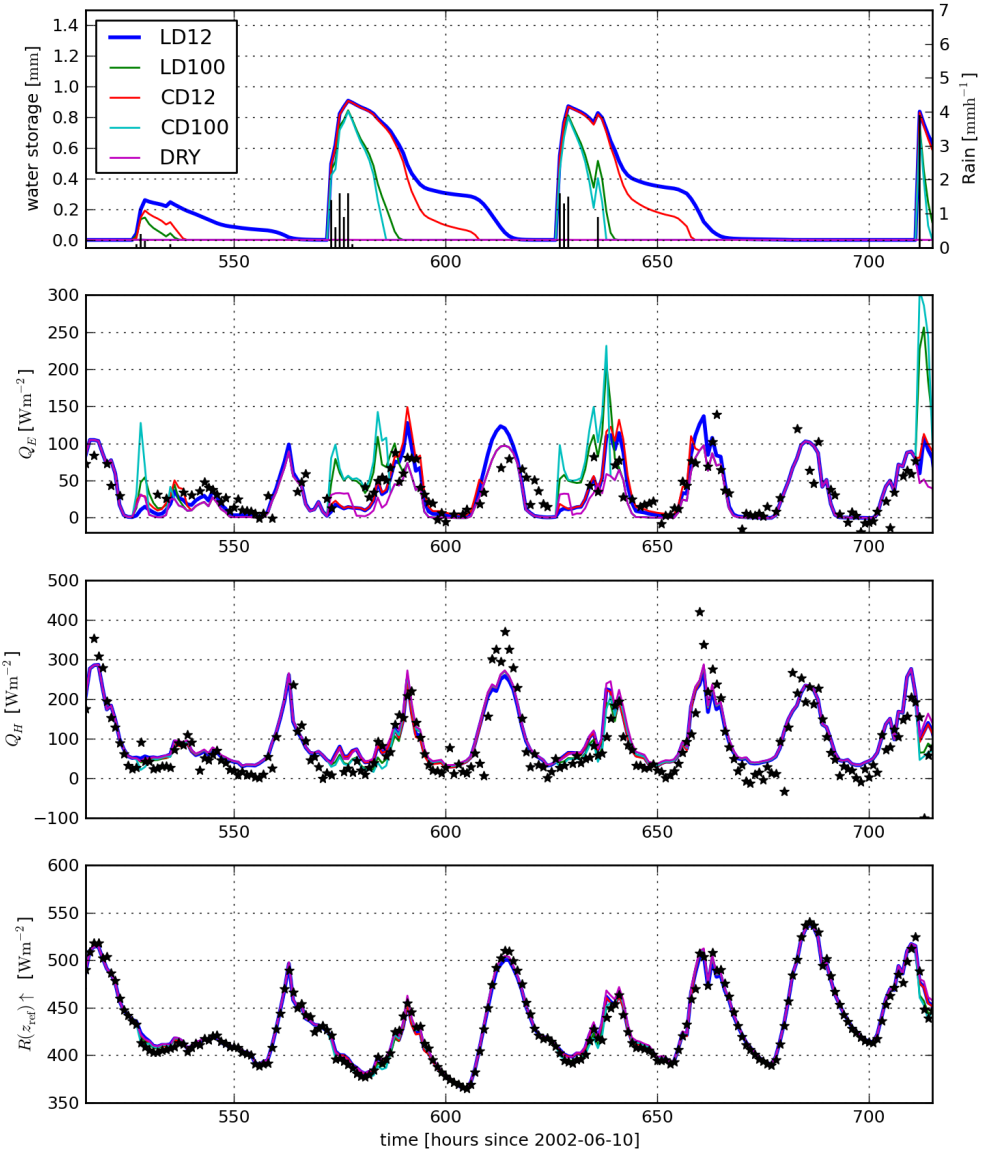

Figure 5.7: Second part of the TERRA-URB runs for the Basel site using different impervious water storage parametrizations. An overview of the model runs using different water-storage parametrizations can be found in Table 5.1.

slightly larger evaporation just after rainfall) in the linear SID is underestimated. In order to capture both this slightly increased evaporation and the persistence in evaporation after the rainfall simultaneously, one needs to develop more advanced (non-linear) interception distributions. Hereby, one also needs to find the corresponding analytical solutions for the effective wet surface fraction that can be easily implemented in surface modes, similar to the 2/3rd power relation when assuming a linear SID. In order to develop such

	LD12	LD100	ND12	ND100	DRY
Q_E	9.3	13.5 (4.2)	10.1 (0.8)	14.6 (5.3)	4.1 (−5.2)
Q_H	71.3	68.2 (−3.1)	70.7 (−0.6)	67.4 (−3.9)	75.2 (3.8)
$L^{\uparrow}$	396.5	395.6 (−0.9)	396.3 (−0.2)	395.4 (−1.1)	397.9 (1.4)

Table 5.4: Modelled annual mean values of Q_{E}, Q_{H} and $L^{\uparrow}$ (units Wm^{-2}) for different water-storage parametrizations (see also Table 5.1) as described at the beginning of Section 5.3.2. The values in brackets are the respective differences with the reference simulation LD12.

water-storage interception distributions, one needs additional observation campaigns at urban sites with a negligible natural fraction to force offline urban modules. These campaigns need to include more observations for latent heat available just after rainfall events.

The 2/3th power relation only accounts for the case of evaporation starting from the saturated case. In the case that the impervious water storage only gets partially filled, Eq. 5.2 assumes that the deep (already wet) water reservoirs get filled up first before the shallow reservoirs start to fill. Hereby, the reservoirs are filled up in the same but opposite manner as evaporation as explained in Section 5.2.1. This may represent the process of water that runs down to the deepest reservoirs first. However, the formulation does not account for the fact that a part of the rain water may remain on the shallow water reservoirs. In order to tackle such shortcomings, one may need to develop even more sophisticated surface-interception distributions.

5.4.3 Impacts of the urban impervious water-storage parametrization on the SEB

A daytime augmented Q_{E} after rainfall of $60\,\mathrm{Wm}^{-2}$ can be explained by evaporation from the impervious surface when comparing the runs LD12 and DRY, see Figure 5.8. In particular, this increase in Q_{E} at the Toulouse site for which the impervious water reservoirs are saturated ($R > 1\,\mathrm{mm}$ in three hours) lasts for 12 hours of daytime on average. An evaporation from the impervious surface of $45\,\mathrm{Wm}^{-2}$ generally leads to a decrease in Q_{H} and $L^{\uparrow}$ of only $25\,\mathrm{Wm}^{-2}$ and $10\,\mathrm{Wm}^{-2}$, respectively. Such events occurred about 35 times throughout the year. Evaporation from the urban environment reaches values exceeding $90\,\mathrm{Wm}^{-2}$ in the case of direct solar radiation just after the rainfall, see Figs. 5.3, 5.4 and 5.9 (compare the runs LD12 and DRY). The indirect impacts of the impervious water storage on Q_{H} and Ł$^{\uparrow}$ could reach $50\,\mathrm{Wm}^{-2}$ and $12\,\mathrm{Wm}^{-2}$ in that case.

The modelled annual-mean evaporation from the urban site of Toulouse during the CAPITOUL campaign during 2004 amounts to $9.3 \pm 0.51\,\mathrm{Wm}^{-2}$ for the reference simulation LD12 (see Table 5.4). The portion arising from the impervious urban surface fraction ($5.2\,\mathrm{Wm}^{-2}$; 56%) was comparable to the portion from the natural surface fraction ($4.1\,\mathrm{Wm}^{-2}$; 44%). The former corresponds to an annual-mean evaporation from the impervious surface per unit impervious surface of $5.6 \pm 0.60\,\mathrm{Wm}^{-2}$. Herewith, $12.5 \pm 1.1\%$ of the precipitation evaporates. The annual-mean impervious evaporation of $5.6\,\mathrm{Wm}^{-2}$

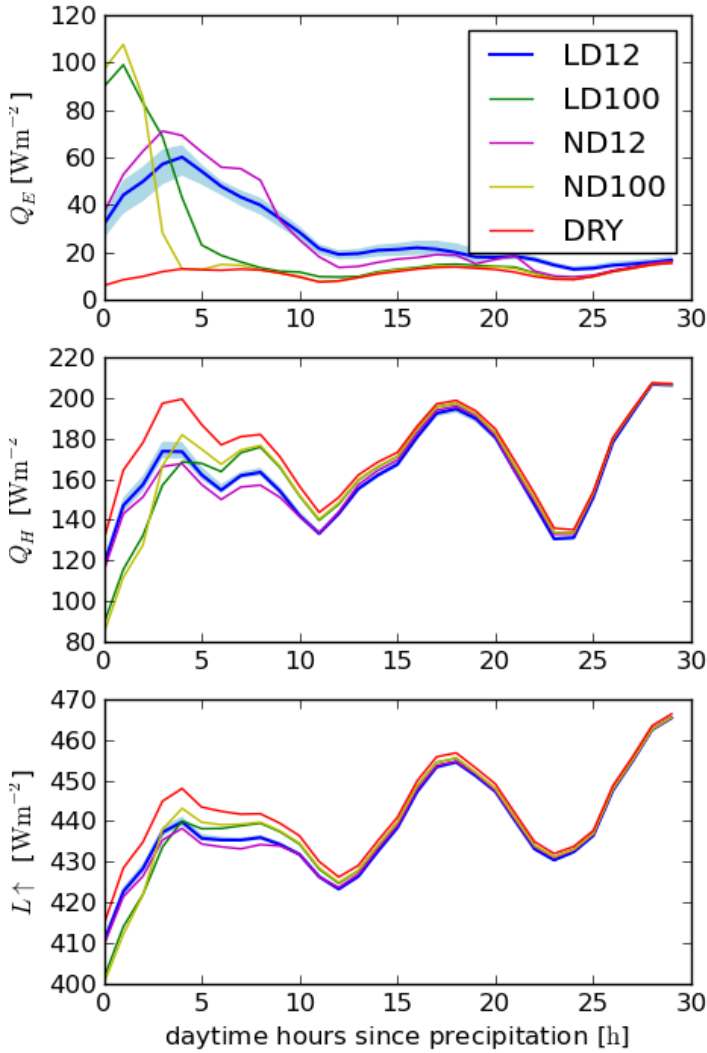

Figure 5.8: Annual-averaged daytime (i.e. the hours for which the incoming solar radiation exceeds 150 Wm^{-2}) impact of water-storage parametrization on latent heat (Q_{E}), sensible heat (Q_{H}), and surface outgoing infra-red radiation ($L\uparrow$) after the rainfall events of more than 1 kgm^{-2} at Toulouse. The model runs (full lines) are described at the beginning of Section 5.3.2.

from the impervious urban surface is much lower, nevertheless not negligible, than values for the heterogeneous natural surroundings ($\simeq 45\,\mathrm{Wm}^{-2}$ for 2005) derived from satellite data (Miralles et al., 2011). The disparity between urban and natural areas suggests

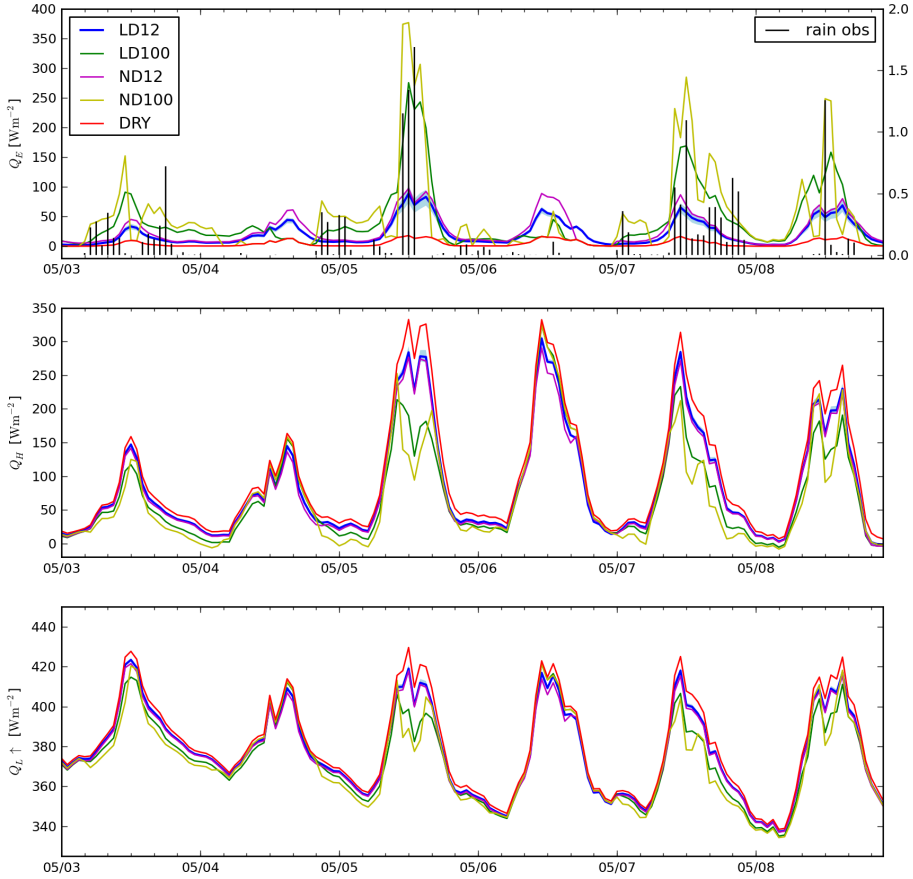

Figure 5.9: Impacts of water-storage parametrization on latent heat (Q_{E}), sensible heat (Q_{H}), and surface outgoing infra-red radiation ($L^{\uparrow}$) for the urban imperivous fraction for large rain events during spring at Toulouse. The model runs (full lines) are described at the beginning of Section 5.3.2.

that the increasing urbanization could have a considerable impact on the (surface) water balance and precipitation in the future. Together with the other urban climate impacts, these changes may ask for mitigation strategies as reviewed by Coutts et al. (2012). Such strategies include climate-sensitive urban design (CSUD) and water-sensitive urban design, e.g. Demuzere et al. (2013), and recent studies under review including Demuzere et al. (2014); Broadbent, A.M., Coutts, A.M., Demuzere, M., Beringer, J., Tapper (2013a,b).

The impacts of the impervious water-storage parametrization on the hourly timeseries of

Q_E, Q_H and $L\uparrow$ (LD12 minus LD100/ND12/ND100) are of the same order of magnitude as the respective changes due to the additional evaporation itself (LD12 minus DRY), see Figure 5.9. This is also the case for the annual-mean values of the respective energy fluxes (after rainfall), see Table 5.4 (Figure 5.8). These impacts have large variability in time after rainfall.

5.4.4 Applicability of the SID and impervious water-storage parameter estimates to other urban areas

As mentioned in Section 5.3.3, the impervious water-storage parameters for Basel are approximated by estimates for the Toulouse urban site. Due to the different urban design, used materials and the morphology of the impervious surface of Basel compared to Toulouse, these water-storage parameter values may be different from their actual values at Basel. Indeed, the urban canopy of Basel is much less dense than that of Toulouse, whereas also the mean building height, height-to-width aspect ratio, building materials of roofs and roads at the Basel site are different. Due to the short period of the IOP encompassing only a limited amount of rain events during the BUBBLE campaign, it was not possible to employ a similar parameter estimateion study for Basel site as for Toulouse site. Yet, the results in Section 5.3.3 demonstrate the added value of employing the SID and these water-storage parameter estimates (cfr. LD12) over an arbitrary impervious water-storage parametrization (cfr. LD100, ND12, ND100 and DRY) for modelling ET at Basel, and possibly at other urban (European) sites as well. As Section 5.4.3 has shown that the water-storage parametrisation affects both ET and the SEB, it is advised to employ the SID and impervious the water-storage parameter estimates from Toulouse in urban models also for other urban sites as a first approximation.

5.5 Conclusions and recommendations

In order to improve the representation of evaporation from urban areas, this paper presents a new impervious water-storage formulation. It provides a physical basis for the representation of the water-storage capacity of the impervious surface and its effective wet surface fraction by assuming a Surface-Interception Distribution (SID). By imposing such a distribution to be a linear function decreasing with reservoir depth and a homogeneous depletion of the reservoirs, this yields a 2/3-th power dependence for the effective wet surface fraction on the stored water on the impervious surface.

Urban impervious water-storage parameters for Toulouse are estimated by forcing the urban climate module TERRA-URB with observations during the CAPITOUL campaign. Hereby, the SID was implemented in TERRA-URB for representing water storage on the urban impervious fraction. A probability density function is constructed by changing the water-storage parameters and by comparing bias-corrected model output and observations after rainfall throughout the year. As observations for latent heat are generally difficult and non-continuous especially during rainfall, the rainfall events have been carefully selected. Our parameter estimation study suggests a maximum impervious water storage of $1.31 \pm 0.20\,\mathrm{kg\,m^{-2}}$ and a maximal evaporative surface fraction of $12 \pm 4\%$. Such a small effective wet surface fraction suggests the presence of roofs, walls and roads that

only have a small storage capacity and therefore dry out immediately, or just remain dry. The effective wet surface fraction may also be reduced by shading effects so that a considerable amount of water in the urban canyon evaporates at a reduced rate.

Offline results of TERRA-URB are evaluated against the urban tower observations for latent heat, sensible heat and upward infra-red radiation. The model simulations are performed at Toulouse centre (Rue de la Pomme) during the CAPITOUL campaign, and at Basel Sperrstrasse during the IOP of the BUBBLE campaign. By employing the SID and using the water-storage parameter estimates in TERRA-URB, both the magnitude, timing and persistence in increased ET after rainfall is captured very well for both sites. In addition, the modelled Q_{E} and $R^{\uparrow}(z_{\mathrm{ref}})$ accounting for the water-vapor opacity explained in chapter 4 are very well reproduced. Our sensitivity study demonstrates that the impact of water-storage parametrization has a large impact on the performance of modelling ET in urban areas. Hereby, the simulations employing the SID and using the water-storage parameter estimates are improved compared to other arbitrary urban impervious water-storage parametrizations. As the sensible heat and upward infra-red radiation are affected indirectly, the impacts on their performance are only minor.

The impacts of the impervious water-storage parametrization on timeseries of Q_{E}, Q_{H} and $L^{\uparrow}$ after rainfall are of the same order of magnitude as their respective changes due to its contribution to the evaporation itself. This also applies for their annual-mean quantities. Due to the large impact of water-storage parametrization on ET and its model performance, it is advised to employ the SID and the water-storage parameter estimates in urban modules as a first good approximation.

Future urban observation campaigns, similar to BUBBLE and CAPITOUL that include continuous multi-annual records of high-quality observations also during rainfall is necessary for the further model improvement of modelling urban ET, or more generally urban climate modelling. In particular, it would allow the development, testing and implementation of more advanced water-storage interception distributions (SID). For instance, it would allow the improvement of the presented 2/3-power relation following from a linear SID. The latter underestimate the amount of shallow water-reservoirs leading to additional, but short-time increase in evaporation. This would also admit investigation of the variability of the impervious water-storage parameters for different urban sites. Furthermore, it could help to better quantify the different contributions to the latent heat, either originating from the urban impervious surface, vegetation in the city, and anthropogenic sources. Such developments would allow a better quantification of ET from urban areas and its impact on the surface energy balance and run-off.

Evaporation from the urban fraction occurs in sudden daytime increases after rainfall when the surface becomes wet. Our model results reveal that the modelled annual-mean evaporation from the urban impervious surface at Toulouse during the CAPITOUL campaign is an order of magnitude lower than ET from the natural surroudings. These results demonstrate that evaporation over urban impervious surfaces behaves very differently from ET of the natural environment. This, together with other urban surface properties, suggests that urban expansion has a considerable impact on the water balance in the future, besides its impact on the energy balance. Apart from the urban climate impacts such as the urban heat island, lower wind speeds and increased turbulence, it is expected that the water storage, evaporation and run-off induced by urbanization affects precipitation, moisture and pluvial flooding as well. These impacts need to be assessed

with urban climate-change and land-use change scenarios with regional climate models such as CCLM. Herein, our new impervious water-storage formulation presented in this manuscript is advised for better modelling the water balance in cities.

Chapter 6

The seasonal dependency of the Belgian urban heat island intensity in CCLM/TU: Model evaluation and assessment of urban climatic drivers

6.1 Introduction

Urban-climate research for the mid-latitudes has mostly focused on quantifying and mitigating the urban heat island (UHI) intensity during heat waves. This is because the UHI intensity reaches peak values at that time. For example, preliminary results of the ESA UHI project (`http://www.urbanheatisland.info`) shows a strong correlation between the mean UHI at 22:00 UTC and mean air-temperature (Fig. 1.8) during the summer months. The large research focus on the summer period also stems from the fact that the instantaneous impact of the UHI during heat waves on human health is clear. For instance, Gabriel and Endlicher (2011) and Laaidi et al. (2011) found that the mortality rates are higher in cities than in the natural surroundings during heat waves for Berlin and Paris, respectively. Yet, urban climate features such as the UHI do not appear during the summer months alone, but also during other seasons including winter. For instance, Giridharan and Kolokotroni (2009) found that the averaged UHI intensity of London is of similar magnitude between the summer and the winter. Furthermore, urban dwellers of Barrow (Alaska) at high-latitude are exposed to less extreme winters with an averaged temperature increase of 2.2 K compared to the hinterlands (Hinkel et al., 2003). Hence in contrast to the summer heat waves for which the UHI mostly deteriorates the thermal comfort, the UHI could enhance the livability of cities at wintertime when cold extremes are tempered.

The specific causes of the urban heat island during the winter season haven't been addressed in detail for the mid-latitudes. In fact, the contributions to the urban heat island could be different than those during the summer. In particular, Giridharan and Kolokotroni (2009) indicate that the peak winter UHI trends for London are not as regular as for summer. In addition, they found that urban-design properties (aspect ratio, surface albedo, plan density ratio, green density ratio, fabric density ratio and thermal mass) cannot explain the changes in outdoor temperatures among different sites around London as much as they did during the summer periods. Lastly, they found that the dependency of the UHI to the meteorological conditions (as indicated by the correlation coefficients from their used climate control models) are more similar among the different urban sites in winter than in summer. As also suggested by the authors (Giridharan and Kolokotroni, 2009), their findings indicate that the dependency of the urban heat island on the meteorological conditions and urban parameters for winter is different than that for summer. This discrepancy of the climatic drivers of the urban heat island intensity between winter and summer could affect the overall variability of the UHI, and also their implications on the thermal comfort throughout the year. Therefore, possible outcomes from urban climate change projections that account for land-use change scenarios could be largely affected by such seasonal dependency of the urban climatic drivers. Moreover, implications of certain urban development and adaptation strategies (for instance for mitigating the urban heat island during heat waves, or better insulation of buildings) on the urban climate and thermal comfort could be different among the seasons as well.

Until recently, research on the role of anthropogenic heat release by human activity (heating of buildings, traffic, domestic, industrial and agricultural activity...) on the regional (urban) climate at the mid-latitudes is limited, and even sometimes believed to be negligible. Still, several quantitative and qualitative methodologies and inventories have been made within recent research activities (Allen et al., 2011; Sailor, 2011; Flanner, 2009; Pigeon et al., 2007; Makar et al., 2006). While it is true that anthropogenic heating is small compared with summertime mid-day solar insolation, it could play a major role in the surface energy balance at times when the urban heat island effect is at its maximum, i.e. during night time and winter (Sailor, 2004). At least for the high-latitudes, Hinkel et al. (2003) argued that the urban heat-island intensity in Barrow (Alaska) stems from extra input of anthropogenic heat release for maintaining interior building temperatures, because its magnitude generally increases with decreasing air temperatures. Moreover, recent research indicates that anthropogenic heat could still play a small but important role and the meso-scale (Sailor, 2004) and on the global scale (Flanner, 2009; Zhang et al., 2013).

This chapter addresses the seasonal dependency of the urban heat island intensity at the regional scales for the mid-latitudes with CCLM coupled to TERRA-URB (hereafter CCLM/TU). Hereby, the influence of anthropogenic heat release versus that of urban structure on the seasonal variability of the urban heat island intensity for Belgium is addressed with model-based sensitivity experiments. This study will allow for more reliable assessment of climate change projections and land-use change scenarios with respect to urban climate and air quality at the regional scales. In order to investigate whether the used urban land-surface module TERRA-URB is able to capture the urban surface-energy balance and its seasonal variability, it is tested in 'offline mode' for a densely built-up urban site first. The latter means that TERRA-URB is forced with meteorological data for wind speed, temperature, and humidity, downward radiation and

precipitation from an observation tower. This is done for an urban site at Rue de la Pomme in the center of Toulouse. This site was chosen because it is the closest mid-latitude site to Belgium for which an annual meteorological forcing dataset is available for a densely built-up urban site to our best knowledge, namely during the "Canopy and Aerosol Particle Interactions in TOulouse Urban Layer" (CAPITOUL) campaign, see Masson et al. (2008). The response of TERRA-URB in terms of the urban surface-energy balance including upward infra-red radiation, reflected short-wave radiation, sensible heat and latent heat are evaluated against observations from the same mast. Secondly, an integration with the regional-climate model CCLM/TU in online mode is performed for Belgium, and evaluated against urban-climate observations for Antwerp and vertical mast profiles. At last, the impact of representing the urban structure versus that of anthropogenic heat release on the urban heat-island intensity is investigated with CCLM/TU for both winter and summer for Belgium.

The remainder of this chapter is structured as follows. We start with a model description of the regional climate model CCLM, the urban land-surface module TERRA-URB and the coupling between the two in 6.2.1. The model configuration of both TERRA-URB in offline mode (i.e. decoupled from the regional-climate model) for Toulouse and the configuration of CCLM/TU (the regional-climate model CCLM coupled to TERRA-URB in online mode) for Belgium can be found in Section 6.2.2. A multi-seasonal evaluation of TERRA-URB in offline mode for Toulouse is presented in Section 6.3.1. Hereby, the importance of the different features implemented in TERRA-URB including the water-vapor opacity, the anthropogenic heat release, and the urban water-storage parametrization, are addressed. An evaluation of CCLM/TU for the urban heat island intensity of Antwerp and for vertical temperature profiles are given in Sections 6.3.2 and 6.3.3, respectively. We discuss the role of nocturnal stability on the urban heat island intensity in Section 6.4.1. The importance of representing the anthropogenic heat release in the coupled model CCLM/TU for winter and summer is examined in Section 6.4.2. The relative impact of representing urban structure versus that of anthropogenic heat release on the urban heat island intensity and the respective mutual interactions for Belgium are discussed in Section 6.4.3. In the scope of this study, limitations and advantages of TERRA-URB employing a "bulk" approach are discussed in Section 6.4.4. Conclusions to this chapter are drawn in 6.5.

6.2 Methodology

6.2.1 Model description

The regional climate model CCLM

The COSMO model (Steppeler et al., 2003) is a full-3D atmospheric numerical model designed for limited-area weather prediction. The model has been created by Germany's National Meteorological Service DWD and is further developed by the Consortium for Small-Scale Modelling (COSMO). It has a compressible non-hydrostatic core for atmospheric dynamics, and accounts for the physical processes, including radiative transfer, cloud and precipitation microphysics, subgrid-scale turbulence, land surface-atmosphere interactions (Doms et al., 2011). The regional climate model CCLM (COSMO-

model in CLimate mode) is based on COSMO, and includes modifications allowing the application on time scales up to centuries (Böhm et al. 2006; Rockel et al. 2008). These modifications comprise the introduction of an annual cycle to vegetation parameters like the plant cover and the leaf area index as well as an externally prescribed, time-dependent CO_2 concentration in the atmosphere. CCLM is further developed by a vast amount of researchers of the CLM-community in -and outside Europe (`http://www.clm-community.eu`). VITO and KU Leuven are formal partners in this network. It is used intensively for regional-climate (impact) studies, and for downscaling future-climate change to the regional scales.

A basic representation of urban land exists in the standard version of CCLM. Hereby, cities are represented by natural land surfaces with an increased surface roughness lengths, a reduced plant cover, adapted leaf-area index and rooting depths. It therefore captures the reduced evapotranspiration that is found over cities. However in this representation, urban areas are still treated as water-permeable soil with aerodynamic, radiative and thermal characteristics similar to the surrounding natural land surface. It therefore can not capture the other extra heating terms, and increased daytime heat storage in the urban structures which leads to prolonged heat release in the evening. Moreover, the surface-layer transfer scheme is not applicable for urban-land use.

Urban land-surface parametrization TERRA-URB

TERRA-URB implements an efficient built-in representation (see Fig. 4.1) of the surface energy balance for urban land-surfaces in TERRA-ML, the standard SVAT model of COSMO and CCLM. A detailed description of the urban extension TERRA-URB can be found in Section 4.2.2.

CCLM/TU: the coupling of TERRA-URB to CCLM

In the coupled CCLM/TU, TERRA-URB, instead of the standard soil module TERRA-ML, is employed for each grid-cell of the horizontal grid, and accounts for both the urban and natural land-cover fraction with a tile approach. Herein, the interactions between the surface and atmosphere above in terms of heat-storage, turbulent exchange of momentum, heat, moisture, and radiative fluxes are determined by TERRA-URB for both the urban and natural land-cover, and weighted according to their respective land-cover fractions. Lastly, the anthropogenic heat is treated as a heat source to the first vertical level above the ground.

6.2.2 Model configuration

Offline model setup for Toulouse

TERRA-URB is configured in offline mode for an urban site at Rue de la Pomme in Toulouse. Hereby, non-stop forcing measurements for a duration of more than one year are available from the "Canopy and Aerosol Particle Interactions in TOulouse Urban Layer" (CAPITOUL) campaign starting in February 2004, see Masson et al. (2008). A

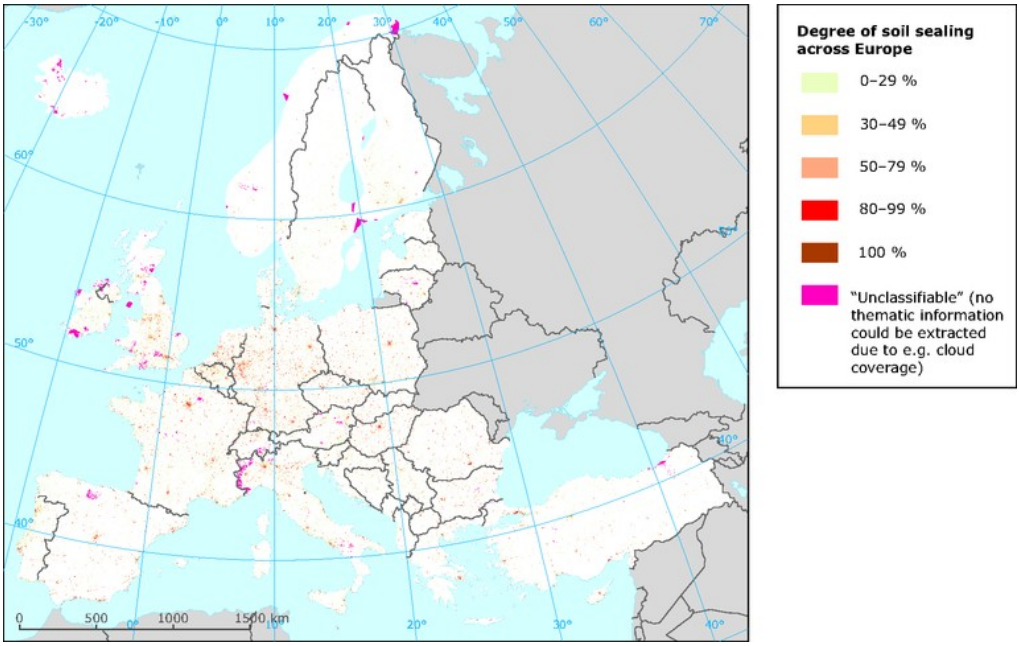

Figure 6.1: Urban impervious land-cover fraction (assigned as urban struction) for Europe. The figure is taken from `http://www.eea.europa.eu/data-and-maps/figures/eea-fast-track-service-precursor`

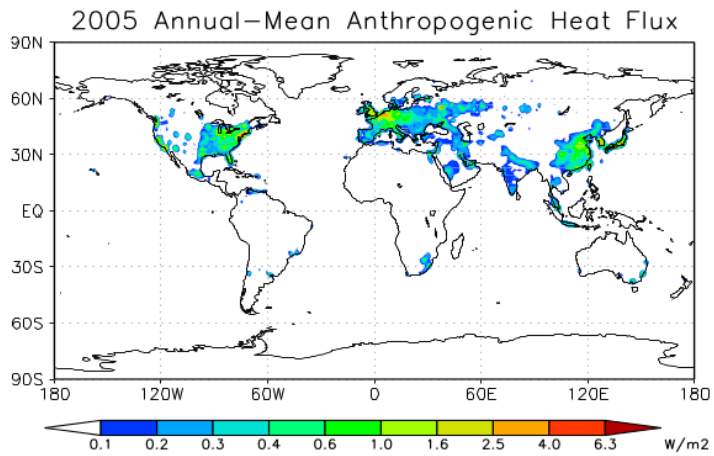

Figure 6.2: The annual-mean energy consumption. The figure is obtained from Flanner (2009).

detailed description of the model setup and forcing data for this site can be found in Section .

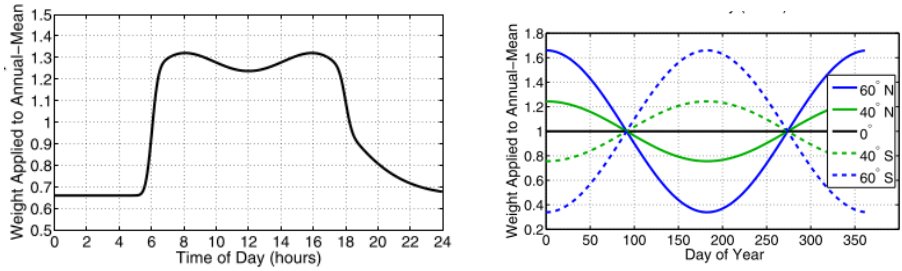

Figure 6.3: Latitudinally-dependent diurnal and seasonal time-distribution functions from Flanner (2009) imposed on the annual-mean anthropogenic heat flux.

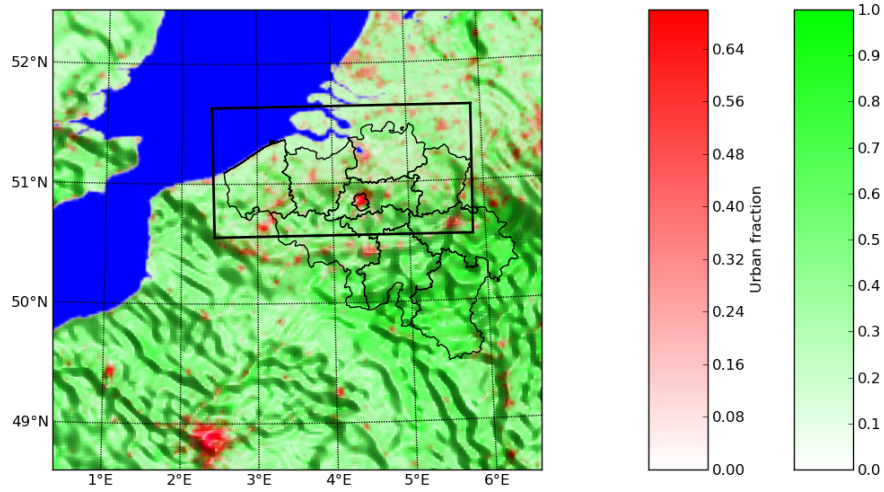

Figure 6.4: The averaged plant-cover fraction and urban fraction for the CCLM domain applied over Belgium at 2.8 km resolution. The shading effect corresponds to the terrain height.

Online model setup for Belgium

The regional climate model CCLM/TU is applied over Belgium for a horizontal model domain of 175 by 175 grid cells with a spacing of 2.8 km resolution (see Fig. 6.4). 40 vertical layers are used with the lowest domain level at 10 m above the ground. The simulation was forced at its lateral boundaries by 6-hourly analysis fields intermediated with 3-hourly forecasts from the operational model of the European Centre for Medium Range Weather Forecasting (ECMWF), available at a spatial resolution of 0.125° in latitude and longitude for the year 2012-2013. We perform a one-year simulation starting in june 2012 with one month of spin-up time.

The soil types, vegetation, and topography are specified with the standard time-invariant

data PrEProcessor (PEP) of CCLM Smiatek et al. (2008). This is processed from various global land-cover data sets for orography and coastlines (GTOPO30), soil data (DSMW) and land-use (GLC2000). Orography and coastlines are extracted from the 30-arc second resolution digital elevation model GTOPO30 (USGS). The vegetation parameters are specified with annual minimum and maximum values for plant-cover fraction, LAI and rooting depth, and depend on the land-use Doms et al. (2011, see their tables 14.3, 14.4, and 14.5). For the extra-tropical northern hemisphere (e.g. Belgium), a growing and resting period is calculated according to latitude. Finally a height correction factor is applied for LAI. The roughness length parameter (over land) depends on both land-use and the subgrid-scale orography.

In addition to the standard PEP prepossessor, an urban fraction overlay is added from the very high-resolution European Soil Sealing of the European Environmental Agency (Maucha et al., 2010) upscaled from 100m (see Fig. 6.1) to the used CCLM grid. Hereby, the urban fraction adopts the specific aerodynamic, thermal and physical characteristics described in Section 4.2.2. The remainder natural fraction adopts the parameters from the standard data preprocessor PEP. Hereby, the standard PEP already accounts for the altered vegetation parameters in urban environments compared to the rural surroundings according to the underlying land-use dataset (this is not the case for the soil type), for instance a reduced plant-cover fraction. For reasons of consistency between the urban fraction overlay and the natural land-use specified by PEP, the dynamic plant-cover fraction assigned to the natural tile is rescaled (thus increased) according to the fraction of this natural tile. This is because the vegetation fraction for the urban fraction is always considered zero.

Similar as in the stand-alone simulations, the anthropogenic heat release is determined from Flanner (2009) (see also `http://www.cgd.ucar.edu/tss/ahf/`). The methodology accounts for country-specific data of energy consumption from non-renewable sources. This was apportioned according to population density (conserving the national total) and converted to annual-mean gridded energy flux at a fine resolution (2.5×2.5 minute). Latitudinally-dependent diurnal and seasonal distribution functions (see Fig. 6.3) are superimposed on the annual-mean (see Fig. 6.2). For each surface grid-cell of the model domain, TERRA-URB adds the anthropogenic heat release to the surface sensible heat flux (see also 4.2.2).

To conclude, urban environments in the input dataset are characterized by reduced vegetation abundance, increased urban structure as compared to the natural surroundings and anthropogenic heat release. A composite image for urbanization (i.e. displaying both urban structure and the vegetation) for the used horizontal grid shown in Fig. 6.4. CCLM/TU only requires an additional computational cost of 3% over the standard version of CCLM.

	$R(z)\uparrow$		
spring	TU	NOWVO	STD
RMSE	5.639	**5.552**	18.536
BIAS	-4.447	**1.970**	-19.601
R2	0.995	**0.997**	0.969
summer	TU	NOWVO	STD
RMSE	**4.336**	8.869	18.813
BIAS	**-0.017**	10.335	-20.027
R2	**0.997**	0.996	0.963
fall	TU	NOWVO	STD
RMSE	**1.912**	4.322	4.608
BIAS	-2.928	**-2.203**	-5.792
R2	**0.998**	0.994	0.990
winter	TU	NOWVO	STD
RMSE	**3.276**	4.195	4.608
BIAS	**-5.633**	-5.962	-7.078
R2	**0.989**	0.982	0.981

Table 6.1: Evaluation of the offline runs at the Toulouse urban site with TERRA-URB (TU), with TERRA-URB without accounting for water-vapor opacity (NOWVO) and with the standard version TERRA-ML (STD) in comparison with mast observations for every season. The root-mean-square error (RMSE), bias (BIAS), and correlation (R2) are given in terms of upward infra-red radiation $R^{\uparrow}(z_{\mathrm{ref}})$ at mast height z_{ref}.

6.3 Evaluation

6.3.1 Multi-seasonal offline evaluation of TERRA-URB for Toulouse

In this section, we perform an offline evaluation with TERRA-URB at a densely built-up urban site in Toulouse during the CAPITOUL campaign first. We employ exactly the same setup and meteorological forcing as described in Section 6.2.2. Hereby, TERRA-URB is forced with observations, an thus decoupled from the regional-climate model CCLM. As a result, we specifically focus on the performance and benefits of the urban module TERRA-URB itself, excluding existing errors and uncertainties arising from all other aspects of regional-climate modelling. As the duration of the offline simulation extends to more than one year, it allows to focus on TERRA-URB's performance for every season.

We start from the reference simulation with TERRA-URB (TU) described in section 4.2.2, in which we also account for water-vapor opacity formulated in Section 4.2.3, the urban water-storage parametrization developed in chapter 5, and anthropogenic heat release from Flanner (2009). This is compared with the results of the standard version of TERRA-ML (STD). In order to address the importance of the different features implemented in TERRA-URB, we perform additional sensitivity simulations by excluding the water-vapor opacity (NOWVO), excluding the anthropogenic heat (TU0), and excluding the urban water-storage parametrization (DRY). We also have performed several sensitivity tests to address the uncertainties of urban-climate modelling on the

	Q_H		
spring	TU	TU0	STD
RMSE	27.463	**26.280**	87.377
BIAS	**4.943**	-11.763	48.575
R2	0.958	0.961	**0.963**
summer	TU	TU0	STD
RMSE	26.999	**26.273**	80.207
BIAS	**3.964**	-10.346	37.714
R2	0.964	0.965	**0.969**
fall	TU	TU0	STD
RMSE	22.268	**21.131**	39.845
BIAS	-4.704	-28.922	**3.957**
R2	0.851	0.865	**0.873**
winter	TU	TU0	STD
RMSE	**29.658**	30.044	36.631
BIAS	-23.932	-50.450	**-22.268**
R2	**0.797**	0.791	0.795

Table 6.2: Evaluation of the offline runs at the Toulouse urban site with TERRA-URB (TU), with TERRA-URB considering no anthropogenic heat (TU0), and with the standard version TERRA-ML (STD) in comparison with mast observations for every season. The root-mean-square error (RMSE), bias (BIAS), and correlation (R2) are given in terms of the sensible heat flux Q_{H}.

vegetation parameters in cities (not shown). The largest sensitivity was found for the rooting depth. Therefore, we compare the results of reference run with TERRA-URB employing a rooting depth of 2.0 m (representative for the large trees at the urban site) with an additional run for which the rooting depth is reduced to the standard upper limit of TERRA-ML 0.5 m (RD05).

The offline results of the different runs listed above are evaluated for the same seasonal periods as in Demuzere et al. (2013) and Pigeon et al. (2008) for easy comparison, see Figure 6.5, and tables 6.1, 6.2 and 6.3. For the score tables, we always compare reference simulations (TU) with the standard version TERRA-ML with its standard water-impermeable rock-class (STD), but also with one of the sensitivity runs with TERRA-URB for which the particular surface-atmosphere energy-transfer component was the most sensitive.

The day-time values of $R^{\uparrow}(z_{\mathrm{ref}})$ (resp. Q_{H}) are largely underestimated (overestimated) for all seasons in the standard version of TERRA-ML (STD). In particular, this leads to very large RMSE-values for Q_{H}. A much better agreement is found for the reference simulation with TERRA-URB for which the daytime underestimation (overestimation) was eliminated (compare TU with STD). This mainly results from the thermal roughness length parametrization employed for the urban land-cover fraction in combination with the new surface-layer transfer coefficients developed in chapter 3, but also by the specification of representative thermal parameters for urban areas from De Ridder et al. (2012). More particular, TERRA-URB captures the enhanced day-time heat-storage uptake (thus by a reduction in sensible heat release) and the subsequent nocturnal heat-storage release (thus

	Q_E		
spring	TU	DRY	STD
RMSE	**12.604**	15.636	15.648
BIAS	**-6.341**	-18.843	-18.831
R2	**0.875**	0.768	0.768
summer	TU	DRY	STD
RMSE	**19.065**	19.384	19.384
BIAS	**-12.845**	-13.004	-13.004
R2	**0.708**	0.684	0.684
fall	TU	DRY	STD
RMSE	**12.089**	12.895	12.838
BIAS	**-9.391**	-16.313	-16.367
R2	0.538	**0.557**	0.556
winter	TU	DRY	STD
RMSE	**12.159**	13.421	13.755
BIAS	**-15.143**	-16.899	-16.571
R2	**0.619**	0.453	0.458

Table 6.3: Evaluation of the offline runs at the Toulouse urban site with TERRA-URB (TU), with TERRA-URB excluding water-storage parametrization (DRY), and with the standard version TERRA-ML (STD) in comparison with mast observations for every season. The root-mean-square error (RMSE), bias (BIAS), and correlation (R2) are given in terms of the sensible heat flux Q_{E}.

by an enhanced sensible heat release) both characteristic for densily-built urban areas. The specification of anthropogenic heat in the reference simulations further compensates for the overall negative bias in Q_{H} (compare TU with TU0) during fall and winter. The large day-time positive bias found with TERRA-URB (similar to the that found in Hénon et al. (2012); Demuzere et al. (2013)), especially for summer during clear-sky conditions when the urban-structure surfaces become much warmer than the air above, was eliminated after accounting for the infra-red opacity of water vapor formulated in Section 4.2.3 (compare TU with NOWVO).

One finds an overall negative bias for Q_{E} for TERRA-URB excluding the water-storage parametrization (DRY) in all seasons, and for the standard version of TERRA-ML using its standard rock class for the impervious urban land-cover (STD). This negative bias is considerably reduced for all seasons if the water-storage parametrization from chapter 5 for the urban impervious surface is activated (compare TU with DRY). Furthermore, when employing a value of $\delta_m = 100\%$ (LD100) instead of taking $\delta_m = 12\%$ estimated in chapter 5 used in the reference simulation (TU), the persistence in daytime evapotranspiration is better captured. In particular, one finds an underestimation of Q_{E} in the evening for spring, which is in agreement with earlier studies (Demuzere et al., 2013; Pigeon et al., 2008). This is related to the fact that the evaluation for which measurements were available include a few days after precipitation has occurred. Hereby, an increase in Q_{E} results from water on the impervious surface that could remain at the impervious surface during the night when there is no evaporation in the model. The delay in evaporation to the next day evening is now better-captured with the reference simulation (TU) taking the estimate $\delta_m = 12\%$. As a consequence, the overall negative bias in Q_{E} was reduced

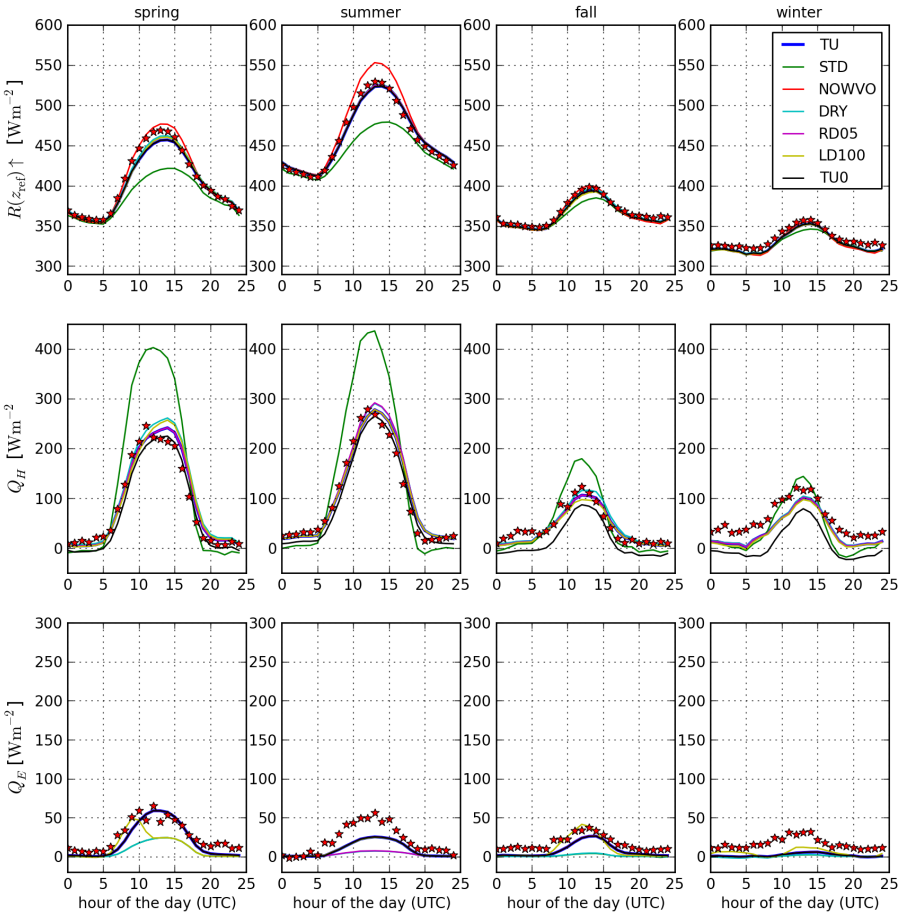

Figure 6.5: Observed (stars) and modelled (lines) diurnal averages for the infra-red upward radiation at mast height ($R^{\uparrow}(z_{\mathrm{ref}})$), sensible heat flux Q_{H} and latent heat flux (Q_{E}) for Toulouse for the different seasons. The blue line (TU) is the reference simulation with TERRA-URB (including impervious water-storage parametrization and infra-red water-vapor opacity). The green line (STD) is the simulation with the standard version of TERRA. The red line (NOWVO), the blue line (DRY) and the purple line (RD05) are equal to the reference simulations, but excluding infra-red water-vapour opacity excluding evaporation from impervious surfaces, and a reduced rooting depth from 2.0 to 0.5 m (the upper limit in the standard TERRA version), respectively. Finally, the gold line are the results with an impervious water storage with $\delta_m = 100\%$ instead of $\delta_m = 12\%$.

in the evaluation during spring (compare TU with LD100).

As stated before, a high sensitivity of the model results on the rooting depth for the vegetation in the city is found for spring. When assuming values of only 0.5 m (which is the upper limit for the standard version of TERRA-ML), the evaporation during rain-free events was too low during summer (RD0.5). A value of 2.0 m is more realistic for the vegetation at the urban site in Toulouse which mainly consists of large trees (which is specified in TU). These trees can maintain the evapotranspiration during the dry periods in summer, because they can get water from the deeper soil-layers. As a result, it partially reduces the negative bias for Q_{E}, but also the day-time positive bias of Q_{H} during summer (compare TU with RD0.5).

An overall negative bias for Q_{E} still persists in the model (TU) compared to the measurements. Especially during the night, the model shows zero evaporation for both urban and natural fractions, whereas a slight positive evaporation persists in the measurements. This discrepancy between model and measurements may indicate anthropogenic sources from heating, air conditioning, households and traffic. It can also originate from deficiencies in the model for the natural fraction that excludes irrigation, or the inaccuracies in the eddy-correlation measurements. Lastly, the underestimation can result from the infiltration of run-off water from the water-impermeable surfaces to the local permeable soil, which is not accounted for in the model. Hereby, more water is disposable to the vegetation in the city, which enhances the ET, and their cooling capacity.

6.3.2 Multi-seasonal online evaluation for Antwerp

The model results with the coupled model CCLM/TU (described in Section 6.2.1) are evaluated with urban-climate observations performed by the Flemish Institute for Technological Research. Hereby, urban climate observations are taken for Antwerp, a city of mediocre size, for which the observations are available from mid-july 2012 onwards. As the focus of the remainder of this thesis is modelling urban heat island intensity, this evaluation is restricted to $T_{2\mathrm{m}}$ observations for an urban site (51.208525N, 4.41022778E) located in the city centre (Koninklijk Lyceum Antwerp; KLA-U hereafter) and a rural site (51.16600833N, 4.5448722E) 10.5 km away (Bioboerderij van Leemputten, Vremde; VRM-R hereafter). The modeled urban heat island (UHI) of Antwerp calculated from the temperature difference between the two stations (KLA-U - VRM-R) is evaluated as well. The urban station (KLA-U) is placed on a roof of a small building surrounded by an open place for children. The rural station (VRM-R) is centrally located on a grassland 150 m away from the closest building. Both measurement set-ups are exactly the same and use the same high-quality temperature sensors (RTD-type PT1000) which are shielded and aspirated (Young Aspirated Radiation Shield, model 43502).

The modeled two-meter temperatures at the respective locations are calculated from the potential temperature at that height:

$$T_{2\mathrm{m}} = \theta(2\,\mathrm{m}) \times \left(\frac{P}{P_0}\right)^{R/c_p}, \tag{6.1}$$

Hereby, the potential temperature is extrapolated from that of the half-level value z_{ref} of the first vertical model level above the surface with the following expression:

$$\theta(z) - \theta(z_{\mathrm{ref}}) = \theta^* \left[\ln(z/z_{\mathrm{ref}}) - \psi_H(z/L) + \psi_H(z_{\mathrm{ref}}/L) + \psi^*(z/L, z/z_*)\right] \tag{6.2}$$

This is done for both the natural and urban land-cover fraction.

The results for mid-summer (21/07/2012 until 21/08/2012) and mid-winter (21/01/2013 until 21/02/2013) are shown in Tab. 6.4, and in Figs. 6.6 and 6.7, respectively. A good agreement is found between the observed and modelled UHI intensity and the reference run TU for both summer and winter. Both the diurnal cycle of the UHI magnitude as well as its daily variability is well captured for TU, which is not the case for the standard version STD. In particular, TU reproduces the observed timing of the maximum UHI occurring at nighttime, whereas in STD, it occurs during daytime leading to negative correlation coefficients. The UHI magnitude is also well-captured in the reference simulation TU, but is largely underestimated in the standard version (STD).

The $T_{2\mathrm{m}}$ values for the urban and rural areas separately are also well-reproduced. However, an overall positive bias is found in summer for both TU and STD at the rural station, whereas an overall negative bias is found in winter. On the one hand, the positive bias for the rural station in summer is slightly larger for TU than for STD. This may follow from the fact that urban structure and anthropogenic heat has a slight impact on the rural areas by advection as well. On the other hand, a similar positive shift from STD to TU in rural areas also leads to an overall reduction in the negative bias in winter.

Even though the TU version yields a dramatic improvement in capturing the UHI intensity for both the summer and winter, it still yields an underestimation. In particular, the average modeled UHI intensity reaches 1.7 K whereas the observed mean UHI intensity is 2.1 K, which is an underestimation of 20%. This is also the case for the extreme values of the UHI intensities (i.e. 90th percentile values). A better agreement is found for the winter period, but still seems to be underestimated in the extreme values of UHI intensity (i.e. the 90th percentile values). The overall underestimation of the UHI intensity near the surface can be related to the too neutral nocturnal vertical temperature profiles during heat waves at nighttime when the urban heat island reaches a maximum. This issue is further discussed in Section 6.4.1 after comparing the model results with vertical temperature profiles in Section 6.3.3.

6.3.3 Evaluation of the vertical temperature profiles of the online simulations with CCLM/TU

The regional climate and air quality is largely determined by the properties of the atmospheric boundary layer (ABL). It is the layer directly influenced by the surface-atmosphere interactions and therefore very distinct from the atmosphere above in terms of wind fields, temperature and turbulence. Furthermore, land-use, in particular urbanization, mainly determines the structure of this boundary layer as well. As pointed out in Section 2.3.4 with an idealized advection model, the ability of representing the overall nocturnal boundary-layer structure is important for modelling the urban heat-island with urban regional climate models. In this section, we focus on the representation of the boundary-layer stability during one large and two short heat-wave of summer 2012 for Belgium for which the urban heat-island reaches a maximum (2012/07/22 until 2012/07/26; 2012/08/13 until 2012/08/20; 2012/09/09 until 2012/09/09). The online model results for Belgium are compared with measurements of nocturnal temperature profiles from two mast towers. The first one is located in an urban/industrial site in

		winter			summer		
		TU	TU0	STD	TU	TU0	STD
URB (KLA)	RMSE	**1.342**	1.478	1.625	1.232	**1.196**	2.009
	BIAS	**-0.966**	-1.937	-2.924	1.317	1.025	**-0.598**
	R2	0.945	**0.945**	0.937	0.964	**0.966**	0.939
RUR (VRM)	RMSE	**1.691**	1.708	1.721	1.476	1.452	**1.363**
	BIAS	**-1.084**	-1.505	-1.827	1.869	1.676	**1.157**
	R2	**0.929**	0.928	0.927	0.954	0.956	**0.961**
UHI (KLA - VRM)	RMSE	**0.932**	1.154	1.375	1.049	**1.012**	2.161
	BIAS	**0.118**	-0.432	-1.097	**-0.552**	-0.650	-1.756
	R2	**0.642**	0.328	-0.283	0.736	**0.762**	-0.341

Table 6.4: Evaluation of the online simulations for CCLM/TU (TU), for CCLM/TU excluding anthropogenic heat (TU0), and for the standard version of CCLM (STD) in comparison with urban-climate observations for mid-summer (2012/07/21 until 2012/08/21) and mid-winter (2013/01/21 until 2013/01/21). The root-mean-square error (RMSE), bias (BIAS), and correlation (R2) are given in terms of $T_{2\mathrm{m}}$ at the URBan site (KLA: Koninklijk Lyceum of Antwerp), that at the RURal site (VRM: Vremde), and in terms of the urban heat island (UHI) represented by the difference (KLA - VRM).

Zwijndrecht (51.243858N, 4.334207E) established by the Vlaamse Milieumaatschappij (VMM), whereas the second one is located in a rural site in Mol (51.217983N, 5.089916E) deployed by the Crisis Management and Decision support unit of the Belgian Nuclear Research Centre (SCK-CEN). As expected, the lapse rate of the nocturnal temperature profile of the urban site and the rural site are very different. The former exhibit more neutral temperature profiles, whereas the latter are very stable. Therefore, we also evaluate the model's ability of reproducing the difference between the profiles. The vertical temperature profiles are also compared with those from the ECMWF analysis at 12.5km horizontal resolution (EC12.5) also used as the forcing for CCLM and CCLM/TU at 2.8km resolution.

Fig. 6.8 shows 'N'octurnal boundary-layer 'T'emperature Profiles (NTP) 'H'ourly-'A'veraged for the heat waves (NTP-HA)) at Zwijndrecht ('U'rban site; NTP-HA@U) and Mol ('R'ural site: NTP-HA@R), and their 'D'ifference (urban minus rural; TP-HA@D). The scores are shown in Tab. 6.5. In the latter, RMSEB refers to the Root-Mean Square Error of the Bias-corrected vertical temperature profiles. It is a measure for the ability of reproducing the stucture (cfr. lapse rate) of temperature profile. The results are consistent among the short and large heat waves characterized by daily-averaged increasing temperatures and by an growing nocturnal UHI intensity.

During the heat waves, the NTP@R are characterized by strong stability resulting from nocturnal infra-red radiative cooling of the surface(-layer) due to clear-sky conditions. EC12.5 produces much stronger negative lapse rates for the nocturnal temperature profiles than CCLM/TU and CCLM (standard) during heat waves for the entire domain for the natural areas. Clearly, EC12.5 has an overall better agreement with the observations for NTP@R than CCLM/TU or CCLM. Differences in the stratification can be explained by either radiation parametrizations leading to differences in nocturnal radiative cooling,

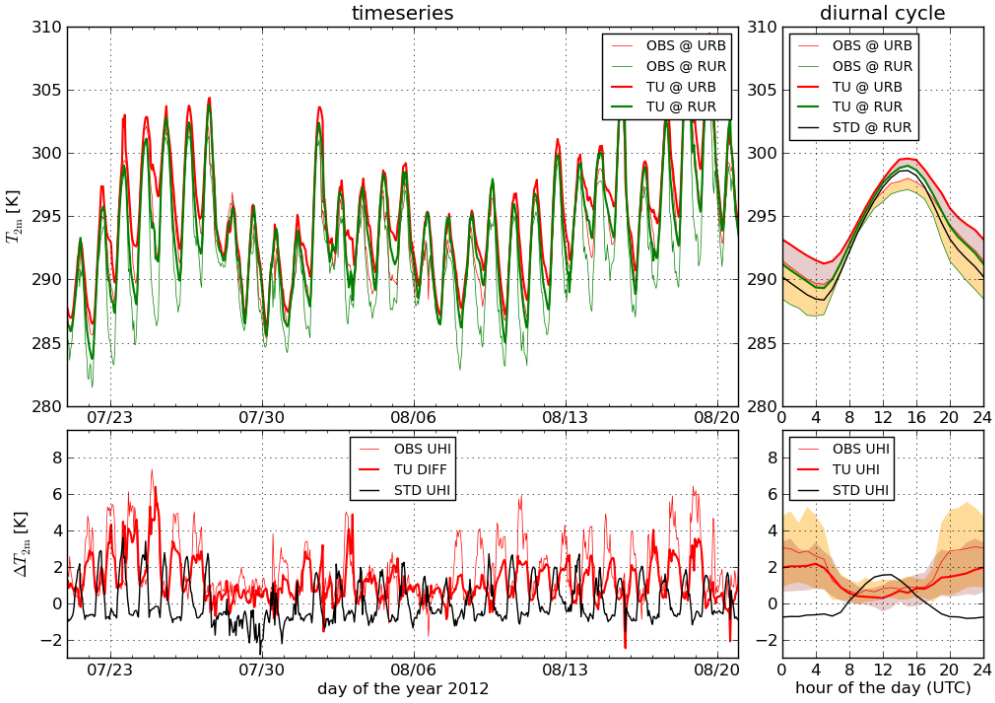

Figure 6.6: Timeseries and mean diurnal cycle for modelled and observed T_{2m} at the URBan site (KLA: Koninklijk Lyceum of Antwerp) and the RURal site (VRM: Vremde) for mid-summer (2012/07/21 until 2012/08/21). Model results for CCLM/TU (indicated by TU) and the standard version of CCLM (indicated by STD) are shown. The urban heat island (UHI) is calculated as the difference between URB-site and RUR-site. The orange and dark-red areas in the upper-right panel represent the averaged UHI for the observations and the model results (only) for CCLM/TU. The orange and dark-red areas in the lower right panel represent the ranges between the 10th and 90th percentiles of the respective urban heat island intensities.

differences in the SVAT-models, differences in the turbulence schemes, and differences in the structures of the upper atmosphere (cfr., the presence of moisture and cloud cover). It can also originate from the difference in surface-land characteristics at the specific rural site. Yet, similar profiles are found in the model at the neighbouring gridcells having distinct land-surface characteristics (roughness length, vegetation index, land-surface type). Lastly, it may originate from differences in the overall land-surface characteristics of the entire domain. For instance, urbanization has not been accounted for in the EC12.5, while it is partially accounted for in the standard CCLM by a reduced vegetation, and in an explicit way for the CCLM/TU with the urban parametrization TERRA-URB.

Close to neutral vertical temperature profiles are found at the urban site (NTP@U). This can be explained by a reduced nocturnal surface cooling (or slightly positive surface heating) at metropole and harbour of Antwerp. A better agreement with the observed NTP@U are found for both CCLM and CCLM/TU than for EC12.5. It stems from the

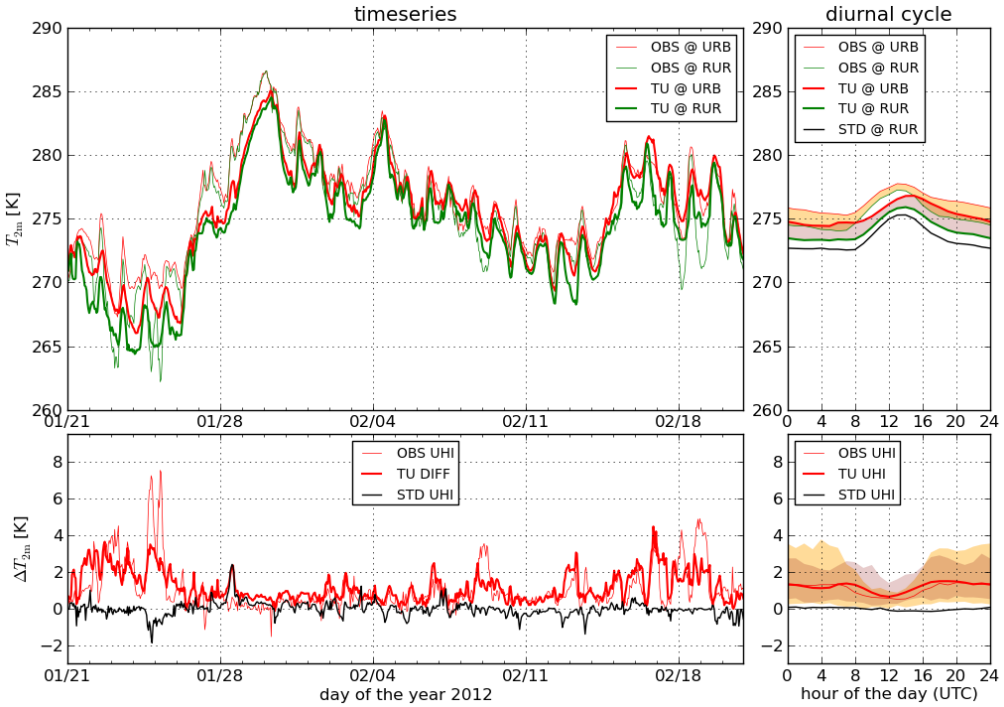

Figure 6.7: Idem as figure 6.6, but for mid-winter (2013/01/21 until 2013/02/21).

fact that urbanization is accounted for by either presuming a rock class (in CCLM) or the explicit representation of urban land-cover fraction (in CCLM/TU).

Lastly, the difference in temperature profiles between the urban mast site and the rural mast site is evaluated for CCLM, CCLM/TU, and EC12.5. The lapse rate of the difference between the observed urban and rural nocturnal temperature profiles (NTP@U - NTP@R) is negative for at least up to a height of mast profiles reaching 114 metres. This is in agreement with chapter 2 in which the UHI impact is found up to 150metre for the metropole of France also for the nocturnal situation during heat waves. The best agreement for the negative lapse rate of NTP@U - NTP@R is found with CCLM/TU. The lapse rate of NTP@U - NTP@R is also negative for the standard CCLM run because the model accounts for the reduced vegetation (and thus an added daytime heat source) in urban areas, but has a smaller value throughout the night. EC12.5 shows a negative lapse rates for NTP@U - NTP@R, which originates from the fact that urbanization is not accounted for at all. The larger negative lapse rate of NTP@U - NTP@R for CCLM/TU compared with those of CCLM and thus better agreement with the observations, stems from a better representation of heat-storage by the urban land-cover fraction during the day. This leads to a reduced surface cooling (or enhanced surface heating) afterwards during the night.

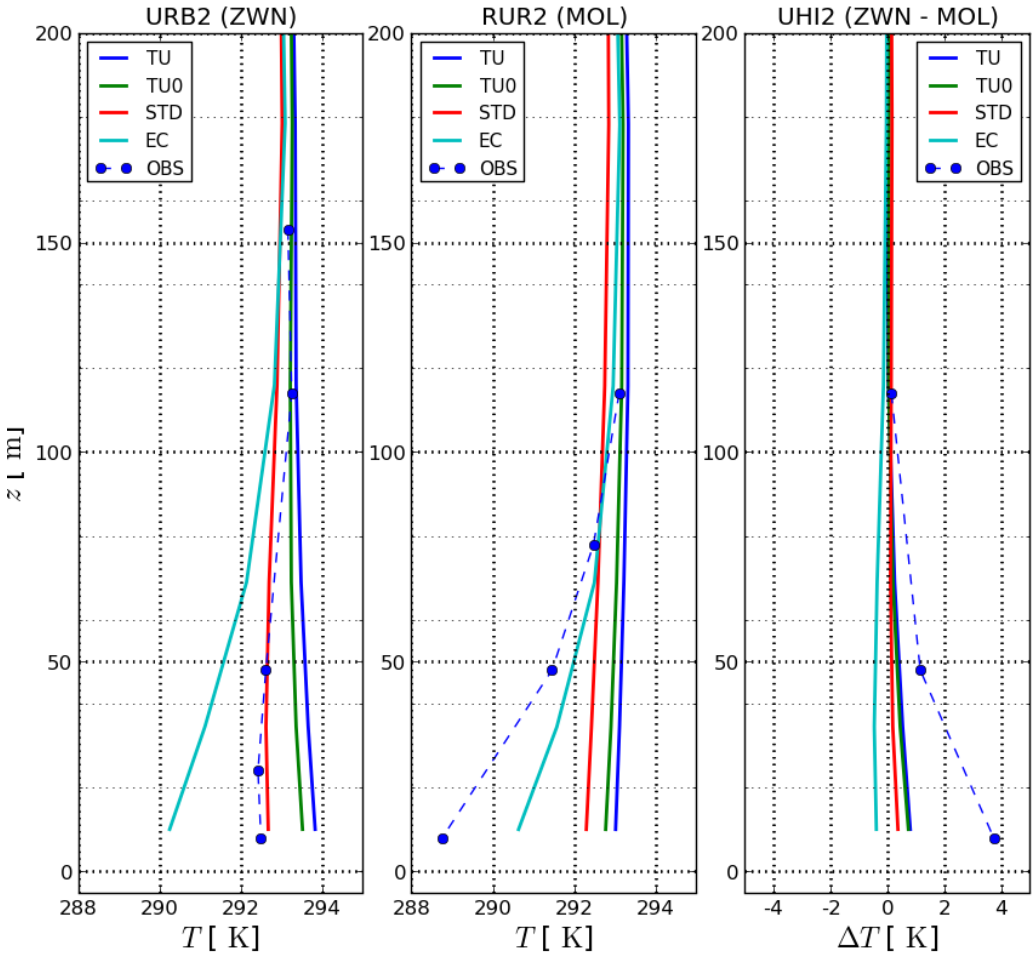

Figure 6.8: Comparison between nocturnal vertical profiles produced by the online simulations with CCLM/TU (TU), with CCLM/TU excluding anthropogenic heat (TU0), and with the standard version of CCLM (STD), and those from observation towers at an urban/industrial site in Zwijndrecht (ZWN), a rural site in Mol (MOL), and their difference (ZWN - MOL). The vertical profiles are averaged for the heat waves during summer 2012 at midnight.

6.4 Discussion

6.4.1 The role of nocturnal stability on the urban heat island intensity

Even though the urban parametrization in CCLM/TU leads to a better contrast in vertical profiles between NTP@U and NTP@R compared to the standard version of CCLM and the ECWMF analysis, the negative difference in lapse rate between the profiles still seems to be underestimated by the model. It has been demonstrated in

URB2 (ZWN)		TU	STD	EC
21H	RMSE	1.20	**1.06**	1.28
	RMSEB	0.70	**0.53**	0.98
	BIAS	**0.24**	-0.40	-1.23
0H	RMSE	1.30	1.29	**1.10**
	RMSEB	0.79	**0.63**	0.95
	BIAS	0.81	**-0.05**	-1.29
3H	RMSE	1.77	1.54	**1.13**
	RMSEB	0.77	**0.65**	0.82
	BIAS	1.24	**0.31**	-1.36

RUR2 (MOL)		TU	STD	EC
21H	RMSE	2.15	2.14	**1.35**
	RMSEB	1.88	1.85	**1.02**
	BIAS	1.91	1.34	**0.20**
0H	RMSE	2.07	2.06	**1.26**
	RMSEB	1.86	1.81	**1.09**
	BIAS	2.05	1.40	**0.70**
3H	RMSE	2.18	2.12	**1.33**
	RMSEB	1.96	1.94	**1.22**
	BIAS	1.99	1.45	**0.23**

UHI2 (ZWN - MOL)		TU	STD	EC
21H	RMSE	**1.74**	1.82	2.18
	RMSEB	**1.42**	1.52	1.83
	BIAS	-1.67	-1.74	**-1.43**
0H	RMSE	**1.80**	1.98	1.86
	RMSEB	**1.45**	1.59	1.72
	BIAS	**-1.24**	-1.45	-1.99
3H	RMSE	1.93	**1.87**	1.96
	RMSEB	**1.41**	1.53	1.64
	BIAS	**-0.75**	-1.13	-1.59

Table 6.5: Evaluation of the vertical profiles produced by the online simulations with CCLM/TU (TU), with CCLM/TU excluding anthropogenic heat (TU0), and with the standard version of CCLM (STD), and those from observation towers at an urban/industrial site in Zwijndrecht (ZWN), a rural site in Mol (MOL), and their difference (ZWN - MOL). The root-mean-square error (RMSE), the root-mean-square error of the bias-corrected profiles (RMSEB) and the overall the bias (BIAS) are calculated seperately for the nocturnal hours (21H / 0H / 3H).

chapter 2 with an idealized advection model that the performance of boundary-layer representation of the regional-climate model affects of the representation of the UHI effect. Neglecting orographically-induced (or other) secondary effects, it has been demonstrated that an underestimation of the nocturnal lapse rate in rural areas particularly leads to an underestimation of the urban heat island effect at ground-level. Hereby, the

underestimation of nocturnal boundary-layer stability during heat waves at the rural sites actually leads to an UHI effect that is spread over a too large depth throughout the boundary layer, hence results in an underestimation of the UHI at ground level.

The above reasoning is consistent with the results from CCLM/TU, namely the too neutral profiles produced with CCLM/TU for the NTP@R profiles in section 6.3.3, the overall underestimation of the UHI in the profiles (NTP@U - NTP@R), and the underestimation in the $T_{2\mathrm{m}}$-values found in Section 6.3.2. Therefore, the model performance at *rural* sites in atmospheric models is very important for simulating the urban heat island intensity - in particular the nocturnal boundary-layer lapse rate. From the above discussion of comparing modeled vertical profiles with and tower observations, it is concluded that the representation of the boundary-layer lapse rate for *rural* areas in CCLM needs to be improved for more reliable assessment of the urban heat island intensity.

6.4.2 The importance of anthropogenic heat on the UHI for Belgium for winter and summer

In this section, we discuss the role of anthropogenic heat on the urban heat island and its seasonal variability. We compare the urban heat island effect for Antwerp for summer and winter reproduced by the reference run (TU) and that by the run excluding anthropogenic heat (TU0), see Fig. 6.9. We focus on the diurnal cycle of the UHI of Antwerp - a city of ordinary size - for the same mid-summer and mid-winter periods. As in the evaluation, this is calculated from the difference between the urban site KLA-U and the reference rural site VRM-R. For the summer period, the urban heat island effect is mainly determined by the urban structure (i.e. by its reduced evapotranspiration, less short-wave reflection, increased day-time storage heat uptake and nighttime release), whereas the additional impact of anthropogenic heat over the urban structure itself is much smaller. In contrast, for the winter period the additional impact of anthropogenic heat is about as large as the impact of urban structure. In fact, the inclusion of anthropogenic heat eliminates the underestimation of the UHI (compare TU and TU0 with observations). This is consistent with the offline results in Section 6.3.1, in wich anthropogenic heat release largely reduces the negative bias in the surface-sensible heat flux, especially in winter. It needs to be noted that the small additional impact of anthropogenic heat in summer does not mean that anthropogenic heat is much less important than urban structure: the importance of anthropogenic heat may become larger in the absence of urban structure. This will be discussed further in the next paragraph.

The ratio of the 90th-percentile UHI effect between TU and TU0 is the same as the ratio of the mean UHI. Therefore, the additional impact of anthropogenic heat increases proportionally to the UHI itself for both winter and summer. In other words, the relative role of anthropogenic heat over urban structure versus the role of urban structure itself remains constant between small and large UHI intensities. This can be explained by the fact that the nocturnal UHI development mainly depends on nocturnal added sources to the surface energy balance in urban areas under variable stable stratifications, and that the development does not depend on the particular nature of the sources, either by storage-heat release or by (night-time) anthropogenic heat. It is striking that the additional contribution of anthropogenic heat to UHI intensity is large compared to the UHI established by urban structure and scarce vegetation, especially during winter.

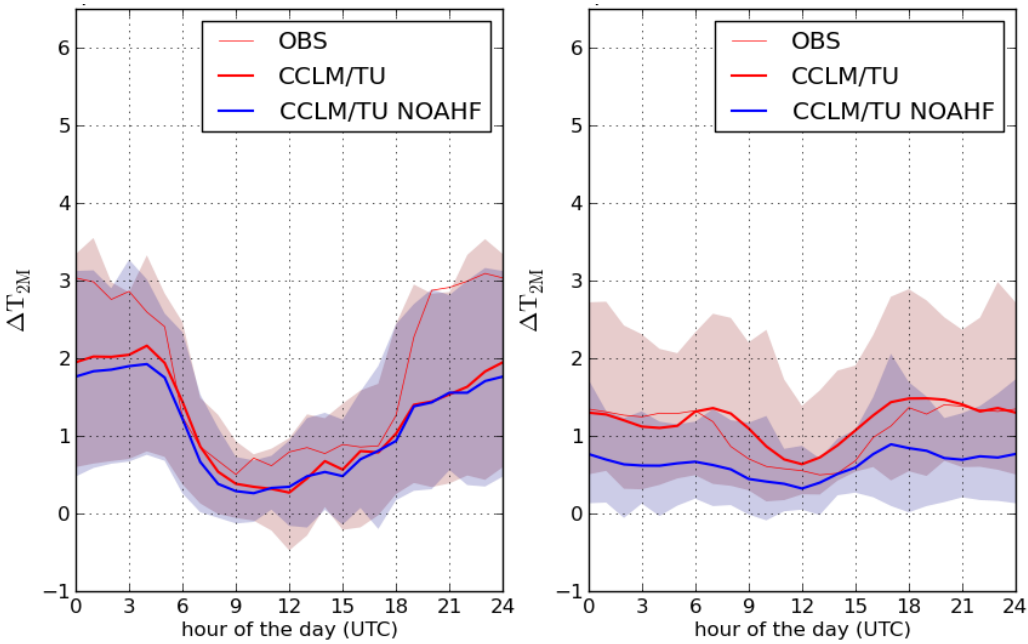

Figure 6.9: The mean diurnal cycle of the UHI (KLA - VRM) intensity for Antwerp showing the additional impact of anthropogenic heat over urban structure. The left panel represents the mean diurnal cycle of the UHI in summer (2012/07/21 until 2012/08/20), and the right panel that for winter (2013/01/21 until 2013/02/20). The thin red line corresponds to the observations. The red line (TU) represents the model results for the reference simulation of CCLM/TU for which anthropogenic heat is included. The blue line (TU0) represents the scenario run CCLM/TU for which anthropogenic heat is excluded. The colored areas are ranges between the 10th and 90th percentile of the urban heat island for each hour. The UHI effect is calculated by the difference between the urban site KLA-U and the reference rural site VRM-R.

Under nocturnal conditions with stable boundary-layer stratification, (the impact of urbanization on the) the small additional anthropogenic heat release (besides the storage heat release) still seems to have a large impact on the urban heat island.

A final remark is that the inclusion of anthropogenic heat does not account for temperature dependency on the energy demand. This temperature dependency can lead to an underestimation of the effect of anthropogenic heat for cold temperatures during winter, whereas the effect may be overestimated for temperate winters. Indeed, as found by Allen et al. (2011), temperature during winter is one of the most important driving factors for anthropogenic heat in cities during winter. The large cooling demand during heat waves increasing the energy consumption may also lead to an underestimation of anthropogenic heat and its impact on the urban heat-island intensity at that time.

6.4.3 The relative role of anthropogenic heat versus urban structure

In this section, we investigate the relative impact of representing urban structure versus that of anthropogenic heat release in CCLM/TU. This is done with the Stein and Alpert (1993) decomposition technique for both summer and winter. This method allows to separate between the pure impacts of the physical processes established by multiple control parameters - in our case urban structure and anthropogenic heat - and the mutual pure interactions between their physical processes. For the full decomposition of two control parameters ($n = 2$), we need $2^n = 4$ simulations. In the first simulation TU00, we both exclude urban structure and anthropogenic heat, in the second simulation TU01, we only include urban structure, but exclude anthropogenic heat. This is the same run as TU0 considered before. In the third simulation TU10, we exclude anthropogenic heat, but include urban structure again. In the last simulation TU11, we both include anthropogenic heat and urban structure, which is the same as the reference simulation TU. The full Stein-alpert decomposition, which is calculated at each grid-cell of the model domain for $T_{2\mathrm{m}}$, with the two control parameters yield:

$$\begin{aligned} \mathrm{TU'0} &= \mathrm{TU0} \\ \mathrm{TU'01} &= \mathrm{TU01} - \mathrm{TU00} \\ \mathrm{TU'10} &= \mathrm{TU10} - \mathrm{TU00} \\ \mathrm{TU'11} &= \mathrm{TU11} - \mathrm{TU01} - \mathrm{TU10} + \mathrm{TU00} \end{aligned} \tag{6.3}$$

where TU'01 is the pure contribution from the physical processes of representing urban structure, TU'10 that of anthropogenic heat release, and TU'11 the contribution of the pure interactions between the two physical processes.

We discuss the respective pure impacts of representing urban structure (TU'01) and that of anthropogenic heat release first (TU'10), in which the other control parameter is absent. The nocturnal (0H; when the UHI maximum is reached) mean $T_{2\mathrm{m}}$-fields and those of the Stein-Alpert decomposition at each gridcell are given in Figs. 6.10 and 6.11 for the earlier mentioned periods during mid-summer and mid-winter, respectively. On the one hand during summer, the pure (i.e. in the absence of urban structure) impact of anthropogenic heat on the UHI intensity is much smaller than that of urban structure (i.e. in the absence of anthropogenic heat release) for summer. The latter reaches values of $+1.97\,\mathrm{K}$ in the model results for Brussels, whereas the former only reaches values of only $+0.68\,\mathrm{K}$. On the other hand during winter conditions, the pure impact of anthropogenic heat becomes larger ($+1.24\,\mathrm{K}$) than that of urban structure ($+0.41\,\mathrm{K}$).

The causes of the seasonal dependency of the pure impacts by the respective control parameters on the UHI are two-fold. At first, the anthropogenic heat is much larger during winter than during summer. At second, the overall incoming radiation is much smaller during winter than during summer, which results in a much smaller conversion of day-time solar irradiation to storage heat by urban structure available for nocturnal storage heat release. The consequential decreased contribution of urban structure to the urban heat island effect during winter is consistent with Giridharan and Kolokotroni (2009) who found that urban-design properties (aspect ratio, surface albedo, plan density ratio, green density ratio, fabric density ratio and thermal mass) cannot explain the changes in outdoor temperatures among different sites around London as much as they did during summer periods.

We now focus on the pure interactions between the physical processes established by the combination of urban structure and anthropogenic heat release (TU'11). For summer, the interactions are negative for the most of the large cities in and around Belgium (Brussels, Ghent, Eindhoven, Lille, with the exception of Antwerp). In particular for the northern part of Brussels, the two control parameters counteract each other. For the centre of Brussels, this was by a value of $-0.21\,\mathrm{K}$ on average. The counteraction between the two control parameters in summer implies that in the presence of urban structure, the impact of anthropogenic heat is even less pronounced than if there would be no urban structure. Analogously, in the presence of anthropogenic heat, the impact of urban structure becomes smaller than if there would be no anthropogenic heat. The latter also means that mitigation of the urban heat island with respect to urban modifications will be less effective in the presence of anthropogenic heat (as is the case) than in the absence of it. For winter, it is striking that the pure interactions are now positive for the large cities (Brussels, Antwerp, Ghent and Nice). For example, they now enhance each other for the most part of Brussels by $+0.25\,\mathrm{K}$. This means that anthropogenic heat has a larger impact in the presence of urban structure than in the absence of it. A possible explanation is the reduced wind speeds established by the urban structure which enhances the effect of anthropogenic heat on the local heating in the city.

Noting the large additional impact of anthropogenic heat over urban structure during winter (both the direct impact and that established by the pure interactions with that from urban structure), the increased energy-efficiency and building-insulation may lower the anthropogenic heat and thus tremendously decrease the UHI build-up, especially during severe winter-temperatures. Noting the small but noticeable additional impact of anthropogenic heat over urban structure during summer, an increasing nocturnal cooling-demand (e.g. of air-conditioning) during more severe heat waves in the future could lead to an important additional anthropogenic heat release. Even though the additional impact on the UHI may be small, it is still crucial to note considering the exponential increase in mortality risk with increased temperatures (Curriero et al., 2002), see also Fig. 1.5. As mentioned above in the Stein and Alpert (1993) analysis, it can also dampen the effect of mitigation strategies with regard to urban structure. However, air-conditioning could have a positive influence on the overall inside thermal comfort. Yet, the consequential increased outside temperatures may induce an additional mortality risk for the disadvantaged populations more vulnerable to heat waves, so that the overall mortality risk still increases. Therefore, the effect of anthropogenic heat may become more important in the future, besides the urban expansion and changes in building materials (e.g. insulation, or albedo of buildings).

6.4.4 Limitations and advantages of the bulk approach

As indicated in Section 4.2.2, a bulk approach has been implemented in TERRA-URB for the representation the urban land-use in CCLM/TU. In this section, the advantages and limitations of the bulk approach for urban regional-climate modelling is discussed. Hereby, we also corroborate our choice of using a bulk approach over a more complex model. Within the scope of urban regional-climate modelling for Belgium, the merits of a bulk approach surpasses those for a more complex urban land-surface model.

The limitations of bulk approaches are given below. Even though bulk approaches

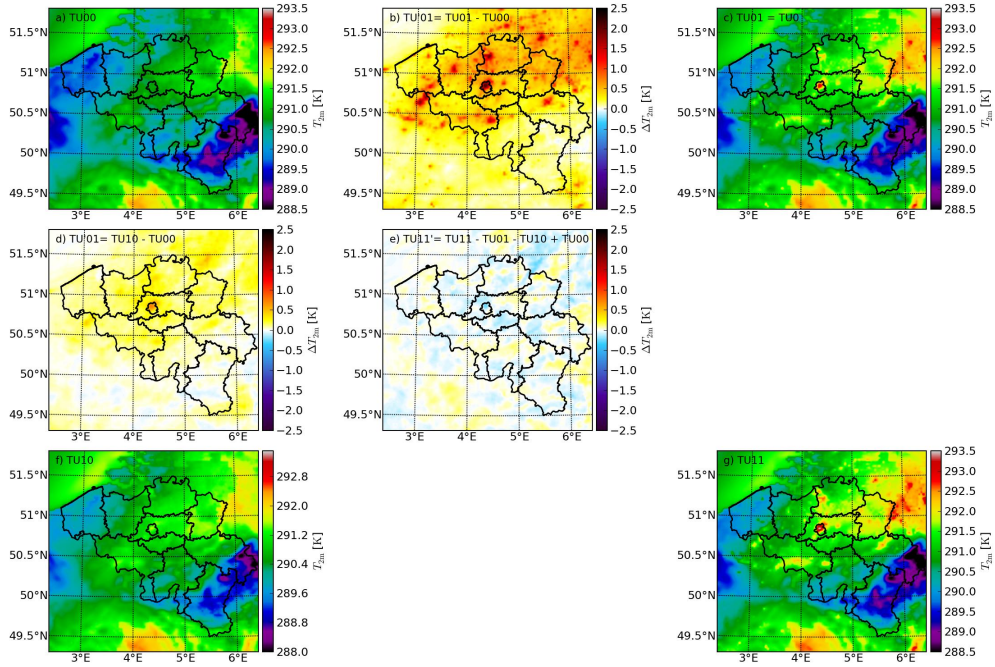

Figure 6.10: Stein and Alpert (1993) decomposition of the impact of urban structure versus anthropogenic heat on the averaged nocturnal (0H) urban heat island during mid-summer (21/06/2012 until 21/07/2012). Panel a (TU00) is the horizontal temperature for the simulation excluding anthropogenic heat and excluding urban structure, panel c (TU01) that from excluding anthropogenic heat and including urban structure, panel f (TU10) that from including anthropogenic heat and excluding urban structure, and panel g (TU11) the reference simulation including anthropogenic heat and urban structure. Panel b shows the pure impact of urban structure in the absence of anthropogenic heat, and panel d that from the pure impact of anthropogenic heat in the absence of urban structure. Panel e shows the pure interactions between the physical processes established by the combination of anthropogenic heat and urban structure. Note that TU01 and TU11 refer to TU0 and TU used in the previous figures, respectively.

represent the (subgrid-scale) differential physical properties between the different land-use (for example, building environments versus parks with vegetation), they do not account for the heterogeneity of used building materials and the specific urban design and morphology within cities. Such heterogeneities may lead to one or more of the complex physical processes described in Section 1.2.1-I within urban environments itself. In particular, the bulk approach can not resolve the heterogeneity of the wind flow (speed and direction) and surface temperatures found within the urban environments, even if one would increase the spatial horizontal resolution of the model. As mentioned in Section 1.2.1-I, this could still lead to important intra-urban temperature contrasts. For instance, Eliasson (1996) found a clear relation between the nocturnal wind speeds and nocturnal air-temperature differences between street canyons and open spaces, especially during clear night hours. A possible reason of such relation between wind speeds and intra-urban temperature differences is that wind speeds inside street canyons remain

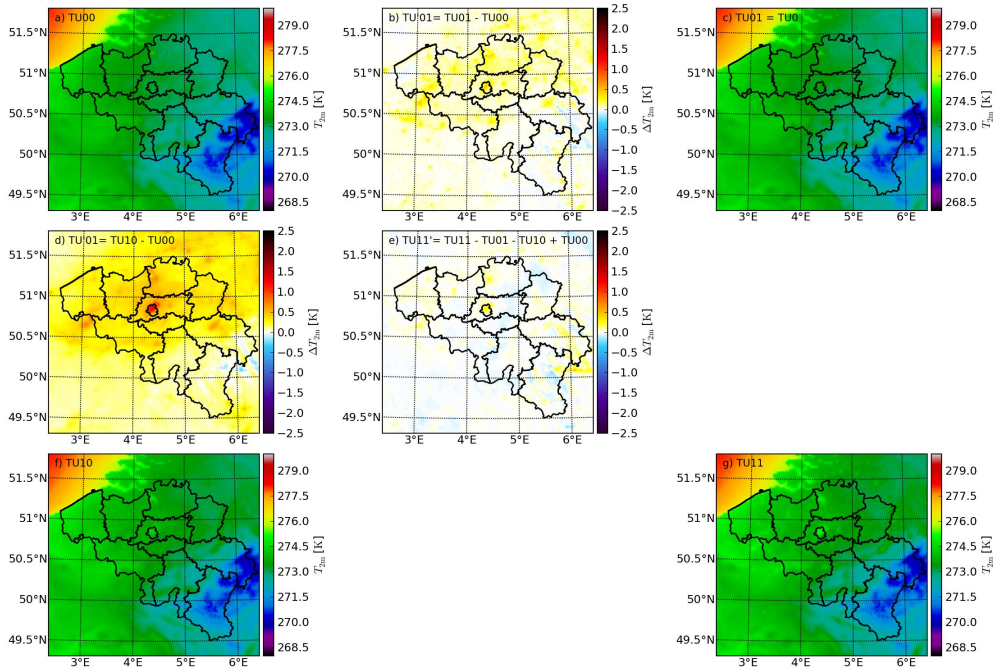

Figure 6.11: Idem as Fig. 6.10, but for mid-winter (2013-01-21 until 2013-02-21).

low, so that the difference in ventilation, hence air-temperature, between canyons and open spaces becomes larger for larger wind speeds. Such intra-urban contrasts in wind and temperature are not resolved by a bulk approach. More complex models compared to more simple approaches (such as the bulk approach) are more flexible and have the potential to better describe the biophysical interactions between the atmosphere and urban surfaces (Grimmond et al., 2011). For instance, more complex models account for different types of surfaces (roofs, walls, roads) in a geometrical configuration (mostly represented as an urban canyon) that explicitly account for the radiation effects depending on the sun position. This way, the more complex schemes partially resolve the subgrid-scale surface-temperature heterogeneity (cfr. roofs, walls, roads) found within urban environments and thus the sub-grid scale micro-climate (resp. air-temperature contrasts near roofs, walls and roads).

The advantages of employing a bulk approach for urban land-surface modelling are given below. Firstly, increasing the model complexity for explicitly representing one or more of the complex physical processes described in Section 1.2.1 (I) can pose practical constraints such as greater computational requirements and the number of parameters requiring specification. In particular, datasets describing the urban morphology and used materials are not available for the entire Belgian domain, which is the domain under study in this chapter. Secondly, interpreting the results from more complex models are generally more difficult than from simple models (e.g. the bulk approach). In addition, the more complicated models are generally more difficult to use and it is even difficult for modellers to identify which are the most critical points of their model (Grimmond et al., 2011). Thirdly, a bulk approach is much easier to integrate in the standard soil modules of

atmospheric models than more complex models. The direct integration of urban land-use in standard soil modules - instead of employing an external urban module for the urban land-use along-side the standard land-surface module for the rural land-use - facilitates the model consistency among the surface types. As a result, model discrepancies of the common processes (cfr. surface-layer transfer schemes or representation of snow cover) leading to artificial differences among urban and rural land use are avoided. Fifthly, thermal and radiative bulk parameters for the urban land-use used in bulk approaches and their uncertainty can be estimated relatively easy (e.g. Demuzere et al., 2008; De Ridder et al., 2012) by combining model results with observations from satellite data or mast measurements. By employing such bulk parameters, the primary radiative, thermal and aerodynamic effects imposed by the urban structural design are a captured in an implicit way by the bulk scheme. Noting the large heterogeneity of urban environments and the consequential complex physical processes (described in Section 1.2.1-I), and the fact that even the most complex models do not include the complete specifications of all exchange processes and variability (examples of such shortcomings are given above), of interest has been what level of improvement in the performance, if any, is obtained with increased model complexity. Therefore, a large number of the urban surface parametrizations was recently evaluated in an international inter-comparison study (Grimmond et al., 2010, 2011). Despite the large efforts of including complex radiation effects imposed by the urban morphology and including the heterogeneity of building materials of street canyons, one of the principal, but striking, conclusions of this study was that simple models perform equally well as more complex ones, which further motivates the choice of employing a bulk approach. Other workers similarly concluded that, for a given model, reducing complexity, e.g., in terms of the number of facets used to represent the urban-structure geometry, in general yield equal performance (e.g. Porson et al., 2009; Ikeda and Kusaka, 2010; Chemel and Sokhi, 2012). As stated by Grimmond et al. (2011), possible reasons are the errors in the urban-landscape parameters needed for the complex schemes. Another possible reason of this striking conclusion is that certain crucial urban-climatic features are still not identified or not accounted for in urban land-surface models. For instance, even the complex schemes still ignore the effects of the intra-urban (cfr. street canyons versus open spaces) variability of the local wind flow imposed by urban design (cfr. open spaces, street directions...). They also ignore the effects of surface-temperature heterogeneity of the urban facets for which the surface-to-air heat exchange will be considerably different (cfr. the sunlit versus shaded parts).

A final remark is that the temperature differences among the surface types represented in more complex models (roofs, walls, and roads) are smaller during the night-time than during the day-time, because of the absence of complex radiation effects established by the solar radiation. It is therefore expected that the explicit representation these different surface types becomes of less importance for nocturnal conditions when the urban heat-island at the regional scale (thus disregarding the possible micro-climates found within the city) reaches a maximum.

6.5 Conclusions and recommendations

In this chapter, the new urban parametrization TERRA-URB for the regional climate model CCLM (the COSMO model in CLimate mode) is evaluated. TERRA-URB extends

the Soil-Vegetation Atmosphere Transfer (SVAT) Model TERRA-ML (the default CCLM SVAT-scheme) for its applicability in urban environments. Afterwards, this chapter focuses on the relative role of anthropogenic heat release versus representation of urban structure on the urban heat island intensity of Belgium for both summer and winter at the regional scale with CCLM coupled to TERRA-URB.

TERRA-URB has been configured and evaluated in offline mode for a densely urban site at Toulouse first. Hereby, TERRA-URB was forced with observations rather than coupling it with the regional-climate model CCLM. These observations include the meteorological quantities and the downward radiation from an observation mast at Toulouse center (France) during the "Canopy and Aerosol Particle Interactions in TOulouse Urban Layer" (CAPITOUL) campaign. The response of TERRA-URB in terms of the urban surface-energy balance including upward infra-red radiation, reflected short-wave radiation, sensible heat and latent heat were evaluated against observations from the same mast, and are reproduced very well. The offline model performance of TERRA-URB is improved by subsequently accounting for its different features. These features include the new surface-layer transfer coefficients (Chapter 3), the water-vapor opacity (Chapter 4), the urban water-storage parametrization (Chapter 5), and the anthropogenic heat release.

Afterwards, CCLM coupled to TERRA-URB has been tested and configured over Belgium for a one-year period starting in June 2012. The results are compared with urban-climate observations for Antwerp. By considering the model results for temperature at an urban and rural ground station, it was found that the urban heat island intensity and its diurnal and daily variability are well reproduced for both winter and summer, though the urban heat island (UHI) during summer was underestimated by 20%. In contrast, the UHI was not well reproduced with CCLM coupled to the standard surface module TERRA-ML. The online model results of CCLM coupled to TERRA-URB are also compared with vertical temperature profiles of observation masts of over 100 m height at an urban station in Zwijndrecht and a rural station in Mol. During the heat-wave periods in 2012, it was found that the profiles are well-reproduced for the urban station. However, the lapse rate for vertical temperature profiles was underestimated for the rural station, which explains the underestimation of the modeled UHI intensity.

Our sensitivity experiments with CCLM coupled to TERRA-URB presented in this chapter has led to an overall better understanding of the climatic drivers of the UHI intensity and their seasonal dependency at the regional scales. It is demonstrated with a Stein-Alpert decomposition that both urban structure, anthropogenic heat release and their interactions determine the seasonal dependency of the nocturnal urban heat island intensity. Remarkably, the averaged contribution of urban structure to the urban heat island for the cities in and around Belgium (+0.41 K for Brussels) is smaller than that from the anthropogenic heat (+1.24 K) during winter. Conversely, the contribution of urban structure (+1.97 K) dominates that of the anthropogenic heat (+0.68 K) during summer, but the latter is still non-negligible. The seasonal dependency of the respective contributions to the UHI stems from the smaller daytime heat storage and larger nocturnal anthropogenic heat release found in cities during winter than during summer.

Complex interactions appear between the respective physical processes established by anthropogenic heat and urban structure, which can amplify or dampen the UHI effect depending on the season. The respective contributions mostly counteract each other during summer (−0.21 K for Brussels), whereas they enhance each other during winter

(+0.25 K). Note that the counteraction in summer means that the presence of urban structure partially masks the contribution anthropogenic heat (or vice versa). The urban climatic drivers of the urban heat island described above are found to be consistent for most of the major cities in and around Belgium.

Within the general assessment under climate change projections (e.g. by downscaling the Representative Concentration Pathways of the IPCC) and of land-use change scenarios at the regional scales in the mid-latitudes the following recommendation is made: One needs to account for the climatic impact of urban structure, anthropogenic heat release, their interactions, and their seasonal dependency simultaneously. Hereby, their respective influences on the urban thermal comfort either in a positive or negative way needs to be considered as well. For instance, the beneficial health impacts by urban modifications alleviating the UHI in summer needs to be compared with the accompanied disadvantageous health impacts in winter. The reduction of the UHI intensity by modifications in urban structure will be dampened in the presence of anthropogenic heat release in summer.

When employing policies for mitigation and adaptation of climate change on the global scale, one needs to account for the possible consequences on the regional scale as well. More particular, policies reducing CO_2 emissions, such as the better insulation of buildings, may also have important effects on the regional scale apart from their effects on the global scale. In fact, such a policy will reduce the anthropogenic heat release during winter and will modify the thermal properties of buildings. Noting the importance of both anthropogenic heat release and urban structure, it is expected that such policies could modify the seasonal dependency of the urban heat island intensity.

Chapter 7

Conclusions and outlook

7.1 Contributions to urban climate modelling research

Urban climate has many consequences on the human society. In this thesis, we have developed a new effecient urban land-surface parametrization TERRA-URB. It extends the SVAT model TERRA-ML for its applicability in urban environments. Hereby, TERRA-ML is the default SVAT model of the regional-climate model CCLM (the COSMO model in CLimate mode), while TERRA-URB is an extension of TERRA-ML including an urban surface class with simplified urban physics in order to capture the urban surface-energy balance. The urban class in TERRA-URB represents the urban structure (roads and buildings) as a rough water-impermeable slab, with appropriate values for the surface roughness length, albedo, emissivity, thermal conductivity and volumetric heat capacity. Both urban and rural land-cover types are accounted for with a tile approach, in which radiative and turbulent fluxes in one horizontal grid cell are weighted according the respective fractional areas.

In order to keep the surface module efficient, we have developed an efficient non-iterative procedure for calculating the surface-layer transfer coefficients that accounts for roughness sublayer effects, and that is generally applicable for urban environments in chapter 3 (Wouters et al., 2012). In particular, the methodology matches very well an iterative procedure for a wide range of aerodynamic and thermal roughness lengths that comprehends both natural and urban land-cover types. Our method is generally applicable to atmospheric models that already use a non-iterative procedure (e.g. the Louis (1979)-type transfer relations), including the regional-climate model CCLM.

TERRA-URB has been tested both in offline and online mode. In the former, TERRA-URB was forced with observed meteorological parameters and downward radiation from an observation mast tower rather than with the atmospheric part of the model itself for a densily-built site in Toulouse center. This way, the response of TERRA-URB in terms of the urban surface-energy balance including upward infra-red radiation, reflected short-wave radiation, sensible heat and latent heat is evaluated against observations from the same mast tower, and these fluxes are reproduced very well. In the latter, TERRA-URB was coupled to the atmospheric part of CCLM, and tested for mid-latitude

temperate climate of Belgium. They could reproduce the diurnal, daily-mean and seasonal variability of the urban heat island very well, which was not possible with the standard version of CCLM. We have further contributed several key developments and insights in the field of urban climate modelling research. This includes the effect of water-vapor opacity on infra-red radiation, a water-storage parameterization and the inclusion of anthropogenic heat. These improvements have lead to a further improvement of the urban modelling results. Their respective roles on urban-climate modelling are listed hereafter.

7.1.1 The inclusion of infra-red water-vapor opacity for urban-climate modelling

A remarkable fact is that most urban parametrizations overestimate the upward infra-red radiation (wave-lengths of more than 5 µm) observed by the tower masts (Grimmond et al., 2011, see their Fig. 5). This was also the case in the initial tests with TERRA-URB. This issue was critical, because the overestimation becomes more pronounced at the time when the urban-climate modelling becomes very relevant, in particular during hazardous heat waves when also the UHI reaches a maximum. Mast measurements for quantifying upward infra-red radiation are typically installed a few tens of meters above roof level. At the same time water vapor that exists between the land-cover and the infra-red sensor can contribute significantly to the absorption and re-emission of infra-red radiation. In order to tackle this issue, we have developed a formulation for the inclusion of infra-red water-vapor opacity in urban land-surface parametrization. This was needed for urban-climate model evaluation with mast sites that are typically several tens of metres above the road level. This resulted in a large positive bias reduction of over $35\,\mathrm{W\,m^{-2}}$ in the upward infra-red radiation generally found in urban land-surface models. In particular, this occurs at day-time when urban surfaces are several tens of degrees warmer than the air above during summer clear-sky conditions with high insolation. This important correction in the urban surface-energy balance allows for a better development, evaluation and comparison of urban climate models in general.

7.1.2 Water retention, evaporation and run-off from urban impervious land-cover

We have developed a water-storage parametrization for modelling the evaporation, water-storage and run-off from the urban impervious surfaces in chapter 5 (Wouters et al., 2014). By considering physically-based surface-interception distribution (SID) of water reservoirs that decreases with depth in a linear way, a comprehensible 2/3-th power dependence on the water-storage was found. The computational efficiency of TERRA-URB allowed us to perform many annual surface model runs in offline mode for estimating the impervious water storage characteristics for urban-stucture surfaces. In particular for a densily-built urban site in Toulouse, the maximum water-content of the impervious surface and the maximum evaporative surface-fractions amounts to $1.31 \pm 0.20\,\mathrm{kg\,m^{-2}}$ and $12 \pm 4\%$, respectively. Employing these water-storage parameters, TERRA-URB successfully reproduces the timing, persistence and magnitude of ET increase after rainfall.

Our sensitivity study demonstrates that the impact of water-storage parametrization has a large impact on the performance of modelling ET in urban areas. It also affects the modelled surface-energy budget in terms of sensible heat and upward infra-red radiation. The modelled annual-mean evaporation from the urban impervious surface during the CAPITOUL campaign is an order of magnitude lower than ET from the natural surroundings.

Our SID water-storage parametrization allows for a more accurate representation of evaporation in urban areas after precipitation. Hereby, the model results employing the SID and using the water-storage parameter estimates are improved in comparison to other arbitrary urban impervious water-storage parametrizations. Therefore, it allows for improved representation atmospheric moisture and precipitation in modelling studies for the present-day and future urban climate change. Herewith, it enables for a more accurate impact assessment of pluvial flooding induced by urban-surface run-off as well.

7.1.3 The role of anthropogenic heat versus urban structure to the urban heat island

Employing state-of-the-art estimates of today's anthropogenic heat release, this thesis proves that the contribution of urban structure to the nocturnal urban heat-island build-up clearly dominates that of the anthropogenic heat release for Belgium during summer. Still, the (nocturnal) anthropogenic heat release has a non-negligible impact at that time. During winter, the contribution of anthropogenic heat release is larger than those arising from urban structure. As a result, anthropogenic heat plays an important role in the seasonal variation of the UHI. The proportion between the impact of urban structure and the additional impact of anthropogenic heat to the UHI is the same for periods of small and large UHI intensities. Moreover, it is demonstrated that complex interactions appear between the respective physical processes established by anthropogenic heat and urban structure. On the one hand, our results indicate a remarkable addition the the UHI intensity from the pure interactions between the physical processes in winter. On the other hand, the two physical processes counteract each other during heat waves in summer. Note that the counteraction in summer means that the presence of urban structure partially masks the contribution anthropogenic heat (or vice versa).

7.1.4 The role of the representation of the PBL in regional climate models

This dissertation explicitly demonstrates that the representation of urban climate features such as the UHI largely depends on the general performance of the regional climate model itself especially during heat waves, not only for urban areas, but also in the surrounding rural areas. One of the most important aspects of the regional climate (modelling) is the interaction of the surface characteristics (i.e. land-use) with the atmosphere above.

It directly determines the structure of the interfacing layer between the ground and the atmosphere above, namely the PBL. It is shown that the representation of features of this boundary layer such as the boundary-layer stability, wind speed, radiative and turbulent processes, not only in but especially outside urban agglomerations, largely affect the

representation of urban climate features such as the UHI. In chapter 2 (Wouters et al., 2013), it is demonstrated with an idealized advection model that the ability of representing the overall nocturnal boundary-layer structure and processes (including stability, radiative cooling and wind speed) is important for modelling the urban heat-island with urban regional climate models. In particular, the overestimation of boundary-layer stability in ARPS was accompanied by an overestimation of the UHI, whereas the underestimation of boundary-layer stability in CCLM has lead to an underestimation of the UHI.

7.1.5 Efficient urban-climate modelling with TERRA-URB is available for a large research network

Our new urban parametrization in CCLM with TERRA-URB is available for the CLM-community for downscaling urban climate at the regional scales. The CLM-community is the large (extra-)European research network (`http://www.clm-community.eu`) that further develops and actively uses CCLM for downscaling regional climate for climate-impact studies in regions all over the world. In particular, a recent urban intercomparison project inside this research network revealed that TERRA-URB is very computationally efficient compared to two other urban parametrizations. It only leads to an additional computational cost of 3% over the standard CCLM model. Two other recently-developed urban parametrizations TEB (Trusilova et al., 2013), and BEP-DCEP (Schubert et al., 2012) implemented in the same model show an additional computational cost of 10% and 15%, respectively. Our improvements with respect to urban climate modelling allows for a better modelling and assessment of present and future urban-climate for any synoptic weather type, including summer heat waves, heavy rain-fall events and extreme winters. Therefore, our efficient and reliable approach of incorporating urban climate at the regional scales allows for its applicability to future urban-climate and air-quality projections employing many ensemble members. It enables to study the urban climate and urban air quality processes for future land-use change scenarios and to propose necessary mitigation or adaptation strategies as well.

7.2 Outlook: the need for improved urban regional climate modelling

7.2.1 The need for further improvements of the representation of the nocturnal boundary layer

The overall performance of representing urban climate features such as the UHI largely depends on the general performance of the used regional-climate model. In particular as cleared out by this thesis, the representation of the nocturnal boundary layer in natural areas is crucial. This is even more important than increasing the complexity of urban climate models noting the rather small differences in the performance between models with different complexity. It is concluded that an overall better representation of the ABL would lead to a more reliable assessment of urban climate and urban air-quality, and the contrast with the natural environment (cfr. the UHI and elevated evening ozone

levels). It may also improve the representation of interactions between different aspects of urbanization (cfr. urban structure versus anthropogenic heat).

7.2.2 The need for improved assignation of anthropogenic heat

Noting the large contribution of anthropogenic heat to the urban climate especially in winter as shown by this thesis, its spatial distribution and variation in time needs to be addressed in more detail. For instance, a large part of anthropogenic heat release may be centralized within certain industrial activities (electricity production, metal processing, data centers...), besides the spatial distribution according to population density and urbanization. The anthropogenic heat release also depends on certain time-dependent factors, for instance cooling demand during heat waves (mentioned before), holidays leading to less energy consumption, and weather conditions (cfr. extreme winters). A first step towards a better assignation of anthropogenic heat is the quantification of the uncertainty by comparing different available datasets for anthropogenic heat release.

7.2.3 The missing link between urban climate modelling at the regional scales and that at the micro-scales

Research focusing on the micro-scale level investigates the wind flow and turbulence transport of mass and heat around buildings. Possible dangers that arise from specific urban-design concepts are studied, such as the development of dangerous wind gusts at holes or corners of buildings. This is established with CFD simulations that are generally evaluated with wind-tunnel experiments. These state-of-the-art tools can explicitly resolve the wind flow around the buildings and in street canyons, and thus explicitly resolve the drag on wind and (vertical) turbulent transport of heat and mass. Therefore, they inherently take into account the urban design allowing for a safer urban planning. Hereby, urban design encompasses different aspects of urban structure, including building sizes, forms and heights, inter-building spacing and street orientations. A particular interesting application is that of the olympic stadium in the Netherlands (van Hooff and Blocken, 2010) to temper the bothersome wind circulation with a minimum of building modifications. A recent development in urban micro-climate CFD modelling is the inclusion of buoyant flow and convective processes in street canyons (Allegrini et al., 2013a). This has been evaluated against very detailed wind-tunnel experiments (Allegrini et al., 2013) and observations (Allegrini et al., 2012b).

One interesting future application of such micro-scale urban climate models is the improvement of efficient urban land-surface parametrization used in urban regional-climate models. In fact, the latter have several existing limitations in the parametrizations of the wind drag, turbulent transport of heat and mass between urban terrain with its variable morphology towards the free atmosphere above (more details on these processes, see section 1.2.1-I). Urban land-surface parametrizations also employ many assumptions that drastically simplify the urban physics. For instance, in urban slab-model approaches as used in this thesis, one typically employs a bluff-rough thermal roughness length parametrization for which the turbulent flux is calculated iteratively within the MOST ("Monin-Obukhov Similarity Theory"). Such turbulent-flux parametrizations can be improved by comparing the model results with CFD simulations employing the same

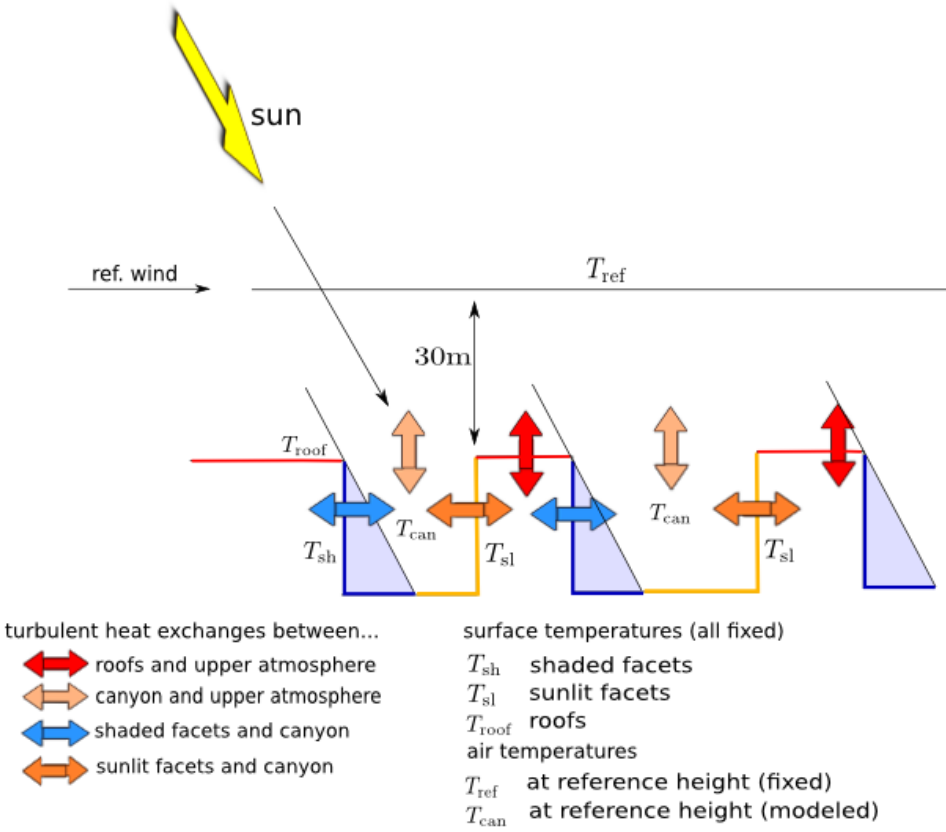

Figure 7.1: Idealized test-case for attributing the flux-partitioning between sunlit and shaded urban facets with CFD.

idealized urban environment. More complex schemes typically perform a turbulent flux-partitioning between the urban facets including roofs, walls and roads (e.g. Masson, 2000; Salamanca et al., 2009; Lemonsu et al., 2012b), all linked to the street-canyon with a homogeneous temperature. Hereby, all facets are considered to have homogeneous surface temperatures as well. Yet, as stated in Section 1.2.4, an increase in the number of facets represented by the model within street canyons does not always lead to better model performance. A possible reason is that it is overruled by the large temperature difference of sunlit and shaded walls. As a result the surface-to-air heat transfer among them are completely different as well, which might overrule the contrasting flux response among the facets. The impact of making the assumption of homogeneous temperatures of the urban facets can be investigated with CFD modelling. Moreover, CFD modelling allows for developing an improved flux-partitioning, for example by employing a flux-partitioning between the sunlit and shaded facets below roof-level as illustrated in Fig. 7.1.

Comparing urban parametrizations with CFD modelling would be a pioneer bridge between the communities of urban CFD modelling at the micro-scale and that of urban-climate modelling at the regional scale in the future. By incorporating the most important

features of urban structure and design on the climate in a simple and efficient way, it would lead to better model performances and wider applicability towards future urban-climate assessment.

7.2.4 Recommendations for improved parameter input datasets

Alongside the representation of urbanization and plant-cover fraction within urban environments, improved representation for the heterogeneity of urban land-use with respect to thermal, radiative properties and roughness would definitely lead to more accurate urban regional climate modelling. Possibly, this data could be derived from the remote sensing of urban morphological aspects combined with datasets for materials being used within cities over Belgium or other countries. Further parameter corrections can be introduced by comparing the obtained parameters with those obtained from model parameter sensitivity studies. Such parameter dependency also needs to be accounted for in land-use models as input for urban climate land-use change scenarios. Even when specifying those parameters to the urban regional-climate models, micro-climate features in the urban environments (for instance established by the local variability in the wind flow) will still not be resolved. Still, the effect of urban design (building sizes, forms and heights, inter-building spacing and street orientations) on the overall turbulent transport momentum and heat at the regional scale could be represented with the model improvements suggested in Section 7.2.3. Further statistical downscaling can be applied for intra-urban temperature variability on the micro-scales for the distinction between street-canyons (accounting for their orientations), back-yards and open spaces, based on the remotely sensed urban morphology. Such a statistical downscaling could be achieved by combining observations with high-resolution CFD results for different cases of urban morphology.

7.3 Recommendations with respect to climate change projections and land-use change scenarios

7.3.1 Inclusion of anthropogenic heat versus urban structure

The inclusion of anthropogenic heat is indispensable for downscaling urban climate. For mid-latitude areas such as Belgium, a future increase (decrease) in anthropogenic heat release leads to less (more) extreme cold air-temperatures in cities during Winter, whereas an increase (decrease) leads to more (less) extreme heat stress in cities during heat waves in summer. Because of the larger contribution of anthropogenic to the urban heat island during winter than in summer, it is expected that relative anthropogenic-heat changes have a larger impact on the extreme cold temperatures in cities at that time. For instance, reducing the anthropogenic heat release in winter by increased energy-efficiency and improved building insulation may have an important impact on the temperature in cities during extremely cold winters. Hereby, the lower temperature may increase the mortality risk during extreme winters (Fig. 1.5). Conversely, changes in anthropogenic heat release have a smaller impact during summer. Yet, The latter could still be crucial noting the increase (of the slope) in mortality risk with increased temperatures.

Within the general assessment of climate change projections (e.g. by downscaling the Representative Concentration Pathways of the IPCC), land-use change scenarios and urban-climate mitigation, one needs to account for the impact of either urban structure, anthropogenic heat, their interactions ànd their seasonal dependency on the regional climate. Hereby, their respective influences on the urban thermal comfort either in a positive or negative way needs to be considered as well. For instance, the beneficial health impacts by urban modifications alleviating the UHI in summer needs to be compared with the accompanied disadvantageous health impacts in winter. The reduction of the UHI intensity by modifications in urban structure will be dampened in the presence of anthropogenic heat release in summer.

The uncertainties, seasonal, diurnal and daytime variability and future changes in anthropogenic heat, but also that of urban structure, in relation to (and in interaction with) the changes in society and global climate needs to be addressed. For instance, anthropogenic heat release during summer may also act as a positive feedback in cities to the expected increase in occurrence of heat waves and increased UHI intensity: Together with growing welfare, it may increase the demand to the energy-consuming infrastructure of air-conditioning, and thus an additional non-negligible and undesirable warming at that time. The uncertainties listed above makes the role of anthropogenic heat release to future urban climate change uncertain as well. Moreover, our results indicate that the impact of any urban-climate mitigation strategy by modifications in urban structure may be overestimated in the presence of anthropogenic heat release in summer (cfr. Counteraction between the physical processes of urban structure and anthropogenic heat for summer).

When employing policies for mitigation and adaptation of climate change on the global scale, one needs to account for the possible consequences on the regional scale as well. More particular, policies reducing CO_2 emissions, such as the better insulation of buildings, may also have important effects on the regional scale apart from their effects on the global scale. In fact, such a policy will reduce the anthropogenic heat release during winter and will modify the thermal properties of buildings. Noting the importance of both anthropogenic heat release and urban structure, it is expected that such policies could modify the seasonal dependency of the urban heat island intensity.

7.3.2 The influence of urban climate on urban air quality

As stated in the introduction, air-quality is hazardous in cities. Furthermore, bad air-quality coincides with urban climate features, more particular with periods of increased UHI intensity. Earlier studies clearly show the impact of urban climate on air-quality. Therefore, air-quality in cities, including the influence of urban climate on urban air quality, needs to be addressed in future urban-climate projections and land-use change scenarios. This can be achieved by coupling air-quality models to urban regional-climate models (such as CCLM/TU) used in the urban-climate projections. An example output of such a modelling strategy for air-quality modelling ozone accounting of the urban-climatic conditions of Brussels during a heat wave of summer 2009 is given in Fig. 7.2.

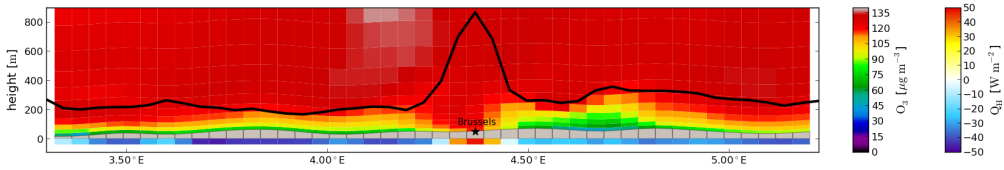

Figure 7.2: Example of air-quality modelling accounting for urban-climatic conditions. The figure shows a Zonal vertical transect through Brussels of ozone concentration modeled by AURORA("Air quality modelling in Urban Regions using an Optimal Resolution Approach"; Mensink et al., 2001). The model takes meteorological input from CCLM/TU for the domain indicated with a rectangle in Fig. 6.4. It is a snapshot (2009/08/16 21:00UTC, local time is 23:00) during the heat wave in august 2009. The z-axis shows the height above sea-level. The black line corresponds to the PBL height simulated by CCLM/TU. The lower colorbar under the orography (grey bars) represents the turbulent surface-heating or cooling at that time.

7.3.3 Interaction between of urban climate and urban water balance

Taking into account the water storage by water-impermeable swaths in urban areas as developed in chapter 5, one can also assess the implementation of existing legislations on the combined effect on pluvial flooding and urban climate. For instance, Vlarem II (`http://www.vlario.be/vademecum-particulieren/vlarem/`; Section 2.3.6.4), which are the Flemish directives for environmental sustainability, decided that a separate system for rainwater and waste water needs be installed in the construction and reconstruction of sewage systems. This leads to a routing of the rainwater from run-off in cities to the natural soil and vegetation in the urban areas. Hereby, one can reduce the risk of pluvial flooding as less water is lost to run-off. As more water is disposable to vegetation in the city (see also Section 6.3.1), this could amplify the cooling capacity of vegetation in cities. In turn, it can have a beneficial effect on the temperature during heat waves in summer.

Bibliography

Alexandri, E., Jones, P., Aug. 2007. Developing a one-dimensional heat and mass transfer algorithm for describing the effect of green roofs on the built environment: Comparison with experimental results. Build. Environ. 42 (8), 2835–2849.

Allen, L., Lindberg, F., Grimmond, C. S. B., Nov. 2011. Global to city scale urban anthropogenic heat flux: model and variability. International Journal of Climatology 31 (13), 1990–2005.

Andreas, E. L., Murphy, B., 1986. Bulk transfer coefficients for heat and momentum over leads and polynas. J Phys Oceanogr 16, 1875–1883.

Arnfield, A. J., Jan. 2003. Two decades of urban climate research: a review of turbulence, exchanges of energy and water, and the urban heat island. Int. J. Climatol. 23 (1), 1–26.

Arya, S. P., 2001. Introduction to micrometeorology, 2nd Edition. Academic Press, San Diego, 420 pp.

Atwater, M., 1974. The radiation model. In: A description of a general three-dimensional numerial simuation model of a coupled air-water and/or air-land boundary layer. Hartford, CT, Ch. Sec. 4 Vol.

Baldauf, M., Seifert, A., Förstner, J., Majewski, D., Raschendorfer, M., Reinhardt, T., Dec. 2011. Operational Convective-Scale Numerical Weather Prediction with the COSMO Model: Description and Sensitivities. Monthly Weather Review 139 (12), 3887–3905.

Basu, R., Dec. 2002. Relation between Elevated Ambient Temperature and Mortality: A Review of the Epidemiologic Evidence. Epidemiologic Reviews 24 (2), 190–202.

Beljaars, A. C. M., Holtslag, A. A. M., Mar. 1991. Flux Parameterization over Land Surfaces for Atmospheric Models. J Appl Meteorol 30, 327–341.

Blümel, K., 2000. An Approximate Analytical Solution of Flux-profile Relationships for the Atmospheric Surface Layer with Different Momentum and Heat Roughness Lengths. Boundary-Layer Meteorol 97, 251–271.

Bohnenstengel, S. I., Evans, S., Clark, P. a., Belcher, S., Jul. 2011. Simulations of the London urban heat island. Q.J.R. Meteorol. Soc. 137 (659), 1625–1640.

Bowler, D. E., Buyung-Ali, L., Knight, T. M., Pullin, A. S., Sep. 2010. Urban greening to cool towns and cities: A systematic review of the empirical evidence. Landscape and Urban Planning 97 (3), 147–155.

Breu, F. X., Guggenbichler, S., Wollmann, J. C., 2009. Planning Systainable cities - Global Report on Human Settlements. UN HABITAT; United Nations Human Settlements Programma, London.

Broadbent, A.M., Coutts, A.M., Demuzere, M., Beringer, J., Tapper, N., 2013a. Temperature variability in a suburb incorporating Water Sensitive Urban Design: Overview of research campaign and methodology. Urban Climate.

Broadbent, A.M., Coutts, A.M., Demuzere, M., Beringer, J., Tapper, N., 2013b. The effect of land surface characteristics on microscale air temperature variability in a suburb incorporating water sensitive urban design. Urban Climate.

Businger, J. A., 1966. Transfer of momentum and heat in the planetary boundary layer. Proc. Symp. Arctic Heat Budget and Atmospheric Ciculation, 305–331.

Byun, D. W., 1990. On the Analytical Solution of Flux-Profile Relationships for the Atmospheric Surface Layer. J Appl Meteorol 29, 652–657.

Cai, G., Du, M., Xue, Y., Li, S., 2008. Analysis of an Urban Heat Sink using Thermal Inertia Model from ASTER Data in Beijing, China. In: Geoscience and Remote Sensing Symposium (IGARSS). Boston, Massachusetts, USA. IEEE International, Boston, Massachusetts, USA, pp. 1346–1349.

Cermak, J. E., Davenport, A. G., Plate, E. J., Viegas, D. X., 1995. Wind climate in cities. Kluwer Academic Publishers, Dordrecht, 772 pp.

Chemel, C., Sokhi, R. S., Feb. 2012. Response of London's Urban Heat Island to a Marine Air Intrusion in an Easterly Wind Regime. Boundary-Layer Meteorology 144 (1), 65–81.

Cheng, Y. G., Brutsaert, W., 2005. Flux–profile relationships for wind speed and temperature in the stable atmospheric boundary layer. Bound.-Lay. Meteorol. 114, 519–538.

Christensen, J., Kumar, K. K., Aldrian, E., An, S.-I., Cavalcanti, I., de Castro, M., Dong, W., Goswami, P., Hall, A., Kanyanga, J., Kitoh, A., Kossin, J., Lau, N.-C., Renwick, J., Stephenson, D., Xie, S.-P., Zhou, T., 2013. The Physical Science Basis. Contribution of Working Group I to the Fifth Assessment Report of the Intergovernmental Panel on Climate Change. Cambridge University Press, UK, Cambridge, Ch. 14, pp. 1217–1308.

Clapp, R. B., Hornberger, G. M., 1978. Empirical equations for some soil hydraulic properties. Water Resour. Res. 14 (4), 601–604.

Cook-Anderson, G., 2004. Urban Heat Islands Make Cities Greener. NASA, 2004–06–29. URL http://www.nasa.gov/centers/goddard/news/topstory/2004/0801uhigreen.html

Cosby, B. J., Hornberger, G. M., Clapp, R. B., Ginn, T. R., 1984. A Statistical Exploration of the Relationships of Soil Moisture Characteristics to the Physical Properties of Soils. Water Resour. Res. 20 (6), 682.

Coutts, A. M., Tapper, N. J., Beringer, J., Loughnan, M., Demuzere, M., Nov. 2012. Watering our cities: The capacity for Water Sensitive Urban Design to support urban cooling and improve human thermal comfort in the Australian context. Progress in Physical Geography 37 (1), 2–28.

Curriero, F. C., Heiner, K. S., Samet, J. M., Zeger, S. L., Strug, L., Patz, J. a., Jan. 2002. Temperature and mortality in 11 cities of the eastern United States. American journal of epidemiology 155 (1), 80–7.

Cuxart, J., Holtslag, A. A. M., Beare, R. J., Bazile, E., Beljaars, A., Cheng, A., Conangla, L., Ek, M., Freedman, F., Hamdi, R., Kerstein, A., Kitagawa, H., Lenderink, G., Lewellen, D., Mailhot, J., Mauritsen, T., Perov, V., Schayes, G., Steeneveld, G.-J., Svensson, G., Taylor, P., Weng, W., Wunsch, S., Xu, K.-M., Sep. 2006. Single-Column Model Intercomparison for a Stably Stratified Atmospheric Boundary Layer. Bound.-Lay. Meteorol. 118, 273–303.

Davies, F., Middleton, D., Bozier, K., Jun. 2007. Urban air pollution modelling and measurements of boundary layer height. Atmospheric Environment 41 (19), 4040–4049.

De Bruin, H. A. R., Ronda, R. J., Van De Wiel, B. J. H., Apr. 2000. Approximate Solutions For The Obukhov Length And The Surface Fluxes In Terms Of Bulk Richardson Numbers. Boundary-Layer Meteorol 95, 145–157.

de Munck, C., Pigeon, G., Masson, V., Meunier, F., Bousquet, P., Tréméac, B., Merchat, M., Poeuf, P., Marchadier, C., Jan. 2013. How much can air conditioning increase air temperatures for a city like Paris, France? International Journal of Climatology 33 (1), 210–227.

De Ridder, K., 2006. Testing Brutsaert's temperature roughness parameterization for representing urban surfaces in atmospheric models 33, 1–4.

De Ridder, K., 2010. Bulk Transfer Relations for the Roughness Sublayer. Bound.-Lay. Meteorol. 134, 257–267.

De Ridder, K., Bertrand, C., Casanova, G., Lefebvre, W., Sep. 2012. Exploring a new method for the retrieval of urban thermophysical properties using thermal infrared remote sensing and deterministic modeling. Journal of Geophysical Research 117 (D17), 1—-14.

De Ridder, K., Lauwaet, D., Maiheu, B., 2014. UrbClim - a fast urban boundary layer climate model. submitted to Urban Climate.

De Ridder, K., Schayes, G., 1997. The IAGL Land Surface Model. J. Appl. Meteor. 36, 167–182.

Deardorff, J. W., 1978. Efficient prediction of ground surface temperature and moisture, with inclusion of a layer of vegetation. Journal of Geophysical Research 83 (C4), 1889–1903.

Demuzere, M., Coutts, A., Göhler, M., Broadbent, A., Wouters, H., van Lipzig, N. P., Gebert, L., 2014. The impact of biofiltration systems, rainwater tanks and urban irrigation on urban canopy evapotranspiration. Submitted to Urban climate.

Demuzere, M., De Ridder, K., van Lipzig, N. P. M., 2008. Modeling the energy balance in Marseille: Sensitivity to roughness length parametrizations and thermal admittance. J. Geophys. Res. 113, 1–19.

Demuzere, M., Oleson, K., Coutts, A. M., Pigeon, G., van Lipzig, N. P. M., Feb. 2013. Simulating the surface energy balance over two contrasting urban environments using the Community Land Model Urban. International Journal of Climatology.

Dickinson, R., 1984. Modeling evapotranspiration for three-dimensional global climate models. Geophysical Monograph Series 29.

Diffenbaugh, N. S., Giorgi, F., Jan. 2012. Climate change hotspots in the CMIP5 global climate model ensemble. Climatic change 114 (3-4), 813–822.

Dimoudi, A., Jan. 2003. Vegetation in the urban environment: microclimatic analysis and benefits. Energy and Buildings 35 (1), 69–76.

Doms, G., Förstner, J., Heise, E., Herzog, H.-J., Raschendorfer, M., Reinhardt, T., Ritter, T., Schrodin, R., Schulz, J.-P., Vogel, G., 2011. A description of the nonhydrostatic regional COSMO model. Part II: Physical parameterization. Deutscher Wetterdienst, 153 pp.

Dyer, A. J., 1967. The turbulent transport of heat and water vapour in an unstable atmosphere. Q.J.R. Meteorol. Soc. 93, 501–508.

Eliasson, I., 1996. Intra-urban nocturnal temperature differences: a multivariate approach. Climate Research 7, 21–30.

Flanner, M. G., Jan. 2009. Integrating anthropogenic heat flux with global climate models. Geophysical Research Letters 36 (2), L02801.

Gabriel, K. M. A., Endlicher, W. R., 2011. Urban and rural mortality rates during heat waves in Berlin and Brandenburg, Germany. Environmental pollution (Barking, Essex : 1987) 159 (8-9), 2044–50.

Garratt, J. R., 1992. The atmospheric boundary layer. Cambridge University Press, UK, 316 pp.

Gaussorgues, G., 1993. Infrared Thermography. Springer, 508 pp.

Giridharan, R., Kolokotroni, M., Sep. 2009. Urban heat island characteristics in London during winter. Solar Energy 83 (9), 1668–1682.

Grasselt, R., 2008. Validation of TERRA-ML with discharge measurements. Meteorologische Zeitschrift 17 (6), 763–773.

Grimmond, C. S. B., Blackett, M., Best, M. J., Baik, J.-J., Belcher, S. E., Beringer, J., Bohnenstengel, S. I., Calmet, I., Chen, F., Coutts, A., Dandou, A., Fortuniak, K., Gouvea, M. L., Hamdi, R., Hendry, M., Kanda, M., Kawai, T., Kawamoto, Y., Kondo, H., Krayenhoff, E. S., Lee, S.-H., Loridan, T., Martilli, A., Masson, V., Miao, S., Oleson, K., Ooka, R., Pigeon, G., Porson, A., Ryu, Y.-H., Salamanca, F., Steeneveld, G. J., Tombrou, M., Voogt, J. A., Younga, D. T., Zhang, N., 2011. Initial results from Phase 2 of the international urban energy balance model comparison. Int. J. Climatol. 31, 244–272.

Grimmond, C. S. B., Blackett, M., Best, M. J., Barlow, J., Baik, J.-J., Belcher, S. E., Bohnenstengel, S. I., Calmet, I., Chen, F., Dandou, A., Fortuniak, K., Gouvea, M. L., Hamdi, R., Hendry, M., Kawai, T., Kawamoto, Y., Kondo, H., Krayenhoff, E. S., Lee, S.-H., Loridan, T., Martilli, A., Masson, V., Miao, S., Oleson, K., Pigeon, G., Porson, A., Ryu, Y.-H., Salamanca, F., Shashua-Bar, L., Steeneveld, G.-J., Tombrou, M., Voogt, J., Young, D., Zhang, N., 2010. The International Urban Energy Balance Models Comparison Project: First Results from Phase 1. J. Appl. Meteor. Climatol 49.

Grimmond, C. S. B., Oke, T. R., 1991. An Evapotranspiration-Interception Model for Urban Areas. Water Resources Research 27 (7), 1739–1755.

Grimmond, C. S. B., Oke, T. R., 1999. Evapotranspiration rates in urban areas. AHS Publ. 259, 235–243.

Grimmond, C. S. B., Oke, T. R., Timothy, R., Jul. 1999. Heat Storage in Urban Areas: Local-Scale Observations and Evaluation of a Simple Model. J. Appl. Meteor. 38 (7), 922–940.

Grossman-Clarke, S., Zehnder, J. A., Loridan, T., Grimmond, C. B., Nov. 2010. Contribution of land use changes to near-surface air temperatures during recent summer extreme heat events in the Phoenix Metropolitan Area.

Guo, X., Zhang, H., Jan. 2007. A performance comparison between nonlinear similarity functions in bulk parameterization for very stable conditions. Environmental Fluid Mechanics 7, 239–257.

Gutman, G., Ignatov, A., 1998. The derivation of the green vegetation fraction from NOAA/AVHRR data for use in numerical weather prediction models. International Journal of Remote Sensing 19 (8), 1533–1543.

Ha, K.-J., Mahrt, L., 2003. Radiative and turbulent fluxes in the nocturnal boundary layer. Tellus 55A, 317–327.

Hamdi, R., Degrauwe, D., Duerinckx, A., Cedilnik, J., Costa, V., Dalkilic, T., Essaouini, K., Jerczynki, M., Kocaman, F., Kullmann, L., Mahfouf, J.-F., Meier, F., Sassi, M., Schneider, S., Váňa, F., Termonia, P., Jan. 2014. Evaluating the performance of SURFEXv5 as a new land surface scheme for the ALADINcy36 and ALARO-0 models. Geoscientific Model Development 7 (1), 23–39.

Hamdi, R., Degrauwe, D., Termonia, P., Sep. 2012. Coupling the Town Energy Balance (TEB) Scheme to an Operational Limited-Area NWP Model: Evaluation for a Highly Urbanized Area in Belgium. Wea. Forecasting 27, 323–344.

Hamdi, R., Schayes, G., Aug. 2007. Validation of Martilli's urban boundary layer scheme with measurements from two mid-latitude European cities. Atmospheric Chemistry and Physics 7 (17), 4513–4526.

Hamdi, R., Termonia, P., Baguis, P., Nov. 2011. Effects of urbanization and climate change on surface runoff of the Brussels Capital Region: a case study using an urban soil-vegetation-atmosphere-transfer model. International Journal of Climatology 31 (13), 1959–1974.

Hamdi, R., Van de Vyver, H., Feb. 2011. Estimating urban heat island effects on near-surface air temperature records of Uccle (Brussels, Belgium): an observational and modeling study. Advances in Science and Research 6 (1), 27–34.

Hara, M., Kusaka, H., Kimura, F., Wakazuki, Y., 2010. Effect of global climate change on urban heat island intensity of Tokyo metropolitan area - winter season case. Nagare, 353–361.

Harman, I. N., Belcher, S. E., Oct. 2006. The surface energy balance and boundary layer over urban street canyons. Q. J. Roy. Meteorol. Soc. 132 (621), 2749–2768.

Hénon, A., Mestayer, P. G., Lagouarde, J.-P., Voogt, J. A., Mar. 2012. An urban neighborhood temperature and energy study from the CAPITOUL experiment with the SOLENE model. Theoretical and Applied Climatology 110 (1-2), 177–196.

Hinkel, K. M., Nelson, F. E., Klene, A. E., Bell, J. H., Dec. 2003. The urban heat island in winter at Barrow, Alaska. International Journal of Climatology 23 (15), 1889–1905.

Holtslag, A. A. M., Ek, M., 1996. Simulation of Surface Fluxes and Boundary-Layer Development over the Pine Forest in HAPEX-MOBILHY. J Appl Meteorol 35, 202–213.

Ikeda, R., Kusaka, H., May 2010. Proposing the Simplification of the Multilayer Urban Canopy Model: Intercomparison Study of Four Models. Journal of Applied Meteorology and Climatology 49 (5), 902–919.

Jain, A. K., 1989. Fundamentals of Digital Image Processing. Prentice Hall, 569 pp.

Kalanda, B. D., Oke, T. R., Spittlehouse, D. L., 1980. Suburban Energy Balance Estimates for Vancouver, B.C., Using the Bowen Ratio-Energy Balance Approach. American Meteorological Society 19, 791–802.

Kanda, M., Kanega, M., Kawai, T., Moriwaki, R., Sugawara, H., Jul. 2007. Roughness Lengths for Momentum and Heat Derived from Outdoor Urban Scale Models. Journal of Applied Meteorology and Climatology 46 (7), 1067–1079.

Kanda, M., Kawai, T., Kanega, M., Moriwaki, R., Narita, K., Hagishima, A., 2005. A simple energy balance model for regular building arrays. Boundary-Layer Meteorology, 423–443.

Kazakova, E., Rozinkina, I., 2011. Testing of Snow Parametrization Scheme in COSMO-Ru: ANalysis and Results. COSMO Newsletter 11, 41–51.

Kunreuther, H., Heal, G., Allen, M., Edenhofer, O., Field, C. B., Yohe, G., Mar. 2013. Risk management and climate change. Nature Climate Change 3 (5), 447–450.

Laaidi, K., Zeghnoun, A., Dousset, B., Bretin, P., Vandentorren, S., Sep. 2011. The Impact of Heat Islands on Mortality in Paris during the August 2003 Heatwave. Environ. Health Perspect. 120 (2), 254–259.

Landsberg, H. E., 1981. International Geophysics Series, Vol. 28: The urban climate. Academic Press, Londen.

Launiainen, J., 1995. Derivation of the relationship between the Obukhov stability parameter and the bulk Richardson number for flux-profile studies. Boundary-Layer Meteorol 76, 165–179.

Lee, H. N., 1997. Improvement of Surface Flux Calculations in the Atmospheric Surface Layer. J Appl Meteorol 36, 1416–1423.

Lee, J. S., 1986. Speckle suppression and analysis for synthetic aperture radar images. Opt. Eng. 25, 636–643.

Lemonsu, A., Belair, S., Mailhot, J., Sep. 2009. The New Canadian Urban Modelling System: Evaluation for Two Cases from the Joint Urban 2003 Oklahoma City Experiment. Bound.-Lay. Meteorol. 133 (1), 47–70.

Lemonsu, A., Kounkou-Arnaud, R., Desplat, J., Salagnac, J.-L., Masson, V., Jul. 2012a. Evolution of the Parisian urban climate under a global changing climate. Climatic Change 116 (3-4), 679–692.

Lemonsu, A., Masson, V., Sep. 2002. Simulation of a Summer Urban Breeze Over Paris. Bound.-Lay. Meteorol. 104 (3), 463–490.

Lemonsu, A., Masson, V., Shashua-Bar, L., Erell, E., Pearlmutter, D., Nov. 2012b. Inclusion of vegetation in the Town Energy Balance model for modelling urban green areas. Geoscientific Model Development 5 (6), 1377–1393.

Li, D., Bou-Zeid, E., Sep. 2013. Synergistic Interactions between Urban Heat Islands and Heat Waves: The Impact in Cities Is Larger than the Sum of Its Parts*. Journal of Applied Meteorology and Climatology 52 (9), 2051–2064.

Li, Y., Gao, Z., Lenschow, D. H., Chen, Z. F., 2010. An Improved Approach for Parameterizing Surface-Layer Turbulent Transfer Coefficients in Numerical Models. Boundary-Layer Meteorol 137, 153–165.

Li, Y., Gao, Z., Li, D., Wang, L., Wang, H., Mar. 2014. An improved non-iterative surface layer flux scheme for atmospheric stable stratification conditions. Geoscientific Model Development 7 (2), 515–529.

Lin, Y.-L., 2007. Mesoscale Dynamics. Cambridge University Press, 630 pp.

Louis, J.-F., 1979. A Parametric Model of the Vertical Eddy Fluxes in the Atmosphere. Boundary-Layer Meteorol 17, 187–202.

Majewski, D., Liermann, D., Prohl, P., Ritter, B., Buchhold, M., Hanisch, T., Paul, G., Wergen, W., Baumgardner, J., Feb. 2002. The Operational Global Icosahedral–Hexagonal Gridpoint Model GME: Description and High-Resolution Tests. Monthly Weather Review 130 (2), 319–338.

Makar, A., Gravel, S., Chirkov, V., Strawbridge, K. B., Froude, F., Arnold, J., Brook, J., 2006. Heat flux, urban properties, and regional weather. Atmos Environ 40, 2750–2766.

Martilli, A., Clappier, A., Rotach, M. W., 2002. An urban surface exchange parameterisation for mesoscale models. BoundaryLayer Meteorology 104 (2), 261–304.

Mascart, P., Noilhan, J., Giordani, H., Feb. 1995. A modified parameterization of flux-profile relationships in the surface layer using different roughness length values for heat and momentum. Boundary-Layer Meteorol 72, 331–344.

Masson, V., 2000. A physically-based scheme for the urban energy budget in atmospheric models. BoundaryLayer Meteorology 94 (3), 357–397.

Masson, V., Gomes, L., Pigeon, G., Liousse, C., Pont, V., Lagouarde, J.-P., Voogt, J., Salmond, J., Oke, T. R., Hidalgo, J., Legain, D., Garrouste, O., Lac, C., Connan, O., Briottet, X., Lachérade, S., Tulet, P., Dec. 2008. The Canopy and Aerosol Particles Interactions in TOulouse Urban Layer (CAPITOUL) experiment. Meteorology and Atmospheric Physics 102 (3-4), 135–157.

Maucha, G., Büttner, G., Kosztra, B., 2010. European validation of GMES Data, Soil Sealing Enhancement.

Mauder, M., Oncley, S. P., Vogt, R., Weidinger, T., Ribeiro, L., Bernhofer, C., Foken, T., Kohsiek, W., Bruin, H. A. R., Liu, H., Nov. 2006. The energy balance experiment EBEX-2000. Part II: Intercomparison of eddy-covariance sensors and post-field data processing methods. Boundary-Layer Meteorology 123 (1), 29–54.

Mensink, C., De Ridder, K., Lewyckyj, N., Delobbe, L., Janssen, L., Van Haver, P., 2001. Computational aspects of Air quality modelling in Urban Regions using an Optimal Resolution Approach. Large-Scale Scientific Computing, Lecture Notes in Computer Science 2179, 299–308.

Miralles, D. G., Holmes, T. R. H., De Jeu, R. A. M., Gash, J. H., Meesters, A. G. C. A., Dolman, A. J., 2011. Global land-surface evaporation estimated from satellite-based observations. Hydrology and Earth System Sciences 15 (2), 453–469.

Monin, A. S., Obukhov, A. M., 1954. Dimensionless Characteristics of Turbulence in the Surface Layer of the Atmosphere. Trudy Geofiz Inst Akad Nauk SSSR 24, 163–187.

Nakayoshi, M., Moriwaki, R., Kawai, T., Kanda, M., Apr. 2009. Experimental study on rainfall interception over an outdoor urban-scale model. Water Resources Research 45 (4), n/a–n/a.

Oke, T., Jan. 1982. The energetic basis of the urban heat island. Q. J. Roy. Meteorol. Soc. 108 (455), 1–24.

Oke, T., 1988. The urban energy balance. Progress in Physical Geography 12, 471–508.

Oke, T. R., 1987. Boundary Layer Climates, 2nd Edition. Methuen and Co. Ltd, London, 435 pp.

Oleson, K. W., Bonan, G. B., Feddema, J., Feb. 2010. Effects of white roofs on urban temperature in a global climate model. Geophysical Research Letters 37 (3), n/a–n/a.

Oleson, K. W., Bonan, G. B., Feddema, J., Jackson, T., Jul. 2011. An examination of urban heat island characteristics in a global climate model. Int. J. Climatol. 31 (12), 1848–1865.

Oleson, K. W., Bonan, G. B., Feddema, J., Vertenstein, M., Grimmond, C. S. B., Apr. 2008. An Urban Parameterization for a Global Climate Model. Part I: Formulation and Evaluation for Two Cities. Journal of Applied Meteorology and Climatology 47 (4), 1038–1060.

Patz, J. A., Campbell-Lendrum, D., Holloway, T., Foley, J. A., Nov. 2005. Impact of regional climate change on human health. Nature 438 (7066), 310–7.
URL http://dx.doi.org/10.1038/nature04188

Paulson, C. A., 1970. The Mathematical Representation of Wind Speed and Temperature Profiles in the Unstable Atmospheric Surface Layer. J Appl Meteorol 9, 857–861.

Pearlmutter, D., Krüger, E. L., Berliner, P., May 2009. The role of evaporation in the energy balance of an open-air scaled urban surface. International Journal of Climatology 29 (6), 911–920.

Physick, W. L., Garratt, J. R., Apr. 1995. Incorporation of a high-roughness lower boundary into a mesoscale model for studies of dry deposition over complex terrain. Bound.-Lay. Meteorol. 74, 55–71.

Pielke, R. A., 2002. Mesoscale Meteorological Modeling, 2nd Edition. Academic Press, San Diego, CA, 676 pp.

Pigeon, G., Legain, D., Durand, P., Masson, V., Nov. 2007. Anthropogenic heat release in an old European agglomeration (Toulouse, France). International Journal of Climatology 27 (14), 1969–1981.

Pigeon, G., Moscicki, M. A., Voogt, J. A., Masson, V., 2008. Simulation of Fall and Winter energy balance over a dense urban area using the TEB scheme. Meteorology and Atmospheric Physics 102 (3-4), 159–171.

Pleim, J. E., 2006. A Simple, Efficient Solution of Flux–Profile Relationships in the Atmospheric Surface Layer. J Appl Meteor Climatol 45, 341–347.

Poelmans, L., Rompaey, A. V., Ntegeka, V., Willems, P., Aug. 2011. The relative impact of climate change and urban expansion on peak flows: a case study in central Belgium. Hydrological Processes 25 (18), 2846–2858.

Porson, A., Harman, I. N., Bohnenstengel, S. I., Belcher, S. E., May 2009. How Many Facets are Needed to Represent the Surface Energy Balance of an Urban Area? Boundary-Layer Meteorology 132 (1), 107–128.

Press, W. H., Teukolsky, S. A., Vetterling, W. T., Flannery, B. P., 1992. Numerical recipes in FORTRAN: The art of scientific computing, 2nd Edition. Cambridge University Press, 934 pp.

Ridders, C. J. F., 1979. A new algorithm for computing a single root of a real continuous function. IEEE Trans Circuits Syst 26, 979–980.

Rockel, B., Will, A., Hense, A., 2008. The Regional Climate Model COSMO-CLM (CCLM). Meteorologische Zeitschrift 17 (4), 347–348.

Rodell, M., Houser, P. R., Jambor, U., Gottschalck, J., Mitchell, K., Meng, C.-J., Arsenault, K., Cosgrove, B., Radakovich, J., Bosilovich, M., Entin, J. K., Walker, J. P., Lohmann, D., Toll, D., Mar. 2004. The Global Land Data Assimilation System. Bulletin of the American Meteorological Society 85 (3), 381–394.

Rosenzweig, C., Solecki, W. D., Hammer, S. A., Mehrotra, S., 2011. No Title. Cambridge University Press, Cambridge, 286 pp.

Rotach, M. W., Vogt, R., Bernhofer, C., Batchvarova, E., Christen, A., Clappier, A., Feddersen, B., Gryning, S.-E., Martucci, G., Mayer, H., Mitev, V., Oke, T. R., Parlow, E., Richner, H., Roth, M., Roulet, Y.-A., Ruffieux, D., Salmond, J. A., Schatzmann, M., Voogt, J. A., Mar. 2005. BUBBLE – an Urban Boundary Layer Meteorology Project. Theoretical and Applied Climatology 81 (3-4), 231–261.

Royne, A., Dey, C., Mells D, Apr. 2005. Cooling of photovoltaic cells under concentrated illumination: a critical review. Solar Energy Materials and Solar Cells 86 (4), 451–483.

Ryu, Y.-H., Baik, J.-J., Kwak, K.-H., Kim, S., Moon, N., Feb. 2013. Impacts of urban land-surface forcing on ozone air quality in the Seoul metropolitan area. Atmospheric Chemistry and Physics 13 (4), 2177–2194.

Sailor, D. J., 2004. The Importance of Including Anthropogenic Heating in Mesoscale Modeling of the Urban Heat Island. In: The 84th AMS Annual Meeting. Seattle.

Sailor, D. J., Feb. 2011. A review of methods for estimating anthropogenic heat and moisture emissions in the urban environment. International Journal of Climatology 31 (2), 189–199.

Salamanca, F., Krpo, A., Martilli, A., Clappier, A., 2009. A new building energy model coupled with an urban canopy parameterization for urban climate simulations—part I. formulation, verification, and sensitivity analysis of the model. Theoretical and Applied Climatology 99 (3-4), 331–344.

Sarkar, A., De Ridder, K., Dec. 2010. The Urban Heat Island Intensity of Paris: A Case Study Based on a Simple Urban Surface Parametrization. Boundary-Layer Meteorol 138, 511–520.

Sarrat, C., Lemonsu, A., Masson, V., Guedalia, D., Mar. 2006. Impact of urban heat island on regional atmospheric pollution. Atmospheric Environment 40 (10), 1743–1758.

Savijärvi, H., Jan. 2006. Radiative and turbulent heating rates in the clear-air boundary layer. Quarterly Journal of the Royal Meteorological Society 132 (614), 147–161.

Schär, C., Vidale, P. L., Lüthi, D., Frei, C., Häberli, C., Liniger, M. A., Appenzeller, C., Jan. 2004. The role of increasing temperature variability in European summer heatwaves. Nature 427 (6972), 332–6.

Schubert, S., Grossman-Clarke, S., Apr. 2013. The Influence of green areas and roof albedos on air temperatures during Extreme Heat Events in Berlin, Germany. Meteorologische Zeitschrift 22 (2), 131–143.

Schubert, S., Grossman-Clarke, S., Martilli, A., May 2012. A Double-Canyon Radiation Scheme for Multi-Layer Urban Canopy Models. Boundary-Layer Meteorology 145 (3), 439–468.

Seaman, N. L., Jun. 2003. Future directions of meteorology related to air-quality research. Environment international 29 (2-3), 245–52.

Smiatek, G., Rockel, B., Schättler, U., Aug. 2008. Time invariant data preprocessor for the climate version of the COSMO model (COSMO-CLM). Meteorologische Zeitschrift 17 (4), 395–405.

Song, Y., Aug. 1998. An Improvement of the Louis Scheme for the Surface Layer in an Atmospheric Modelling System. Boundary-Layer Meteorol 88, 239–254.

Steeneveld, G. J., Wokke, M. J. J., Groot Zwaaftink, C. D., Pijlman, S., Heusinkveld, B. G., Jacobs, A. F. G., Holtslag, A. A. M., 2010. Observations of the radiation divergence in the surface layer and its implication for its parameterization in numerical weather prediction models. Journal of Geophysical Research: Atmospheres 115, D06107.

Stein, U., Alpert, P., 1993. Factor separation in numerical simulations. J. Atmos. Sci. 50, 2107–2115.

Steppeler, J., Doms, G., Schättler, U., Bitzer, H. W., Gassmann, A., Damrath, U., Gregoric, G., Jan. 2003. Meso-gamma scale forecasts using the nonhydrostatic model LM. Meteorology and Atmospheric Physics 82 (1-4), 75–96.

Stewart, I. D., Oke, T. R., Dec. 2012. Local Climate Zones for Urban Temperature Studies. Bulletin of the American Meteorological Society 93 (12), 1879–1900.

Stull, R. B., 1988. An Introduction to Boundary Layer Meteorology, first edit Edition. Kluwer Academic Publishers, 670 pp.

Stull, R. B., 2005. Meteorology For Scientists And Engineers, third edit Edition. Brooks/Cole, 550 pp.

Sugawara, H., Narita, K., 2008. Roughness Length for Heat over an Urban Canopy. Theor. Appl. Climatol. 95, 291–299.

Taha, H., 1997. Urban climates and heat islands: albedo, evapotranspiration, and anthropogenic heat. Energy and Buildings 25 (2), 99–103.

Taha, H., Akbari, H., Rosenfeld, A., Huang, J., 1988. Residential cooling loads and the urban heat island – the effects of albedo. Build. Environ. 23 (4), 271–283.

Trusilova, K., Früh, B., Brienen, S., Walter, A., Masson, V., Pigeon, G., Becker, P., Oct. 2013. Implementation of an Urban Parameterization Scheme into the Regional Climate Model COSMO-CLM. Journal of Applied Meteorology and Climatology 52 (10), 2296–2311.

United Nations, 2009. World Urbanization Prospects, the 2009 Revision. United Nations, Department of Economic and Social Affairs, Population Division, New York.
URL `http://esa.un.org/unpd/wup/doc_highlights.htm`

Uno, I., Cai, X. M., Steyn, D. G., Emori, S., 1995. A simple extension of the Louis method for rough surface layer modeling. Boundary-Layer Meteorol 76, 395–409.

van den Hurk, B., Holtslag, A., Jan. 1997. On the bulk parameterization of surface fluxes for various conditions and parameter ranges. Boundary-Layer Meteorol 82 (1), 119–133.

Van Weverberg, K., De Ridder, K., Van Rompaey, A., 2008. Modeling the Contribution of the Brussels Heat Island to a Long Temperature Time Series. J. Appl. Meteor. Climatol. 47, 976–990.

Velasco, E., Pressley, S., Grivicke, R., Allwine, E., Molina, L. T., Lamb, B., Aug. 2010. Energy balance in urban Mexico City: observation and parameterization during the MILAGRO/MCMA-2006 field campaign. Theoretical and Applied Climatology 103 (3-4), 501–517.

Viterbo, P., Beljaars, A. C. M., Mahouf, J.-F., Teixeira, J., 1999. The representation of soil moisture freezing and its impact on the stable boundary layer. Q J R Meteorol Soc 125, 2401–2426.

Voogt, J. A., Grimmond, C. S. B., 2000. Modelling surface sensible heat flux using surface radiative temperatures in a simple urban area. J Appl Meteorol 39, 1679–1699.

Wittich, K.-P., Hansing, O., Dec. 1995. Area-averaged vegetative cover fraction estimated from satellite data. International Journal of Biometeorology 38 (4), 209–215.

Wouters, H., De Ridder, K., Demuzere, M., Lauwaet, D., van Lipzig, N. P. M., 2013. The diurnal evolution of the urban heat island of Paris: a model-based case study during Summer 2006. Atmospheric Chemistry and Physics 13 (17), 8525–8541.

Wouters, H., De Ridder, K., Lipzig, N. P. M., Jun. 2012. Comprehensive Parametrization of Surface-Layer Transfer Coefficients for Use in Atmospheric Numerical Models. Boundary-Layer Meteorology 145 (3), 539–550.

Wouters, H., Demuzere, M., Ridder, K. D., Van Lipzig, N. P. M., 2014. The impact of water-storage parametrization on urban climate modelling. submitted to Urban Climate.

Xue, M., Droegemeier, K. K., Wong, V., 2000. The Advanced Regional Prediction System (ARPS) - A multi-scale nonhydrostatic atmospheric simulation and prediction model. Part I: Model dynamics and verification. Meteorol. Atmos. Phys. 75, 161–193.

Xue, M., Droegemeier, K. K., Wong, V., Shapiro, A., Brewster, K., Carr, F., Weber, D., Liu, Y., Wang, D., Feb. 2001. The Advanced Regional Prediction System (ARPS) - A multi-scale nonhydrostatic atmospheric simulation and prediction tool. Part II: Model physics and applications. Meteorol. Atmos. Phys. 76 (1-4), 143–165.

Yang, K., Tamai, N., Koike, T., 2001. Analytical Solution of Surface Layer Similarity Equations. J Appl Meteorol 40, 1647–1653.

Zhang, G. J., Cai, M., Hu, A., Jan. 2013. Energy consumption and the unexplained winter warming over northern Asia and North America. Nature Climate Change 3 (5), 466–470.

Zilitinkevich, S. S., 1970. Dynamics of the atmospheric boundary layer. Leningrad Gidrometeor, 291 pp.

FACULTY OF SCIENCE
DEPARTMENT OF EARTH AND ENVIRONMENTAL SCIENCES
DIVISION OF GEOGRAPHY
Celestijnenlaan 200E
B-3001 Heverlee
hendrik.wouters@ees.kuleuven.be
ees.kuleuven.be/geography/rcs/